ALICE-TDR-016

CERN-LHCC-2013-020
March 3, 2014

Technical Design Report

for the

Upgrade of the ALICE Time Projection Chamber

The ALICE Collaboration*

*See list of authors in App. C

Executive summary

This Technical Design Report describes the upgrade of the ALICE Time Projection Chamber (TPC), which is an integral part of the ALICE upgrade strategy after LHC Long Shutdown 2 (LS2) [1]. The main design considerations and technical specifications are summarized in the following.

In Chap. 1 the chief scientific goals of the future ALICE physics program are briefly reviewed and the resulting requirements for the TPC upgrade are presented. The expected increase of the LHC luminosity after LS2 to about 50 kHz in Pb–Pb implies that TPC operation with a gating grid is no longer possible. This motivates the choice of GEMs for the new readout chambers, since they feature intrinsic ion blocking capabilities that avoid massive charge accumulation in the drift volume from back-drifting ions, and prevent excessive space-charge distortions. However, GEMs do not feature the same opacity for ions as a gating grid. The requirement to keep the distortions at a tolerable level leads to an upper limit of 1 % for the fractional ion backflow (IBF) at a gas gain of 2000. The resulting space-charge distortions are less than 10 cm in most of the TPC drift volume and can be calibrated with sufficient precision. The achievement of this goal is the result of a major R&D effort presented in this document. The replacement of the existing MWPC-based readout chambers by GEMs implies also the necessity for new readout electronics that accommodate the negative signal polarity and enable continuous data readout. Moreover, the high data rate requires data compression by a factor of about 20 in order to match the anticipated bandwidth to permanent storage. This implies that significant pattern recognition and data format optimization must be performed online. The present particle identification (PID) capability via the measurement of the specific ionization $\mathrm{d}E/\mathrm{d}x$ and the combined momentum resolution of the central barrel tracking system must be retained by the TPC upgrade.

Most of the main components of the existing TPC, including the field cage, the endplates, the gas system and services will be reused after the upgrade. A short overview of those components is given in Chap. 2.

The choice of the detector gas is presented in Chap. 3. The requirements in terms of drift velocity, diffusion, gas gain, and ion mobility lead to Ne-CO_2-N_2 (90-10-5) as a baseline gas mixture for the TPC.

The technical solution that was chosen for the new readout chambers is presented in Chap. 4. Their design is such that the segmentation in azimuth and the division into inner and outer readout chambers (IROCs and OROCs) is identical to those of the existing detector. The new readout chambers will employ stacks of four GEM foils for gas amplification and anode pad readout. Quadruple GEM stacks have proven to provide sufficient ion blocking capabilities at the required gas gain of 2000 in Ne-CO_2-N_2 (90-10-5), in particular when GEM foils with large hole pitch are used. The size of the readout chambers, in particular of the OROCs, favors the use of large-size GEM foils manufactured with the single-mask technology. Such foils were recently implemented successfully in the new KLOE-2 tracking system. Application of this technique allows production of the readout chambers such that a single large GEM foil per layer can be used in the IROCs, and three large GEM foils per layer in the OROCs. The readout pad structure of the existing TPC, with three different pad sizes that increase from small to large radii, will be modified only slightly for the new readout chambers. The local position resolution of the GEM detectors, in particular at short drift distances, is slighly worse than that of the present system due to the lack of a pad response

function. However, this has no observable effect on the combined momentum resolution of the ALICE central barrel system, as shown in Chap. 7. At the same time, the difference in coupling to the readout plane will reduce the detector occupancy in GEMs compared to that in the existing MWPC. To ensure safe operation and long-term reliability, a careful quality assurance procedure for GEM foils and readout chambers at the various assembly stages is being developed and described in Chap. 4.

The main results from R&D with small and full-sized prototypes are discussed in Chap. 5. In a quadruple GEM system including foils with large hole pitch, ion backflow values below 1 % at a gas gain of 2000 and an energy resolution $\sigma(^{55}\mathrm{Fe}) = 12\,\%$ are observed. These operational conditions match safely the requirements of the detector and leave room for further optimizations. The ion backflow results are well described by a microscopic detector simulation based on the Garfield++ framework. Test beam results from a full-size IROC prototype equipped with a triple GEM stack show that the same $\mathrm{d}E/\mathrm{d}x$ resolution as in MWPC-based readout chambers can be achieved. Some of the possible further R&D directions, including COBRA GEMs and MicoMegas, are described in Chap. 9.

The new TPC front-end electronics and readout system is discussed in Chap. 6. The main specifications remain unchanged with respect to the existing detector. However, new characteristics have to be incorporated: The front-end ASIC has to amplify and process signals with opposite polarity as compared to those of an MWPC. The detector signals have to be sampled continuously while concurrently the aquired data is transferred off-detector. Finally, the data throughput will be strongly increased with respect to the current system. The SAMPA project aims at delivering an ASIC fulfilling these requirements. The SAMPA ASICs connect to the common read-out unit (CRU), which provides the interface to the online computing system, the trigger system and the DCS, through optical fibers via the GBT link. Both, SAMPA and CRU, are common solutions for different ALICE subsystems and are described in a separate Technical Design Report on the upgrade of the readout and trigger system [2].

In Chap. 7 an evaluation of the performance of the upgraded TPC is presented. Using a microscopic simulation of the TPC with GEM readout, the intrinsic momentum and $\mathrm{d}E/\mathrm{d}x$ resolutions are found to be the same as with the existing TPC, if the local energy resolution does not exceed $\sigma(^{55}\mathrm{Fe}) = 12\,\%$. No significant deterioration of the tracking efficiency nor the momentum resolution is observed when event pileup, corresponding to collision rates of 50 kHz, is introduced. The $\mathrm{d}E/\mathrm{d}x$ resolution slightly worsens with increasing occupancy from 5.5 % in isolated pp events without pileup to about 7.5 % in central Pb–Pb at 50 kHz. This behaviour is similar when using MWPC or GEM and is understood in terms of an increasing overlap of clusters.

Detailed calculations of the ion space-charge density in the TPC caused by back-drifting ions from the amplification region are presented. The time it takes for ions to drift to the central electrode is close to 160 ms, leading to an average pileup of ions from about 8000 collisions in the TPC drift volume at an interaction rate of 50 kHz. At a gas gain of 2000 in Ne-CO_2-N_2 (90-10-5) and an ion backflow of 1 %, this results in space-charge distortions that stay below 10 cm in most of the TPC volume, with the exception of the innermost region (small r) and at the largest drift length, where radial distortions up to 20 cm are observed. In order to reach the intrinsic track resolution of the TPC of a few hundred μm, distortion corrections with a precision on the level of 10^{-3} need to be performed. It is demonstrated that statistical fluctuations of the collision rate and of the charged-particle multiplicity lead to temporal variations of the space-charge density that are of the order of a few percent, i.e. significantly larger than the required precision of the correction. This implies that the space-charge density and thus the space-charge distortion corrections must be determined as a function of time during the data acquisition. Detailed studies demonstrate that a given space-charge configuration can be considered as static over time intervals of ~ 5 ms.

The strategy for online reconstruction and calibration is discussed in Chap. 8. Online reconstruction is necessary in order to achieve data compression by a factor of 20 as compared to the raw data size, and

to allow for permanent storage of the data. Such compression factors can be achieved if the association of clusters to tracks can be performed online, which implies also the necessity for sufficient online correction of the space-charge distortions. We argue that the standard TPC tracking scheme including the use of a coarse distortion correction map that can be determined online provides high tracking and cluster association efficiency. Moreover, it provides sufficient spatial accuracy to allow efficient matching of the TPC tracks to the Inner Tracking System (ITS), which is necessary to conduct the subsequent calibration steps. The final space-point calibration is based on a residual distortion correction employing external reference track information from the ITS and the Transition Radiation Detector (TRD). In this step, the residual space-charge density fluctuations, which require an updated residual correction map every 5 ms, are addressed. We demonstrate that the available track statistics accumulated over such time intervals is adequate to determine the residual distortions in a grid of sufficient spatial granularity, and with a precision that is consistent with the intrinsic resolution of the TPC.

Chapters 10 and 11 discuss the detector control system and installation, commissioning and services. Most of the aspects presented here build on the existing system and profit from the experience gained with it.

The project organization and considerations on budget and time schedule are discussed in Chap. 12. The ALICE TPC collaboration has gained a significant number of new collaborators with considerable experience and manpower to carry out the upgrade project. The overall CORE cost of the project of 9.2 MCHF is consistent with the ongoing funding requests in different countries. The overall time line of the project matches the current LHC schedule and foresees that the upgraded TPC will be ready for operation after LS2.

Contents

Chapter 1

Physics objectives and design considerations

Studies of heavy-ion collisions at the Large Hadron Collider (LHC) are ideally suited to probe fundamental properties of QCD, including its non-perturbative aspects related to color charge deconfinement, and the restoration of chiral symmetry. In particular, heavy-ion collisions allow the detailed characterization of the Quark-Gluon Plasma (QGP), and the nature of the phase transition between QGP and normal hadronic matter.

ALICE[1] at the LHC is dedicated to these studies [1]. Operation of the ALICE detector in collisions of ^{208}Pb-ions at $\sqrt{s_{\rm NN}} = 2.76\,\text{TeV}$ in 2010 and 2011 (integrated luminosity $\mathscr{L}_{\rm int} = 0.16\,\text{nb}^{-1}$) has demonstrated its excellent tracking and particle identification (PID) capabilities in an environment of large charged-particle densities. The lead-ion campaigns in RUN 2 after the LHC Long Shutdown 1 (LS1), starting in 2015, will conclude the initial LHC heavy-ion programme with $1\,\text{nb}^{-1}$.

A significant increase of the LHC luminosity for heavy ions is expected in RUN 3 after Long Shutdown 2 (LS2), leading to collision rates of about 50 kHz and $\mathscr{L}_{\rm int} = 10\,\text{nb}^{-1}$. This implies a substantial enhancement of the sensitivity to a number of rare probes that are key observables for the characterization of strongly interacting matter at high temperature.

In order to fully exploit the scientific potential of the LHC in RUN 3, ALICE plans to extend its physics programme by improving its detector performance. As an integral part of the ALICE upgrade strategy, this Technical Design Report describes the concept of a novel readout scheme, based on GEM[2] technology, that will be implemented in the Time Projection Chamber (TPC) upgrade. The present MWPC[3]-based readout chambers will be replaced by a GEM system to match the TPC readout rate with the increased Pb–Pb collision rate of the LHC in RUN 3. At the same time, the front-end electronics and readout system will be replaced in order to match the new readout chamber technology and increased data rates. After these upgrades, the data collection rate of the TPC will be increased by about a factor 100 in the high-luminosity environment of the LHC in RUN 3, while the tracking and PID capabilities of the present TPC will be retained.

1.1 Physics Objectives

The scientific goals of the upgraded ALICE detector are described in a comprehensive Letter of Intent [2]. They are aimed at improving measurements for understanding heavy-quark production at low transverse

[1] A Large Ion Collider Experiment (ALICE)
[2] Gas Electron Multiplier (GEM)
[3] Multi-Wire Proportional Chamber (MWPC)

momentum (p_{T}), mechanisms of quarkonium production and interaction in the QGP, initial temperature and partonic equation of state, possible effects of chiral symmetry restoration, parton energy loss, medium modification and its dependence on properties of the parton and the QGP, and exotic hadronic states. To accomplish these, the following measurements will be undertaken in the central barrel of the ALICE detector:

- Yields and azimuthal distributions of hadrons containing heavy quarks (c, b) to study the mechanism of heavy-quark thermalization in the QGP.
- Production of quarkonia at low p_{T}, in particular the study of their possible dissociation and regeneration mechanisms in the QGP.
- Low-mass dielectron production to extract information on early temperature and the partonic equation of state, and to characterize the chiral phase transition.
- Jets and jet correlations, in particular their structure and particle composition, to study the mechanism of partonic energy loss in medium and its dependence on parton color-charge, mass and energy.
- The production of nuclei, anti-nuclei and hyper-nuclei as well as exotic hadronic states such as the H-dibaryon.

These measurements require excellent charged-particle tracking capabilities as well as a variety of PID techniques in the central barrel, down to the lowest possible p_{T}. Measurements at low transverse momenta typically imply small signal-to-background ratios, which limits the applicability of standard low-level triggering schemes. As a consequence, the detectors and readout systems must allow to operate at very high readout and data acquisition rates in order to collect sufficient statistics.

1.2 Upgrade concept

A significant increase in the sensitivity of ALICE to these observables is achieved by major upgrades of its detectors and readout systems in the central barrel of the experiment. A new Inner Tracking System (ITS) improves by a factor 3 the resolution for secondary vertices and extends its tracking capabilities to lower transverse momenta [3]. Moreover, the material budget of the ITS is reduced from 1.1 % of X_0 per detector layer to to 0.3 % for the three inner layers and 0.8 % for the four outer layers. The performance of the new ITS will significantly expand the physics reach of the ALICE central barrel, in particular in the heavy-flavor and low-mass dielectron sector.

On the other hand, precision measurements of the key observables outlined above require tracking and PID information from the TPC. In order to conduct the envisaged physics programme with optimum precision, exploiting the full LHC luminosity, the TPC will be upgraded. This upgrade is intended primarily to overcome the rate limitation of the present system, which arises from the gated operation of the MWPC-based readout chambers.

The ALICE TPC is the largest detector of its type, with an overall active volume of about 90 m^3 [4, 5]. The TPC employs a cylindrical field cage with a central high voltage electrode at $z = 0$ (for a definition of the ALICE coordinate system see App. A.1) and a readout plane on each endplate. It covers full azimuth in $|\eta| < 0.9$ and provides charged-particle tracking over a wide transverse momentum range. The readout planes consist of 72 MWPC-based readout chambers, with a total of about 550,000 readout cathode pads.

Charged-particle tracking and PID via ionization energy loss ($\mathrm{d}E/\mathrm{d}x$) in the TPC is accomplished by the measurement of the ionization of up to 159 samples along a trajectory of $\sim$160 cm. In pp and central

Pb–Pb collisions a resolution $\sigma(\mathrm{d}E/\mathrm{d}x)/\langle \mathrm{d}E/\mathrm{d}x\rangle$ of about 5.5 % and 7 % is achieved, respectively. Further PID capabilities arise from topological reconstruction of the weak decays of strange hadrons and gamma conversions.

The readout chambers are operated with an active bipolar Gating Grid (GG) which, in the presence of a trigger, switches to transparent mode to allow the ionization electrons to pass into the amplification region. After the maximum drift time of $\sim$100 μs the GG wires are biased with an alternating voltage $\Delta V = \pm 90$ V that renders the grid opaque to electrons and ions. This protects the amplification region against unwanted ionization from the drift region, and prevents back-drifting ions from the amplification region to enter the drift volume. In particular, the latter would lead to significant space-charge accumulation and drift-field distortions. Due to the low mobility of ions ($\mu_{\mathrm{ion}} = \mathcal{O}(10^{-3}) \cdot \mu_{\mathrm{electron}}$), efficient ion blocking requires the GG to remain closed for $\sim$180 μs after the end of the event readout, corresponding to the typical time it takes the ions in a Ne-based gas mixture to drift from the anode wires to the GG. This gating scheme leads to an intrinsic dead time of the TPC system of $\sim$280 μs, implying a principal rate limitation of the present TPC to about 3.5 kHz. It should be noted that due to the present TPC readout system the data rate is limited to $\sim$300 Hz for central Pb–Pb collisions.

Operation of the TPC at 50 kHz cannot be accomplished with an active ion gating scheme. On the other hand, back-drifting ions from the amplification region of a MWPC without gate will lead to excessive ion charge densities and drift distortions that render precise space-point measurements impossible. The proposed scheme therefore entails replacement of the existing MWPC-based readout chambers by a multi-stage GEM system. GEMs have proven to operate reliably in high-rate applications and provide intrinsic ion blocking capabilities, therefore enabling the TPC to operate in a continuous, ungated readout mode at collision rates of 50 kHz. The TPC upgrade increases the readout rate by about two orders of magnitude as compared to the present system, thus giving access to previously inaccessible physics observables. As an example, the low-mass dielectron invariant mass spectrum is shown in Fig. 1.1, accumulated in a typical yearly heavy-ion run ($\sim 3\,\mathrm{nb}^{-1}$) with the current (left) and upgraded (right) TPC.

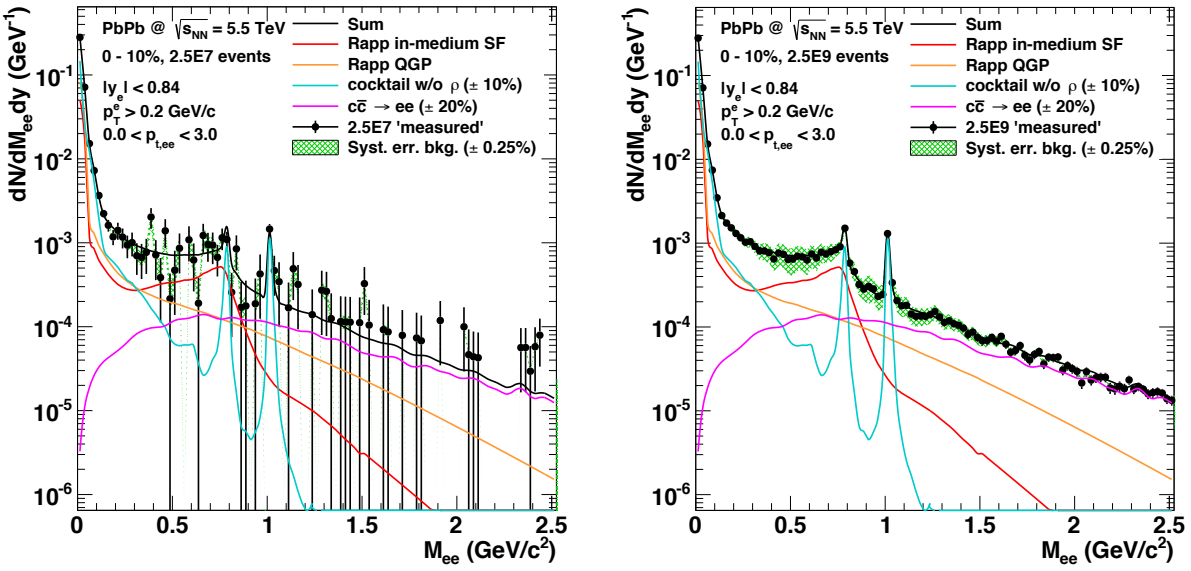

Figure 1.1: Inclusive e^+e^- invariant mass spectrum for 0 – 10 % most central Pb–Pb collisions at $\sqrt{s_{\mathrm{NN}}} = 5.5$ TeV, assuming $2.5 \cdot 10^7$ events (left panel) and $2.5 \cdot 10^9$ events (right panel). The spectra include a set of tight primary track cuts based on the new ITS system to suppress leptons from charm decays. Also shown are curves that represent the contributions from light hadrons (blue), charm (magenta) and thermal radiation from a hadronic gas (red) and a QGP (orange). The figures are from [2].

1.3 Design considerations

The present document describes a proposal for a new readout scheme of the ALICE TPC, based on GEM technology. The main considerations for the design of the system and choices of technologies are summarized in the following.

- The new GEM-based readout chambers must provide sufficient ion blocking to keep the resulting drift field distortions in Pb–Pb collisions at a tolerable level. The distortions must be correctable without deterioration of the online reconstruction efficiency and the final momentum resolution of the detector.
- The new readout scheme requires a complete redesign of the TPC front-end and readout electronics system. The new electronics must accommodate the negative signal polarity of the GEM detectors and the continuous readout scheme. Additionally, the minimization of the ion space-charge density requires the operation of the readout chambers at the lowest possible gas gain, leading to a front-end noise requirement of ENC[4] of around $670\,e$.
- The limited bandwidth of the data acquisition system requires significant online data reduction. The present scheme foresees that cluster finding and association to tracks is performed in an online computing system to achieve the required data compression factor of ~ 20.
- The upgraded TPC must preserve the performance of the existing system in terms of momentum and $\mathrm{d}E/\mathrm{d}x$ resolution. This requires that the space-charge distortions must be corrected to the level of the intrinsic spatial track resolution of the TPC, i.e. to a few hundred μm. The present $\mathrm{d}E/\mathrm{d}x$ performance of the TPC requires a precise equilibration and normalization of the ionization energy loss throughout the entire TPC volume. Moreover, the local energy resolution of the readout chambers must not exceed $\sigma(^{55}\mathrm{Fe}) = 12\,\%$ at 5.9 keV. The latter is affected by the transparency of the GEM system to primary electrons and demands a careful optimization of the operational point with respect to electron collection efficiency and ion blocking.
- The upgrade of the TPC readout chambers and electronics must allow the re-use of the existing hardware to the greatest possible extent. This applies in particular to the existing field cage, gas system, cooling, and services.

1.4 Detector overview

The requirements for the TPC upgrade listed above have led to the technical design presented in this document. In the following section we summarize briefly the main aspects of the proposed solution.

The overall dimensions of the TPC will remain unchanged. Also the segmentation of the readout planes into Inner and Outer Readout Chambers (IROCs and OROCs), 18 each on either endplate, will be preserved. This permits to re-use most of the components of the existing field cage and endplate structures. The powering scheme of the field cage will be adapted to match the higher terminating voltages determined by the GEM system.

The upgraded TPC will be operated with a Ne-CO_2-N_2 (90-10-5) gas mixture. This choice is mainly driven by the higher ion mobility in neon as compared to argon, which leads to less space-charge accumulation in the drift field.

The new TPC readout chambers will be equipped with quadruple GEM stacks for gas amplification. Comprehensive R&D studies have shown that conventional triple GEM stacks using standard geometry GEM foils will not lead to sufficient ion blocking. In prototype measurements with quadruple GEM

[4] Equivalent Noise Charge (ENC)

systems, ion backflow fractions $< 1\,\%$ have been reached at a gas gain of 2000 and an energy resolution of $\sigma(^{55}\mathrm{Fe}) = 12\,\%$ at 5.9 keV. These operational conditions will preserve the intrinsic $\mathrm{d}E/\mathrm{d}x$ resolution and keep the space-charge distortions at a tolerable level.

A new front-end electronics and readout system is being developed. The design of the new electronics is driven by the requirement of low-noise operation and the challenges of continuous readout and high data rate.

The upgraded TPC will provide similar momentum resolution as the present system. However, the operation in continuous readout at high luminosity demands for innovative calibration and correction schemes, in particular with respect to space-charge distortions. Moreover, significant data reconstruction will have to be performed online to allow efficient data compression. With the design presented in this document, these requirements can be fulfilled.

A summary of the TPC parameters is given in Table 1.1.

Detector gas	Ne-CO_2-N_2 (90-10-5)
Gas volume	90 m^3
Drift voltage	100 kV
Drift field	400 V/cm
Maximal drift length	250 cm
Electron drift velocity	2.58 cm/μs
Maximum electron drift time	97 μs
$\omega\tau$ ($B = 0.5$ T)	0.32
Electron diffusion coefficients	$D_T = 209\,\mu m/\sqrt{cm}$, $D_L = 221\,\mu m/\sqrt{cm}$
Ne^+ drift velocity	1.632 cm/ms
Maximum Ne^+ drift time	153 ms
Readout chambers	
Total number	$2 \times 2 \times 18 = 72$
Readout technology	4-GEM stack, single mask, standard (140 μm) and large (280 μm) hole pitch
Gas gain	2000
Ion back flow	< 1 %
Energy resolution at 5.9 keV	12 %
Inner (IROC)	
Total number	$2 \times 18 = 36$
Active range	$848 < r < 1321$ mm
Pad size	4×7.5 mm^2 $(r\phi \times r)$
Pad rows	63
Total pads (IROC)	5504
S:*N*	20:1
Outer (OROC)	
Total number	$2 \times 18 = 36$
Active range	$1346 < r < 2461$ mm
Pad size (inner)	6×10 mm^2 $(r\phi \times r)$ ($1346 < r < 2066$ mm)
Pad rows (inner)	70
Total pads (inner)	6656
Pad size (outer)	6×15 mm^2 $(r\phi \times r)$ ($2086 < r < 2461$ mm)
Pad rows (outer)	25
Total pads (outer)	3200
Total pads (OROC)	9856
S:*N*	30:1
Readout electronics	
Number of channels	552,960
Signal polarity	negative
Dynamic range	$30 \times$ MIP
System noise (mean)	670 e
PASA conversion gain	20 (30) mV/fC
PASA peaking time	160 (80) ns
ADC number of bits	10
ADC sampling rate	10 (20) MHz
Power consumption	< 35 mW/ch
Operating conditions and data rate	
Collision rate in Pb-Pb	50 kHz
Raw event size (Pb-Pb min bias)	20 MByte
Online data compression factor	20

Table 1.1: Synopsis of parameters of the upgraded TPC.

Chapter 2

Mechanical structure, field cage, and gas system

2.1 Introduction

The upgraded TPC consists of the current structures of the detector, where the new readout chambers and electronics will replace the existing ones. Thus, the field cage, the endplates, the insulating volumes, the service support wheels, the I-bars, and the gas system will remain the same. These structures and systems are described elsewhere [1]. In this chapter a brief overview of the mechanical structure of the TPC is given, with emphasis on aspects relevant for the integration of the new readout chambers.

2.2 Field cage

The field cage is composed of four concentric cylinders which define the drift volume and the inner and outer insulating volumes. These cylinders, the field cage vessels and the containment vessels, are held together by the endplates. A schematic view of this assembly is shown in Fig. 2.1. They are made of composite material, namely a Nomex honeycomb structure sandwiched between layers of prepreg composite and Tedlar. The Tedlar foils provide gas tightness. Field-defining strips are employed to degrade the potential from the central electrode, an aluminized mylar foil at the center, to nearly ground potential close to the readout chambers.

The inner and outer voltage-degrading strips are suspended on 18 Macrolon rods each. These rods are also used to circulate the gas through tiny holes along their length, such that the gas flows radially outwards and does not exert any force on the central electrode. Some of these rods are also used to house services such as optical elements for the laser system, the high voltage cable to the central electrode, and the four removable and water-cooled resistor rods for the voltage degrading (see Fig. 2.2).

2.3 Endplates

The endplates keep together the field cage and containment vessels, and also hold the readout chambers. These are arranged in 18 sectors, each one covering 20^{o} in azimuth. The cutouts of the endplates define the dimensions of the part of the chamber bodies which form the exterior surface of the endplates. The gas tightness is ensured by one O-ring on the endplate, one on the chamber body and a sealing foil in between. The chambers are mounted such that the whole body is inserted into the field cage and then moved back into the endplate, where it is fixed from the inside. This allows to maximize the active area of the detectors, but requires that the whole chamber is brought into the drift volume for insertion. The full dimensions of the chambers bodies are determined by the geometry of the endplates, and in

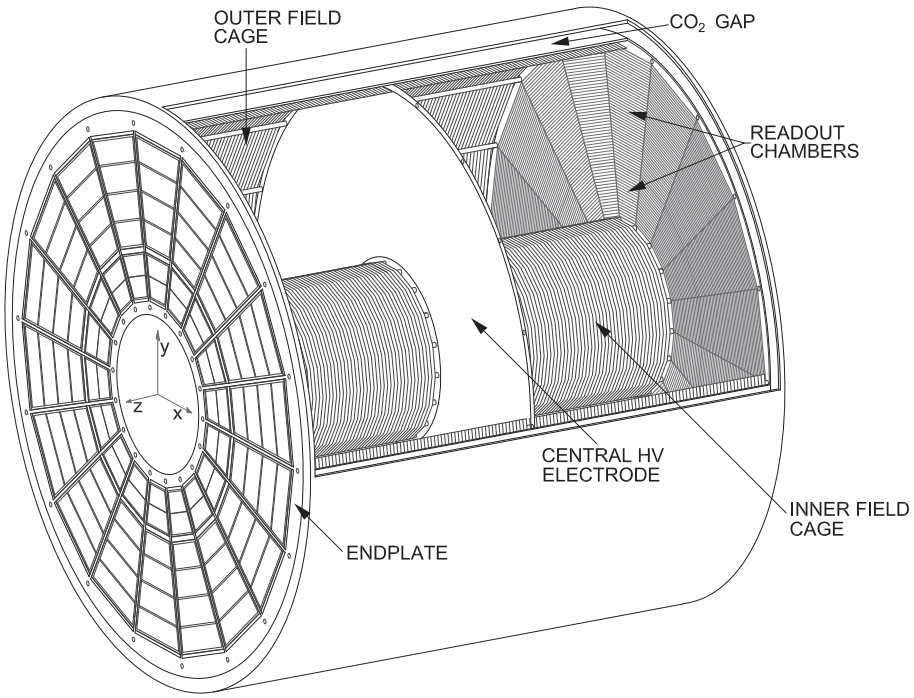

Figure 2.1: Schematic view of the ALICE TPC.

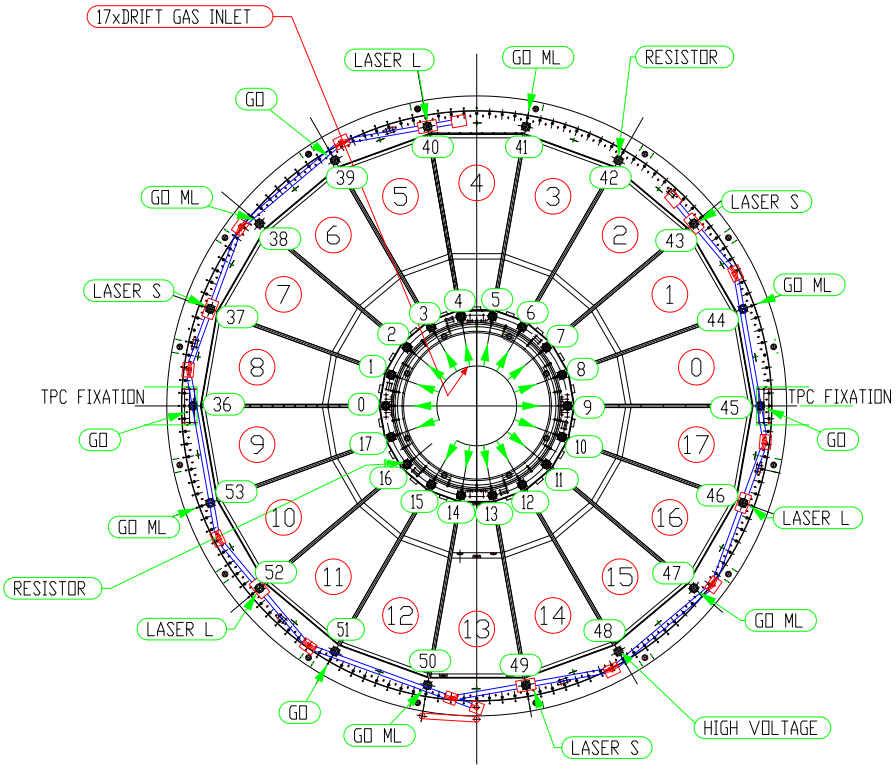

Figure 2.2: View of one of the endplates of the TPC; the different types of rods are indicated.

particular by the fixations on the endplate. A specialized mounting tool is used to install the chambers in place. Special care has to be taken of the small clearances that occur during this operation, as shown in the detailed views in Fig. 2.3 for the IROC and Figs. 2.4 and 2.5 for the OROC.

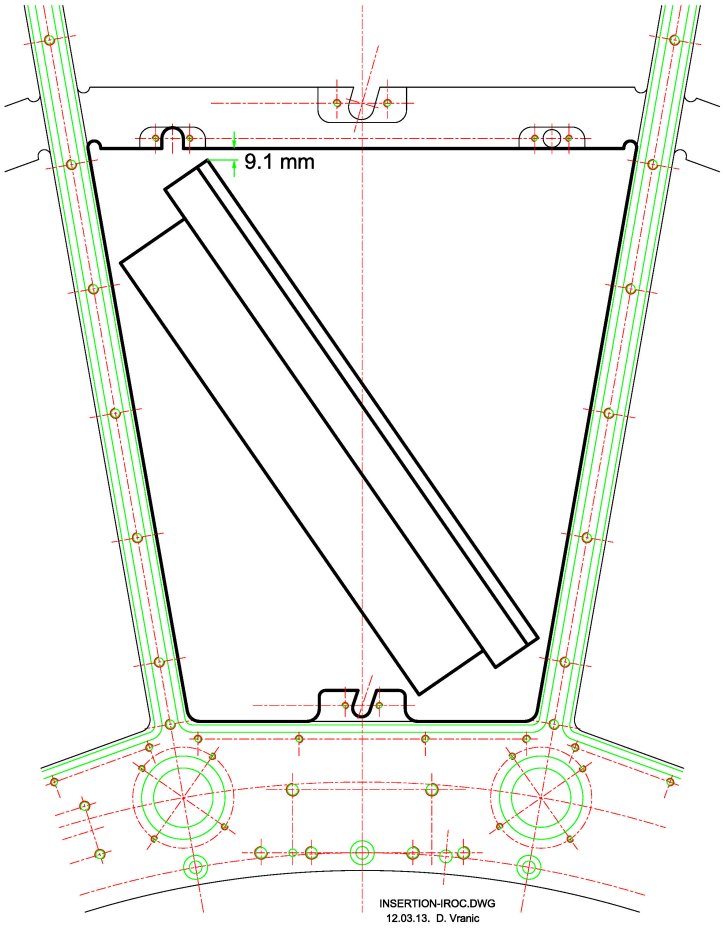

Figure 2.3: During the insertion of an IROC through the endplate the minimum clearance is 9 mm.

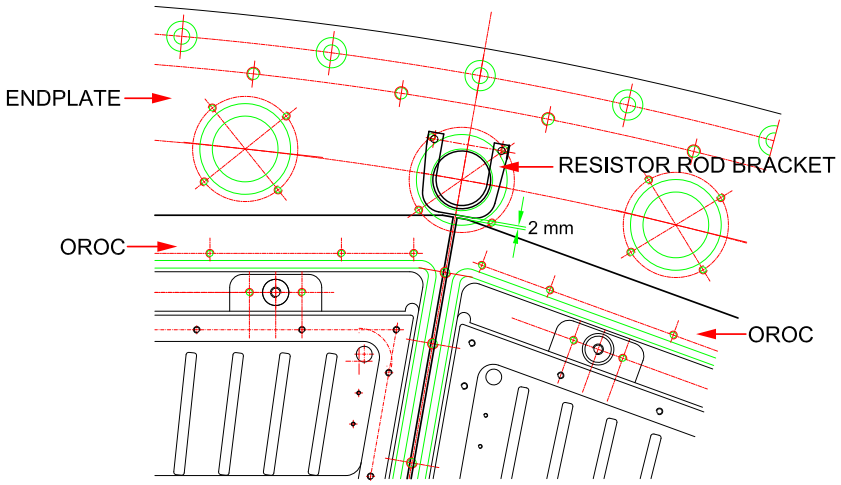

Figure 2.4: Insertion detail of an OROC. In the last stage, while moving the OROC back into its final position on the endplate, the clearance between the chamber and the bracket that holds the rod is only 2 mm.

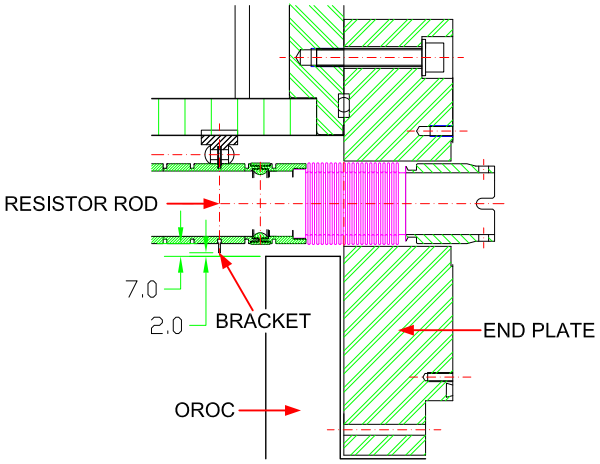

Figure 2.5: Side view of the clearance between the OROC and the rod bracket.

2.4 Last resistor and skirt

The field cage has provisions for matching the drift field at the interface between the drift volume and the readout chambers. On one hand, the resistor chain in the voltage dividers are terminated on the ground side by a last, external resistor. The value of this resistor is tuned such that the drift field matches the ground equipotential plane defined at the wire chambers. The potential of the gating grid is then fine-tuned to minimise field distortions in this region, resulting in a potential of some -70 V. On the other hand, there is a gap of a few cm between the outer side of the OROCs and the outer field cage, where the ground defined by the endplates would produce sizeable field distortions. In order to avoid this, a so-called skirt electrode is placed in this gap, as illustrated in Fig. 2.6.

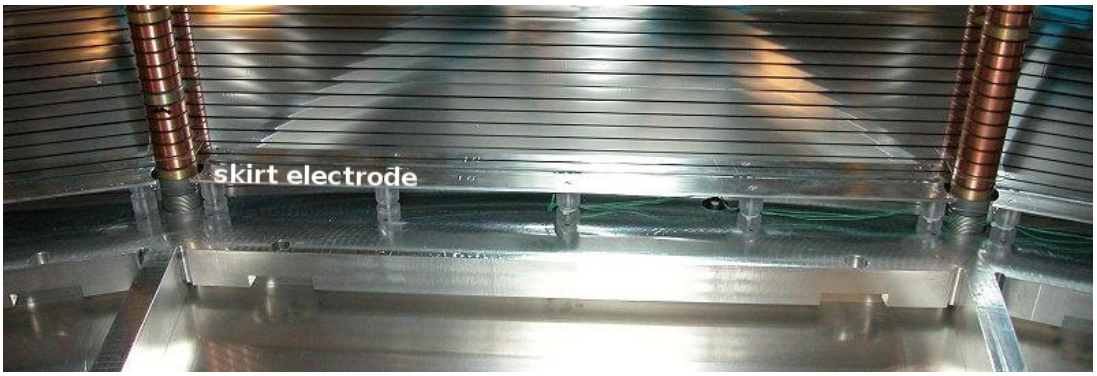

Figure 2.6: Detail of the ground side of the outer field cage showing the skirt electrodes elevated from the endplate in order to homogenize the electric field in the gap between OROCs and field cage.

In the case of the upgraded TPC, the potential on the GEM electrode facing the drift volume will amount to 3 – 4 kV. This means that the skirt electrode will be set to a comparable potential, for which the feedthrough connector will be replaced. For the tuning of the potential of the last strip via the last resistor, though, an extra power supply to provide the necessary voltage while allowing to sink the current across the voltage dividers will be necessary.

2.5 Service Support Wheel

The Service Support Wheels (SSWs) are installed in front of, and mechanically decoupled from, the endplates. Their function is to hold the Front-End Cards (FECs) and their cooling panels and associated services. Currently, each SSW supports 2800 kg of weight. The FECs are connected to the pad connectors at the chambers via flexible cables. The low voltage to the FECs is supplied via bus bars installed in

the spokes of the SSW. The wheels themselves can be reused for the upgraded detector, but the frames that hold the FECs may have to be replaced if new pad planes or FECs result in a different configuration of the readout partitions. The 18 cutouts of the SSW are finally covered by flat cooling panels in order to thermally isolate the endplates from the surrounding environment.

2.6 Gliders and I-bars

The TPC is inserted into and extracted from its position in the space-frame of the experiment by gliding it on two rails with four pairs of teflon gliders installed on opposite sides, front and rear, on the endplate and on the SSW. The relative position of these gliders is monitored at all times during gliding operations. Finally, in order to keep the two field cage vessels well aligned, a set of so-called I-bars are used to push or pull the set of inner cylinders against the outer set. A view of the TPC with SSW, I-bars and gliders on the rails is shown in Fig. 2.7.

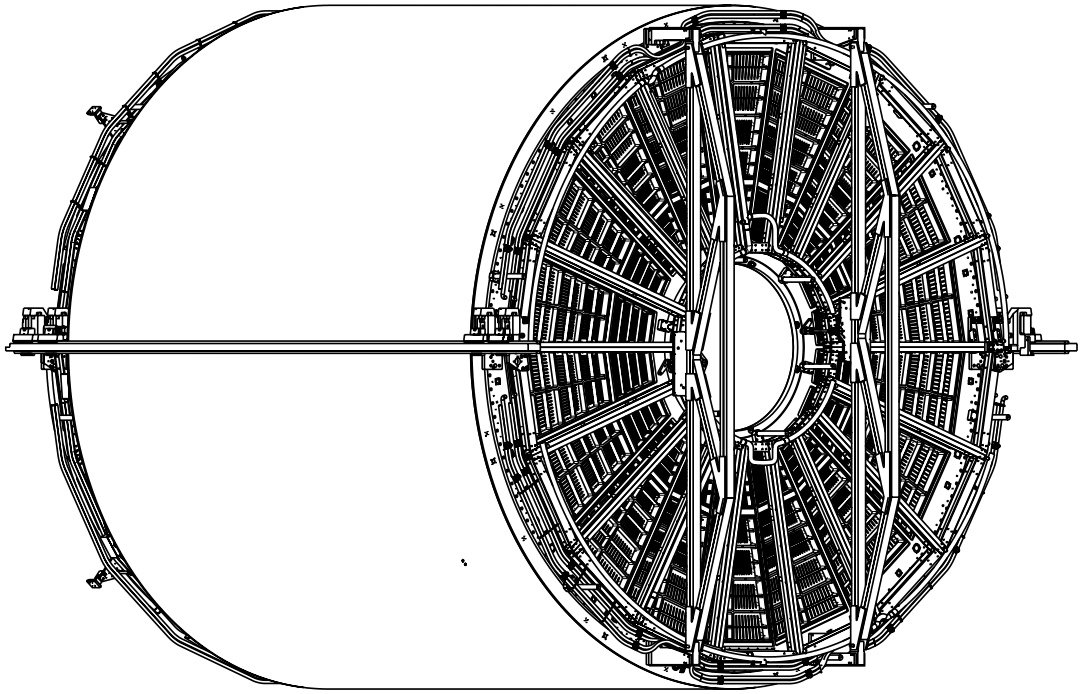

Figure 2.7: Overall view of the full TPC with SSW, I-bars and rails.

2.7 Gas system

The gas system is a closed-loop system where most of the gas is recirculated through the detector at about $15\,m^3/h$ with a regulated compressor module. The pressure in the TPC relative to atmospheric is kept constant with better than 0.1 mbar precision. Oxygen and water are removed from the gas with cartridges filled with a copper catalyzer. Some 50 l/h of mixed gas is continuously added to the system. A small amount of gas is exhausted through an analysis line which provides a measurement of the O_2 and H_2O contents, as well as the gas composition. Periodic samples are taken to analyze the gas with a gas chromatograph. The excess gas is exhausted through a regulated flowmeter. A high-pressure gas storage is used as a buffer to accumulate or release gas such that the system can absorb atmospheric fluctuations without interruptions. The system, schematically shown in Fig. 2.8, is arranged in functional

modules distributed on the surface, in the shaft, and in the cavern. A PLC[1] controls the system and a SCADA[2] system provides a suitable user interface. The mixer unit is designed to mix up to three gases. Default gases are Ne, CO_2, and N_2, but the mixer could inject Ar and CF_4 in the desired proportions by simply recalibrating the mass flow controllers for these gases. In the case of neon as noble gas, a filling procedure where CO_2 is trapped in molecular sieve cartridges minimizes wasting of neon during this operation. The technique does not work for argon, which is however a low cost gas. In summary, no significant hardware nor software modifications are needed in the gas system for any foreseen scenario for the upgraded TPC.

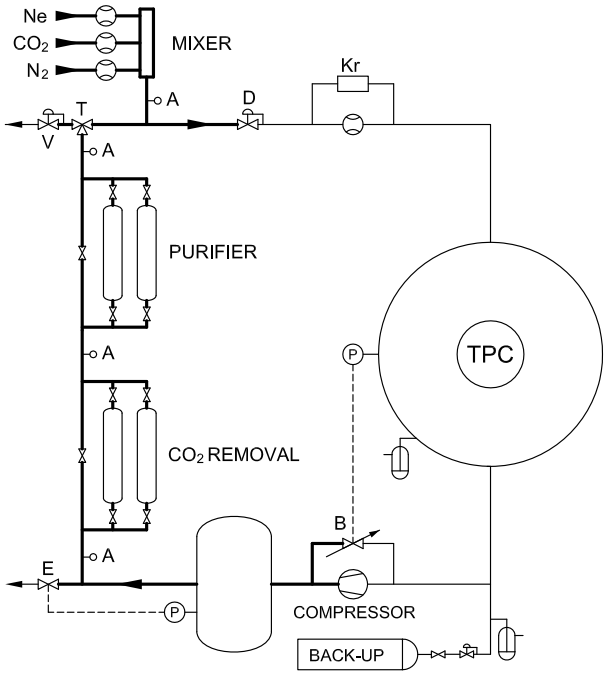

Figure 2.8: Schematic diagram of the TPC gas system.

[1]Programmable Logic Controller (PLC)
[2]Supervisory Control and Data Acquisition (SCADA)

Chapter 3

Gas choice

The current TPC, which employs MWPCs as readout chambers, uses Ne-CO_2 (90-10) as operating gas mixture. The addition of 5% N_2 has also been successfully tried out. The transport properties of these two mixtures, shown in Fig. 3.1, are very similar, while, due to the higher quencher contents, the operational stability of the chambers is improved in the case of the mixture containing N_2. At the high rates foreseen for RUN 2, 10 kHz Pb–Pb, further stability to the wire chambers will be provided by replacing the Ne by Ar. Detailed simulations have shown that, with Ar-CO_2 (90-10), similar resolutions in momentum and $\mathrm{d}E/\mathrm{d}x$ can be achieved as in Ne mixtures. With a triggered gating grid, space charge distortions remain at the level of 1 cm with this gas, at a slight reduction of the event rate to tape.

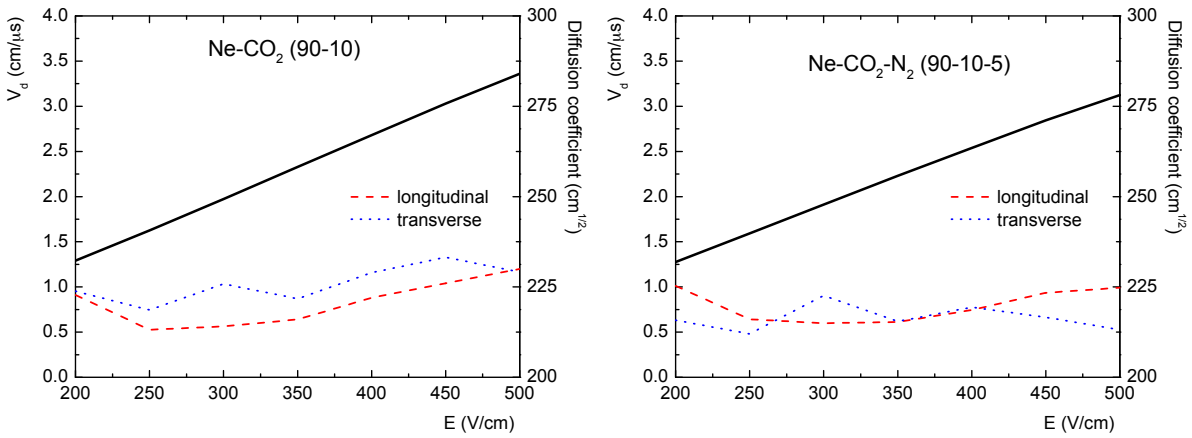

Figure 3.1: Drift velocity and diffusion at moderate electric fields. (Left) Ne-CO_2 (90-10). (Right) Ne-CO_2-N_2 (90-10-5).

The space charge distortions expected in the upgrade scenario are an important criterium in the gas choice for RUN 3. An example of the distortions calculated for a few candidate gas mixtures is shown in Fig. 3.2. The mobility of Ar^+ ions in Ar is $1.52\,\mathrm{cm^2V^{-1}s^{-1}}$, about three times lower than that of Ne^+ ions in Ne ($4.08\,\mathrm{cm^2V^{-1}s^{-1}}$). We disregard here the effect of drifting CO_2^+ ions in these mixtures. Since the ion backflow is similar for these two noble gases (see Sec. 5.1.3), the different mobilities result in larger space-charge distortions in argon, even at a factor of 2 lower gain.

Admixtures of CO_2 or CF_4 to neon are attractive for the upgraded TPC. Both perform similarly in terms of space-point distortions. Due to the differences in the $\omega\tau$ factor, CO_2 performs better in $r\varphi$, but CF_4 does better in r. CF_4 provides a very high drift velocity and thus results in a reduced event pileup, which is however not a critical issue for this TPC (see Sec. 7.3). On the other hand, the use of CF_4 in the current TPC would have to be thoroughly validated for compatibility with all materials of the detector and the gas system, before it could be regarded as a suitable operating gas.

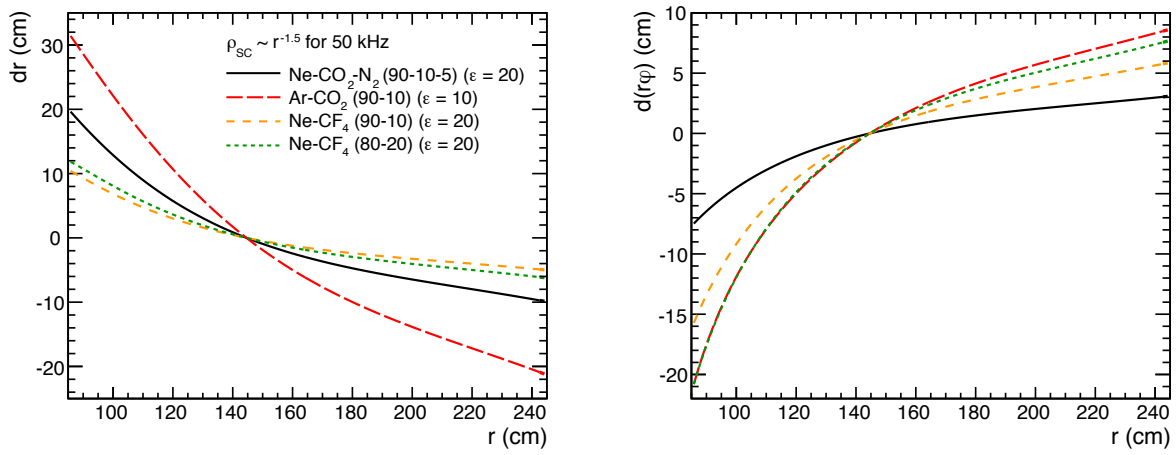

Figure 3.2: Radial and azimuthal distortions for four gas mixtures as a function of r at $z = 0$, where the distortions are largest. The parameter ε is defined in Eq. (4.2).

In the anticipated configuration of our GEM system rather large transfer fields are used. However, at fields around 4 kV/cm amplification starts in Ne-CO_2, as shown in Fig. 3.3, which reduces the ion back-flow performance and also reduces the stability. An increased concentration of CO_2 rapidly decreases the drift velocity unless the field cage voltage is increased beyond its certified limits. The addition of N_2 alleviates both issues as shown in the figure and explained in [1].

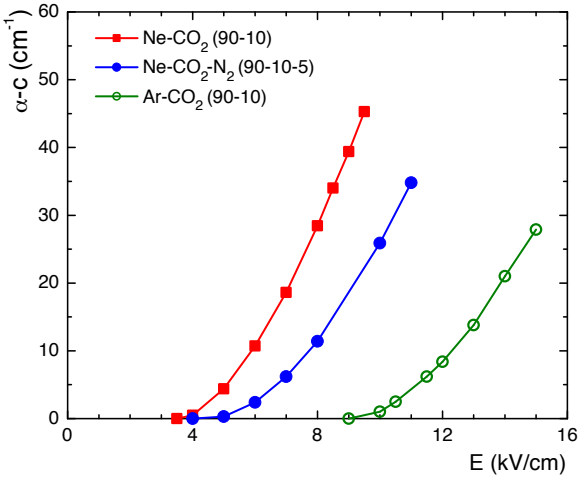

Figure 3.3: Effective Townsend coefficient for three gas mixtures as a function of the electric field strength. The onset of gain is shifted by 1 kV/cm by the admixture of N_2 to the neon mixture. For the argon mixture it is substantially higher.

The base gas mixture is therefore Ne-CO_2-N_2 (90-10-5). The basic properties of the most interesting gas mixtures is summarized in Tab. 3.1.

Gas	Drift velocity v_d (cm/μs)	Diffusion coeff. D_L ($\sqrt{\text{cm}}$)	D_T ($\sqrt{\text{cm}}$)	$\omega\tau$	Eff. ionization energy W_i (eV)	Number of electrons per MIP N_p (primary) (e/cm)	N_t (total) (e/cm)
Ne-CO_2-N_2 (90-10-5)	2.58	0.0221	0.0209	0.32	37.3	14.0	36.1
Ne-CO_2 (90-10)	2.73	0.0231	0.0208	0.34	38.1	13.3	36.8
Ar-CO_2 (90-10)	3.31	0.0262	0.0221	0.43	28.8	26.4	74.8
Ne-CF_4 (80-20)	8.41	0.0131	0.0111	1.84	37.3	20.5	54.1

Table 3.1: Properties of a few gas mixtures used in modern TPCs. The diffusion coefficients are evaluated at 400 V/cm.

Chapter 4

Readout chambers

4.1 Introduction

An interaction rate of $R_{\mathrm{int}} = 50\,\mathrm{kHz}$ for minimum bias Pb-Pb interactions is expected after the luminosity upgrade of the LHC during LS2 [1]. At these rates particle tracks from $N_{\mathrm{pileup}} = 5$ events on average will be superimposed in the drift volume of the TPC at any given time: $N_{\mathrm{pileup}} = R_{\mathrm{int}} \times t_{\mathrm{d}} \approx 50\,\mathrm{kHz} \times 100\,\mu\mathrm{s} = 5$, where t_{d} is the maximum electron drift time in the TPC[1]. A continuous, untriggered readout of the TPC is the obvious mode of operation in such a scenario with overlapping events, precluding the use of a gating grid. In the absence of the gating grid, however, ions created in the multiplication region must be prevented from drifting back into the drift volume by other means.

This will be achieved by using Gas Electron Multiplier (GEM) [2] foils as charge amplifier instead of conventional MWPCs. The GEM consists of a $50\,\mu$m thin insulating Polyimide foil with Cu-coated surfaces, typically $2-5\,\mu$m thick. The foil is perforated by photo-lithographic processing, forming a dense, regular pattern of (double-conical) holes. In the standard geometry the holes have an inner diameter of $\sim 50\,\mu$m, an outer diameter of $\sim 70\,\mu$m, and a pitch of $140\,\mu$m. Other geometries, e.g. with a larger pitch and thus a smaller optical transparency, are considered for the ALICE TPC readout chambers. Figure 4.1 shows an electron microscope photograph of a standard GEM foil.

The small dimensions of the amplification structures lead to very large electric field strengths $\mathcal{O}(50\,\mathrm{kV/cm})$, sufficient for avalanche creation, inside the holes of the GEM foil when a moderate voltage difference of typically $200-400\,\mathrm{V}$ (depending on the gas) is applied between the metal layers.

The dynamics of charge movement and avalanche creation inside the GEM holes is complicated. Figure 4.2 shows a simulation performed with the Garfield / Magboltz [3] packages, illustrating the suppression of ion backflow from the amplification region. In this simulation the avalanche is started by two electrons, that are guided into the GEM hole by the drift field. The ions created in the avalanches closely follow the electric field lines because of their much smaller diffusion. Most of the ions are collected on the top side of the GEM foil, because the field inside the GEM hole is much higher than the field above the hole. Only a few ions drift back into the drift volume. The extraction of avalanche electrons from the hole proceeds more efficiently by applying a higher transfer field below the GEM.

The electrons can then be transferred to another amplification stage or collected at the anode. Typically 3 or 4 GEM foils are combined in a stack, leading to effective gains (see Eq. (4.1)) of the order of $10^3 - 10^4$ and at the same time guaranteeing a stable operation without the occurrence of discharges [5].

The effective gain of a GEM detector is determined by measuring the current at the readout anode I_{anode} for a given rate R of incident X-rays, each X-ray conversion producing N_{ion} ionization electrons:

[1] A discussion of pileup and occupancies is given is Sec. 6.2.

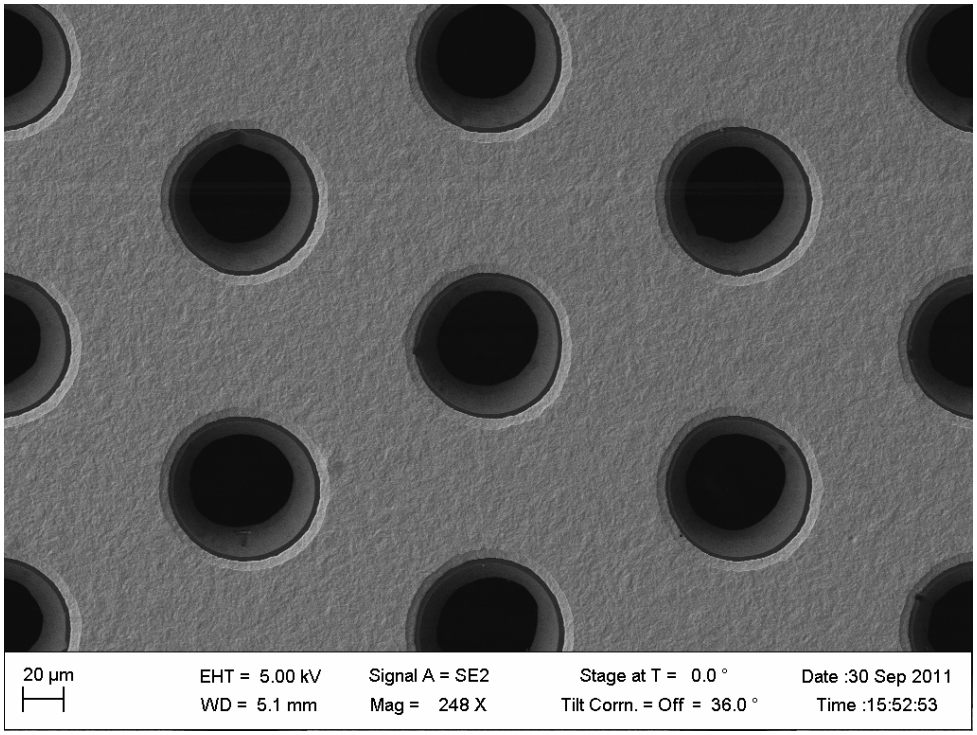

Figure 4.1: Electron microscope photograph of standard GEM foil with hole pitch 140 μm.

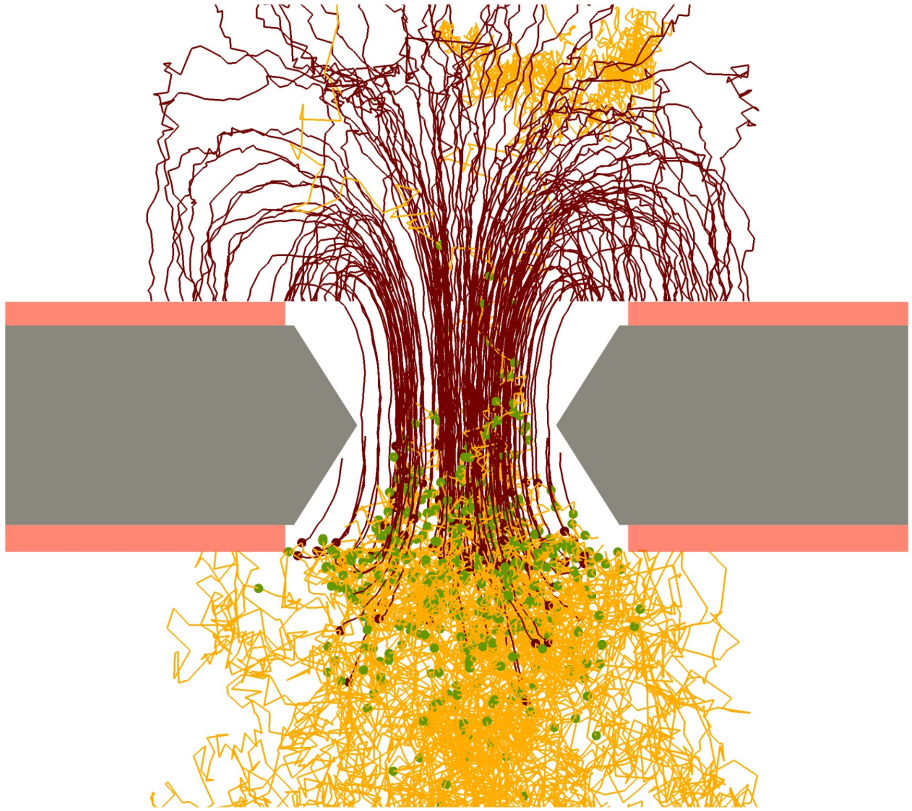

Figure 4.2: Garfield / Magboltz simulation of charge dynamics for electrons (two in this simulation) entering into a GEM hole [4]. Electron drift paths are shown as light lines, ion drift paths as dark lines. Dots mark places where ionization (multiplication) processes have occurred. The paths have been projected onto the cross section plane.

$$G_{\mathrm{eff}} = \frac{I_{\mathrm{anode}}}{eN_{\mathrm{ion}}R} \quad . \tag{4.1}$$

Defined in this way, Eq. (4.1) corresponds to the gain seen by the readout, and takes into account charge losses in the GEM structures.

We define the ion backflow as[2] the ratio of cathode to anode current,

$$IB = \frac{I_{\mathrm{cathode}}}{I_{\mathrm{anode}}} = \frac{1+\varepsilon}{G_{\mathrm{eff}}} \quad , \tag{4.2}$$

with ε being the number of ions drifting back into the drift region from the amplification region per incoming electron. Note that *IB* also includes a contribution from ions created during the ionization process. Ion backflow values of $IB = 0.25\,\%$ have been reached experimentally in conditions which were more advantageous than the ones in ALICE, e.g. a high magnetic field (4 T) and a low drift field (200 V/cm) [6].

Detectors based on GEM amplification were pioneered by the COMPASS experiment at CERN [7–10], and are now routinely used in several high-rate particle physics experiments like LHCb [11], PHENIX [12], and TOTEM [13]. New applications include the use of GEM-based detectors in KLOE-2 [14] and CMS [15].

The usage of GEM detectors as readout chambers in the ALICE TPC, however, is a new domain of application of these detectors with regard to several aspects:

- The ion backflow from the detector must be carefully optimized. A value of 1 % is necessary in order to achieve the goal of limiting drift field distortions due to space charge to well below 10 cm in most of the drift volume. This value has been established in the default gas mixture Ne-CO_2-N_2 (90-10-5). At a gain of 2000, which is needed for a signal-to-noise-ratio of 20, this corresponds to $\varepsilon = 20$, i.e. 20 ions flowing back into the drift region per incoming electron.

- Special attention must be given to a high electron collection efficiency of the GEM system, in particular when the operational conditions are optimized for small ion backflow (see Sec. 5.1.3). Finite electron transparancy, in particular in the first layer, leads to a degradation of the local energy resolution due to a loss of primary electrons, that will eventually compromise the $\mathrm{d}E/\mathrm{d}x$ performance of the detector. Simulations have shown that a local energy resolution equivalent to 12 % at 5.9 keV is sufficient to preserve the present $\mathrm{d}E/\mathrm{d}x$ resolution of the TPC (see Sec. 7.2.3).

- For a Ne-based gas mixture the dependence of the Townsend coefficient on the electric field is steeper compared to the standard Ar-based mixtures, with which most GEM detectors have been operated until now. In order to be able to apply the very asymmetric fields above and below the GEM, required for maximum ion backflow suppression, without entering a regime of avalanche multiplication in the gaps between GEM foils, a small admixture of N_2 is added to the detector gas (see Chap. 3).

- At a rate of primary ionization clusters of $100\,\mathrm{kHz/cm^2}$ for an IROC at a radius of $r = 85\,\mathrm{cm}$ (for $\mathrm{d}N_{\mathrm{ch}}/\mathrm{d}\eta = 500$) the current density at the readout anode at a gain of 2000 is $\sim 1\,\mathrm{nC/(cm^2\,s)}$, assuming that all primary particles are MIPs. With a safety factor of 10, which takes into account the contribution of highly ionizing particles, background, secondaries, etc., the upper limit for the rate and the current density is $10\,\mathrm{kHz/mm^2}$ and $0.1\,\mathrm{nC/(mm^2\,s)}$, respectively. Both values are far

[2] There appear different definitions of the term *ion backflow* in the literature. We choose this definition since it can be easily measured.

below experimentally verified limits of rate capability ($> 100\,\mathrm{kHz/mm^2}$) for GEM detectors [9, 16]. Nevertheless, the long-term operation in ALICE requires careful testing of all materials used in the detector construction concerning their aging properties.

In the following we describe the concept of the GEM-based readout chambers and show the design choices that are consistent with the above considerations.

4.2 Mechanical structure

The readout chambers are installed on both end plates of the cylindrical gas vessels of the TPC. The two readout planes are azimuthally segmented into 18 sectors of trapezoidal shape, each sector covering 20°, as shown in Fig. A.2. Each sector is further divided into two different chambers, called Inner Readout Chambers (IROCs) and Outer Readout Chambers (OROCs). The dimensions of the ALICE readout chambers are shown in Fig. 4.3. These dimensions, as well as the segmentation, are taken over from the original ALICE TPC design and will remain unchanged after the upgrade.

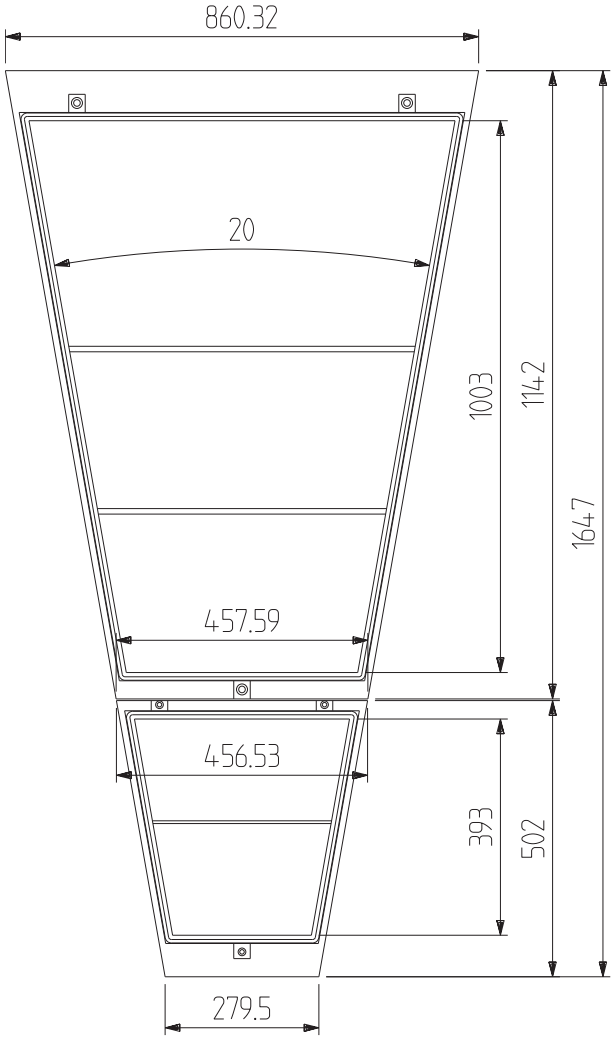

Figure 4.3: Dimensions (mm) of the ALICE TPC readout chambers.

Figure 4.4 shows an exploded view of a GEM IROC. It consists of the following components:

– a trapezoidal aluminum frame (*alubody*),

– a support plate made of fiberglass (*strong back*),

– the pad plane (multilayer PCB) and

– the GEM stack including a cover electrode.

The corresponding view of a GEM OROC is depicted in Fig. 4.5.

We intend to rebuild the complete readout chambers including the alubodies. This allows (i) to fully adapt the mechanics to the GEM amplification scheme, (ii) to rearrange the connector layout to the new front-end electronics and to optimize the accessibility of the front-end cards, and (iii) to start production and testing of the chambers well in advance of the end of LHC RUN 2.

The overall design of the alubodies will be very similar to the existing ones. The mechanical stability of the chambers will be more than sufficient to prevent deformations due to gravitational forces and the tension on the GEM foils. Minor modifications will be introduced for the feedthroughs of the high-voltage (HV) supplies, the mounting of the boxes with the resistor chains for the HV, the cut-outs for connectors of the front-end cards, and the mounting of the GEM planes.

The pad plane consists of a single multi-layer PCB for the IROCs, and, for production reasons, between two and four PCBs for the OROCs. The final segmentation depends on the choice of number of readout channels per FEC. The size of the readout pads of the present TPC matches the expected occupancy during RUN 3 and will therefore be kept. Some reshuffling of pads and traces to connectors is needed in order to accommodate the GEM stacks and the new front-end cards. For improved stiffness and gas tightness, the pad plane with a thickness of 2 mm will be glued to a strong back plate of 3 mm thickness made of fiber-glass reinforced epoxy. This design has proven to provide extremely good gas tightness[3] and stability in the original version of the readout chambers.

The technique for insertion and mounting the chambers into the TPC will be taken over from the original ALICE TPC (see Sec. 11). Special care has to be taken in order not to expose the GEM foils to dust during the mounting procedure.

4.3 GEM planes

4.3.1 General structure

The electrons created by ionizing particles traversing the active volume of the TPC drift towards the end plates, where they are amplified in order to induce a detectable signal in the readout pads. In the new readout chambers, the amplification will be provided by avalanche creation inside the GEM holes. In order to achieve the required gain and at the same time provide a sufficiently high suppression of back flowing ions, a stack of four GEM foils will be used for all chambers. A schematic drawing of a GEM stack is shown in Fig. 4.6.

The mechanical layout of the GEM stage follows a modular design wherever possible to allow pre-assembly and testing of individual components at every stage. The introduction of dead zones is kept to a minimum, so as not to deteriorate the resolution of the chambers.

The size of GEM foils needed for the ALICE IROC and OROC exceeds that of most of the currently operating GEM detectors. The conventional method of GEM foil patterning requires photo-lithographic processes based on two masks with identical hole patterns, placed on the two sides of the copper-coated base foil, and aligned with a precision of 1 μm with respect to each other in order for the holes to be perpendicular to the surface. These alignment requirements limit the maximum size for GEMs produced

[3] The overall oxygen contamination in the current TPC at a flow of 15 m^3/h is of the order of 1 ppm.

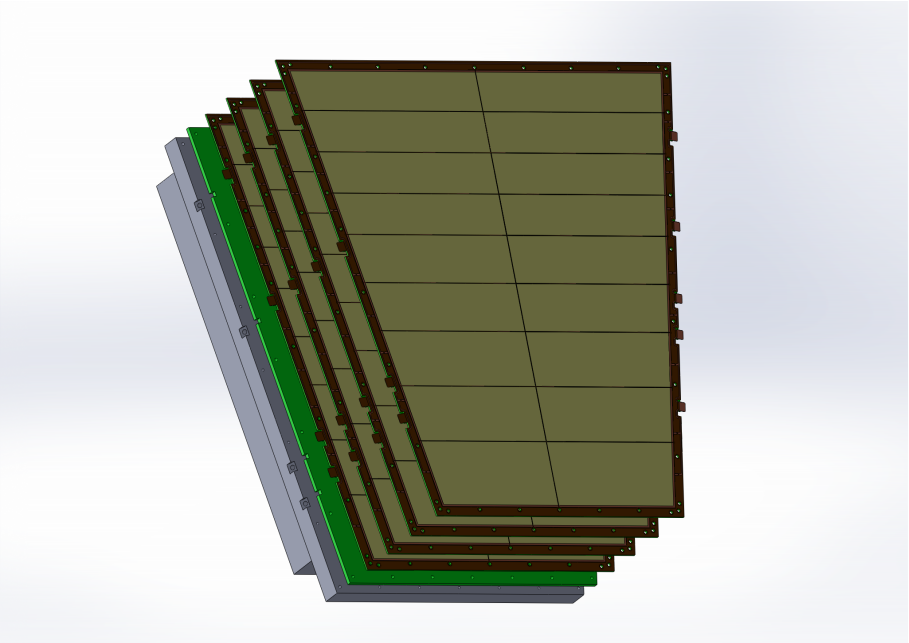

Figure 4.4: Exploded view of a GEM IROC.

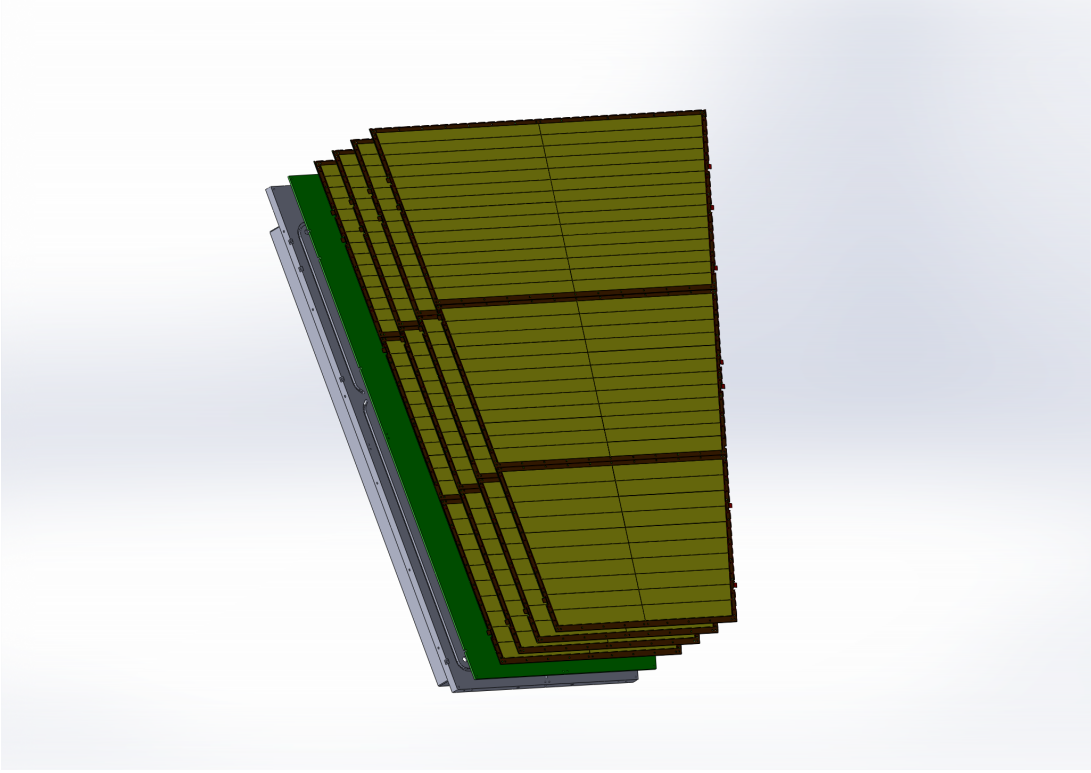

Figure 4.5: Exploded view of a GEM OROC.

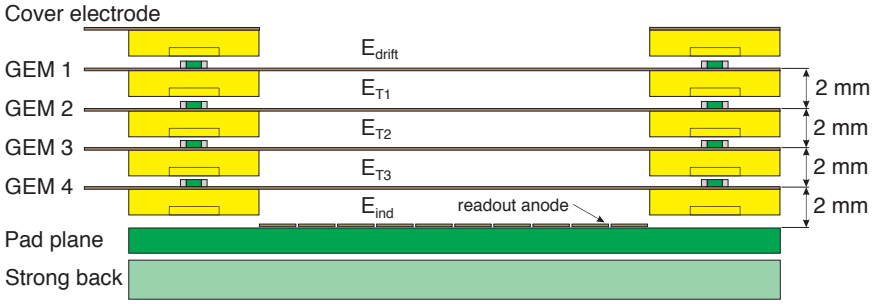

Figure 4.6: Schematic exploded cross section of the GEM stack. Each GEM foil is glued onto a 2 mm thick support frame defining the gap. The designations of the GEM foils and electric fields used in this TDR are also given. E_{drift} corresponds to the drift field, $E_{\mathrm{T}i}$ denote the transfer fields between GEM foils, and E_{ind} the induction field between the fourth GEM and the pad plane. The readout anode (see Eq. (4.2)) is indicated as well. The drift cathode is defined by the drift electrode not shown on this schematic.

with this technique. Another important constraint is the size of the industrially available base material and of the machinery required for the processing, both being presently limited to a width of 600 mm.

The first limitation can be bypassed by employing a single-mask technique [17]. This technique has proven to deliver comparable results with respect to homogeneity and gain performance of the GEM-foils as the standard technique. A small decrease in gain by 25 % has been observed in comparison with a standard GEM at the same conditions, which can easily be compensated for by a slight increase of the operating voltage.

Large-size foils with single-mask GEM technique have been pioneered in the framework of R&D for the cylindrical GEM tracker of the KLOE-2 detector by the RD51 collaboration [18]. For the construction of the full-size KLOE-2 tracker, which has been completed recently [19], a total of 50 large-size single-mask foils with active areas of up to $430 \times 700\,\mathrm{mm}^2$ have been produced at CERN. After thorough testing with QA criteria similar to the ones to be adapted for ALICE (see Sec. 4.7), only eight bad foils were identified. Most of the problems were related to an over-etching of the polyimide, a problem which, according to the CERN workshop, has been resolved in the meantime. GEM foils with even larger active areas ($990 \times (220-455)\,\mathrm{mm}^2$) are now routinely being produced in the framework of developments for the CMS muon system [15, 20]. At the time of writing this TDR, six full-size triple-GEM detectors with single-mask GEM foils have been built by the CMS GEM collaboration. This collaboration also measured the uniformity of the gain of a final detector to be within 12 – 15 % (RMS). The GEM foils needed for the ALICE TPC[4] are of a similar size. Hence the single-mask technique can be considered mature for application to the ALICE TPC.

In order to reduce the total charge stored in the GEM foil, one side of the foil is segmented into HV sectors with a surface area of approximately $100\,\mathrm{cm}^2$, as shown in Figs. 4.8 and 4.12. The inter-sector distances are reduced to $200\,\mu\mathrm{m}$. Each HV sector is powered separately through high-ohmic SMD[5] loading resistors soldered directly onto the foil and connected to a HV distribution line implemented on the boundary of the foil. This scheme has proven to reduce the probability of discharges propagating between GEM foils and from the last GEM foil to the readout circuit [5]. Figure 4.11 shows a detailed view of the segmented side of an IROC GEM foil with the loading resistors in place and the frame of the next GEM layer on top of it. The voltages to each GEM foil are supplied by two external HV sources, one for each side of the foil (see Sec. 4.4).

The GEM foils will be pre-stretched with a force of $10\,\mathrm{N/cm}$ on all four sides using a stretching technique developed at GSI and TUM, making use of a pneumatical method. A frame originally designed for the stretching of stencils for PCB assembly was modified to meet the stretching force needed for GEM foils.

[4] See Tab. 4.1

[5] Surface Mount Device (SMD)

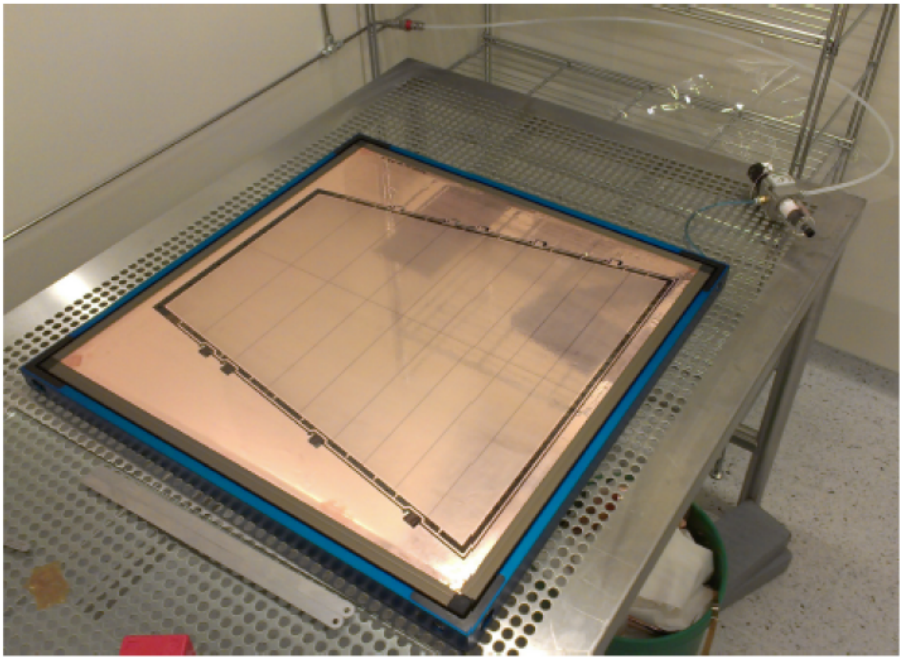

Figure 4.7: Photograph of an IROC GEM foil in the stretching frame.

The system is shown in Fig. 4.7. The stretching force is applied by springs integrated in the frame. For mounting, the spring tension is released by the pneumatic system. When the pressure is taken away, the foils are tensioned.

The foils in the stretching frames are then positioned on a custom-made alignment plate for gluing of the support frames made of glass-fiber reinforced plastics. The width of the frames is chosen to be 10 mm to match the outer edges of the pad plane and for sufficient stability. The total thickness of the frames is constrained by the distance between the layers in the stack of 2 mm. The frames also include a grid of very thin bridges of $\sim 400\,\mu$m thickness intersecting the active area of the detector, which serves as spacer in order to guarantee sufficiently small sagging of the foils due to electrostatic forces. The spacer grid is aligned with the HV sector boundaries of the GEM foils in order to minimize the dead area.

Four framed GEM foils are stacked on top of each other above the pad plane and fixed to it by non-metallic screws. Our prototype studies have shown that this can be achieved without wrinkles even for the trapezoidal shape of foils needed for ALICE (see Sec. 5.2.3). The top side of GEM 1 facing the drift electrode of the TPC is covered by one extra frame which is metallized on the top side (see Fig. 4.6). The potential applied to this cover electrode is adjusted to homogenize the electric field in the drift region above the first GEM.

4.3.2 Inner readout chambers

The first batches of large-area GEM foils for the ALICE IROC prototype (see Sec. 5.2) with a size of $500 \times 470\,\text{mm}^2$ were produced at CERN during the last year. Quality assurance tests have been implemented in order to identify GEM defects both at macroscopic and microscopic levels as early during the assembly stage as possible (seeSec. 4.7 for a detailed discussion of QA procedures).

Figure 4.8 shows the top view of the design of an IROC GEM foil, including the segmentation into 18 HV sectors, powered from both sides of the foil. Figure 4.9 shows a photograph of a prototype foil used in the first beam tests (see Sec. 5.2).

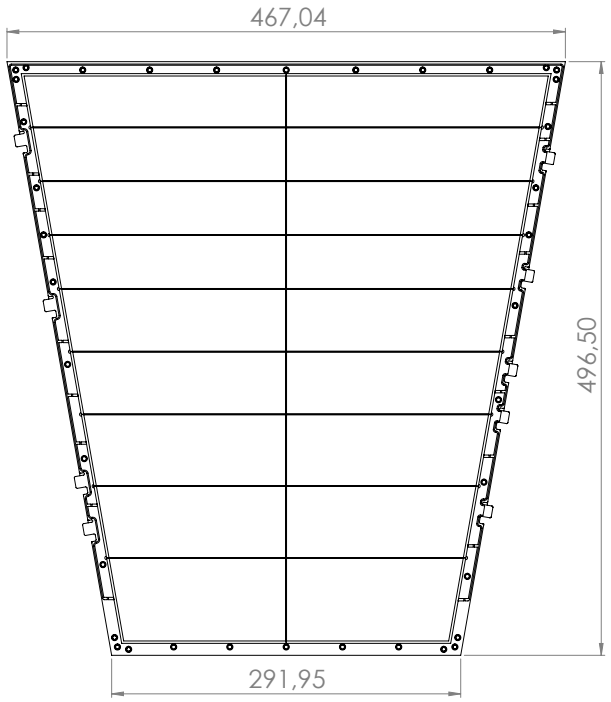

Figure 4.8: Dimensions of an IROC GEM foil.

4.3.3 Outer readout chambers

The size of an OROC as given in Fig. 4.3 would require GEM foils with a size of more than 1000 mm length and 900 mm width, which is beyond the limits of today's technology. The obvious solution is to segment the active area into three independent detector modules, tiled in radial direction. With this scenario we end up with foil sizes of $900 \times 400\,\mathrm{mm}^2$ or smaller. This is well in accordance with what has already been achieved at the CERN production site in recent developments for ALICE prototypes and other experiments [14, 15, 21]. Figure 4.12 shows the dimensions of the three modules for one ALICE OROC, each having a width of ~ 360 mm. The division in separate smaller detector modules is also expected to increase the yield of foils and facilitate their handling. For stability of the frames, however, a minimum width of 10 mm is required. This will create two insensitive zones of 20 mm width in radial direction in each OROC. Corresponding gaps are also foreseen in the pad layout, making room for fixation holes for the frames. The design of the foils allows to distribute the power to all HV sectors from two sides of the detector, without the need for HV lines between sectors. Thus, the gaps between HV sectors will also be as small as $200\,\mu$m as for the IROC case. The number of HV sectors is 20, 24, and 30 for the three detector modules.

Table 4.1 summarizes the parameters of the four different types of GEM foils needed for the upgraded TPC:

Detector	Size (cm^2)	Active area (cm^2)	No. of HV sectors	No. of foils
IROC	54×54	1678.0	18	144
OROC 1	70×54	1997.3	20	144
OROC 2	77×54	2240.5	24	144
OROC 3	91×54	2949.0	30	144

Table 4.1: Parameters of GEM foils for the ALICE TPC.

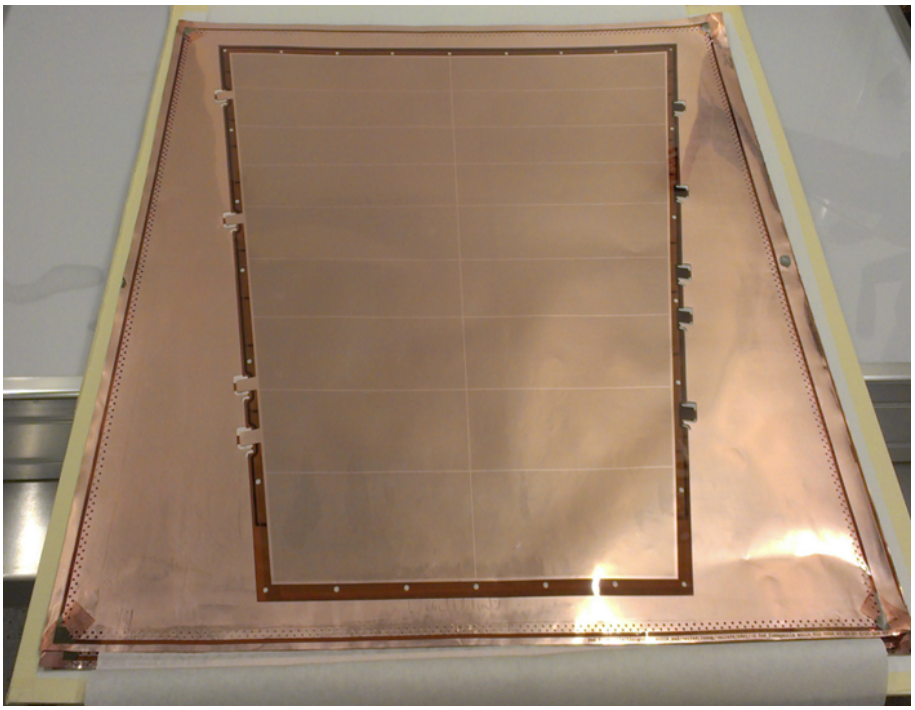

Figure 4.9: Photograph of an IROC GEM foil. The outer part is required for stretching and alignment and is cut away after the frame has been glued onto the foil.

4.4 High voltage supply

4.4.1 System overview

Extensive studies have shown that by reducing the capacitance between the two metal surfaces of a GEM foil the probability of discharges in a GEM detector can be significantly reduced [5]. To this end, one side of the GEM foil is segmented into individually powered HV sectors with a surface of $\sim 100\,\mathrm{cm}^2$, limiting the amount of charge which is involved in case of occasional sparks.

The potential at the segmented side of the GEM foil is defined through large $\mathcal{O}(\mathrm{M}\Omega)$ bias resistors. The potential at the unsegmented side is supplied directly, i.e. without bias resistor. This scheme has the advantage that in case of a temporary or permanent short circuit across a GEM foil in one or several HV sectors a voltage drop over the bias resistor occurs only for the affected sectors, while the rest of the foil remains fully operational without change of potential.

In a standard GEM detector, e.g. as used for the COMPASS experiment [7], the GEM foils are oriented such that the segmented sides face the drift electrode. In case of a discharge between the two sides of a GEM foil a voltage drop then occurs only on the segmented side, whereas the unsegmented side remains at its nominal potential. This prevents the propagation of the discharge to the next GEM foil or to the readout circuit.

In the case of the ALICE TPC, however, this scheme cannot be applied to the first GEM foil in the stack, because its potential on the side facing the drift electrode defines the drift field, which has to remain constant under all circumstances. Therefore, GEM 1 will be mounted with the unsegmented side facing the drift electrode, as shown in Fig. 4.13. In this way, its potential will be defined by the voltage U_{GEM} applied to the GEM stack. Considering the moderate voltage drop across GEM 1, this scheme is expected to be safe in terms of discharge propagation despite the inverted orientation of the foil.

The potentials at the GEM electrodes are defined by an external voltage divider network, which is housed in a box mounted to the backside of the alubodies. Therefore, nine HV-feedthroughs are needed for the

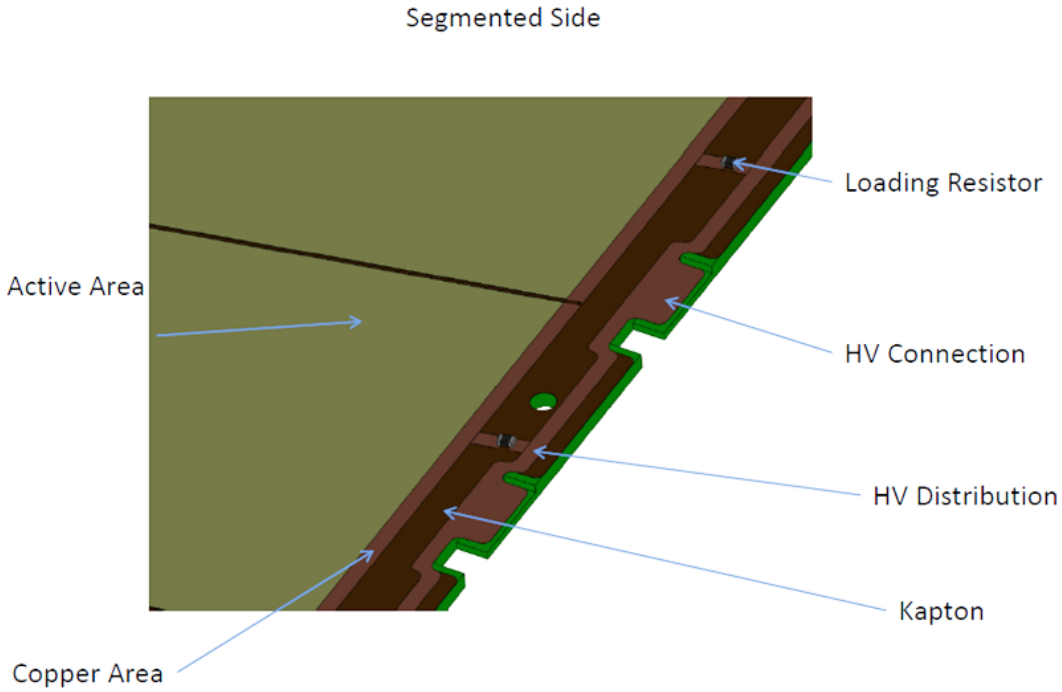

Figure 4.10: Detailed view of the HV distribution on the segmented side of an IROC GEM foil.

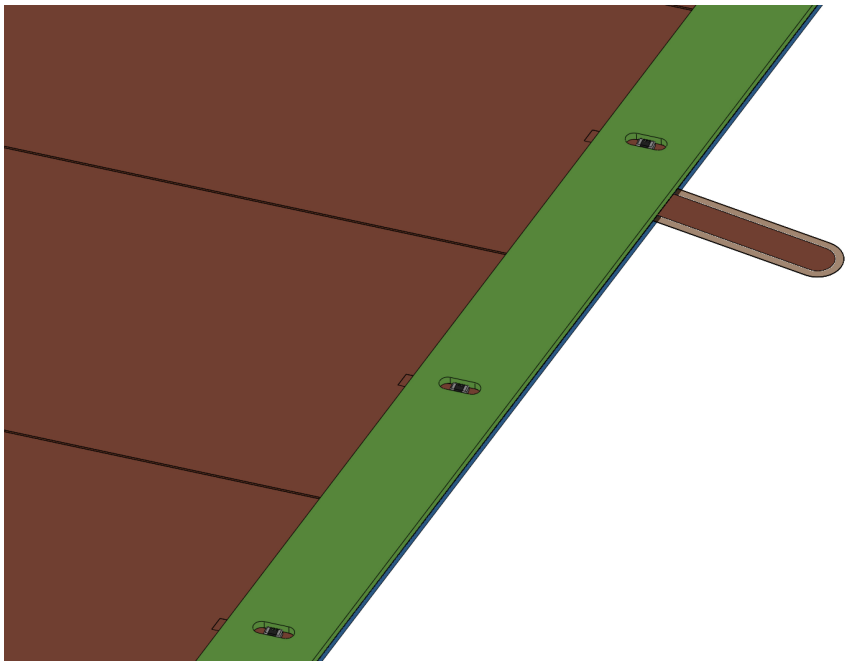

Figure 4.11: Bias resistors and HV supply of an IROC GEM foil.

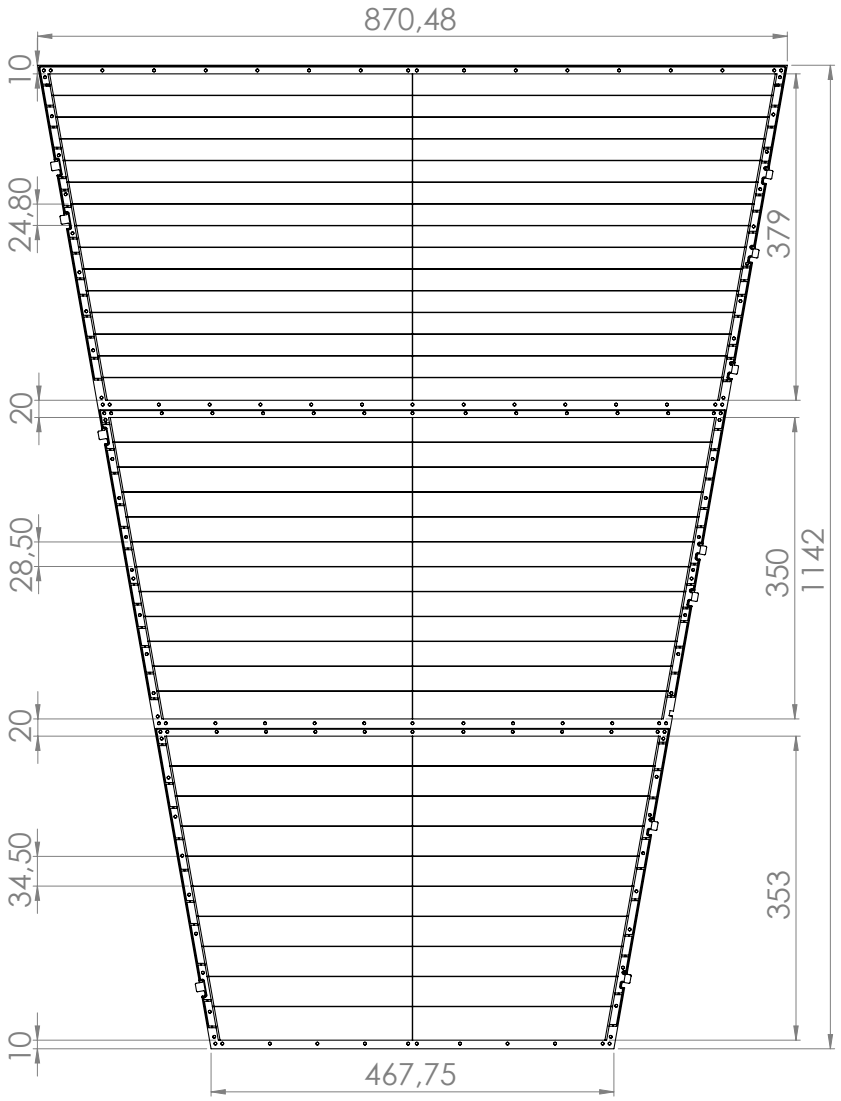

Figure 4.12: Dimensions (mm) of OROC GEM foils. The active area of the OROC is divided into three individual GEM stacks of different sizes.

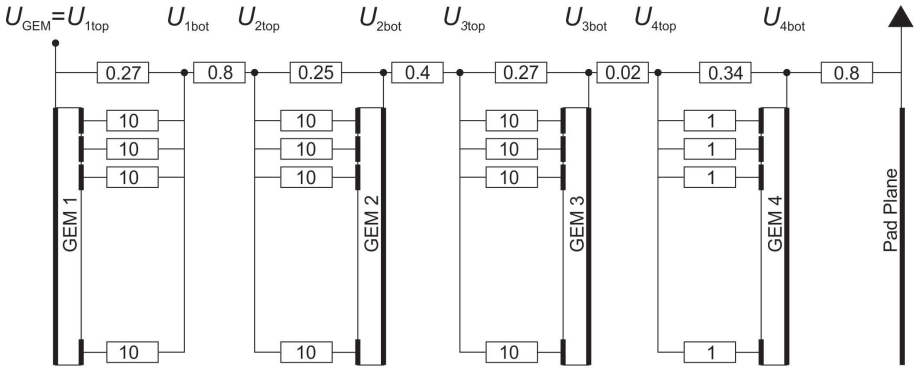

Figure 4.13: Schematics of the HV distribution scheme for a GEM detector module. The resistor values are given in units of MΩ and correspond to the field settings of Tab. 4.2.

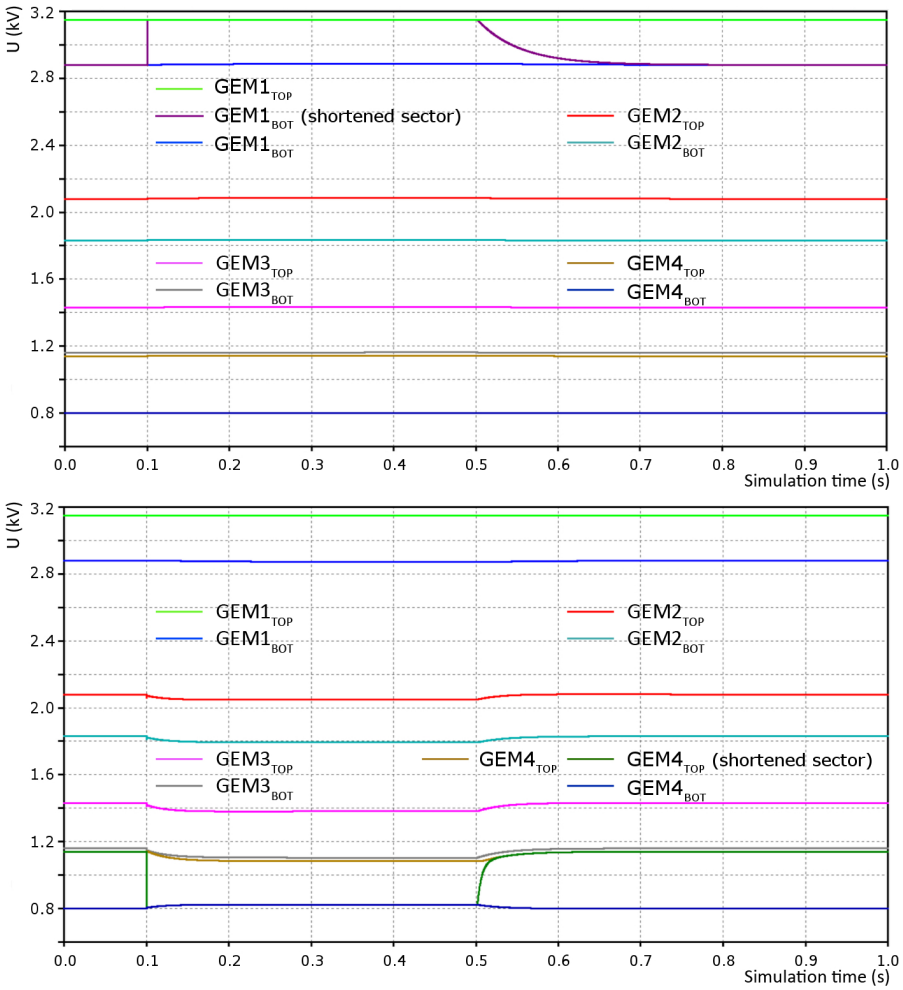

Figure 4.14: Potentials at all GEM electrodes of a quadruple GEM stack in case of a temporary short circuit between the two electrodes of GEM 1 (top panel) and GEM 4 (bottom panel), occurring at time 0.1 s and lasting until 0.5 s.

four GEM foils and the cover electrode of each detector module. The values of the resistors in the network are chosen such that an effective gain of 2000 and a minimum ion backflow of around 0.5 – 1 % is provided. The voltage necessary to achieve a given gain will vary between modules due to variations of GEM foil parameters like e.g. hole diameters. In order to have a homogeneous drift field in the drift volume of the TPC, the potential at the top electrode of GEM 1 has to be the same for all modules. Thus, the potential difference across GEM 4 will be adjusted with the use of a remote controlled regulation circuit in parallel to the resistor defining the coarse potential drop.

Figure 4.14 (top panel) shows the absolute potentials at all four GEM foils of a stack during an event where a temporary short circuit (due to a discharge) occurs between the two electrodes of GEM 1 (upper panel). Due to the bias resistors at the bottom side in case of GEM 1, the potential at the bottom side increases to the value of the top side (blue curve). The potential at the top side of GEM 1 does not change, as required for a constant drift field. Figure 4.14 (bottom panel) displays the analogous situation for GEM 4, which has the bias resistors on the top side. Here, the potential at the bottom side remains approximately constant in order to minimize the probability of the discharge propagating to the readout pads. The short circuits result in an increase of the overall current through the resistive divider of 1.4 μA for the case of GEM 1, and of 25.4 μA for the case of GEM 4.

For online monitoring of space-charge effects it is essential to measure the currents on all GEM sectors with a high frequency of the order of ms and a precision of $\sim$ 100 pA. The current measurement will be implemented in the HV divider box, and the data will be included in the TPC data stream (see Sec. 10.3).

In this way, the data are readily available for online calibration. We also intend to include in the HV distribution boxes the possibility to send a pulse to the lowest GEM electrode, which then induces signals on all electronic channels of a given module for calibration purposes. This will be accomplished by a coupling capacitor, which will however be disconnected during normal operation for reasons of operational safety. The voltage divider boxes have to be accessible from the outside in order to allow for access during a shutdown period of the experiment.

The high voltage system for the GEM stacks requires good voltage stability (ripple and noise $<50\,\mathrm{mV}$), high precision current measurement (resolution 1 nA), a fast trip mechanism, adjustable ramp speeds, full remote controllability and output voltages up to 6 kV at a maximum current of 1 A. While a single HV channel is required for each IROC, the three OROC modules will be powered separately but synchronously for reasons of flexibility and stability. In total, therefore, 144 HV channels are needed for the GEM stacks, plus the same number for the cover electrodes.

4.4.2 Typical HV settings

In order to minimize the backflow of ions produced in the amplification region, the electric field configuration of the GEM stack as well as the sharing of the gain among the four amplification stages is optimized, thus bringing the ALICE TPC to a novel mode of operation of a GEM detector. Our measurements on small test detectors, reported in Sec. 5.1.3, show that an ion backflow of less than 1 % can be achieved with a quadruple GEM system at typical voltage settings shown in Tab. 4.2. At an effective gain of $2 \cdot 10^3$ in the GEM stack this corresponds to $\varepsilon < 20$ back-drifting ions per electron reaching the GEM stack. In order to achieve this result, a configuration was used, where the second and the third GEM foils have a pitch of $280\,\mu$m in contrast to the standard $70\,\mu$m. Such large-pitch foils have a smaller optical transparency and therefore block ions more effectively. Strategies for an even further reduction of the ion backflow will be discussed in Sec. 9.

Drift Field				$= 0.4\,\mathrm{kV/cm}$
Potential at top of GEM 1			$= 3150\,\mathrm{V}$	
ΔU_{GEM1}	$= U_{1\mathrm{top}} - U_{1\mathrm{bot}}$	$= 270\,\mathrm{V}$		
Transfer Field 1 (E_{T1})	$= (U_{1\mathrm{bot}} - U_{2\mathrm{top}})/0.2\,\mathrm{cm}$			$= 4.0\,\mathrm{kV/cm}$
Potential at top of GEM 2			$= 2080\,\mathrm{V}$	
ΔU_{GEM2}	$= U_{2\mathrm{top}} - U_{2\mathrm{bot}}$	$= 250\,\mathrm{V}$		
Transfer Field 2 (E_{T2})	$= (U_{2\mathrm{bot}} - U_{3\mathrm{top}})/0.2\,\mathrm{cm}$			$= 2.0\,\mathrm{kV/cm}$
Potential at top of GEM 3			$= 1430\,\mathrm{V}$	
ΔU_{GEM3}	$= U_{3\mathrm{top}} - U_{3\mathrm{bot}}$	$= 270\,\mathrm{V}$		
Transfer Field 3 (E_{T3})	$= (U_{3\mathrm{bot}} - U_{4\mathrm{top}})/0.2\,\mathrm{cm}$			$= 0.1\,\mathrm{kV/cm}$
Potential at top of GEM 4			$= 1140\,\mathrm{V}$	
ΔU_{GEM4}	$= U_{4\mathrm{top}} - U_{4\mathrm{bot}}$	$= 340\,\mathrm{V}$		
Collection/Induction Field (E_{ind})	$= U_{4\mathrm{bot}}/0.2\,\mathrm{cm}$			$= 4.0\,\mathrm{kV/cm}$

Table 4.2: Typical high voltage settings for $IB < 1\,\%$ in a quadruple GEM in Ne-CO_2-N_2 (90-10-5) at an effective gain of $2 \cdot 10^3$. Note the high transfer field in the 1st and 2nd gap, whereas E_{T3} is very low. The potentials at the top of the 4 GEM foils are given as well.

4.5 Readout pad plane

The electrons emerging from the last GEM stage induce a fast signal on the readout pads. A very precise determination of the position in two-dimensional space of an arriving electron cluster can be achieved if the signal is distributed over several adjacent pads. In this case a suitable weighting of these signals will yield a resolution much better than the typical pad size. Charge sharing is achieved by the combination

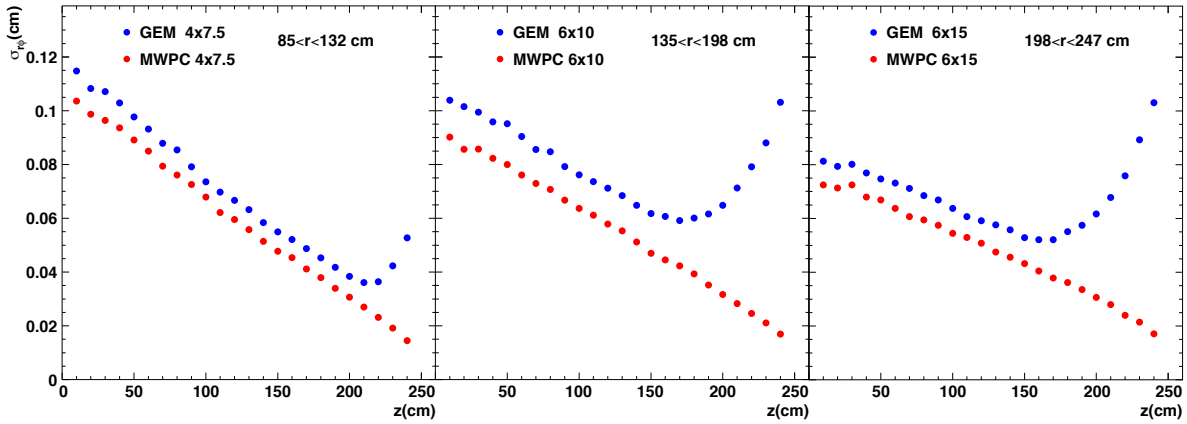

Figure 4.15: Point resolution in the magnetic bending plane $r\varphi$ as a function of z for (blue) GEM and (red) MWPC amplification, with (left panel) $4 \times 7.5\,\mathrm{mm}^2$, (middle panel) $6 \times 10\,\mathrm{mm}^2$, and (right panel) $6 \times 15\,\mathrm{mm}^2$ pads, respectively.

of several effects: spread of the drifting charge clouds due to diffusion and track inclination, intrinsic response width of the amplification stage due to diffusion in the GEM stack, finite hole distance, and signal induction in the induction gap. The fraction of the total charge in the avalanche which is induced on a given pad as a function of the distance between the center of the pad and the arrival point of the electron initiating the avalanche is described by the Pad Response Function (PRF). Amplification in a multi-GEM detector results in a narrower PRF compared to that of an MWPC, approximately equal to the width of the charge cloud emerging from the last GEM.

In a microscopic simulation of the TPC it was studied whether diffusion in the drift gas is sufficient to provide adequate charge sharing despite the smaller PRF, when GEM detectors are combined with the present readout pad geometry. For the following studies, single tracks with minimum energy loss, a flat distribution in polar angle θ and zero azimuthal inclination (i.e. very high momentum) have been used. It should be noted that a finite azimuthal inclination of tracks gives a dominant contribution to the point resolution, so that the differences between MWPC and GEM amplification shown in the following would be washed out. In this sense, the simulation results correspond to a worst-case scenario. A purely projective PRF was assumed for the GEM case, i.e. no broadening of the charge cloud in the GEM stack was taken into account. Exponential gain fluctuations for single electrons in the GEM stack were included. The average gain was adjusted such that a signal-to-noise ratio of 20 for the most probable value was reached. A Gaussian shaping with $\sigma = 100\,\mathrm{ns}$ was applied and the resulting signal was sampled at 10 MHz.

Figure 4.15 shows the position resolution in the azimuthal $r\varphi$ coordinate as a function of the z-coordinate of the cluster (the drift distance increases towards smaller values of z) for the three different pad sizes used in the current pad planes (see Tab. 4.3). For drift distances larger than about 30 cm for the small pads and 80 cm for the larger pads, the resolution achieved with GEM readout is only about 10 % worse than for the MWPC-based readout, despite the large pad size compared to the GEM PRF. In this region, diffusion provides sufficient broadening of the charge cloud, such that clusters with more than a single pad dominate, as shown in Fig. 4.16.

For shorter drift distances, however, the resolution gradually deteriorates due to the appearance of single-pad clusters. As expected, the effect is strongest for the OROCs with large pads and $z > 180\,\mathrm{cm}$. It should be noted, however, that short drift distances correspond partially to regions outside the nominal acceptance of the ALICE central barrel ($|\eta| < 0.9$). This implies that, even with the present pad granularity, the position resolution with GEM detectors will decrease by no more than 20 % for tracks in $|\eta| < 0.75$. It is shown in Chap. 7 that this does not affect the momentum resolution, especially in the high pileup scenario.

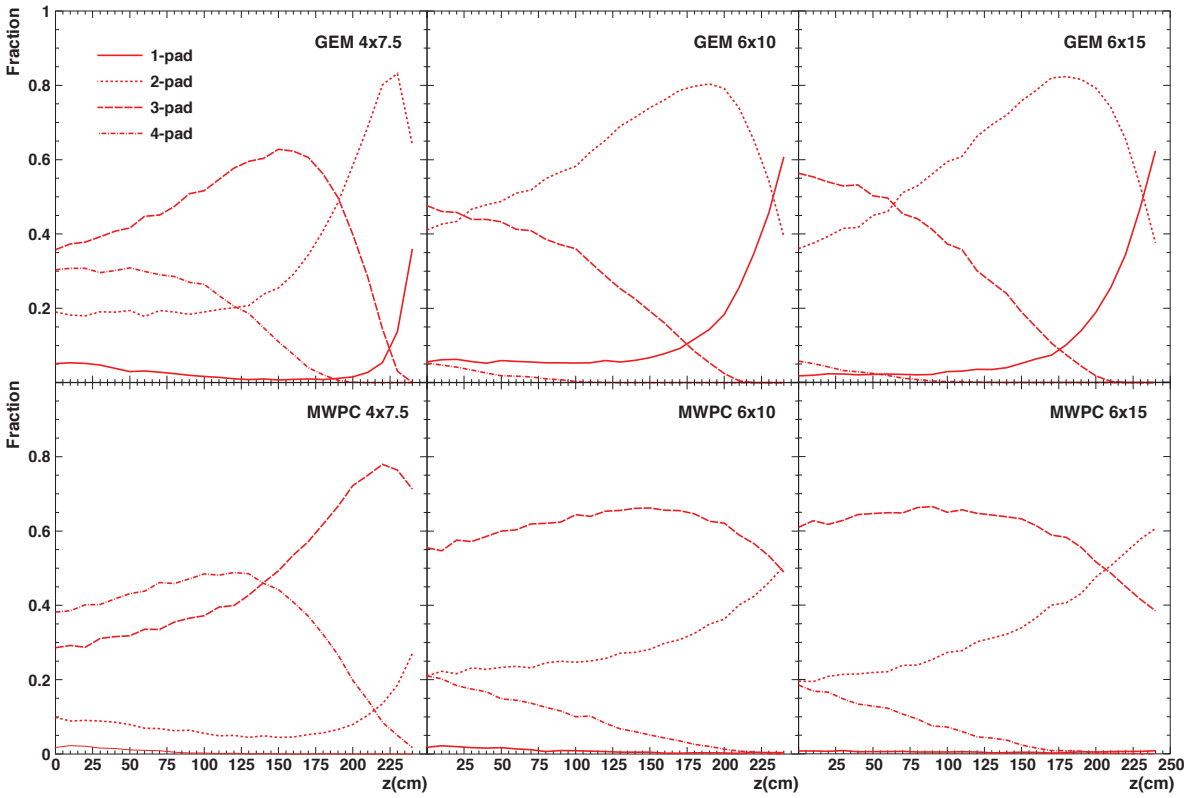

Figure 4.16: Fraction of one-, two-, three- and four-pad clusters for a (top row) GEM-based readout and (bottom row) an MWPC-based readout, with (left) $4 \times 7.5\,\mathrm{mm}^2$, (middle) $6 \times 10\,\mathrm{mm}^2$, and (right) $6 \times 15\,\mathrm{mm}^2$ pads, respectively.

The effect of the different PRF for GEMs and MWPCs is also visible in Fig. 4.17, where the average size of clusters for the different pad sizes as a function of radius r is presented. Since clustering is performed in pad rows, i.e. a cluster extends over several pads within a given pad row and over several time bins, the cluster size is given in units of its area in $r\varphi$-z coordinate space, i.e.

$$A_{\mathrm{cl}} = N_{\mathrm{bins}} \times (\text{pad width}) \times (\text{time bin width}) \; . \tag{4.3}$$

Here, N_{bins} is the number of bins above threshold in pad and time units, pad width is 0.4 or 0.6 cm, and time bin width is given by the drift velocity divided by the sampling frequency. For all radii, the GEM readout gives an approximately 20 % smaller cluster size than the MWPC readout, mainly in $r\varphi$-direction, due to the smaller PRF. Within a given pad size the cluster size increases with decreasing r because of the increasing average polar inclination of tracks, which extends the clusters in time direction. The steps in cluster size at $r \approx 140\,\mathrm{cm}$ and 200 cm appear because of the increasing pad size, which, combined with the polar inclination of tracks, mostly affects the extension of a cluster in time.

On the one hand, the smaller cluster size with GEM readout reduces the occupancy of the detector. However, the larger number of single-pad clusters will make it more difficult to disentangle overlapping clusters. The number of single-pad clusters can be reduced using Chevron-shaped pads, which could restore the spatial resolution of the MWPC-based readout, at the expense, however, of a larger occupancy. It should be noted that occupancy prohibits a larger pad size in radial direction, at least for the IROCs, which would allow to operate the TPC at a lower gain while maintaining a given signal-to-noise ratio. This in turn would decrease the distortions due to ion backflow, as can be seen from Eq. (4.2). The use of a low diffusion gas, like the CF_4 option discussed in Chap. 3 and Sec. 9.2, would reduce the occupancy and therefore allow larger pad sizes in radial direction, or Chevron-shaped pads.

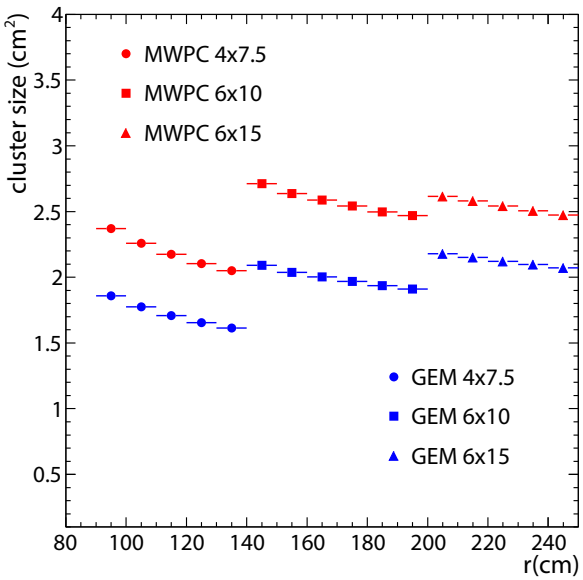

Figure 4.17: Cluster size as defined in Eq. (4.3), as a function of radius r and the corresponding pad sizes, for (blue) GEM and (red) MWPC readout.

		Pad size (mm^2)	Number of rows	Number of pads
IROC	$(841 < r < 1321\,\text{mm})$	4×7.5	63	5504
OROC	$(1346 < r < 1696\,\text{mm})$	6×10	35	2944
OROC	$(1716 < r < 2066\,\text{mm})$	6×10	35	3712
OROC	$(2086 < r < 2461\,\text{mm})$	6×15	25	3200
TPC total	$(2 \times 18$ sectors)		158	552,960

Table 4.3: Dimensions and parameters of readout planes and pads.

In conclusion, the current choice of pad sizes, optimized for occupancy and resolution with an MWPC-based readout, provides sufficient space-point resolution even for the case of GEM amplification without decreasing the pad size. The good momentum resolution in the acceptance of the barrel detectors of ALICE will be maintained after the upgrade, as shown in Chap. 7. It should be noted that the smaller PRF for GEM detectors reduces the occupancy of the detector. Thus, it allows to operate the TPC with a Ne-CO_2-N_2 (90-10-5) gas mixture also at the luminosity foreseen after the upgrade of the LHC.

Figure 4.18 shows the design of the pad plane for the OROC, where the division of the GEM detectors in three separate modules has been taken into account. There are two dead areas under the frames of the foils. Moreover, the transition between medium and large pads has been moved up by 8 cm with respect to the current pad plane. This results in 1 pad row less in the new pad plane, i.e. 1.3 % less pads as compared to the current system.

Table 4.3 summarizes the pad sizes for the different regions of the readout chambers. In total, the pad re-arrangement in the OROCs results in 0.8 % less pads in the TPC as compared to the currect system.

4.6 Interface to front-end electronics

The front-end electronics is described in Chap. 6. The signals induced on the readout pads are routed to connectors on the backside of the pad plane. As in the present system, short flexible flat cables will be used to decouple the weight of the FEE[6], which is supported by the service support wheel, from the

[6]Front-End Electronics (FEE)

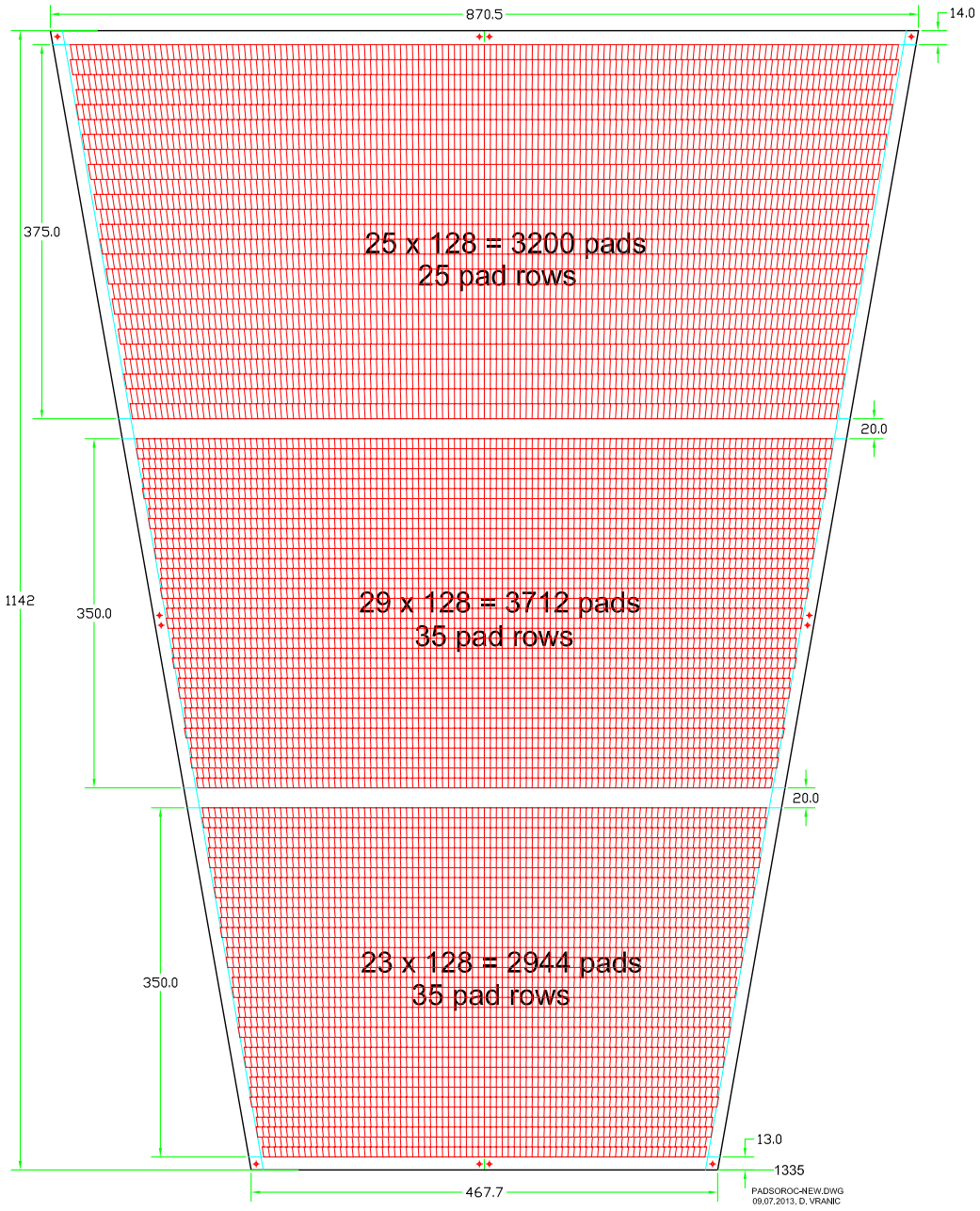

Figure 4.18: Pad layout of an ALICE OROC. The gaps have been introduced to allow fixation of the GEM detector modules. Units are in mm.

readout chambers and the field cage. The signal routing must be optimized in order to minimize the trace length. The exact configuration of the connectors, flat cables and cards is still a matter of optimization and has thus not been decided upon yet.

4.7 Quality assurance of GEM foils

The proper selection of the GEM foils to be assembled into the readout chambers is of major importance.

COMPASS was the first large-scale experiment to use GEM-based detectors. Quality assurance procedures for all detector components have been established in order to guarantee a uniform and stable operation of the COMPASS readout chambers [7]. These procedures have successfully been applied and extended to other projects like LHCb [22], PHENIX [12], TOTEM [13] and the SuperFRS [23, 24], and will be adopted to a large extent for the ALICE TPC.

In this section we will go through the transportation requirements and the characterization process, in particular optical and electrical uniformity checks, that are essential in order to minimize the risk of initial failure and in order to ensure the long-term stable operation of the modules. A methodology has been developed for some of the characterization steps. These will be treated separately in the following.

4.7.1 Electrical characterization

The first electrical quality assurance test consists of measuring the leakage current in each GEM HV sector in response to an applied voltage across the foil. The test is performed in a dry nitrogen environment to avoid instabilities related to water or dust. In order to measure the leakage current, a setup as shown in Fig. 4.19 is used.

The components of this setup are: a desiccator with a gas flowmeter, an electrometer, a high voltage source and a computer to control the ramping of voltages and to read and store the current measurements. A voltage is applied between the unsegmented side and one of the HV sectors on the other side of the foil, with all the other sectors grounded. The voltage is ramped in steps up to a final potential difference of 550 V between the two sides of the GEM foil, which is slightly below the breakdown limit of GEM foils in N_2 gas. Once the GEM is fully charged, the current drops and saturates at the leakage current through the GEM HV sector under study, which should normally be $\lesssim 0.1$ nA. Foils with leakage currents larger than ~ 0.5 nA are rejected and returned for re-cleaning. The foil is kept at maximum voltage for up to 30 min. If the foil is stable during this time with a leakage current smaller than 0.5 nA, it is accepted and given to the next characterization setup (optical scanning).

A typical leakage current evolution during the electrical characterization is shown in Fig. 4.20. Figure 4.21 shows a second example of a leakage current test, where a HV sector experienced several discharges, but could be fully recovered after flushing with N_2. In cases where continuous discharges are observed, the foil is rejected and returned for re-cleaning.

4.7.2 Optical scanning characterization

After a foil has passed the coarse visual inspection and the static electrical quality assurance testing, it is subjected to precision optical inspection using a high resolution camera. In this way the geometrical characteristics of the GEM foil can be studied. In particular, the distributions of inner and outer hole diameters and the hole pitch for both surfaces of the foil are measured. It is well known that a variation of the inner hole diameter causes a variation of the intrinsic gain of the foil. The dispersion of the distributions can be taken as a quantitative indicator of the general foil uniformity. Foils not meeting the specifications over the full surface (i.e. copper hole diameter typically $70\,\mu\text{m} \pm 5\,\mu\text{m}$, polyimide hole diameter typically $55\,\mu\text{m} \pm 5\mu\text{m}$) are rejected.

In addition, the method is suited to identify smaller defects which were not detected in the first visual

Figure 4.19: Leakage current measurement setup.

inspection step. Defects in the form of under- or over-etched areas in the foils can occur during the manufacturing process. Other defects may come in the form of chemical residues from the production process, droplets of glue or dust attached to the foil, very large holes, missing holes, etc. All of them may cause operational instabilities; such foils are rejected and possibly re-cleaned.

The setup used for this purpose is based on a back-illuminated light table with area $100 \times 100\,\mathrm{cm}^2$. It accommodates a full foil used for an IROC or OROC. In Fig. 4.22 the scanner used for this optical characterization is shown [25]. A 9 Megapixel camera with a single pixel size of $1.75\,\mu\mathrm{m}^2$ is mounted on an *x*-*y* positioning system above the light table. The optical system has a resolution of 144 light points per mm and a field of view (single image) of $6.1 \times 4.6\,\mathrm{mm}^2$. After compression, the total image size is about 20 MByte. Up to 32,000 individual images are required to cover the full active area.

During the scanning procedure the diameters of inner and outer holes, the pitch between holes and their shape are recorded. Distributions of the diameter, the width of the polyimide rim (the distance between the border of the outer and inner holes), and the pitch are shown in Fig. 4.23. Parameters describing the shape of the hole are obtained from an ellipse interpolation with a sigma of $0.52\,\mu\mathrm{m}$. A suitable criteruim to determine e.g. the maximum allowable rim width (see tail in middle panel of Fig. 4.23) will be established.

A two-dimensional map of the GEM foil characteristics is used to visualize the uniformity of measured parameters as a function of position on the foil. Figure 4.24 shows an example of the spatial variation

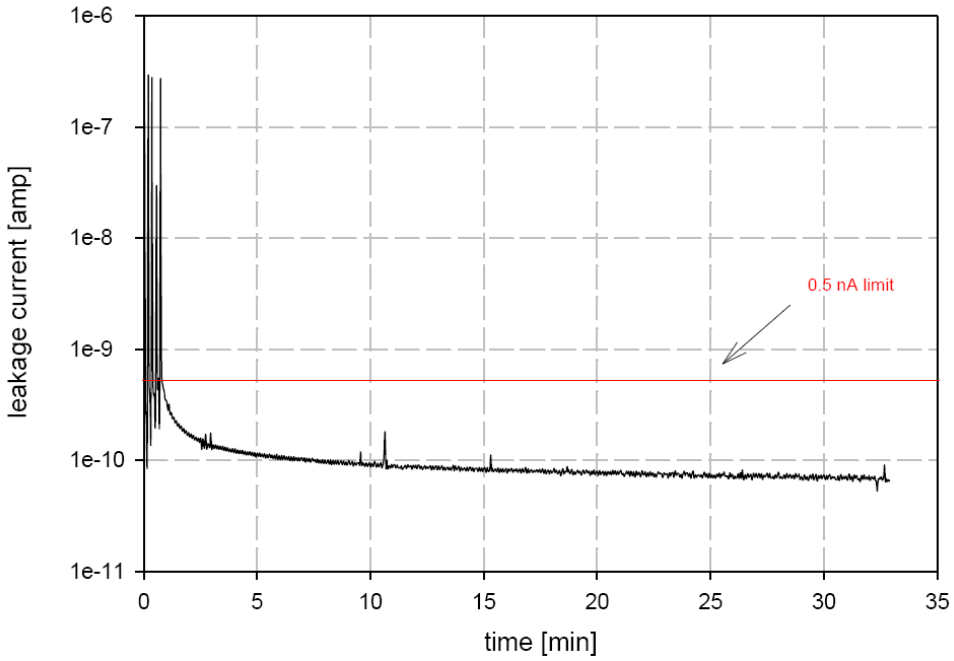

Figure 4.20: Leakage current evolution during electrical characterization of an accepted GEM foil. The spikes at early times correspond to the five voltage steps scanned through during ramping up at the beginning of the test. After the target voltage has been reached, the current quickly drops below 1 nA. It is then measured for as long as 30 min.

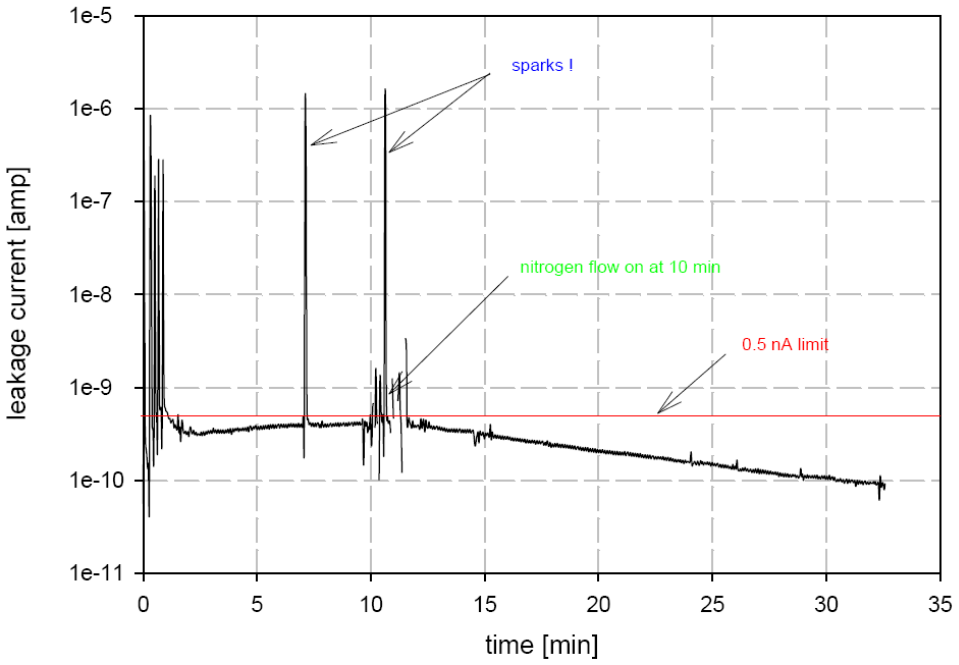

Figure 4.21: Leakage current results from a recovered GEM foil.

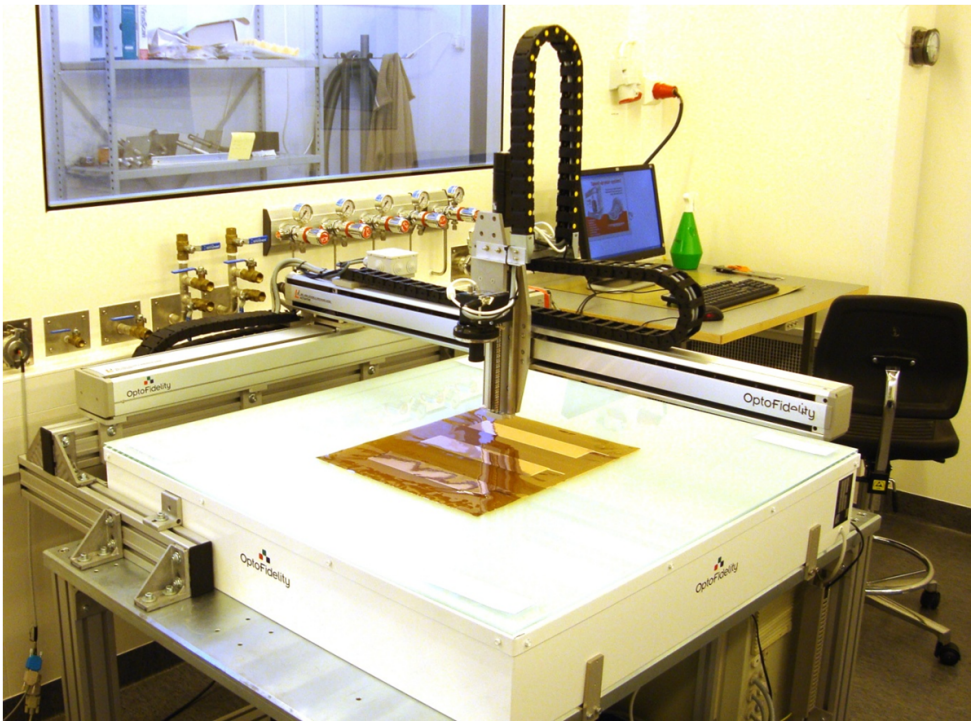

Figure 4.22: Setup of the high resolution scanning system.

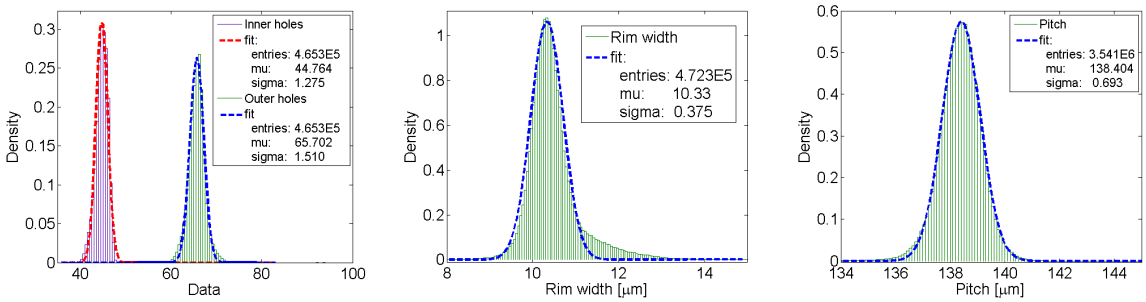

Figure 4.23: Distributions of inner and outer hole diameters (left panel), the rim width (middle panel), and the pitch between holes (right panel).

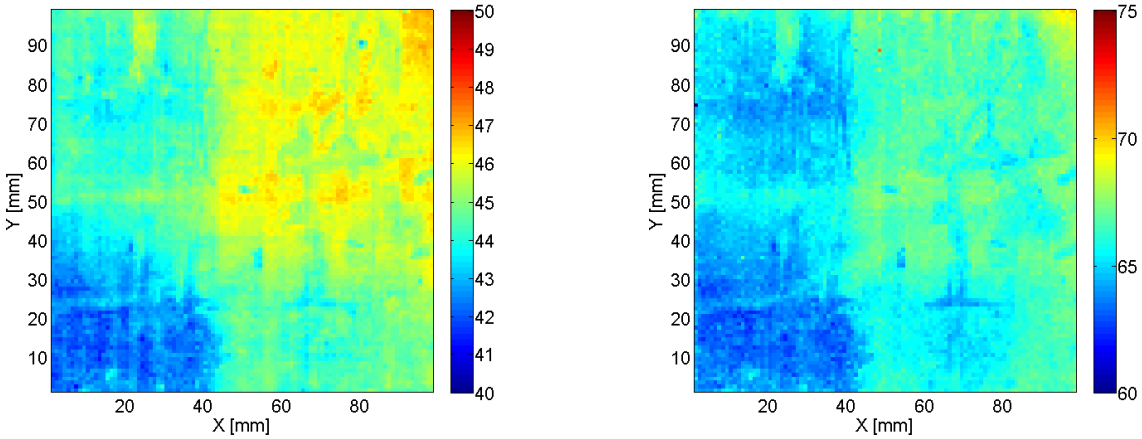

Figure 4.24: Map of hole diameters of a $10 \times 10\,\mathrm{cm}^2$ GEM foil. (Left) inner hole diameter, (right) outer hole diameter.

of the diameters of the inner and the outer holes. Here, the diameters of holes are averaged over an area of $1\,\mathrm{mm}^2$. Maps such as these can be used during assembly of the GEM stack to avoid accumulation of unwanted features in similar positions over the stack area.

4.7.3 GEM gain mapping

To evaluate the uniformity of the gain distribution, a mapping of the gain of each GEM foil is performed. An acceptance criterion can be specified for the gain variation across the surface of the foil, e.g. 10 % (RMS). In order to determine the gain map of a GEM foil, a setup as shown schematically in Fig. 4.25

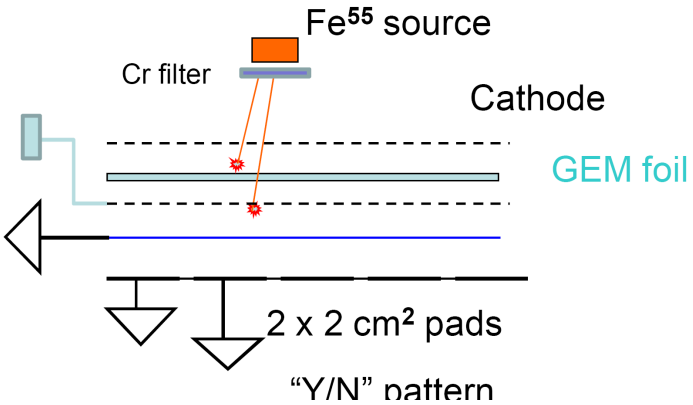

Figure 4.25: Schematics of the setup for the gain mapping measurement.

is used. It includes the GEM foil under test and a reference detector, typically a multiwire proportional chamber or alternatively a Micromegas detector. The reference detector detects the primary ionization that takes place either above or below the GEM foil. In addition, a pad readout geometry is used to record a 2D map of the foil under test. The source on top of the detector is used to illuminate the entire GEM foil, making it possible to measure the gain and its evolution in time without having to scan over the detector surface. A prototype of this setup, shown in Fig. 4.26, has been built at Yale University.

By illuminating the whole active area with a source, a double spectrum is measured for each pad, as shown in Fig. 4.27. The low-amplitude spectrum corresponds to X-rays absorbed below the GEM, whereas the high-amplitude one corresponds to X-rays absorbed above the foil. The ratio between the position of the two main peaks is therefore proportional to the gain of the GEM foil for this particular pad area. The uniformity of the gain is then obtained from the variations of the gain of each pad with

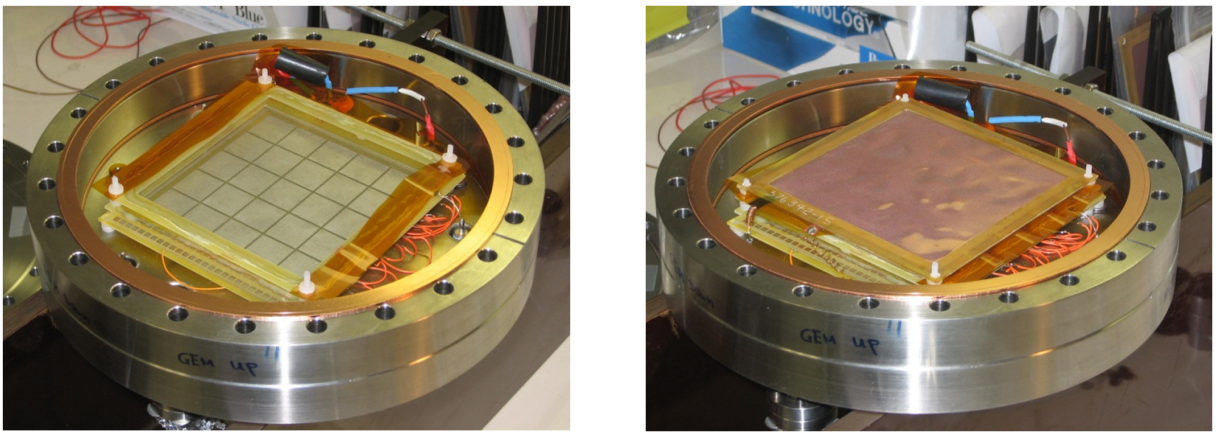

Figure 4.26: (Left) Gain map setup. (Right) Flange together with the multiwire proportional chamber and the GEM foil under test.

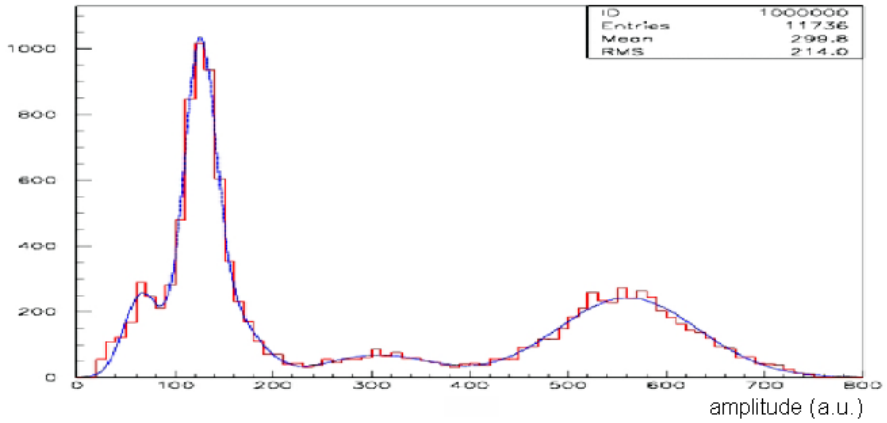

Figure 4.27: Pulse height distribution for a single pad.

respect to the mean gain value. For the particular example shown in Fig. 4.28, the pad dimensions were $2 \times 2\,\mathrm{cm}^2$, and the total area of the GEM foil was $10 \times 10\,\mathrm{cm}^2$, resulting in the 5×5 bin gain map shown.

For the GEM foil test illustrated in this figure, the mean gain obtained was 23 with a dispersion of 4.8 % (RMS). At the same time this setup also permits mapping of the energy resolution of a single GEM foil, and thus a measurement of the uniformity of the expected energy resolution.

4.8 Quality assurance of chambers

Once the GEM stacks are mounted on the IROCs or OROCs, the completed chambers need to pass further tests. They are installed in test boxes which provide a gas volume and a small field cage with a drift electrode and a voltage divider. The box is flushed with the nominal gas at a reasonable flow.

The first test is the gas tightness test. The pad plane structure may exhibit leakage if not properly assembled. For testing this, the oxygen contamination in the gas outlet of the test box is measured with an appropriate oxygen sensor. In order to provide final oxygen levels compared to the current ones in the TPC, levels of $1-2\,\mathrm{ppm}$ in the test box at flows of $20\,\mathrm{l/h}$ should be achievable. However, viscous leaks, e.g. through tortuous paths between the pad plane and the alubody, can be difficult to detect by this method, unless the gas pressure in the test box is kept lower, by a few mbar, than the ambient pressure. Therefore, the gas system utilized for these tests will contain provisions for producing a controlled underpressure in the test box.

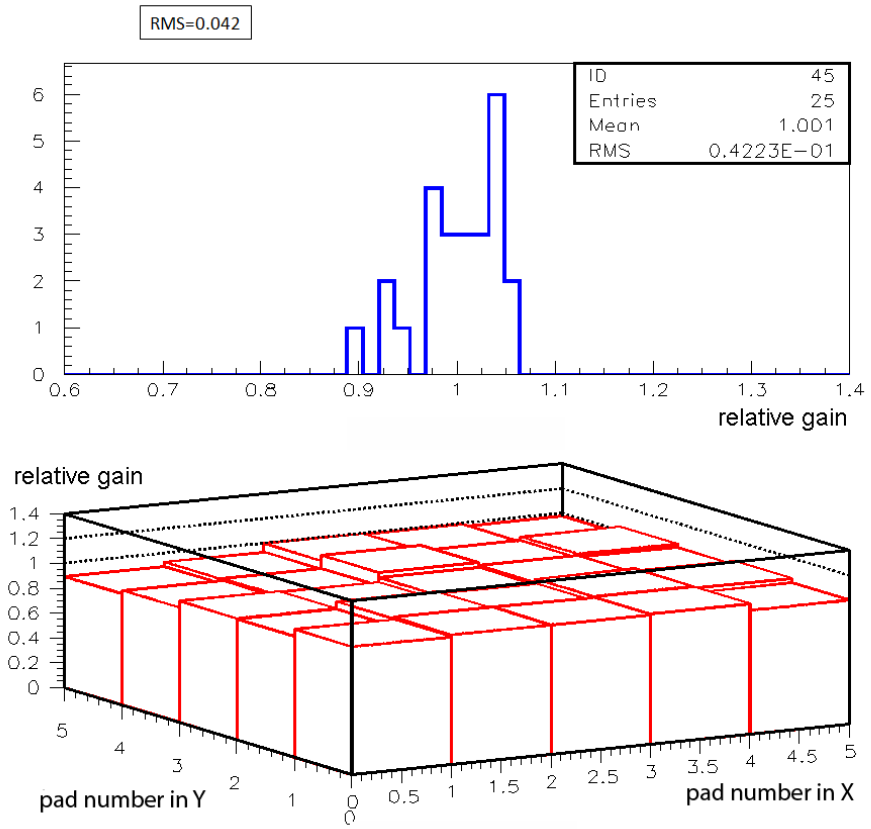

Figure 4.28: Relative gain distribution (top panel) and map (bottom panel) of a single GEM foil.

The next test is to produce the gain curve as a function of the applied voltages in order to characterize each chamber. All chambers should deliver similar gains at similar voltages, and should hold at least a factor of 2 higher gain than the anticipated operational gain.

The measurement of the uniformity of the gain across the active area follows next, with a coarser granularity than in the previous QA of the foils. This test assures that the stack is properly mounted and clean.

Finally, a long-term test is carried out. The chamber is operated at a gain higher than the nominal value for one or two days, while being irradiated with e.g. an Fe^{55} source. During this test the relevant parameters are periodically recorded: currents, main peak position for the Fe^{55} spectrum, FWHM of the main peak, ambient conditions, oxygen and water concentrations. The chamber must hold this test without any trips or current excursions.

Once a chamber passed all these tests (timescale ~ 1 week per chamber) it is validated and properly stored in a sealed environment under controlled temperature and pressure until its installation in the TPC field cage. About 80 chambers will be built and tested this way in several construction and testing sites. A convenient split is two test sites for all IROCs and two for all OROCs.

Chapter 5

R&D with prototypes

In this chapter the R&D carried out with small and large prototype chambers is described. The obtained ion backflow performance and the comparison with detailed simulation studies is presented in Sec. 5.1. The construction and in-beam operation of a full-size prototype of an IROC, assembled with three GEM foils, is described in Sec. 5.2.

5.1 R&D with small prototypes

In this section the question of the minimization of the ion backflow of a GEM structure is addressed. To this end, scans of field configurations are performed, and various GEM structures are investigated, in particular triple and quadruple stacks assembled with standard and double-pitch foils. The resulting performances are compared with simulations. The energy resolution and the stability of the emerging solutions are also investigated or in the process of being demonstrated. Although various gas mixtures have been tried out, we focus here on results obtained with the baseline mixture Ne-CO_2-N_2 (90-10-5). The detectors are irradiated with sufficiently low X-ray rates in order to avoid building up positive space-charge near the foils, since as it was found out this severely affects the measured ion backflow.

5.1.1 Experimental setup

Several small detector systems were built and set up in various labs within the scope of this R&D effort.

Setup for gain stability measurements

Measurements are performed to monitor the gain stability of a GEM stack over time, including the response to changes in high voltage and radiation levels. For this purpose, a GEM chamber under test is continuously irradiated while its current is periodically measured. The ambient temperature and pressure are also recorded, together with the water content of the gas, which plays an important role in charging-up processes of GEM foils. A single-wire proportional counter is operated in the same gas stream and its gain monitored via the position of the ^{55}Fe line for correction purposes. Both the GEM detector and the wire counter are installed in a box which may be flushed with N_2 for further moisture reduction.

CERN ion backflow setup

The detector housing used for ion backflow measurement at CERN comprises a GEM holder and a field cage. The GEM box is equipped with HV feedthroughs for up to four 10×10 cm^2 foils and a pad plane subdivided into 16×16 pads. All pads are connected together to a DC voltmeter for measurement of the current. The field cage, constructed from Rohacell to permit irradiation with X-rays, is 8 cm deep and has a drift electrode and 10 strips made of copper. The drift electrode is powered with one channel of a

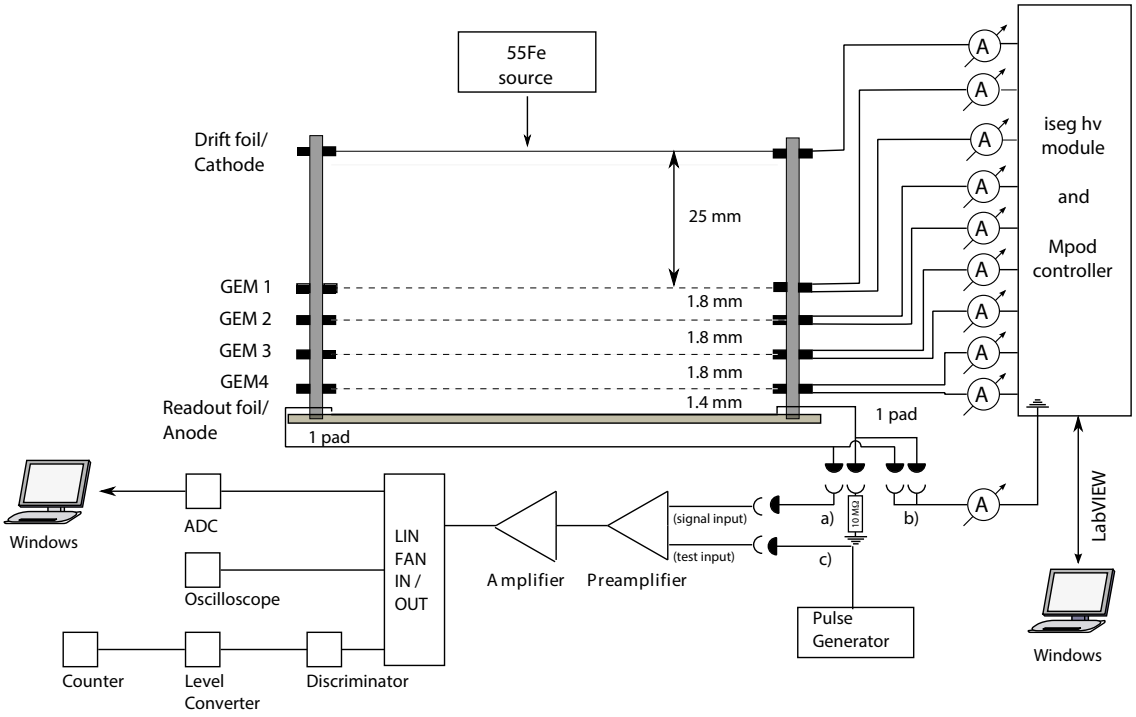

Figure 5.1: Sketch of the Munich quadruple GEM setup.

HV power supply and its current is measured with a floating picoammeter with 100 pA resolution. The field cage is powered with a second HV channel so that the current through its $10 \times 10\,\mathrm{M}\Omega$ resistors does not add to the small current on the drift electrode. A last, external resistor ensures reasonable matching of potentials of the last strip and the top GEM electrode. The gas is supplied from a premixed bottle for the reference measurements with Ar-CO_2 (70-30) and from a mixer for the other gas mixtures. The HV is supplied with programmable power supplies for convenient scanning of gains and fields. A small, silver-anode X-ray tube is used as source of radiation.

Munich ion backflow setup

The Munich detector has been specifically built to measure ion backflow. The geometrical configuration is summarized in Tab. 5.1. It features a short drift length, individual control of each HV electrode, and the possibility to irradiate the detector from the top and a side wall. Standard $10 \times 10\,\mathrm{cm}^2$ GEM stacks are used.

Drift gap	25 mm
Transfer gap 1	1.8 mm
Transfer gap 2	1.8 mm
Transfer gap 3	1.8 mm
Induction gap	1.5 mm
Thickness top window	150 μm
Thickness side window	50 μm

Table 5.1: Properties of the Munich test detector in the quadruple GEM configuration.

The readout consists of 512 strips, that can be either read out individually or connected via analog summation cards to a total of 16 channels. By setting the appropriate jumper one can select the corresponding size of the readout area, while all other strips remain grounded.

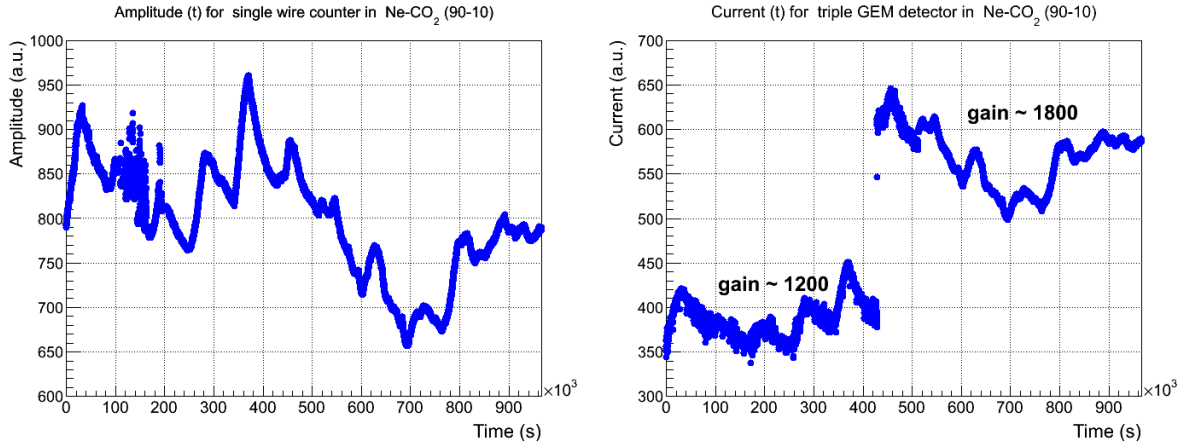

Figure 5.2: Signal amplitude in the single wire counter (left panel) and current in the triple GEM (right panel) as a function of time with a Ne-CO_2 (90-10) gas mixture and 180 ppm of water.

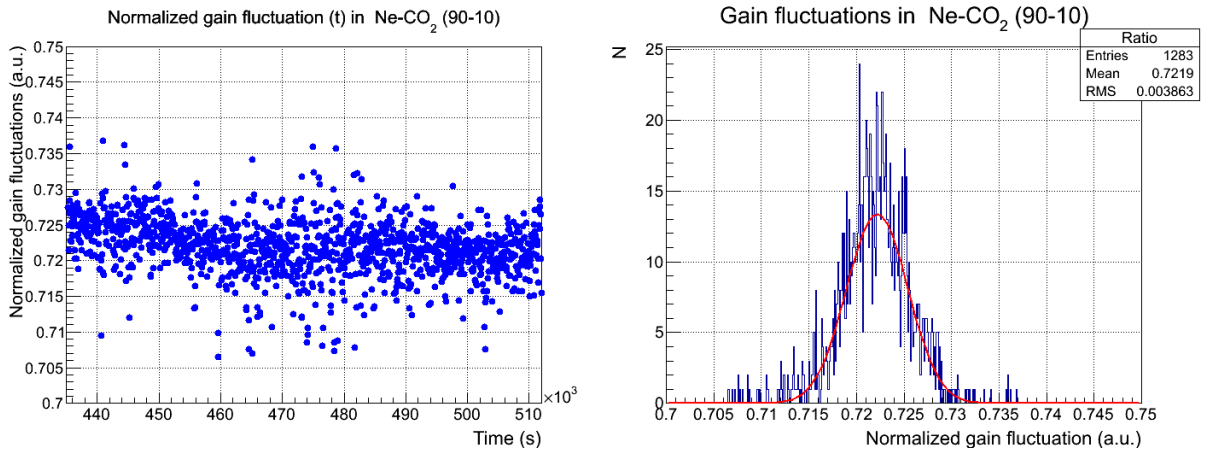

Figure 5.3: (Left) GEM current corrected by the gain of the single wire counter as a function of time, during the few hours following an increase in the GEM gain. (Right) Projected distribution fitted with a Gaussian. The relative variation is 0.45 %.

The picoammeters used to measure all currents contain a wireless transmission unit which allows them to be kept at a floating potential. They are able to measure currents down to 0.1 nA at up to ∼5 kV. These picoammeters are connected to each electrode as shown in Fig. 5.1. All currents are measured simultaneously and therefore should sum up to zero. The readout of the pads is realized with conventional spectroscopy amplifiers and a multichannel analyzer for recording pulse height spectra. Two small X-ray tubes, with gold and silver targets, are used to irradiate the detector.

The ion backflow and ε used in the following are defined according to Eq. (4.2). The gain is determined by the usual method of recording the current at the pad plane and the rate of absorbed X-rays of known energy.

5.1.2 Gain stability measurements

Several gain stability measurements have been carried out in order to demostrate that the gain in a GEM system is stable with time, even under changing conditions of gain or irradiation rate.

As an example, it is shown in Figure 5.2 the long term behavior of a triple GEM setup. The measurements were performed in Ne-CO_2 (90-10). The right-hand panel shows the current of the triple GEM stack over a period of more than 11 days, in the middle of which the gain was increased from 1200 to 1800. The observed fluctuations are due to gas pressure, temperature, and perhaps composition fluctuations, as

confirmed by the pulseheight data of a single-wire proportional counter used as reference (left panel). The wire counter data is used to correct the gain variations of the GEM detector. In Fig. 5.3 the corrected GEM gain is shown for a period of about 21 hours, just after the gain was increased. Within this time the corrected gain remains very stable, within 0.45 %, as indicated by the fit of the right panel of the figure. Thus, no settling time is observed after changing the operating conditions. It should be noted that a humidity level of about 180 ppm of water was maintained for the entire period.

5.1.3 Results of ion backflow measurements

Baseline solution

A suitable working point in terms of ion backflow and local energy resolution was found by utilizing a quadruple GEM system in which the foils in layer 1 and 4 have a standard hole pitch (Standard, 140 μm), whereas the foils in layer 2 and 3 have a hole pitch that is two times larger (Large Pitch, 280 μm). This arrangement, denoted S-LP-LP-S, allows to block ions efficiently by employing asymmetric transfer fields and foils with low optical transparency. An increasing sequence of gas gains down the GEM stack helps reducing the ion backflow since ions created in the inner two layers are blocked more efficiently. On the other hand, the efficiency for electron transmission, in particular in the first two layers, is also affected by this configuration. Therefore, a combined optimization with respect to both ion backflow and energy resolution is mandatory.

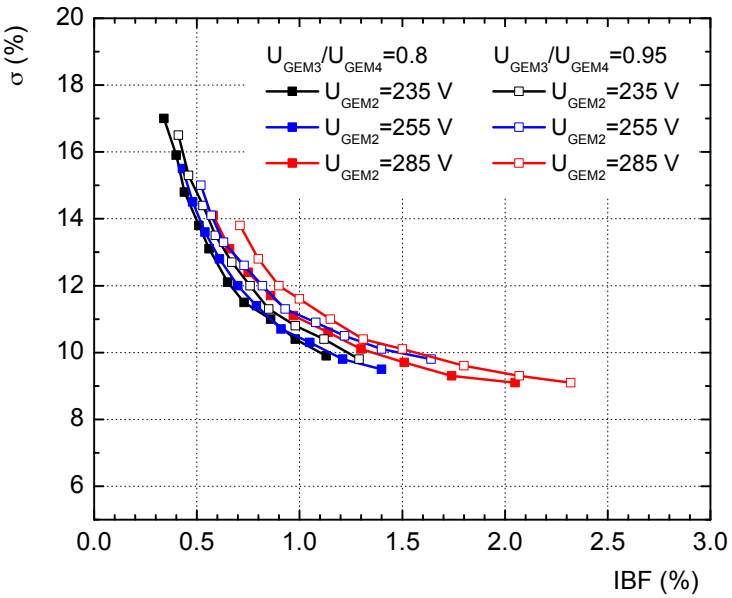

Figure 5.4: Correlation between ion backflow and energy resolution at 5.9 keV in a quadruple S-LP-LP-S GEM in Ne-CO_2-N_2 (90-10-5) for various settings of ΔU_{GEM2}. The voltage on GEM 1 increases for a given setting between 225 and 315 V from left to right. The voltages on GEM 3 and GEM 4 are adjusted to achieve a total effective gain of 2000, while keeping their ratio fixed. The transfer and induction fields are 4, 2, 0.1 and 4 kV/cm, respectively.

In Fig. 5.4 the ion backflow and energy resolution at 5.9 keV obtained with a S-LP-LP-S arrangement are summarised for various voltage settings, illustrating the competing mechanisms of electron transmission and ion blocking. The results are obtained in a Ne-CO_2-N_2 (90-10-5) gas mixture for different combinations of ΔU_{GEM1} and ΔU_{GEM2}, and at different ratios $\Delta U_{\mathrm{GEM3}}/\Delta U_{\mathrm{GEM4}}$. Clearly the ion backflow improves for lower gains at GEM 1 and GEM 2, while the energy resolution deteriorates accordingly. Typical values of ion backflow around 0.7 % at energy resolutions of $\sim$12 % are reached. This performance fulfills the requirements for maximum allowable space-charge distortions and proper $\mathrm{d}E/\mathrm{d}x$

resolution of the detector, and defines the baseline solution for the detector configuration presented in this TDR: a quadruple GEM system of the type S-LP-LP-S. A full set of typical HV settings for optimal operation is shown in Tab. 4.2.

In the next sections we describe the R&D evolution from the commonly used standard S-S-S triple GEM stack to the final S-LP-LP-S configuration and the systematic optimizations by scanning various settings of GEM voltages and transfer fields. Further understanding on the behaviour of the quadruple system is also provided.

Ion backflow results for a triple GEM setup

Extensive studies were performed with triple GEM detectors aimed at minimizing the ion backflow of the structure. In order to find the optimal settings, the transfer fields E_{T1} and E_{T2} were varied systematically while the voltage across GEM 3 was used to keep the gain at the desired value. The effective gain was kept at ∼2000, the drift field at 400 V/cm and the induction field at 4 kV/cm, while the X-ray rate was always lower than a few tens of nA/cm^2. Several gas mixtures have been studied, although results are shown only for the baseline gas mixture Ne-CO_2-N_2 (90-10-5).

As described in Sec. 4.1, ion backflow suppression in a GEM system is based on an asymmetric field configuration within the stack. This concept was proposed by the International Linear Collider (ILC) community and described in [1]. Following this concept, the values of E_{T1} and E_{ind} are maximized, whereas E_{T2} is set at a minimum value to achieve maximum blocking of the ions produced at GEM 3. In addition, the potential differences across the three GEMs follow an increasing order, such that

$$\Delta U_{GEM1} < \Delta U_{GEM2} < \Delta U_{GEM3} \, . \tag{5.1}$$

In this way, most of the ions are produced on GEM 3 and must enter the blocking region.

As an illustrative result, in Fig. 5.5 the ion backflow is shown as a function of E_{T1} for several E_{T2} values in Ne-CO_2-N_2 (90-10-5). A decrease of the ion backflow as a function of E_{T1} is observed due to the increasing extraction efficiency of GEM 1. The best performance is reached at the lowest applied E_{T2} (0.1 kV/cm).

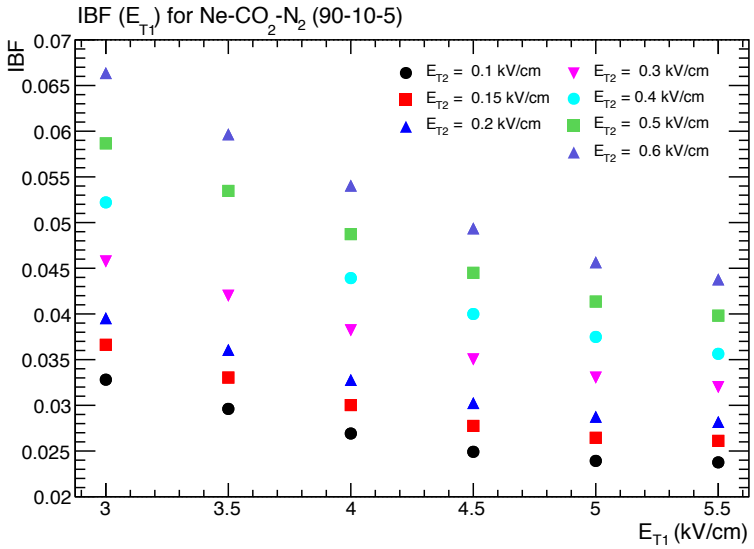

Figure 5.5: Ion backflow in a triple GEM detector as a function of E_{T1} for several values of E_{T2}.

In conclusion, the ion backflow in triple GEM systems can be reduced to ∼2.5 % after careful optimization of the voltage and field settings. This number falls short of the requirements by more than a factor of

two. No strong dependence on the gas mixture has been observed in any measurement (not shown here). Therefore, structures with four GEMs, including those with large hole pitch, are considered next.

Ion backflow results with quadruple GEMs

As the next step towards a minimization of ion backflow, systematic studies of systems with four GEMs were performed. The selected results presented in this section were obtained for various configurations of quadruple GEM stacks, measured with different experimental setups. These studies include also the use of foils with large hole pitch (LP) [2], 280 μm, that are combined with foils that have the standard hole pitch of 140 μm (S). The ion backflow was measured simultaneously with the energy resolution using an ^{55}Fe X-ray source. All measurements presented here are for the baseline gas mixture Ne-CO_2-N_2 (90-10-5). The gain was systematically adjusted to 2000 by tuning ΔU_{GEM3} and ΔU_{GEM4} while maintaining a defined ratio between the two.

Several HV scans were carried out with a structure composed of four standard foils (S-S-S-S). As an example, a two-dimensional scan of the ion backflow as a function of E_{T2} and E_{T3} is shown in Fig. 5.6, where ion backflow values of 2 % are reached for low values of E_{T2}. The energy resolution, expressed as the sigma of a gaussian fit to the 5.9 keV peak divided by the mean value, is about 11 %.

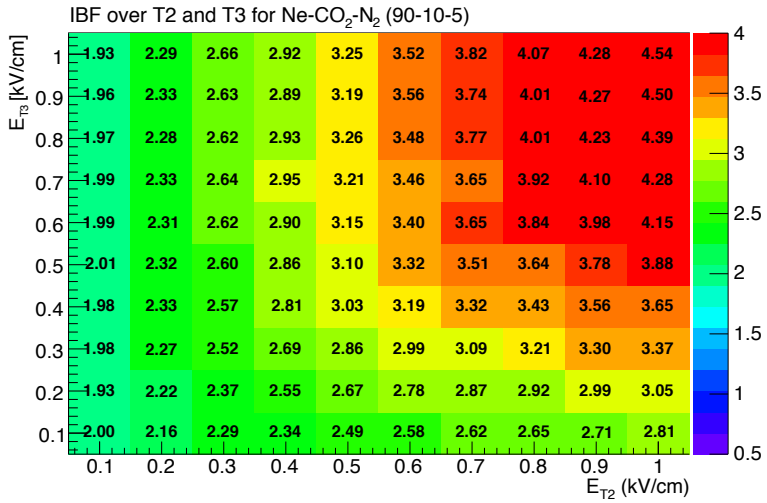

Figure 5.6: Two-dimensional scan of the ion backflow in a quadruple stack of standard GEMs (S-S-S-S) as a function of E_{T2} and E_{T3}. E_{T1} and E_{ind} are both 4 kV/cm, and the voltages across the GEMs are tuned, in an increasing sequence, to achieve an effective gain of 2000.

In the next step, one large-pitch foil is introduced to form a configuration of the type S-S-LP-S, aiming at improving the ion backflow by applying a low transfer field (E_{T2}) just above the large-pitch GEM with low optical transparency. The two-dimensional scan shown in Fig. 5.7 illustrates that the ion backflow for this configuration indeed improves as E_{T2} decreases and, to a lesser extent, as E_{T3} increases. It should be noted that the use of large-pitch foils efficiently prevents accidental alignment of the holes of consecutive foils. Ion backflow values below 1.5 % are achieved in the S-S-LP-S configuration.

This mechanism of ion blocking can be reinforced by introducing a second large-pitch foil in the quadruple GEM stack, forming a S-LP-LP-S structure, where the two large-pitch GEMs are mounted in the core of the stack. A scan of the E_{T2} field for such a configuration is shown in Fig. 5.8. Ion backflow values as low as 0.34 % are obtained for high E_{T2} and low E_{T3}. In this configuration ions are absorbed at the top side of GEM 4 due to the low field above, and the remaining ones are focussed between two (typically misaligned) large-pitch foils and partially absorbed at the bottom of GEM 2. On the other hand, the energy resolution observed in this configuration, also shown in Fig. 5.8, is insufficient and requires a more detailed optimization of the voltage configurations.

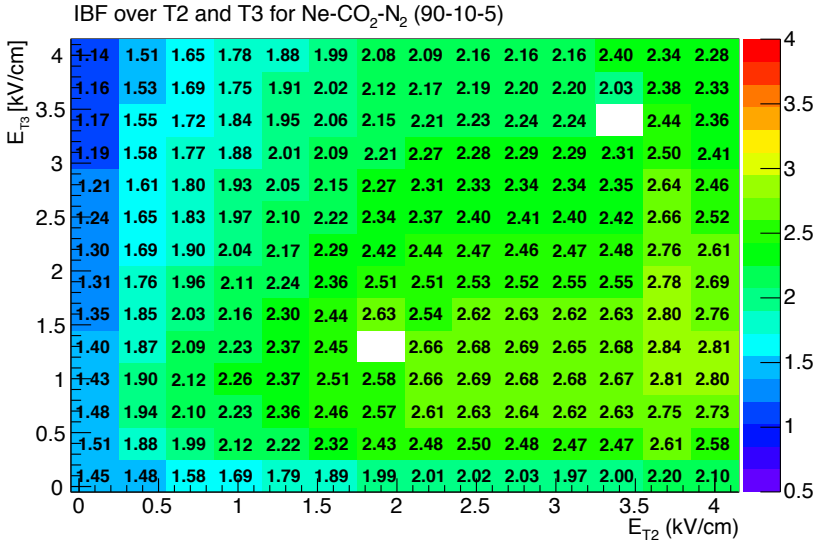

Figure 5.7: Two-dimensional ion backflow scan as a function of E_{T3} and E_{T2} for a quadruple GEM of the type S-S-LP-S (large pitch GEM in 3^{rd} position). E_{T1} and E_{ind} are both 4 kV/cm, ΔU_{GEM1} = 233 V, ΔU_{GEM2} = 250 V, and ΔU_{GEM3} and ΔU_{GEM4} are adjusted to achieve the nominal gain of 2000.

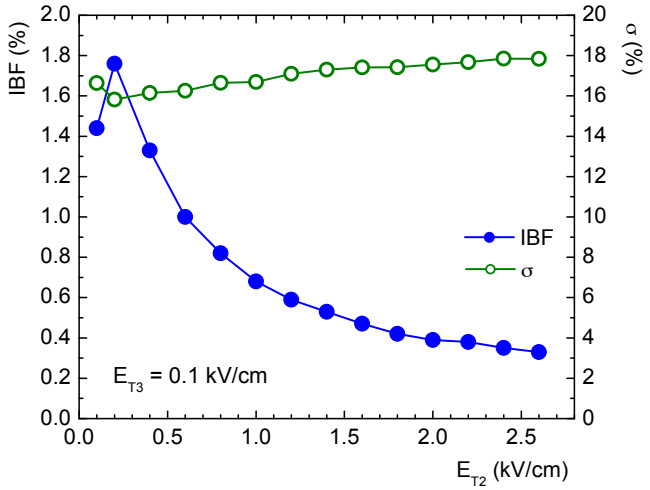

Figure 5.8: Ion backflow and energy resolution in a quadruple S-LP-LP-S GEM as a function of E_{T2} for E_{T3} = 0.1 kV/cm. E_{T1} and E_{ind} are both 4 kV/cm, and the voltages across the GEMs are in increasing sequence to achieve an effective gain of 2000.

The low ion backflow values achieved so far provide room for the optimization of the energy resolution by tuning other settings, such as the voltages across the GEM foils. For the same S-LP-LP-S arrangement as before, Fig. 5.9 (left panel) illustrates the dependence of the ion backflow and the energy resolution on ΔU_{GEM1} for three settings of ΔU_{GEM2}. A significant improvement of the energy resolution can be achieved by the appropriate choice of ΔU_{GEM1} and ΔU_{GEM2}, at the expense of only a moderate increase of the ion backflow. As quoted above, values of ion backflow around 0.7 % at energy resolutions of $\sim$12 % can be reached, which fulfils the detector requirements.

In conclusion, suitable ion backflow figures can be achieved in a S-LP-LP-S quadruple GEM system, but a simultaneous optimization of ion backflow and energy resolution must be made. The correlation between the energy resolution and the square root of the ion backflow as shown in the right panel of Fig. 5.9 demonstrates that the transparency of the system to electrons and the fraction of backflowing ions are closely related. In settings where the ion backflow is large i.e. $1/\sqrt{IB} \to 0$, energy resolutions well below 10 % at 5.9 keV are observed, which is consistent with the expectation for ideal electron

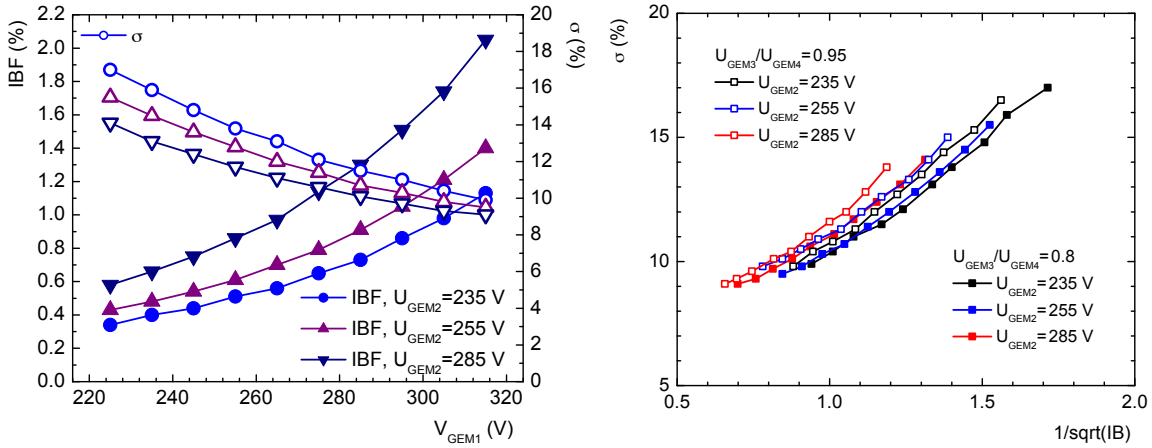

Figure 5.9: (Left) Energy resolution at 5.9 keV and ion backflow in a quadruple S-LP-LP-S GEM as a function of ΔU_{GEM1} and various settings of ΔU_{GEM2}. (Right) Correlation between energy resolution and $1/\sqrt{IB}$ for various settings of ΔU_{GEM1}, ΔU_{GEM2} and $\Delta U_{\mathrm{GEM3}}/\Delta U_{\mathrm{GEM4}}$. The voltage on GEM 1 decreases for a given setting between 225 and 315 V from left to right. The voltages on GEM 3 and GEM 4 are adjusted to achieve a total effective gain of 2000, while keeping their ratio fixed. The transfer and induction fields are 4, 2, 0.1 and 4 kV/cm, respectively.

transparency. At small ion backflow, there is an almost linear correlation between the energy resolution and $1/\sqrt{IB}$. Since the energy resolution is most sensitive to losses of primary electrons that occur in the first GEM layers, this strong correlation suggests that most of the remaining backflowing ions are produced in the first GEM layers as well.

More systematic studies remain to be performed, where further voltage settings and stack arrangements will be tried out. Given the performance and the flexibility in the choice of operational parameters demonstrated in this section, we have confidence that a working solution for the ALICE TPC upgrade will be reached with an ion backflow ≤ 1 %, based on a quadruple GEM system.

5.1.4 Discharge probability studies

Extensive studies of the discharge behaviour of standard triple GEM systems were carried out previously [3]. However, the detector concept for the ALICE TPC upgrade proposed in this TDR differs considerably from these well-studied configurations. Therefore, detailed discharge probability studies of the S-LP-LP-S quadruple GEM system at the proper voltage settings in Ne-CO_2-N_2 (90-10-5) are presently being performed.

We have already confirmed earlier discharge rate measurements [3] obtained by irradiating a standard triple GEM with highly ionising particles at very high gains. While evidence exists that the addition of N_2 to the Ne-CO_2 mixture reduces the discharge probability, the operation of a triple stack in a configuration typical for minimising the ion backflow (increasing gain sequence and low E_{T2}) does increase the discharge rate. The addition of a fourth foil is expected to improve the situation. In order to assess the robustness of quadruple stacks with the inclusion of large-pitch foils and ion backflow settings several discharge measurements are being carried out in various laboratories. The studies will be focussed on operation at nominal or slightly higher than nominal gains with various types of radiation, including alpha, beta and X-ray radioactive sources, and minimum ionizing and heavy-ion beams. The latter include tests with 150 GeV/c pion beams at the CERN SPS[1], and with proton and heavy-ion collisions in the ALICE cavern at the LHC.

The experience of the GEM-based muon trigger detector of LHCb can serve as a reference to judge the required discharge performance of the detectors [4]. In this case a discharge probability of 10^{-12}, as

[1] Super Proton Synchrotron

measured with a close-to-MIP beam, was considered satisfactory since the detectors had survived during this beam test the number of sparks expected in 10 years of operation in the LHC [5] at the quoted rate. The determination of a reasonable discharge probability limit with highly ionising particles can be done by scaling the energy deposition to MIPs. These results shall be confirmed by operating a well-certified full-size prototype detector under LHC conditions.

5.1.5 Comparison with simulations

Simulation studies with Garfield

The ion backflow is studied with the Garfield++ simulation package [6] and compared with experimental measurements presented in the previous section. The geometry of the detector, the material properties of the GEM, the voltage configurations, and the boundary conditions are defined in ANSYS [7]. This program calculates the electric field in the detector with a finite elements analysis method. For the calculation of the properties of gas mixtures and transport properties of electrons in a given electric field, the simulation packages Heed [8] and Magboltz [9] are used. In the simulation studies, the gas mixtures Ar-CO_2 (90-10), Ar-CO_2 (70-30), Ne-CO_2 (90-10), and Ne-CO_2-N_2 (90-10-5) are used, although results shown here are for the latter mixture only. The drift of electrons and the avalanche inside a hole are studied with a microscopic transport and avalanche method. In Garfield++, this method tracks the electron path at the molecular level using the drift velocity and the diffusion, Townsend and attachment coefficients as calculated by Magboltz from the various electron-gas cross sections. Penning effects are introduced in the calculation of the gas gain. Because a microscopic transport calculation for ions is not available in this package, transport parameters such as the ion mobility as a function of the field over the gas density (E/N) are set by hand according to [10–12]. The diffusion of ions is given by the thermal diffusion of $D_{\mathrm{L}} = D_{\mathrm{T}} = \sqrt{2k_BT/qE}$, where k_B is the Boltzmann constant, T the temperature, E the electric field and q the electrical charge. A Monte Carlo integration technique is utilized for tracking of ions. In these simulations, the Munich detector configuration, as described in Sec. 5.1.3, is used.

It has been found in the course of these studies that the alignment of the holes of GEM 1 and GEM 2 crucially affect the resulting ion backflow in a triple GEM system. Since the hole alignment between standard GEMs cannot be controlled in the measurements, misalignments between GEM 1 and GEM 2 are introduced as a free parameter in the simulations in order to describe the experimental results.

Figure 5.10 shows the probability distribution of the minimum distance between holes for two randomly positioned GEM layers of 140 μm pitch. The mean and most probable values of the distribution are 50 μm and 70 μm, respectively; therefore, a misalignment of 50 μm is a reasonable value.

Figure 5.11 shows ion backflow in a 3-GEM stack as functions of E_{T1} and E_{T2} in Ne-CO_2-N_2 (90-10-5) for a misalignment of 45.9 μm. Although some difference in *IB* is observed for $E_{\mathrm{T2}} \geq 0.7$ kV/cm and $E_{\mathrm{T1}} \leq 3.5$ kV/cm, the measured ion backflow for $E_{\mathrm{T2}} \leq 0.6$ kV/cm is well described by the simulations.

As E_{T2} decreases and E_{T1} increases, the number of ions drifting back into the drift region from GEM 3 is reduced and the contribution of ions from GEM 2 becomes relatively large. The consistency of the misaligment values used in the simulations has been checked by comparing measurements of the ion backflow performed with the same detector setup but with different gas mixtures: Ar-CO_2, Ne-CO_2, and Ne-CF_4. The measurements are always reproduced best in the simulations when using misalignment values between 40 and 50 μm. The uncertainties in the mobility, longitudinal and transverse diffusion of ions at low electric field, where no measurements exist, might add an additional systematic uncertainty to the comparison between simulations and measurements.

The measured ion backflow in Ne-CO_2-N_2 (90-10-5) with two different quadruple GEM configurations (with one and two large pitch foils) has been compared with the corresponding simulations. The results are shown in Fig. 5.12. In the simulations various combinations of misalignment for GEM 2 and GEM 3 were considered, otherwise the voltage settings are identical. In general, good agreement is achieved

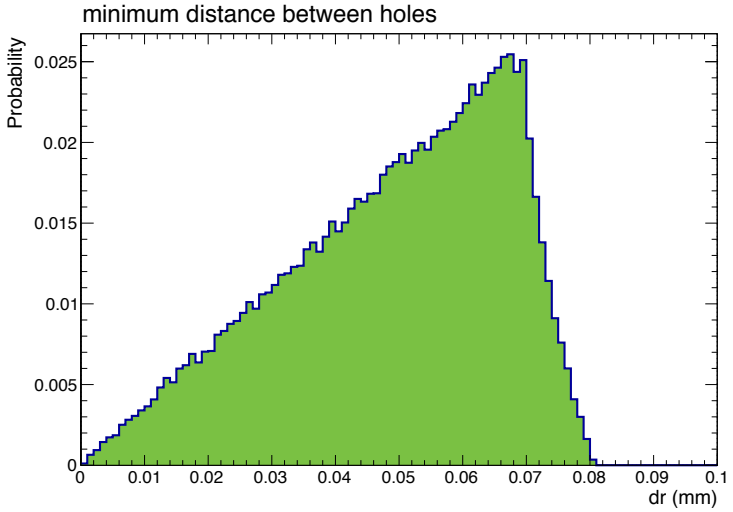

Figure 5.10: Probability distribution of the distance between closest holes in two randomly aligned GEM layers with pitch 140 μm.

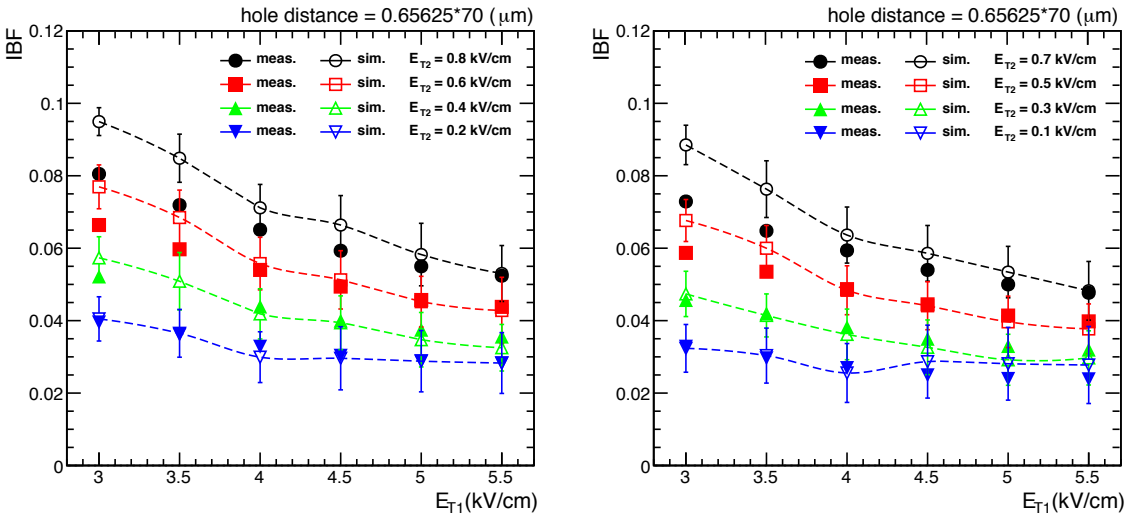

Figure 5.11: Ion backflow in Ne-CO_2-N_2 (90-10-5) as function of E_{T1} for different settings of E_{T2} for a triple GEM configuration. The data from measurements (closed symbols) and simulations (open symbols) with a misalignment of 45.9 μm is distributed on the two panels for better visibility.

between simulations and measurements. In particular, the observed improvement from S-S-LP-S to S-LP-LP-S is well described by the simulations. This indicates that the qualitative behavior of multi-GEM stacks in terms of ion backflow is well understood, in spite of an incomplete knowledge of ion transport parameters and the uncertainty expected from alignment.

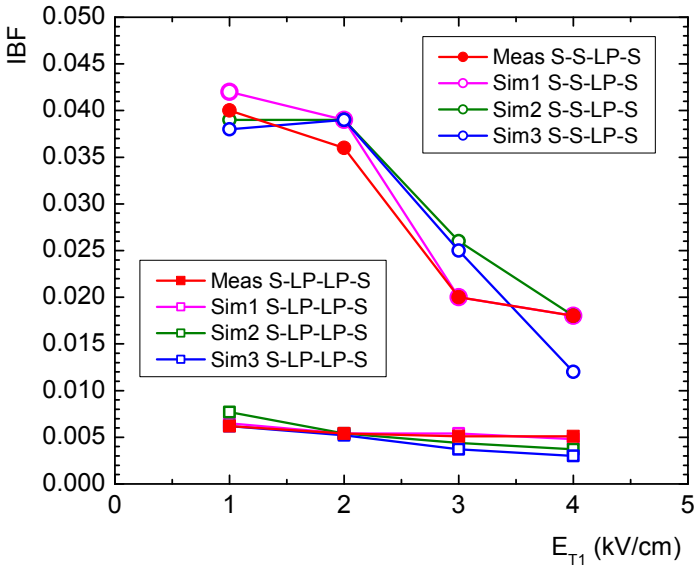

Figure 5.12: Comparison of ion backflow simulations (open symbols) with measurements (closed symbols) as a function of E_{T1} in Ne-CO_2-N_2 (90-10-5) for two quadruple GEM configurations. The circles represent an S-S-LP-S arrangement, where the voltages across the GEMs are 220, 270, $\sim$275 and $\sim$280 V, respectively. The squares represent an S-LP-LP-S arrangement, where the voltages across the GEMs are 230, 280, $\sim$290 and $\sim$320 V, respectively. For both arrangements the comparison has been done for $E_{T2} = 3.7$ kV/cm, $E_{T3} = 0.2$ kV/cm and $E_{Ind} = 4$ kV/cm. In the measurements the gain is adjusted to 2000, and the simulations follow the same settings. The different simulation setups labeled Sim 1 to Sim 3 were performed with three different sets of foil misalignment.

5.2 Full-size IROC prototype

A full-size prototype of a TPC Inner Readout Chamber (IROC) equipped with a triple GEM readout stage was built. The goal was to study aspects of GEM integration on a large-size chamber and to validate the dE/dx capabilities of a GEM-based TPC. Moreover, issues of operational stability are studied under LHC running conditions.

5.2.1 Detector design

The prototype is assembled on a spare MWPC IROC of the TPC [13]. It is a trapezoidal chamber with dimensions $497 \times (292-467)\,\mathrm{mm}^2$. The chamber, after removing the wires, was equipped with three GEM foils. The mechanical structure of the chamber is described in Sec. 4.2.

GEM foils

Four large area GEM foils were produced at CERN using the single-mask technique. The top side of the trapezoidal foil is segmented into 18 individually powered sectors with an area of $\sim$100 cm^2 each (see Fig. 5.13). The inter-sector gap is 400 μm, the same as the thickness of the spacer grid of the mounting frames (see next paragraph). An additional 100 μm of copper between the edges of the sector and its active area (GEM holes) is added to account for possible misalignment during the production of the foil. The diameter of the biconical holes is $\sim$50 μm (inner) and $\sim$80 μm (outer). The hole pitch is 140 μm.

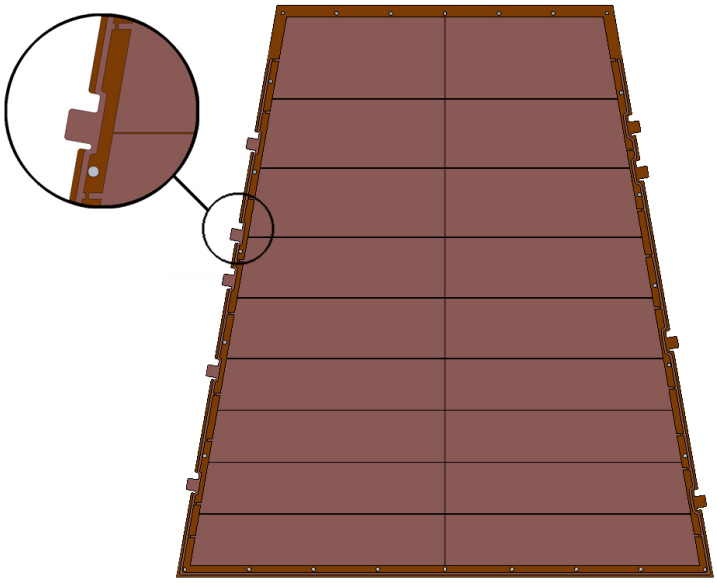

Figure 5.13: Layout of a prototype GEM foil; the top side is segmented into 18 sectors.

The HV distribution traces run along three sides of the foil. It consists of 2 mm copper paths and connection flaps (5 for the top side, 4 for the bottom). Sectors are powered in parallel via loading resistors soldered directly on the foil in the designed place between the distribution path and a sector (more on HV supply in Sec. 5.2.4). The bottom (not segmented) side of the foil is connected directly to the HV, therefore no distribution path is needed.

Support frames

The foils are glued on 2 mm fiberglass (G10) frames (see Fig. 5.14a) and then mounted in a stack. The frames contain a 400 μm thick spacer grid whose role is to prevent the foils to approach each other due to electrostatic forces. Each grid is aligned with the sector boundaries, so no additional dead area is introduced.

When the stack is mounted, the loading resistors fit into grooves milled in the bottom side of the frame placed above. Framed foils, therefore, lie flat on top of each other with 2 mm distance between them.

The sides of the frames include grooves for the HV flaps and wires. They are aligned with feed-throughs machined in the alubody of the chamber (see Fig. 5.14b). The HV wire runs through this groove to the flap where it is soldered, as shown in Fig. 5.14c so that all material is contained within the dimensions of the alubody; this is necessary for mounting the readout chambers on the TPC endplates [13].

The frames, after production in the CERN workshop, were polished, cleaned in an ultrasonic bath and dried in an oven, in order to remove remaining pieces of fiber and dust of e.g. G10 material, which may spoil the electrostatic integrity of the foils.

5.2.2 Quality assurance (QA)

All four foils are tested before and after framing to validate them for the final assembly. These tests include optical and high voltage tests, as foreseen for the large-scale production of the TPC chambers (see Sec. 4.7 for more details). In the following subsection, we will focus on the main results of the QA tests and its implications for the operation of the prototype.

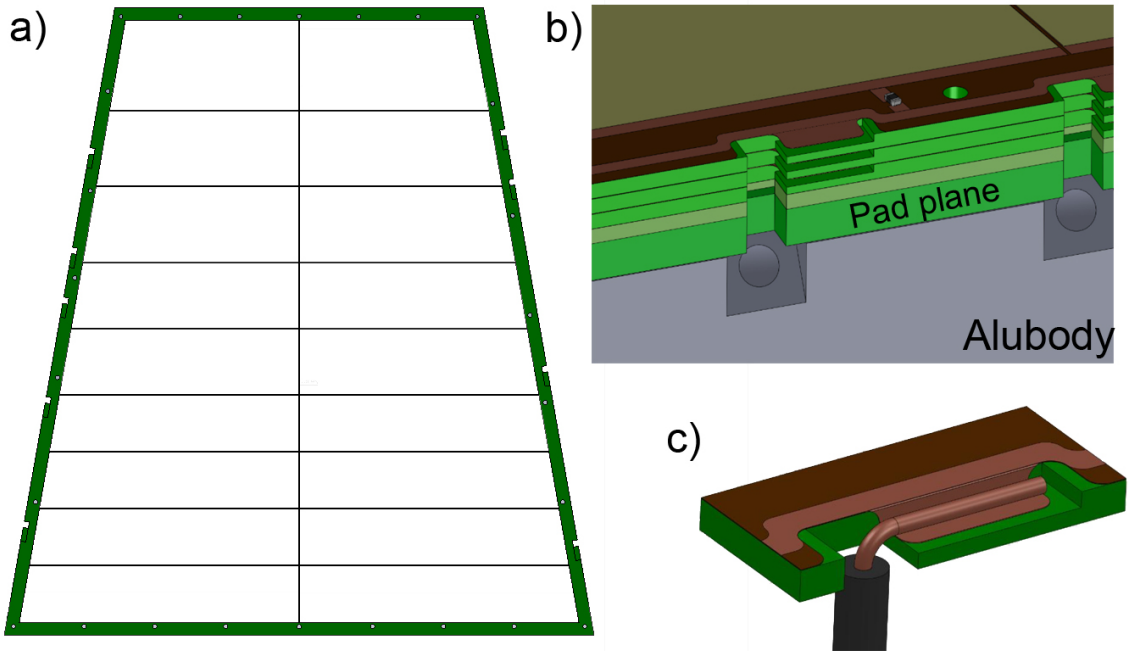

Figure 5.14: (a) Layout of the support frame. (b) Detail of the provisions for connecting each sector to its HV wire. (c) HV wire connected to the flap.

Optical check

The main tasks of this QA step are to check the hole size uniformity across the GEM active area and to record the mechanical features of the foils. Large-size defects on the copper or Kapton layers may increase the probability of electrical breakdown. Big mechanical defects, like cuts, may result in short circuits between the top and bottom side of a foil.

The measured diameter of the inner (Kapton) holes varies between 40 and 50 μm. The outer (copper) holes have a diameter of 70 – 80 μm. The variations of the hole sizes may come from the etching process and are within reasonable limits. The pitch of $\sim$140 μm is constant over the foils, since it is defined by the printed mask.

HV tests

A HV test is performed at each step of the detector assembly. The testing procedure is similar to the one which will be applied for QA of the final foils (see Sec. 4.7), therefore only a few particular aspects of the procedure and the results are described in this subsection.

During the HV test each sector of the foil is ramped up twice to 550 V while the surrounding sectors are kept at ground potential. During the first ramp, the leakage current (I_{leak}) and the discharge rate are measured at five voltage steps during the ramp. Sectors are connected via protection resistors with value 100 MΩ. Typical leakage currents vary between 0 and 0.3 nA. Sectors drawing currents higher than 5 nA do not pass the test. Also, if the number of discharges at each ramping step exceeds 2 in about a minute, the procedure is stopped and the sector fails the test. For the second test, the sectors are ramped up to 550 V directly. To pass the test, a sector should stand at this potential without sparking for a few minutes.

All foils (72 sectors) are tested before and after framing the foils.

Before assembling the detector, all sectors in all four foils were stable and had low and acceptable leakage currents.

5.2.3 Detector assembly

Gluing the foils

All foils were glued onto the fiberglass (G10) frames. Before gluing, the foils are stretched on a pneumatic stretching tool with a tension of 10 N/cm. Once the foil is stretched, it is positioned on its frame and aligned with metal pins. A heavy aluminum plate (milled in a way to prevent it from touching the active area of the foil) is used to press the foil onto the frame. The epoxy used is ARALDITE 2011 [14]. The full assembly is kept for 24 hours under a hood heated to 60 °C. Subsequent steps of the gluing procedure are shown on Fig. 5.15.

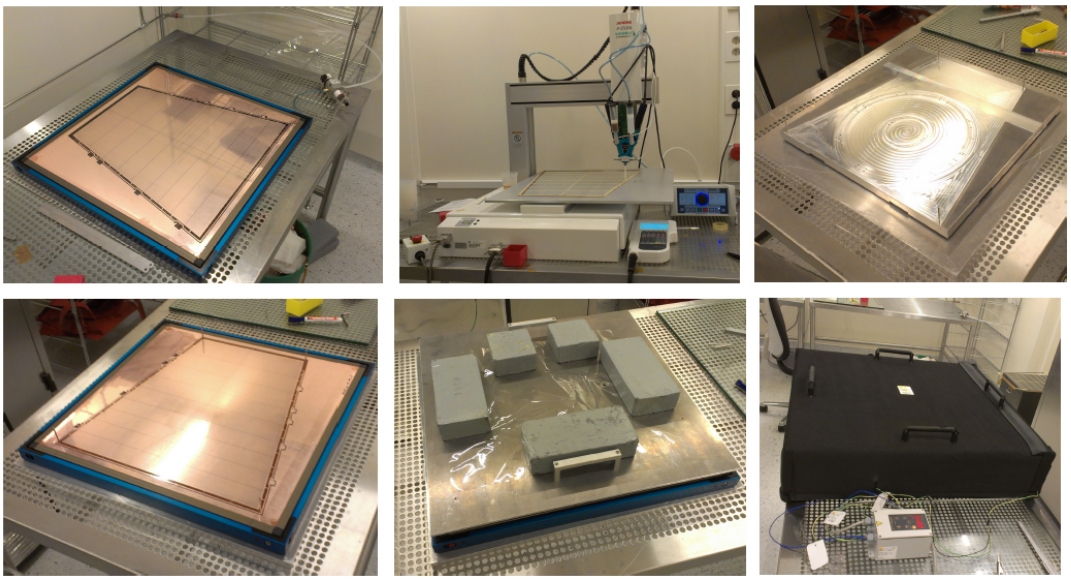

Figure 5.15: Foil gluing procedure. The different mounting steps are described in the text.

GEM stack

After gluing, the remaining material surrounding the frames is cut off, and the framed foil (see Fig. 5.16a) is ready for a new HV test. After the test, the loading resistors (1 and 10 MΩ SMD) are soldered as shown in Fig. 5.16b. Next, the three foils are mounted in a stack on the alubody of the chamber, with the unsectorized side facing the pad plane. Exceptionally, for this prototype an additional frame was mounted between the last (bottom) GEM foil and a pad plane in order to increase the induction gap from 2 to 4 mm.

Six HV wires are soldered to the HV flaps on each foil. High voltage is applied to the wires via SHV connectors on the other side of the alubody. The wires run through feed-throughs drilled in the aluminum frame of the chamber, which are then sealed with epoxy. The GEM stack is finally screwed to the alubody with nylon screws.

Test box with field cage

The chamber is mounted in a test box (see Fig. 5.16d), which contains a drift cathode and a rectangular field cage with dimensions of $57 \times 61\,\mathrm{cm}^2$. The drift electrode is made of 50 μm aluminized Kapton foil. The field cage has 8 field-defining strips (see Fig. 5.17) with a pitch of 15 mm. The strips are interconnected with 1 MΩ resistors.

The maximum drift distance to GEM 1 is 10.6 cm. The last strip of the field cage is located 1 mm below the position of that foil (see Fig. 5.17). Therefore, the potential of the last strip, which is grounded via a

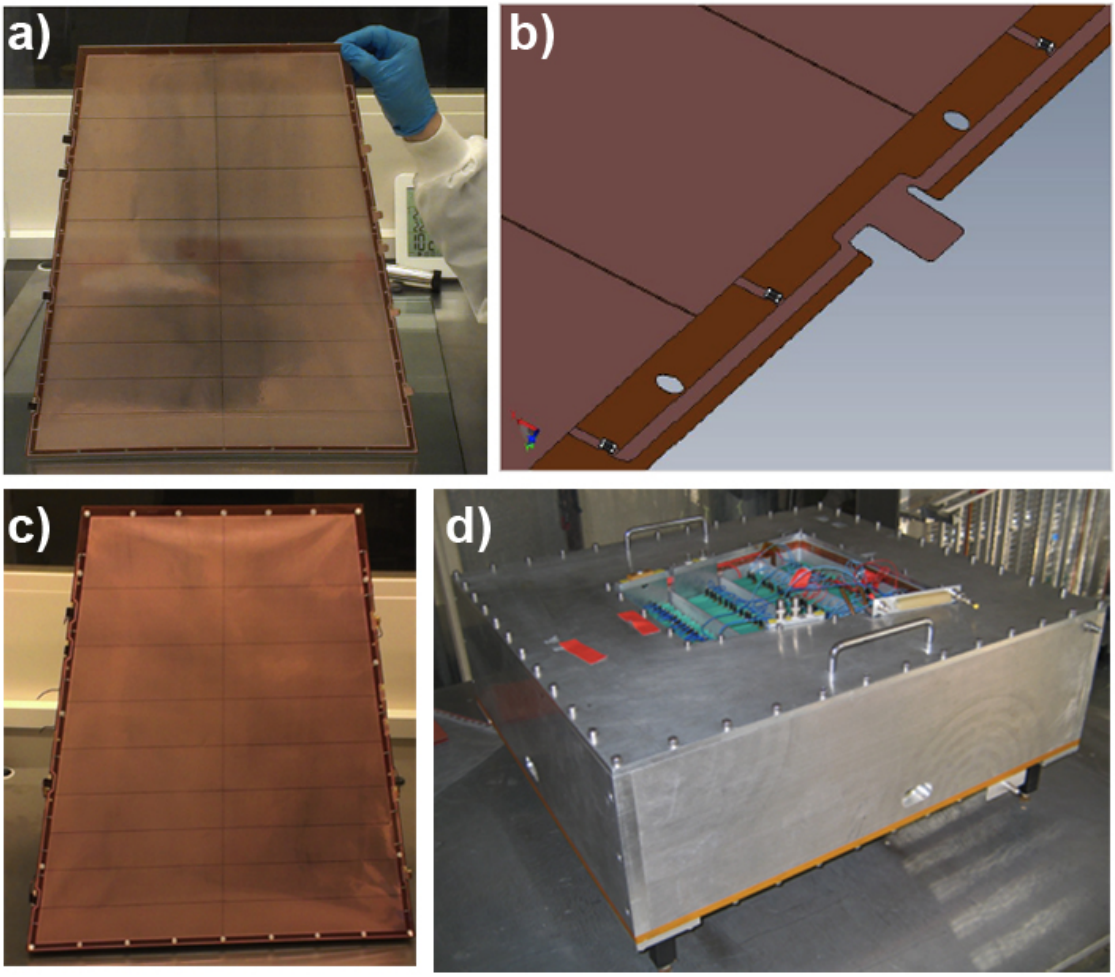

Figure 5.16: (a) Framed GEM foil (b) HV connection to a GEM sector through the loading resistors. (c) GEM stack mounted on the alubody. (d) chamber mounted in the test box.

3.33 MΩ resistor, is adjusted by applying a voltage in order to match the drift field at the top electrode of GEM 1.

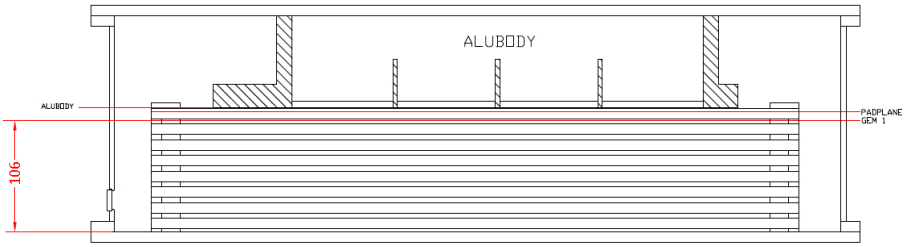

Figure 5.17: Cross section of test box with field cage and mounted IROC. The position of the first foil in the GEM stack is marked by a red line and labeled.

Two walls of the test box, closest to the parallel sides of the chamber, were machined to install mylar windows for measurements with beam and radioactive source.

5.2.4 HV supply

The detector is powered using an ISEG EHS 8060n 8-channel 6 kV high voltage module for the three GEM foils and the last strip voltage of the field cage, and by an ISEG HPn300 30 kV module for the drift electrode. The system features high precision current measurements (resolution 1 nA) on each HV

channel, adjustable ramp speeds and full remote control, which allows a global shutdown in case any channel trips. The powering scheme of the GEM-stack is displayed in Fig. 5.18.

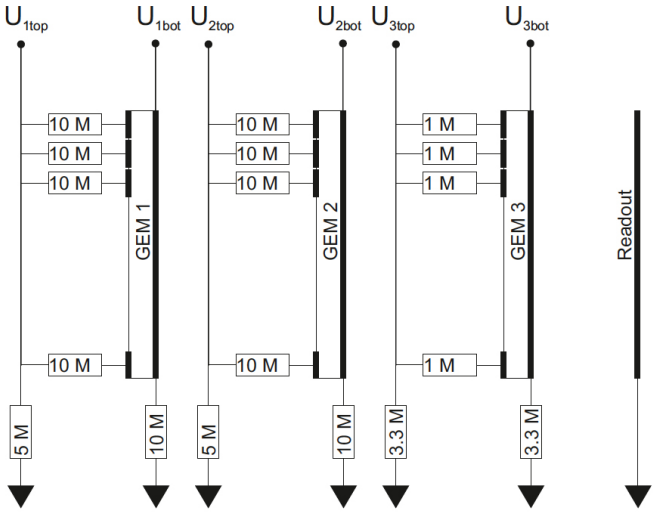

Figure 5.18: Schematics of the HV distribution of the prototype, showing the loading and grounding resistors.

Loading resistors (R_{L}) are installed for each sector on the top side of each foil. In addition, each channel is grounded through grounding resistors (R_{G}). Placing loading resistors on the top side of the foil assures that in case of a discharge across a foil, the voltage drop occurs only on the top side, whereas the bottom side stays at its nominal potential. This helps prevent the propagation of the discharge to the next foil or to the pad plane and readout electronics. Moreover, in case of occasional sparks, the loading resistors limit the current supplied by the power supply before it trips. Loading resistors also decrease the current flowing through the sector in case of a short circuit between top and bottom sides of the foil.

The values of R_{L} were chosen keeping in mind the current densities expected in the future Pb–Pb collisions at 50 kHz at a gain of 2000, which is roughly $5\,\mathrm{nA/cm^2}$ (500 nA per GEM sector). Such a current may result in a significant potential drop across a large loading resistor, thus reducing the gain. Therefore $10\,\mathrm{M\Omega}$ resistors were chosen for GEM 1 and GEM 2, whereas $R_{\mathrm{L}} = 1\,\mathrm{M\Omega}$ for GEM 3 .

Large resistors to ground for each channel are chosen to assure safe discharge of the GEM foils after a HV trip. Such connection will result in a constant DC current to ground which must not exceed the current limit of each channel. On the other hand, in case of a short across a foil in one or several sectors, the rest of the sectors should remain fully operational. Therefore, the value of R_{G} on the top side should be high enough to allow sufficient current supply through the shortened sectors, whereas the resistor to ground for the bottom side should be as low as possible in order to avoid reverse currents into the HV supply. The HV powering scheme with the chosen loading and grounding resistors is shown in Fig. 5.18.

Each sector can be treated as an individual capacitor in parallel with the other sectors on the foil. A time constant *RC* for (dis-)charging the foil is given by the full capacitance to the foil and the sum of loading and grounding resistances. In case the time constant is higher for the top side of the foil than for the bottom one, the potential of the top electrode may decrease to zero slower than the bottom one. This would result in a sudden increase of the potential difference between the electrodes which may lead to breakdown or even damage of the foil.

The example described above is simplified and does not take into account other parasitic elements or the influence of different elements in the HV circuit on each other. Nevertheless, it shows the importance of a proper choice of all electronic elements in the HV circuit used for powering the GEM stack. The final choice of the grounding resistors was done after performing a set of transient SPICE simulations and measurements of the discharge decay times. For the measurements a model of a GEM foil was made

with equivalent capacitors and resistors corresponding to the GEM assembly. The voltage difference across both sides of the equivalent GEM was recorded on an oscilloscope. The values of the grounding resistors were 5 MΩ, 5 MΩ and 3.33 MΩ for the top side of GEM 1, GEM 2, GEM 3, and 10 MΩ, 10 MΩ and 3.33 MΩ for the bottom sides, respectively. This configuration allows to run the detector with several shortened sectors in GEM 1 or GEM 2 and up to 2 shortened sectors in GEM 3, using the HV settings described in the next paragraph.

HV settings for the prototype

We work with two groups of HV settings: the so-called "standard" settings, typically used for triple GEM structures, and the so-called "ion backflow (IBF) settings", where the field configurations are aimed at minimizing the ion backflow. Each setting can be scaled in order to vary the total gain. Both are defined in Tab. 5.2.

	Standard	IBF
Drift Field	0.4 kV/cm	0.4 kV/cm
ΔU_{GEM1}	276 V	225 V
Transfer Field 1	2.57 kV/cm	3.8 kV/cm
ΔU_{GEM2}	252 V	235 V
Transfer Field 2	2.57 kV/cm	0.60 kV/cm
ΔU_{GEM3}	221 V	285 V
Induction Field	2.57 kV/cm	3.8 kV/cm

Table 5.2: Standard and ion backflow high voltage settings for a gain of ∼2000 in Ne-CO_2 (90-10).

The standard settings are inherited from the COMPASS experiment [15] where GEM detectors are operated in Ar-CO_2 (70-30). In Ne-CO_2 (90-10) however, since the amplification in this mixture starts at lower electric fields, a scaling factor (SF) between 69 – 73 %, resulting in gains between 2000 and 6000, is applied. The standard settings are optimized for maximum stability according to the principles of stable operation described in [16]. The highest amplification takes place in the first GEM and decreases in subsequent stages. These settings however are not optimized for minimum ion backflow. In the case of the ion backflow configuration, where the voltages were optimised in the lab, only the GEM voltages ($\Delta U_{\mathrm{GEM}i}$) were scaled with factors of 100, 103, 105 and 107 %. In addition four different values of E_{T2} were used: 200, 400, 600 and 800 V/cm. Combining different values of SF and E_{T2} together 16 ion backflow settings were tested. The value of the ion backflow for these settings, in Ne-CO_2 (90-10), varies between 3 % and 6.5 %. The approximate gains for all 16 combinations of ion backflow settings vary between 1000 and 6000. The highest amplification in this configuration occurs in GEM 3.

The nominal drift field of the ALICE TPC, $E_{\mathrm{drift}} = 400\,\mathrm{V/cm}$, is also applied to the prototype. The potential on the last strip of the field cage is equal to the potential on GEM 1 top.

5.2.5 Prototype commissioning

The prototype in the test box was tested in the lab with Ar-CO_2 (90-10) and Ne-CO_2 (90-10) gas mixtures, with standard HV settings, and irradiated with a ^{55}Fe X-ray source.

For the commissioning of the detector, ∼250 pads (∼75 cm^2) were connected to a charge sensitive preamplifier and the signal was digitized with a multi-channel analyzer for measuring the X-ray spectrum. A picoammeter is used to measure the gain by counting the rate of absorbed X-rays in the gas and measuring the current in the pad plane. Figure 5.19 shows the measured effective gain of the chamber for both gas mixtures.

Figure 5.20a shows the energy spectrum of ^{55}Fe obtained in Ar-CO_2 (90-10) at 86 % of the standard settings, which corresponds to a gain of around 6000 (see next paragraph for more details). Figure 5.20b shows the spectrum obtained in Ne-CO_2 (90-10) at 75 % of the standard settings, which corresponds to a

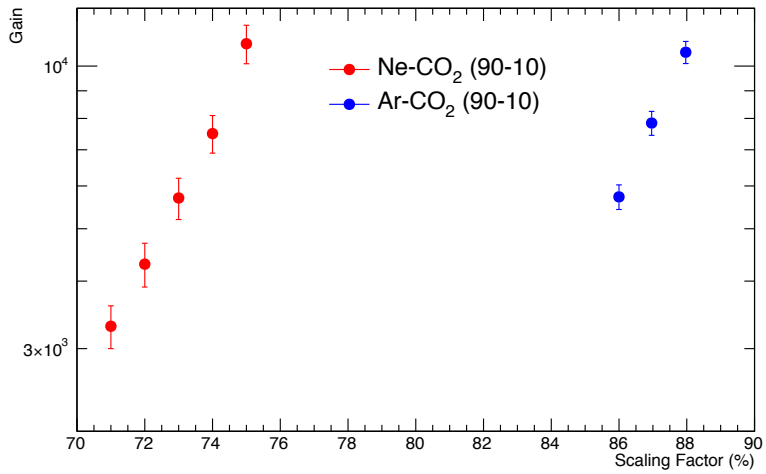

Figure 5.19: Effective gain of the chamber as a function of HV, expressed in terms of the scaling factor of the standard settings.

gain of around 11000. The energy resolution of the main peak for both measurements is between 10 and 11 % (sigma).

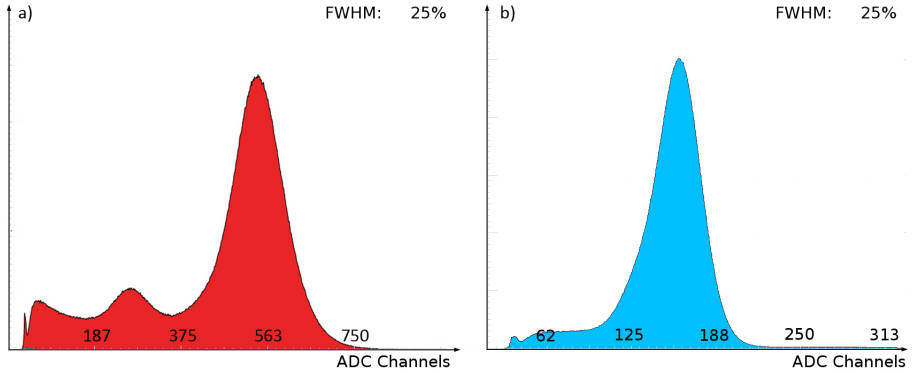

Figure 5.20: ^{55}Fe spectra obtained in Ar-CO$_2$ (90-10) (left panel) and Ne-CO$_2$ (90-10) (right panel).

5.2.6 Test campaign at the CERN PS

Experimental setup

The d$E/$dx resolution of the GEM IROC prototype was evaluated in a test beam at the CERN PS with beams of either e^+ and π^+ or e^- and π^- with momenta ranging from 1 to 6 GeV/c.

For each type of beam both standard and ion backflow high voltage settings are used (see Sec. 5.2.4). The drift field is 400 V/cm and the gas mixture Ne-CO$_2$ (90-10) as in the current TPC. Two scintillators are used for beam definition, and a Cherenkov counter and a Pb-Glass calorimeter are used for online particle identification.

The prototype is equipped with 10 front-end cards, covering about 1200 pads (see Fig. 5.21a). The readout electronics have been borrowed from the LCTPC (Linear Collider TPC) collaboration. The width of the readout region is 6 – 7 cm (see Fig. 5.21b).

The system has an RMS noise of about 600 electrons. The zero suppression threshold is 2 ADC counts, corresponding to about 2000 electrons (120 ns peaking time and 12 mV/fC conversion gain). The sampling frequency is 20 MHz.

The FECs are read out using the current TPC readout system [13]: Two Readout Control Units (RCU)

send the data to a Local Data Concentrator PC, which contains the receiving ReadOut Receiver Card (RORC) and runs the ALICE data acquisition system DATE. The corresponding trigger logic is handled by a Local Trigger Unit (LTU) and a Busy Box [13]. Data transfer and trigger communication are based on optical links. The beam detectors, scintillators, Cherenkov counter and Pb-Glass calorimeter, are read out through a classic CAMAC system into a PC running a LabView acquisition system. In order to synchronize the events from both systems, a busy logic is implemented in the CAMAC system which incorporates the busy status of both systems. Thus, the CAMAC leads the acquisition. The two data streams are subsequently merged into a single data file based on the proper synchronization of the trigger and an event tag. This allows the online visualization of the detector response to different particle species, as selected by the beam detectors.

The average DAQ rate was 500 events/spill (where the spill length was 0.5 s) for a beam intensity of about 2000 particles/spill.

dE/dx measurements

For the measurement of the $\mathrm{d}E/\mathrm{d}x$ resolution, only events with isolated tracks are selected. Additional cuts are applied on the number of clusters per track and the cluster drift time.

Figure 5.22 (left) shows the distribution of cluster maxima as a function of the pad row number. The first rows show low amplitudes due to a mapping error in the readout electronics. Moreover, a few pad rows with low gain are observed. These are related to the HV sector boundaries and the position of the spacer grid. After gain equilibration, the overall spread is reduced (right) but the lower gain in the first pad rows and at the positions of the spacer is still visible. The calibration of these pad rows requires a more sophisticated procedure. For the present analysis, 17 low-gain pad rows out of 63 are excluded. It should be pointed out that the distance between the GEM sectors, 400 μm in this prototype, (see Sec. 5.2.1) will be reduced by a factor of 2 in the final design (see Sec. 4.3.1). In addition, the number of spacer grid bridges in the support frames will also be reduced. No correction for pressure and temperature variations are applied because the runs are rather short.

The $\mathrm{d}E/\mathrm{d}x$ of each track is defined as the truncated mean of the 5 – 75 % highest of up to 46 cluster charges. An example $\mathrm{d}E/\mathrm{d}x$ spectrum of 1 GeV/c electrons and pions recorded at a gain of about 5000 is shown in Fig. 5.23. The $\mathrm{d}E/\mathrm{d}x$ distributions are fitted with a Gaussian function to obtain the mean value $\langle \mathrm{d}E/\mathrm{d}x \rangle$ and the width of the distribution $\sigma(\mathrm{d}E/\mathrm{d}x)$. The relative resolution, defined as

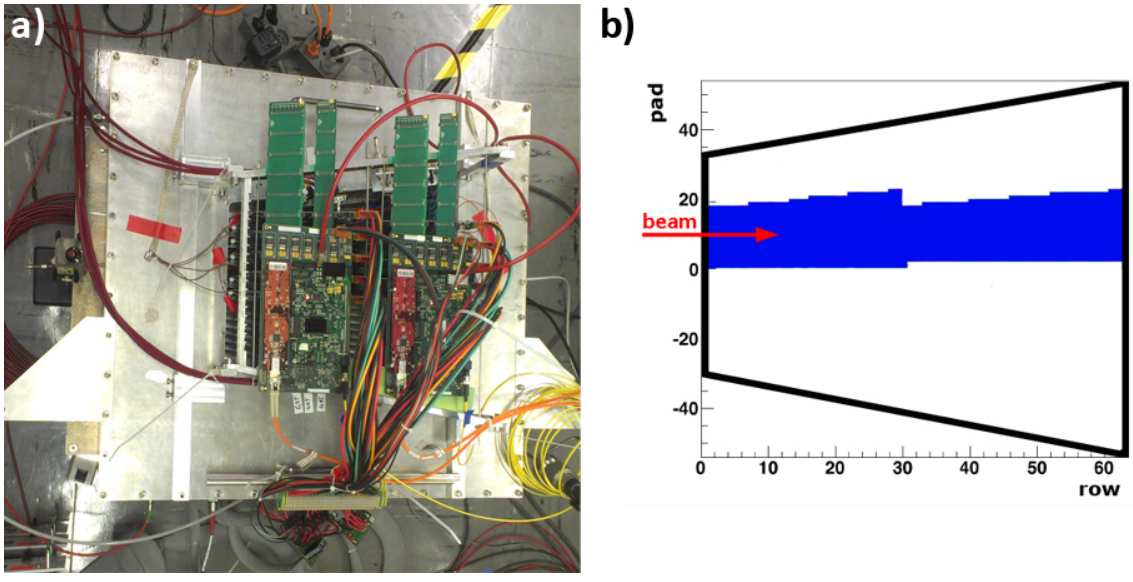

Figure 5.21: (a) Detector equipped with the front-end electronics. (b) Schematic view of the read out region of the chamber.

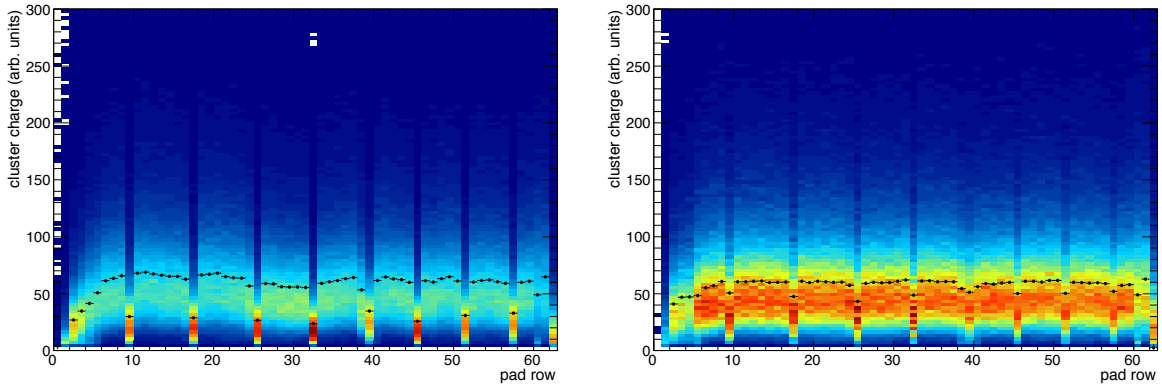

Figure 5.22: Gain profile before (left panel) and after (right panel) the gain equalization for the 63 pad rows. The structure of the spacer grid can be clearly seen in both panels.

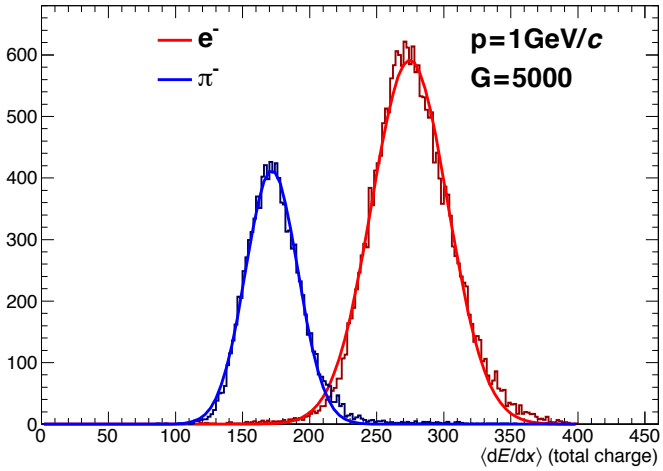

Figure 5.23: $\mathrm{d}E/\mathrm{d}x$ spectrum of 1 GeV/c electrons and pions at a gain of 5000.

$$\frac{\sigma\left(\mathrm{d}E/\mathrm{d}x\right)}{\langle \mathrm{d}E/\mathrm{d}x\rangle}, \tag{5.2}$$

is derived for pions and electrons, for different momenta and HV settings. Figure 5.24 shows the results obtained within this analysis. All ion backflow settings yield similar $\mathrm{d}E/\mathrm{d}x$ resolution at a given beam momentum and particle type. No significant dependence on the gas gain is observed within the range under study. The results for the standard settings are slightly better than those for the ion backflow settings.

The corresponding separation power, defined as

$$S_{\mathrm{AB}} = \frac{2\left|\langle \mathrm{d}E/\mathrm{d}x\rangle^{\mathrm{A}} - \langle \mathrm{d}E/\mathrm{d}x\rangle^{\mathrm{B}}\right|}{\sigma\left(\mathrm{d}E/\mathrm{d}x\right)^{\mathrm{A}} + \sigma\left(\mathrm{d}E/\mathrm{d}x\right)^{\mathrm{B}}} \tag{5.3}$$

for two particle types A and B, is shown in Fig. 5.25, for electrons and pions at all measured particle momenta and HV settings. At a given beam momentum, asymptotic separation powers are reached for gains above ∼1500.

This $\mathrm{d}E/\mathrm{d}x$ performance can be compared with results of a MC[2] simulation shown in Fig. 5.26. The

[2]Monte Carlo (MC)

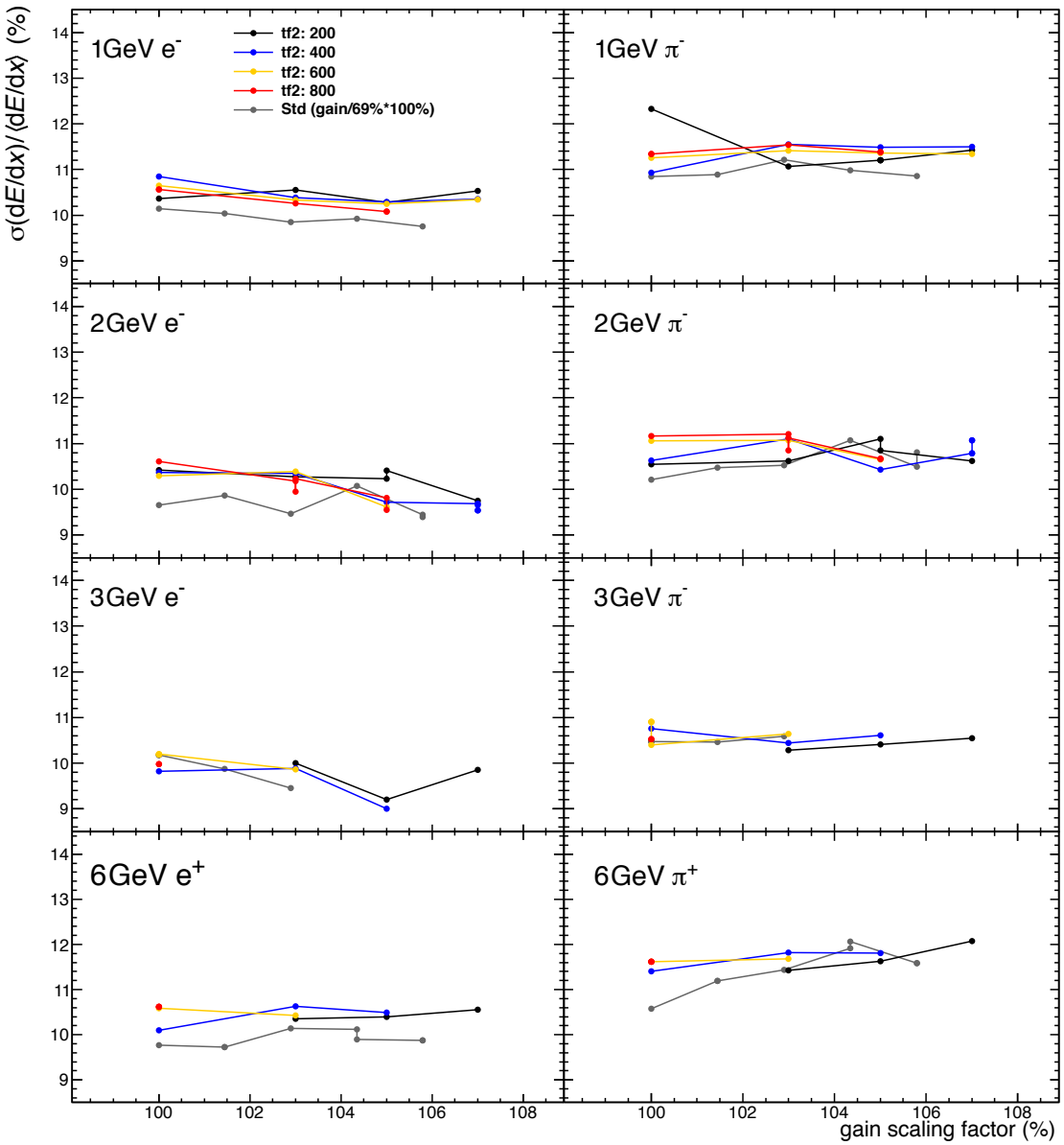

Figure 5.24: The relative $\mathrm{d}E/\mathrm{d}x$ resolution measured for different HV settings for electrons and pions with momenta ranging from 1 to 6 GeV/c. Only 46 pad rows are used for the analysis. In the standard settings (grey curve) the gain ranges from 2000 to 6000; in the ion backflow settings (coloured curves) the gain ranges from 1000 to 6000.

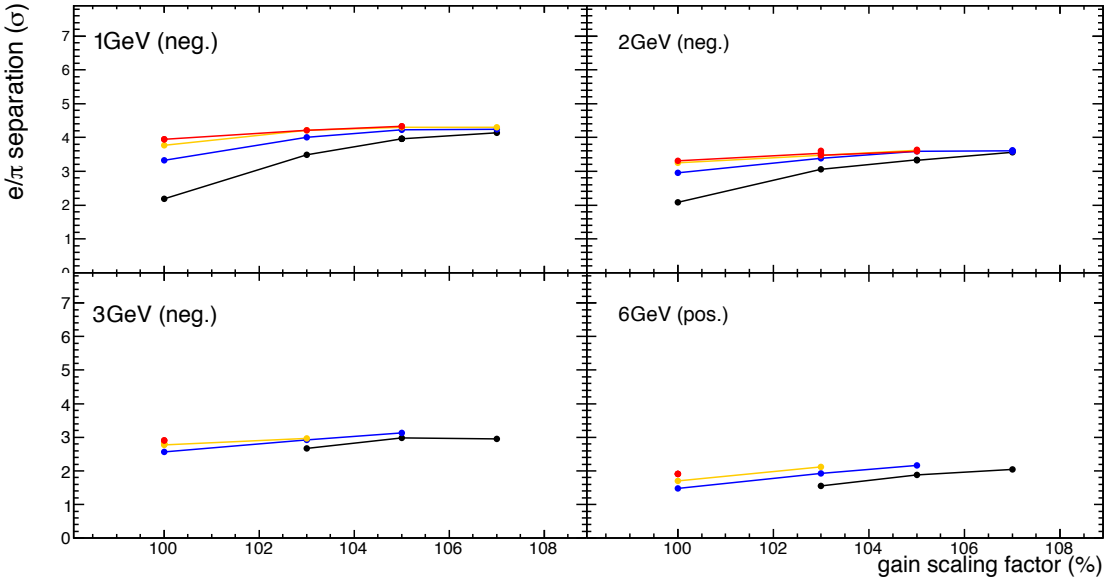

Figure 5.25: Separation power between pions end electrons with $1-6\,\mathrm{GeV}/c$ momentum measured for different HV settings. In the standard settings (grey curve) the gain ranges from 2000 to 6000; in the ion backflow settings (colourful curves) the gain spans between 1000 and 6000 (see Sec. 5.2.4 for more details).

simulated $\mathrm{d}E/\mathrm{d}x$ spectrum for $1\,\mathrm{GeV}/c$ pions obtained with 46 pad rows in a GEM stack yields a relative energy resolution of $\sim$10.5 %. This is slightly better than our test beam results. Nevertheless, the $\mathrm{d}E/\mathrm{d}x$ resolution observed in the GEM IROC is compatible with that of the MWPC IROCs. Therefore these measurements corroborate that the $\mathrm{d}E/\mathrm{d}x$ resolution of the upgraded TPC will be preserved.

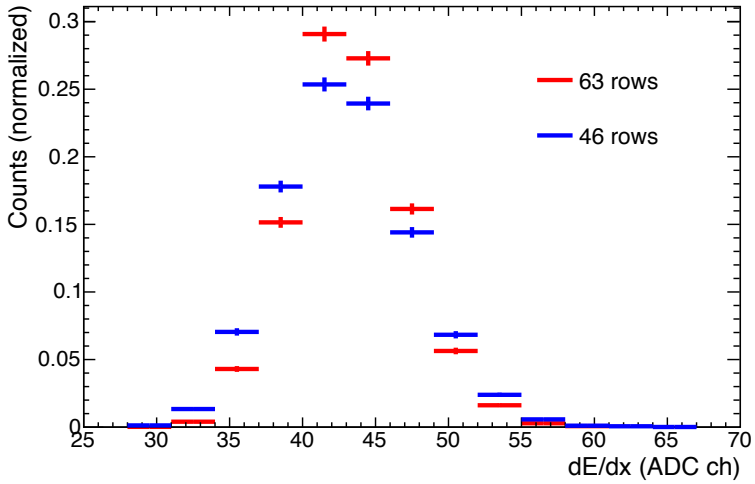

Figure 5.26: Simulated $\mathrm{d}E/\mathrm{d}x$ spectrum for $1\,\mathrm{GeV}/c$ pions using information from all 63 rows (red) and for 46 rows (blue) as in the data from test beam. The resulting relative resolution is 10.5 % (9.0 %) for 46 (63) rows.

Chapter 6

Front-end electronics and readout

This section reviews the requirements for the front-end electronics (FEE) and describes the general architecture and the basic building blocks of the readout chain.

6.1 System overview

The requirements for the front-end and readout electronics are derived from the detector performance requirements. The argumentation for many items is based on the successful implementation of the current TPC readout system (as described in [1, 2]). The three main changes for the front-end electronics with respect to the existing system are related to the new concept of continuously reading data from an ungated GEM TPC:

1. The GEM readout provides signals with opposite polarity as compared to those generated in an MWPC.
2. The continuous readout scheme necessitates the development of electronics that can concurrently sample the detector signals and transfer the aquired data off the detector.
3. The continuous readout in conjunction with the step-up in interaction rate (and thus detector occupancy) leads to a strongly increased data throughput.

The readout system for the GEM TPC is shown schematically in Fig. 6.1. The current signals are passed from the pads on the detector's readout plane to the front-end cards (FEC), located a few cm away, via flexible Kapton cables. In the FEC, a custom-made FE[1] ASIC[2], the SAMPA chip, processes the data from 32 individual front-end channels concurrently. The SAMPA is common among different ALICE subsystems (see Sec. 6.4). The first stage of the SAMPA is a charge-sensitive preamplifier and shaping amplifier, which transforms the currents induced in the pads into differential semi-Gaussian voltage signals. These signals are continuously digitized and processed by a DSP[3]. Concurrently, the acquired data are transferred to the GBTx ASIC [3], which multiplexes them and transmits them via the versatile optical link components [4] to a Common Readout Unit (CRU). Also the CRU is a common ALICE development. It serves as interface to the online farm, trigger and detector control system, and is situated off-detector in a control room close to the online farm. The common ALICE electronics projects, SAMPA and CRU, are described in more detail in a separate Technical Design Report [5].

[1] Front-End (FE)
[2] Application-Specific Integrated Circuit (ASIC)
[3] Digital Signal Processor (DSP)

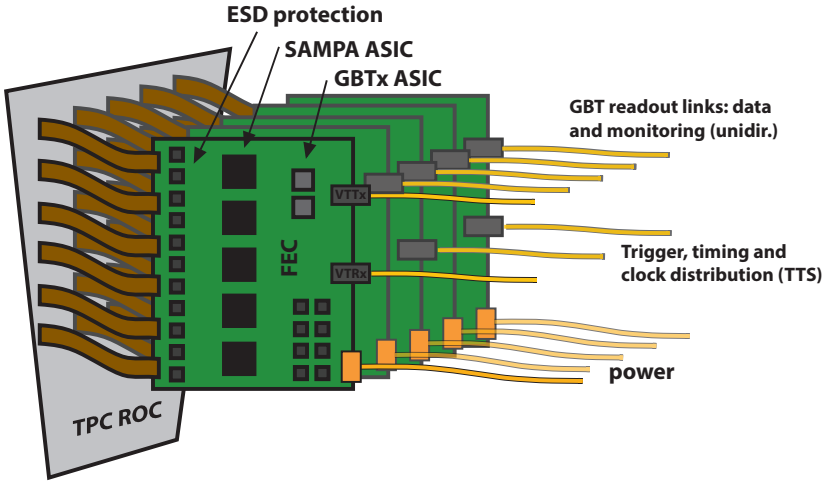

Figure 6.1: Schematic of the readout system of the GEM TPC. The two main building blocks of the FEE are shown: The front-end ASIC SAMPA on the front-end cards (FECs). The FECs connect to a Common Readout Unit (CRU), located off-detector in the control room, through radiation hard GBT links.

In addition to the continuous readout mode, also a triggered mode has to be supported for calibration purposes and for running at lower interaction and/or trigger rates. Here, the processing of the continuously sampled data stream starts upon arrival of a first-level trigger; only the data corresponding to the detector drift time ($t_\mathrm{d} \approx 100\,\mu$s) is frozen in the data memory and read out.

6.2 Pileup and occupancies

At Pb–Pb collisions with $\sqrt{s_\mathrm{NN}} = 2.76\,$TeV densities of primary tracks of $\langle \mathrm{d}N_\mathrm{ch}/\mathrm{d}\eta \rangle_\mathrm{cent} \approx 1600$ and $\langle \mathrm{d}N_\mathrm{ch}/\mathrm{d}\eta \rangle_\mathrm{mb} \approx 400$ were measured for the most central collisions (0-5 %) and for minimum bias collisions, respectively [6]. By scaling with $(s_\mathrm{NN})^{0.15}$ [7] to the full LHC energy of $\sqrt{s_\mathrm{NN}} = 5.5\,$TeV this translates to $\langle \mathrm{d}N_\mathrm{ch}/\mathrm{d}\eta \rangle_\mathrm{cent} \approx 2000$ and $\langle \mathrm{d}N_\mathrm{ch}/\mathrm{d}\eta \rangle_\mathrm{mb} \approx 500$ for central and minimum bias Pb–Pb collisions, respectively.

At 50 kHz interaction rate, the average number of interactions within a time window of $t_\mathrm{d} \approx 100\,\mu$s is $N_\mathrm{pileup} = 5$. The expected primary track densities can be expressed conveniently by introducing an equivalent charged-particle pseudo-rapidity density $\mathrm{d}N_\mathrm{ch}/\mathrm{d}\eta$, which has the mean value $\langle \mathrm{d}N_\mathrm{ch}/\mathrm{d}\eta \rangle_\mathrm{equiv} = 2500$ for $N_\mathrm{pileup} = 5$. For central events (embedded in 4 minimum bias events) the value is $\mathrm{d}N_\mathrm{ch}/\mathrm{d}\eta|_\mathrm{equiv} = 4000$. This is still well below the primary charged particle multiplicity for central Pb–Pb collisions originally anticipated when the current TPC was designed ($\mathrm{d}N_\mathrm{ch}/\mathrm{d}\eta \approx 8000$).

The relative fluctuation of the number of charged tracks inside the TPC drift volume $\sigma_{N\mathrm{ch}}/\langle \mathrm{d}N_\mathrm{ch}/\mathrm{d}\eta \rangle_\mathrm{equiv}$ can be written as

$$\frac{\sigma_{N\mathrm{ch}}}{\langle \mathrm{d}N_\mathrm{ch}/\mathrm{d}\eta \rangle_\mathrm{equiv}} = \frac{1}{\sqrt{N_\mathrm{pileup}}} \sqrt{1 + \left(\frac{\sigma_{N_\mathrm{MB}}}{\mu_{N_\mathrm{MB}}} \right)^2} \,. \tag{6.1}$$

With $N_\mathrm{pileup} = 5$ and the relative fluctuation of the number of minimum bias events $\sigma_{N_\mathrm{MB}}/\mu_{N_\mathrm{MB}} \approx 1.15$ this leads to $\sigma_{N\mathrm{ch}}/\langle \mathrm{d}N_\mathrm{ch}/\mathrm{d}\eta \rangle_\mathrm{equiv} \approx 0.68$. The relative fluctuations of the equivalent multiplicity as a function of N_pileup are depicted in Fig. 6.2. For $N_\mathrm{pileup} = 5$ the equivalent multiplicity will stay below $(1 + 3 \times 0.68)\langle \mathrm{d}N_\mathrm{ch}/\mathrm{d}\eta \rangle_\mathrm{equiv} \approx 7500$ for 99.7 % (corresponding to $3\,\sigma_{N\mathrm{ch}}$) of the time intervals ($\sim 100\,\mu$s).

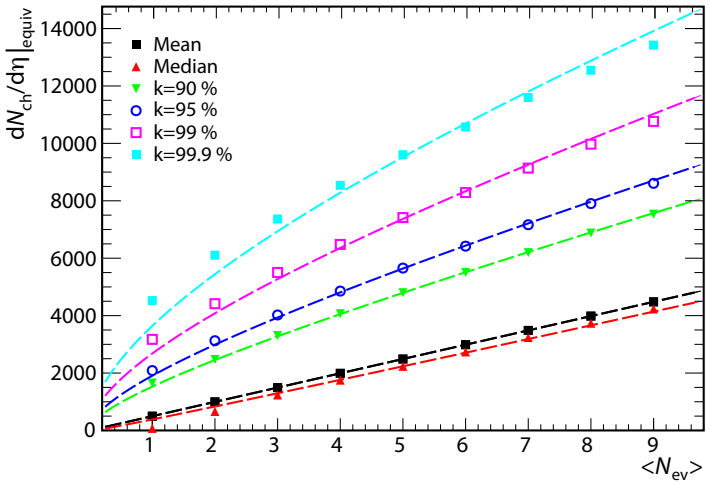

Figure 6.2: Equivalent multiplicity as function of mean number of events including kth order statistics (the kth-smallest value). E.g. at 50 kHz collision rate (for $N_{\text{pileup}} = 5$) there is a < 1 % probability that the equivalent multiplicity is larger than 7500.

6.3 Data rates and bandwidth considerations

The following estimates of data rates are based on measured sizes of isolated events (no pileup). We assume unchanged shaping, sampling and zero suppression parameters of the FE ASIC. In RUN 1 the size of minimum bias TPC events for $\sqrt{s_{\text{NN}}} = 2.76$ TeV Pb–Pb collisions is 13.6 MByte. Several factors have to be considered when extrapolating the data volume to RUN 3. An increase of the pad occupancies[5] by a factor 1.25 must be expected due to the larger charged particle multiplicities at $\sqrt{s_{\text{NN}}} = 5$ TeV. Moreover, an additional factor of 1.25 accounting for the deterioration of the compression ratio of the zero suppression and run-length encoding must be incorporated at these larger occupancies[6]. On the other hand, the cluster sizes are reduced by a factor 0.8 due to the new readout technology (see Fig. 4.17), and overlap of clusters reduces the data volume by a small factor. With these considerations in mind we conservatively assume an average event size of 20 MByte for an isolated event in the TPC.

An average data rate from the TPC of 50 kHz $\times$ 20 MB = 1 TByte/s is expected for RUN 3. The average pad occupancies will be around 15 %, increasing to up to 27 % for the innermost pad row, as can be seen in Fig. 6.3. For a central event at $R_{\text{int}} = 50$ kHz we find occupancies of up to 42 % for the innermost pad row, but even more extreme variations should be considered: for $\mathrm{d}N_{\text{ch}}/\mathrm{d}\eta|_{\text{equiv}} = 7500$ occupancies of up to 80 % may be occasionally reached.

Table 6.1 summarizes the number of front-end channels, the bandwidth requirements (based on the average expected occupancies) and the resulting distribution of FECs, SAMPAs, optical components (VTTx[7] and VTRx[8]) and readout and TTS[9] fibers. Here a segmentation of each TPC sector into 5 readout partitions is used: 2 for the IROC and 3 for the OROC (following the GEM segmentation, Sec. 4.5). The bandwidth requirement is calculated using a safety factor of ~ 2 on the expected average data rates to incorporate also local occupancy variations due to geometry. This factor depends on the occupancy distribution on the given readout partition and on the buffer size in the SAMPA ASIC and is presently being verified in detailed simulations of the full readout architecture.

[5] Pad occupancy is the fraction of samples within a given time window exceeding the zero suppression threshold.
[6] This is the worst case scenario. Overlap of the clusters will actually reduce the impact of this effect.
[7] Versatile Twin Transmitter (VTTx)
[8] Versatile Transceiver (VTRx)
[9] Trigger and Timing distribution System (TTS)

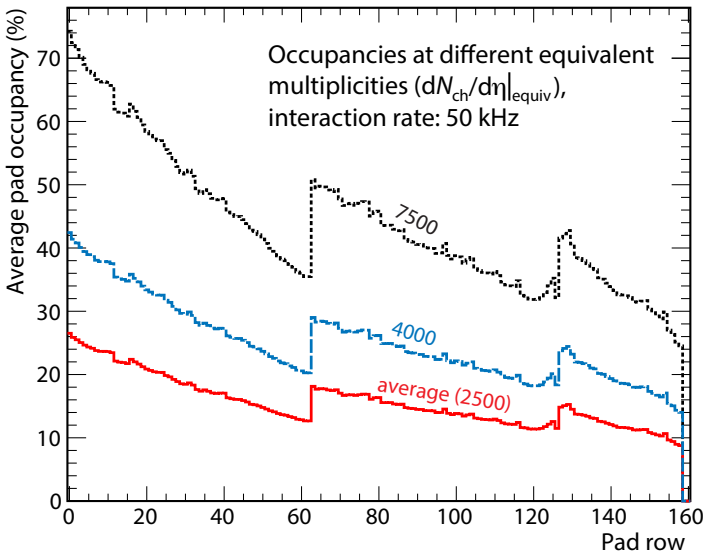

Figure 6.3: Expected average occupancies within a given time window for equivalent multiplicities of $dN_{ch}/d\eta|_{equiv} = 2500$, 4000 and 7500. The data is extrapolated using measured occupancies in isolated (no pileup) events recorded in 2010.

		IROC 1	IROC 2	OROC 1	OROC 2	OROC 3	TPC
Avg. data rate / chan.	(Mbit/s)	22	16	15	13	11	
Req. bandwidth / chan.	(Mbit/s)	40	30	30	25	20	
Front-end channels		2304	3200	2944	3712	3200	552,960
Total data rate	(Gbit/s)	50	50	45	50	35	8280
Total bandwidth	(Gbit/s)	100	100	90	100	70	
FECs (5 SAMPAs each)		15	20	19	24	20	3528
SAMPAs		75	100	95	120	100	17,640
GBTx ASICs		30	40	38	48	20	6336
Versatile link twin transmitter (VTTx)		15	20	19	24	0	2808
Versatile link transceiver (VTRx)		8	10	10	12	20	2160
GBT uni-directional data links (3.2 Gbit/s)		30	40	38	48	20	6336
GBT uni-directional TTS links		8	10	10	12	10	1800

Table 6.1: Data rates and bandwidth requirement and partitioning of SAMPAs, FECs, optical components, readout and TTS fibers with 5 readout partitions per TPC sector. The acronyms are explained in the text. The numbers in the last column show the sum over the 2×18 TPC sectors. The uni-directional versatile links [4] for the data to be sent to the CRU and online farm are driven by bi-directional optical transceivers (VTRx) or uni-directional twin transmitters (VTTx). Since the bandwidth needs in the up- and downstream directions are asymmetric, less VTRx are needed to receive trigger and timing information via the ALICE TTS[4] system. We aim at installing one TTS link on every second FEC.

6.4 Common front-end ASIC

The readout of the detector signals is done by a 32 channel FE ASIC that is developed as a common solution for different ALICE sub-detectors. The concept assumes the integration of low-noise analog components and continuously operating, digital functionality on the same silicon die.

The SAMPA project at the University of São Paulo in Brazil targets the design, simulation, validation and production of a signal acquisition and digital processing ASIC based on TSMC 0.13 μm mixed signal technology [5]. This ASIC will comply with the requirements defined by the upgrade of the TPC, as well as the ALICE Muon tracking detector.

6.4.1 Overview

A schematic of the SAMPA is shown in Fig. 6.4. The data fed into each of the 32 channels is processed by a PreAmplifier/ShAper circuit (we reuse the name PASA from the current system for this block), a SAR[10] ADC[11] and a DSP. Before being read out, the data are temporarily buffered in an event memory and multiplexed. The PASA and DSP have configurable parameters that can be accessed via a common logic and interface unit.

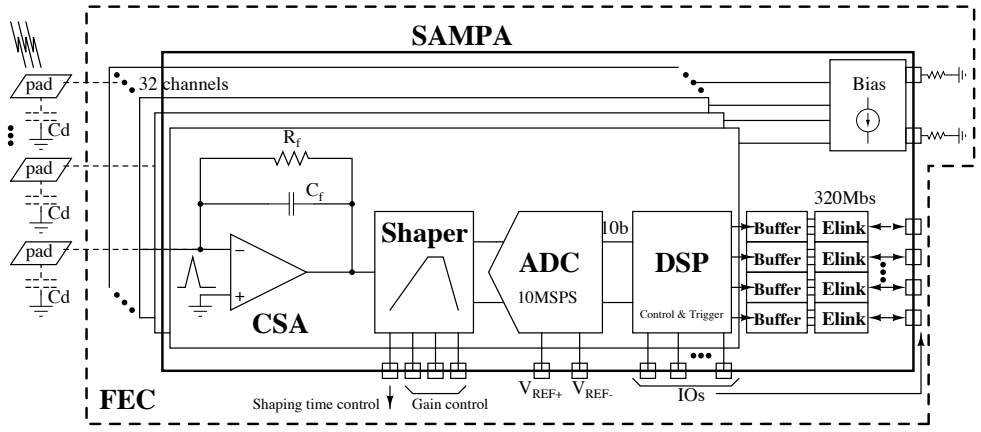

Figure 6.4: Schematic of the SAMPA ASIC for the GEM TPC readout, showing the main building blocks.

6.4.2 General requirements for the analog part

The requirements for the SAMPA are summarized in Tab. 6.2 and discussed in the following:

- The requirement on the signal-to-noise ratio (*S*:*N*) is taken over from the current system [1, 2]. In order to reach the required detector resolution, a *S*:*N* ratio of 20:1 and 30:1 for MIPs[12] is required for the IROCs and OROCs, respectively[13]. At the same gas gain it is larger in the OROCs due to the longer pads, which collect more ionization due to the longer track length seen.
- If the noise level of the current system (670 electrons) is retained, the required *S*:*N* can be achieved by applying an effective gain of 2000 in the GEM stack. The maximum pad and time bin for each charge cluster of a MIP track in this case corresponds to a charge of typically 2.1 to 3.2 fC (1.3 to 2×10^4 electrons).

[10] Successive Approximation Register (SAR)
[11] Analog-to-Digital Converter (ADC)
[12] Minimum-Ionizing Particle (MIP)
[13] The *S*:*N* ratio is calculated using the maximum pad and time bin for each charge cluster.

		RUN 1 (measured)	RUN 3 (requirement)
Signal polarity		Pos	Neg
Detector capacitance (range)	(pF)	12 – 33.5	12 – 33.5
S:*N* ratio for MIPs (IROC)		14:1	20:1
(OROC 6×10 mm^2 pads)		20:1	30:1
(OROC 6×15 mm^2 pads)		28:1	30:1
MIP signal	(fC)	1.5 – 3[14]	2.1 – 3.2
System noise (at 18.5 pF, incl. ADC)		670 e	670 e
PASA conversion gain (at 18 pF)	(mV/fC)	12.74	20 (30)
PASA return to baseline	(ns)	< 550	< 500
PASA average baseline value	(mV)	100	100
PASA channel-to-channel baseline variation (σ)	(mV)	18	18
PASA shaping order		4	4
PASA peaking time	(ns)	160	160 (80)
PASA crosstalk		< 0.1 %[15]	< 0.2 %
PASA integrated non-linearity		0.2 %	< 1 %
ENC (PASA only, at 12 pF)		385 e	385 e
ADC voltage range (differential)	(V)	2	2
ADC linear range (differential)	(fC)	160	100 (67)
ADC number of bits		10	10
ADC sampling rate	(MHz)	10 (2.5, 5, 20)	10 (20)
Power consumption (analog & digital)	(mW/ch)	35	< 35

Table 6.2: Measured PASA and ALTRO parameters for the current system (RUN 1) and the requirements for the upgraded front-end electronics (SAMPA parameters for RUN 3). The parameters are explained in the text.

– A dynamic range of the electronics of 100 fC allows the measurement of the ionization signals of low momentum particles, which may produce signals 30 times larger than those of a MIP. With respect to the current system the linear range is reduced for the benefit of a better resolution around the threshold level.

– To minimize the quantization error[16], the conversion to digital values should take place with a precision of at least 10 bits.

– The conversion gain (20 mV/fC) is chosen such that the maximum expected output signal matches the amplifier voltage swing and the input dynamic range of the ADC (2 V peak-to-peak). In order to approximately match the signal amplitudes in IROCs and OROCs, a second conversion gain setting of 30 mV/fC can be used in the IROCs. In this case the linear range is decreased from 100 fC to 67 fC.

– The large number of front-end electronics channels and a requirement for an overall power consumption < 20 kW gives a limit of 35 mW per channel. The heat is removed from the readout modules with the existing water cooling system (see Sec. 11.4.3).

– Special care has to be taken to protect the system against potential corruption of data and control registers caused by radiation (Single Event Effects).

– The electronics will be located in an area with limited access. High reliability is thus a requirement.

[14] For the higher gain anticipated in the original TDR the value was 4.8 fC for the OROCs.

[15] The requirement was < 0.3 %.

[16] The RMS value of the quantization error is $1/\sqrt{12} \approx 0.29$ LSB. It becomes smaller with larger bit depth.

6.4.3 Signal shaping

The shaping parameters determine the size and shape of the individual charge clusters. The signal from an ionizing particle on an individual readout pad spreads in time due to the longitudinal diffusion D_{L} and due to the track inclination angle λ. The mean width of the charge clusters in z direction in units of time is given by:

$$\sigma^2_{\mathrm{time}} = \frac{1}{v_{\mathrm{d}}^2}\left(D_{\mathrm{L}}^2\, z_{\mathrm{d}} + \frac{\tan^2\lambda\; L^2_{\mathrm{pad}}}{12}\right) + \sigma^2_{\mathrm{PASA}}\,, \tag{6.2}$$

where z_{d} is the drift length for the given cluster and σ_{PASA} is the approximate sigma of the semi-gaussian signal output of the PASA. It is related to the shaping time t_{FWHM} like $\sigma_{\mathrm{PASA}} \approx t_{\mathrm{FWHM}}/2.4$. For Ne-$CO_2$-$N_2$ (90-10-5), the first term of Eq. (6.2) varies between 135 ns for tracks at mid-rapidity ($\eta = 0$, long drift length) and 175 ns for tracks at $\eta \approx 0.9$ (see Fig. 6.5). A value of $\sigma_{\mathrm{PASA}} = 80$ ns (160 ns peaking time, 190 ns FWHM), slightly shorter than the signal width, had been chosen for the current TPC readout [1] in order to ensure that the cluster shape in time direction is not dominated by the PASA response. For the upgraded system these considerations remain the same. Therefore, the same shaping parameters as found in the current readout system can again be chosen.

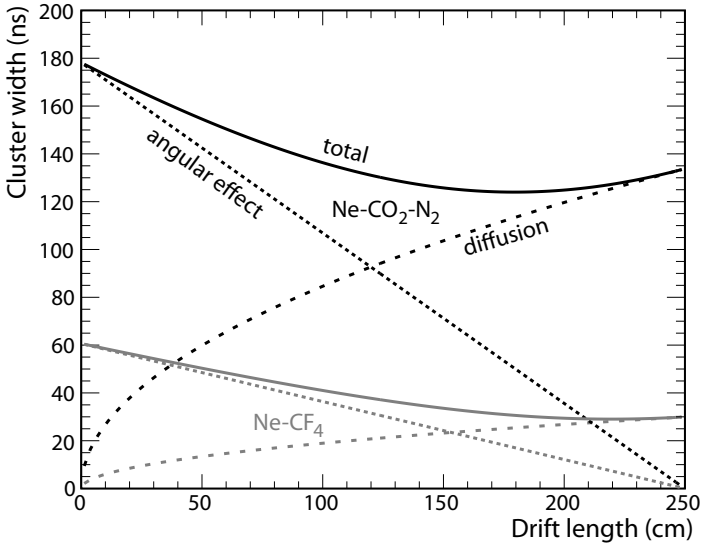

Figure 6.5: Length of clusters in time units for the baseline gas mixture Ne-CO_2-N_2 (90-10-5) and for Ne-CF_4 (90-10), calculated using Eq. (6.2) at a radius in the center of the OROC medium pad region and without the contribution of σ_{PASA}.

6.4.4 Noise

The Equivalent Noise Charge (ENC) requirement of 670 e (mean system noise) is discussed in this section. Such a noise performance is possible to achieve, as the noise distributions measured with the current system and test data taken with the S-ALTRO demonstrator ASIC show (discussed in detail in the following).

Noise on the current system

For the current TPC the ENC specification was < 1000 e at a total capacitance of 25 pF. The measured noise distributions for all readout chambers and separately for the three different pad sizes (small pads on IROC and medium and long pads on OROC) are shown in Fig. 6.6 (left panel). On the installed system

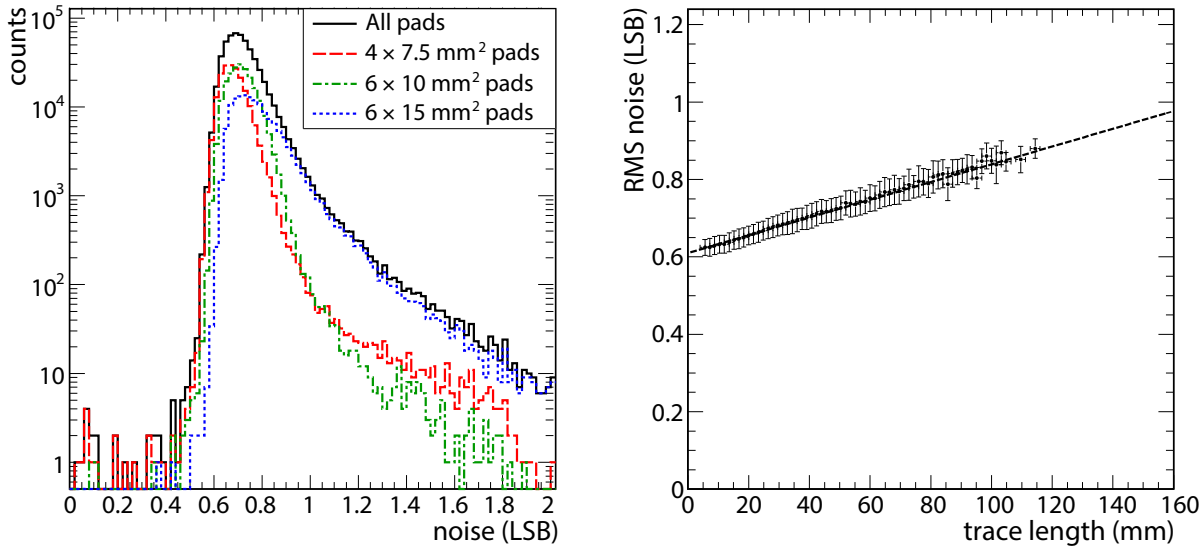

Figure 6.6: (Left) Noise distribution for all FEE channels on all readout chambers and separately for the different pad sizes for the current TPC [8]. (Right) Correlation of noise and the trace length on the padplane PCB for the medium-sized pads ($6 \times 10\,\mathrm{mm}^2$). A straight-line fit describes the data well (compare to Tab. 6.3).

a noise of 0.71 LSB[17] was achieved. At an average PASA gain of 12.74 mV/fC (at 18.5 pF average detector capacitance), with 2 V linear range and with a 10 bit ADC this corresponds to an ENC value of 670 e. Only a small fraction of channels exceeds the specified requirement of a noise lower than 1000 e (corresponding to ~ 1 LSB): 0.3 % for the IROC region, 0.2 % for the OROC medium pad region and 4.9 % for the OROC large pad region [8].

Noise dependence on capacitance

The right panel in Fig. 6.6 shows how the noise correlates with the additional capacitances given by the varying trace lengths on the padplane PCB[18]. A straight-line fit describes the data well and suggests a capacitance of about 1.3 pF per cm of trace length. This correlation can be done for the different pad size regions on the IROC ($4\times7.5\,\mathrm{mm}^2$) and OROC ($6\times10\,\mathrm{mm}^2$ and $6\times15\,\mathrm{mm}^2$). The extracted noise features are given in Tab. 6.3.

Table 6.4 shows a breakdown of the capacitance contributions from individual elements for the current system. The values range from 12 to 33.5 pF. For the upgraded system, a reduction of these values will be very challenging, but could be possible by using wider flexible cables with larger distances between the traces, a thicker pad plane PCB, a larger distance between the pad plane PCB and the metallic ROC body (thicker *strong back*), as well as by possibly further minimizing the trace lengths.

Noise contributions

The theoretical noise of the amplifier alone[19] is about 300 e at zero capacitance. Also the ADC contributes to the total noise with both input-referred noise[20] and quantization noise[21]. The total contribution of the ADC is ~ 300 e. The measured total noise values between 570 e (laboratory) and 670 e (current TPC system noise, see Fig. 6.5) also include all other effects like the finite input capacitance, contributions from board design, power and ground and pickup of different kinds.

[17] Least Significant Bit (LSB)

[18] Printed Circuit Board (PCB)

[19] The main amplifier noise sources are the series thermal noise from the ESD protection circuit, the (flicker) noise from the input transistor and the parallel thermal noise from the feedback transistor.

[20] Input-referred noise consists mainly of the sampling noise due to resistors and "kT/C" noise.

[21] Quantization noise is the difference between the actual analog value and the quantized digital value of an ideal ADC

			IROC	OROC		System
Pad size		(mm^2)	4×7.5	6×10	6×15	
Trace length	(range)	(mm)	4.6 – 114.7	5.6 – 113.9	5.4 – 146.8	
	(mean)		39.2	45.5	60.2	47.1
System noise	(mean)	(LSB)	0.67	0.7	0.78	0.71
	(at zero tr. length)		0.589	0.603	0.624	
	(vs trace length)	(LSB/mm)	$2.1 \cdot 10^{-3}$	$2.2 \cdot 10^{-3}$	$2.3 \cdot 10^{-3}$	$2.2 \cdot 10^{-3}$
PASA noise slope (simulated)		(e/pF)		17		17
ENC	(most probable)	(e)	634	653	672	650
	(PASA)		475	500	525	500
	(ADC)			420		420
Mean capacitance (extracted)		(pF)	17.4	18.8	20.2	18.5

Table 6.3: System parameters and ENC values for the current TPC readout system (MWPCs and PASA) for the three different pad size regions [9, 10].

	Capacitance (pF)			
	IROC	OROC 6×10	OROC 6×15	Mean
Chip packaging		2		2
Traces on FEC		1 – 3		2
Connector on FEC		0.5		0.5
Flexible cables (long)	7 (12)	7	7	7
Connector on padplane		0.5		0.5
Traces on padplane [range]	5 [0.5 – 14]	6 [1 – 15]	8 [0.5 – 20]	6
Pad to Ground	0.2	0.4	0.6	0.5
Sum [range]	17.2 [12 – 28]	18.4 [12.5 – 29]	20.6 [12 – 33.5]	18.5

Table 6.4: Contributions and sum (mean value and range in square brackets) of capacitances for the current TPC readout (MWPCs and PASA) for the three regions with different pad sizes [9, 10].

Table 6.5 shows that simulations of the analog part of the SAMPA ASIC show the same noise performance as those performed for the current PASA. It can thus be concluded that the noise performance on the system level can be retained.

Noise considerations for mixed analog and digital ASIC designs

The two major differences between the SAMPA architecture foreseen for the readout of the GEM TPC (see Fig. 6.4) and the existing system based on the two ASICs PASA and ALTRO are:

- The analog signals are being processed at the input of the chip while concurrently the previously aquired data are processed and shipped off through the serial interfaces (continuous readout).
- Low-noise analog components and complex digital functions are implemented on the same silicon die.

The feasibility of the second item was demonstrated by the Super-ALTRO (S-ALTRO) chip [11]. The S-ALTRO is a 16 channel demonstrator ASIC that was designed with the readout of the ILC-TPC in mind. On a small area (3.07 mm^2/channel) sensitive analog components and massive digital functionalities are integrated on the same chip. The S-ALTRO chip showed that by using careful design techniques the effect of the integration on the noise performance is small.

[22] Measurements with first SAMPA prototypes will be carried out during 2014.

		Current TPC (PASA)	PCA16	S-ALTRO	SAMPA
Simulated	(w/o ADC)	244e (@0 pF) 385e (@12 pF) 480e (@18 pF)	220e (@0 pF) 320e (@10 pF)	260e (@0 pF)	480e (@18 pF)
Measured	(w/o ADC) (Laboratory) (System)	385e (@12 pF) 570e (@12 pF) 670e (@18.5 pF)	270e (@10 pF)	550e (@0 pF)	

Table 6.5: Simulated and measured ENC values for the current readout (PASA, 160 ns peaking time and 70 Ω resistance in the ESD network are fixed parameters) and for PCA16 (at 120 ns peaking time with no resistance in the ESD network) and S-ALTRO (at 120 ns peaking time and with 62 Ω resistance in the ESD network). A first simulation result for the SAMPA ASIC is also added[22] for the same parameters used in the current PASA (at 160 ns peaking time and with 70 Ω resistance in the ESD network). Note also that often slightly different values of the input capacitance were used in the results presented here. They are specified in the table.

Each S-ALTRO channel contains a low noise PASA, a pipeline ADC and a DSP unit. The 10 bit ADC samples the output of the PASA at a frequency of up to 40 MHz before providing the digitized signal to the DSP which performs baseline subtraction, signal conditioning and zero suppression. The PASA used in the S-ALTRO is based on the 16 channel Programmable Charge Amplifier (PCA16) prototype [12]. It is programmable in terms of gain and peaking time and can operate with both positive and negative polarities of input charge. With respect to the PCA16 ASIC the input protection has been increased by adding a larger series resistor.

Table 6.5 gives an overview of simulated and measured ENC figures, comparing the performance of the original TPC PASA to values from tests using the PCA16 and the S-ALTRO in different configurations. System measurements with the PCA16 have resulted in ENC values on-detector[23] of 0.52 LSB and 0.55 LSB, as measured by the ILC-TPC collaboration [13] and with the ALICE TPC GEM IROC prototype in 2012, respectively[24]. With the S-ALTRO demonstrator chip an ENC value of 547 e was measured in a laboratory setup[25] [11]. This value was achieved with a chip with the input pins unbonded. It includes all other noise sources, in particular pickup from the DSP, but also random noise from PASA and ADC and the quantization error.

It can be concluded that the integration of low-noise analog components and complex digital functions on the same silicon die is possible. The design experiences from the S-ALTRO demonstrator are transferred to the design of the SAMPA.

6.4.5 Further requirements for the analog part

Some further important requirements are given in the following.

- The DC level of the PASAs differential output (baseline) should be kept at a value sufficiently close to the bottom of the circuits dynamic range, in order to preserve the maximum dynamic range (see Tab. 6.2).
- The baseline values have to be very stable in time in order to guarantee that the zero suppression can work efficiently.
- The signals have to return to the signal baseline within < 500 ns without undershoot.

[23] The settings used were 120 ns peaking time and 12 mV/fC conversion gain.

[24] A conversion to ENC is difficult, since the exact conversion gain is unknown. At 12 mV/fC the measured values would correspond to 520 e and 550 e, respectively.

[25] The settings used were 120 ns peaking time, 12 mV/fC conversion gain and 1 V bias decay voltage. The CDM input pad was connected.

– Synchronous pulsing of all 32 channels must be possible without loss of resolution.

– Crosstalk between adjacent channels can deteriorate the energy and position resolution and, therefore, has to be kept below 0.2 %.

6.4.6 Electrostatic discharge protection

The input of the SAMPA may be exposed to ESD[26] events. Semiconductor devices usually offer device-level ESD protection based on the charge device model (CDM) or the human body model (HBM). However, device-level ESD specifications may not be sufficient to protect the SAMPA when connected to a readout detector. Some experience with destructive discharges exists in the collaboration. The current TPC readout system was suffering from such events in the first two years of operation at the LHC. The destructive events could be traced to the energy stored in capacitors used in the HV network (4.7 nF). In case of a discharge inside the MWPC the charge stored in these capacitors (6 μC) would be released and injected through the readout pad into a FE channel, making it insensitive to further signals. In certain cases, presumably for large discharge events, a low impedance path was produced between the power (Vdd) and ground planes of one amplifier. As a consequence, the voltage regulator on the corresponding FEC could not supply the nominal voltage any longer, making the whole FEC unusable. After removing the HV capacitors in 2011 the amount of stored energy was reduced by a factor 10. After this intervention no more destructive events have been observed.

Models for discharges in gaseous detectors are not available. However, laboratory tests have been carried out using a capacitor connected to a needle with micrometric adjustment. The needle was lowered onto pads on a test board connected to the inputs of a PASA chip. The capacitor was charged to different voltages by a high voltage generator in order to simulate discharge events of different severity. Such discharges are probably different from those in a gaseous detector, but help to understand the limitations of the ESD protection. It was found that a charge of a few hundred nC is sufficient to destroy the ESD network at the input of a PASA channel. Larger charges of a few μC may create a short between Vdd and ground. By inserting resistors before the input to the PASA, the tolerated charge could be increased to the required level. However, quite large resistors had to be used (several hundred Ω).

Problems with destructive discharges have appeared in a similar manner also during prototype GEM tests both in the ALICE test at the PS and with ILC-TPC prototype tests. In GEM detectors discharges generally begin with a sudden, radiation-induced breakdown of the gas rigidity in one GEM, normally the last in a cascade of multipliers. The capacitance of one GEM segment is slightly smaller than 5 nF and the charge stored is 1.5 μC. The discharge may propagate to other electrodes such that a fraction (up to all) of the stored charge can be delivered to the readout pad.

Additional resistances and capacitances (protection diodes) at the input to the SAMPA will have a negative impact on the noise performance. Therefore, the best strategy is to implement device-level ESD specifications based on the HBM and add system-level protection on the front-end card level after additional testing to derive a realistic estimation of the expected ESD energy, wuth keeping the best possible noise performance in mind.

6.4.7 Analog-to-digital conversion

The analog signal output of the PASA is sampled, at a rate of 10 MHz, by an ADC with 10-bit dynamic range. The requirement on the power consumption (below 35 mW per front-end channel) calls for low power ADCs. This requirement can be met by SAR ADCs implemented with a low power switching technique. They allow implementations with a low power consumption around 2 mW per channel.

[26] ElectroStatic Discharge (ESD)

Sampling frequency

A shaper peaking time of 160 ns preserves partially the spatial characteristics of the drifting electron clusters (see Sec. 6.4.3). In RUN 1 it was found that this feature can be best taken advantage of in the clusterization process when a sampling frequency of 10 MHz is chosen. Consequently, also for the GEM TPC readout this sampling frequency represents the optimum. The maximum electron drift time of $\sim 100\,\mu$s is in this case divided into about 1000 time bins, each corresponding to a drift distance of about 2.8 mm.

6.4.8 Digital signal processor

The digitized TPC signals are further processed by a set of digital circuits integrated into the DSP part of the SAMPA, which are described below.

Pedestal subtraction

The DC level of the PASAs differential output (baseline or pedestal) has to be subtracted from the ADC output for each channel in order to perform efficient zero suppression. A fixed pedestal subtraction mode, where one value can be subtracted for each channel for all time bins, has shown to be sufficient for the current system. The baseline values are actually extremely stable over time, requiring only very rarely pedestal calibration runs; a feature that should be kept.

Digital filter

Since the GEM signals do not feature a tail, the necessity to minimize the pileup effect of subsequent signal tails by a tail cancellation filter is removed.

A calculation and subtraction of the moving average may help to correct possible perturbations of the baseline produced by non-systematic effects. The value to be subtracted from the current samples is the moving average of the signal itself and of some previous samples. Fast variations in the signal, like clusters, are excluded from the baseline calculation. Such a filter is implemented in the ALTRO ASIC but could not yet be successfully used during data taking. The reason lies in the fact that in rare cases the calculation of the value to be subtracted may fail, resulting in a pedestal shift and failure of the zero suppression.

Data compression using zero suppression

If no data compression were applied in the front-end electronics, the 552,960 readout channels of the GEM TPC would produce data at a rate of 7 TByte/s (100 Mbit/s per channel). To reduce this throughput, it is foreseen to compress the data via zero suppression (ZS). In this mode all data words are dropped inside the SAMPA if their value is so close to the reference level (baseline or pedestal) that they can be assumed to not contain any useful information. In practice, a fixed threshold is applied for the data in each channel, and only values above this threshold are kept. The resulting signal clusters are run-length encoded, which requires the addition of two extra words, describing the start time and length of the non-suppressed cluster.

To remove glitches, the minimum number of consecutive samples needed to define a valid signal can be configured[27]. If needed, a number of pre- and post-samples that should be kept before and after a peak can be defined[28]. In order to perform the zero suppression, the pedestal is subtracted. The zero suppression threshold is naturally determined as a multiple of the width of the baseline distribution (noise). Pedestal and noise values are measured in a dedicated pedestal run and the measured values for

[27] A minimum of 2 consecutive time bins above threshold is required in the current readout system.

[28] This feature is not used in the current readout system.

each channel are then used to configure the filter. The threshold must be configurable for each individual front-end channel.

This technique is a lossy technique; small clusters or tails of clusters may be discarded. It achieves compression ratios which are roughly inversely proportional to the TPC occupancy. For occupancies of 15 % and 42 % the data compression ratio is about 0.18 and 0.5, respectively. Table 6.6 compares the compression ratio with a different running scenario (see below).

	minimum bias	central
Average occupancy	0.15	0.24
Compressed data size (ZS)	0.18	0.28
Compressed data size (Huffman)	0.21	0.25

Table 6.6: Expected average pad occupancies and approximate data compression ratios (compressed data size relative to raw data size) for two different data compression modes.

Other compression scenarios

Instead of (or in addition to) zero suppression, lossless transformations like variable length codes (e.g. Huffman coding) or lossy compression methods like vector quantization may be applied to compress the data.

Small ADC values occur very often in the data stream of a gaseous detector like the TPC, but larger ones are more rare. The distribution is approximately exponential. The expected size of the data can be reduced if short words are used for frequent values and longer ones for rare values. The theoretical lower bound on the average word size that can be achieved by this strategy is called the entropy of the data source[29]. Huffman coding [14] approaches this bound and is easy to implement. Only if the distribution of input values is too extreme the method can run into problems. In such a case events can become larger than uncompressed.

A TPC is obviously not a stochastic data source, as the ADC values found in adjacent pads are highly correlated. Therefore, it could be possible to compress the data to an even lower bit rate than the entropy of the ADC values. In other words, there could be representations of the TPC data that have a lower entropy than the formats described above. Various methods like differentiation, prediction, etc. have been evaluated, but in the end none of these approaches yield results that are much better than plain Huffman coding (see [1] and references therein).

Huffman coding has been applied to TPC events before. The entropy analysis results in about 6 bits per sample for cluster data, depending somewhat on the abundance of overlapping clusters due to high occupancy. A noise of 0.7 ADC counts requires about 1.3 bits per sample for coding the baseline/pedestal. Applying Huffman coding to non-zero-suppressed data will result in a compression ratio of about 0.3 for an occupancy of 27 %, which is expected for the inner pad rows.

Huffman coding can be implemented in the SAMPA for encoding and in an FPGA[30] on the online farm side for decoding. It will give comparable or even better compression factors than ZS for occupancies larger than 25 % (see Tab. 6.6), while ZS reduces the event size by a large margin at low occupancies. Huffman coding is lossless, while ZS implies typically a loss of 15 % of the total charge of a MIP cluster. Both methods require similar resources for implementation and suffer from the same drawbacks, i.e. that the data volume might increase in case of noisy channels (by a larger factor in case of Huffman coding)

[29]The entropy of the data source can be computed as the sum over the probability of the occurrence of an ADC value multiplied by the logarithm of the probability; the sum running over the set of all possible words that are output by the data source.

[30]Field Programmable Gate Array (FPGA)

and that the output format is more prone to errors induced e.g. by SEUs[31] than the raw ADC data. The first problem has to be taken care of by the output module in the SAMPA; the latter can be solved by applying error detection and correction techniques to the transmission protocol.

Event memory

The data read out from 32 channels is transferred into the SAMPA event memory. Before transferring the data from each channel off-chip, it is temporarily buffered here. Naturally occurring bursts with higher occupancy lead to temporarily increased data rates, which have to be smoothed properly by the event memory. The event memory in this case serves as a de-randomizing buffer, ensuring that the data throughput is always below the bandwidth of the serial output links from the SAMPA. The optimal size of this buffer has to be found in simulations. In the undesirable case where the data rate is too high for an extended period, the data will have to be truncated, which will be marked in the data stream.

The event memory can also be used as a lookup table to generate patterns to be read out through the output links for test purposes.

Interfaces

The data are read from the event memory and transferred to four electrical links (*e-links*) with bandwidth 320 Mbit/s each.

For control and monitoring of the SAMPA the GBT-SCA[32], a dedicated ASIC implemented in CMOS 130 nm using radiation tolerant techniques is used. It implements the I^2C protocol[33] towards the SAMPA chips and is controlled via a dedicated slow control e-link from a GBTx chip.

6.4.9 Testing

The ASICs have to be thoroughly tested before assembly on the front-end cards. Even minimal mechanical damage may lead to loss of assembly quality. Due to the large number of chips to be tested, an automatized testing bench is required in order to guarantee reliable sorting and book-keeping.

In the manufacturing process for the original FECs for the ALICE TPC about 40,000 PASA and ALTRO chips each were tested at Lund University. A semi-automatic test system had been developed, with the test procedures described in [2] and on the web page [15]. A pick-and-place robot moved chips from the trays (see Fig. 6.7) and placed them in the test socket which opened and closed by compressed air control. The test boards with the socket carried buffer memories to allow the communication and operation of the chip under test to go on at nominal speed. Extensive testing takes quite long time per chip. It was not judged meaningful to automatize the exchange of chip trays as the robot could be loaded for about 4 hours of testing.

Each chip was tested for about 1 minute (the ALTRO slightly longer, the PASA slightly shorter). All supply currents were measured, all DC levels checked. The ALTRO channels were excited by a sinus waveform which was digitized and verified, thus checking all bits of the analog-to-digital conversion. All memory cells were checked by downloading test patterns and reading back. The PASA channels were excited by a step-voltage, feeding charge into the preamp input over a small capacitor. The waveform, sampled with a 12 bit ADC at 40 MHz was compared to the expectation and the amplifier gain was recorded. Chips were sorted in three categories depending on the test result: accepted, slightly outside the acceptance limits and failure. A test protocol for each chip was stored and a summary of the test results was published [9].

[31] Singe Event Upset (SEU)
[32] Slow Control Architecture (SCA)
[33] Inter-Integrated Circuit (I^2C)

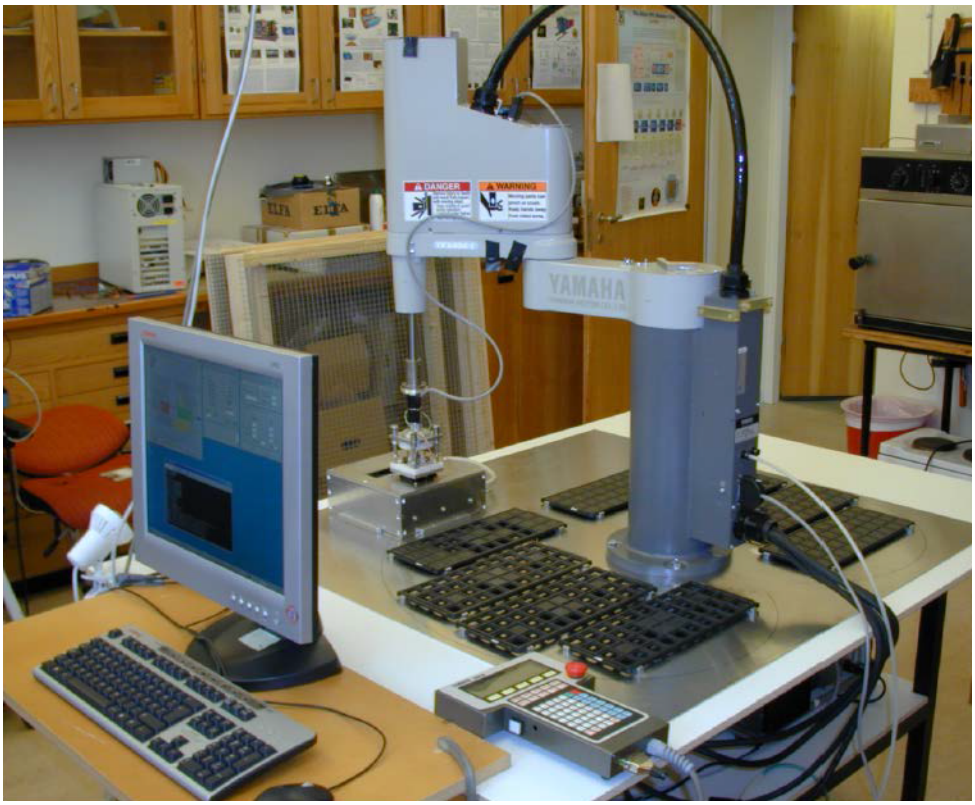

Figure 6.7: Image of the PASA and ALTRO testing robot at Lund University.

All equipment and software for testing is still available and can be used for the new SAMPA by modifying the test card with a different socket, different output buffering and some other minor changes. The analog test pulsing feature can remain unchanged, but the procedures for ALTRO and PASA testing will have to be merged.

6.5 Front-end card

The front-end card (FEC) contains the complete readout chain for amplifying, shaping, digitizing, processing, and buffering the TPC signals. The FEC must be designed as an integral part of the detector to obtain the best performance for the experiment.

6.5.1 Partitioning

The FEC plays a crucial role in the optimization of the detector performance. Some boundary conditions are given in the following:

1. **Available space**: the number of pads on the IROCs of the current TPC is as high as can be read out with the present channel density of the electronics (16 channels per ASIC). In order to manage this, the mechanical mounting of the FECs, as well as their cooling, is the result of a large engineering and construction effort. The resulting density of hardware has led to many difficulties in maintenance operations. However, for the OROCs the space situation is much more relaxed.

2. **Reuse of mechanical structures**: with a new FEC with equal size one may take advantage of reusing the mechanical support and cooling structures.

3. **Pad plane segmentation**: due to the size of the OROC, the pad plane PCB will have to be segmented. Since traces can not cross PCB segments, not all configurations for the traces are possible.

4. **Trace lengths**: higher intergation of the readout system (more channels per FEC) could lead to longer trace lengths on the pad plane PCB with a negative impact on the noise performance.

5. **Flexible signal cables**: the trace density on the Kapton signal cables connecting to the readout chambers also directly relates to the noise behavior.

6. **Readout link**: the GBTx ASIC [3] can multiplex 10 (14) e-links with (without) forward error correction enabled. This number together with the number of output e-links per SAMPA (4) makes only certain combinations attractive. Not using all inpus to the GBTx ASIC effectively means a waste of useful bandwidth.

7. **Readout scheme**: when the data are shipped off-detector, they are ordered in such a way that the information from all pads with hits are sent in consecutive order following the pad row structure and directed to the same cluster finder instance (see Sec. 8.1.2).

The 6$^{\text{th}}$ requirement basically defined the number of SAMPA chips per FEC to be 5 (or 7). Such a scheme with 5 readout partitions per TPC sector is summarized in Tab. 6.1. The last requirement (data ordering) can always be achieved in the CRU, which gathers the data from many FECs.

6.5.2 PCB design and layout

A simplified layout of the FEC is shown in Fig. 6.8. The FEC receives the analog signals from the readout chamber through a set of flexible cables. To minimize the trace lengths and thus noise (but also crosstalk), the SAMPAs have to be positioned very close to the input connectors. The signals are processed by 5 SAMPAs, with an estimated maximum power consumption of less than about 1 W per SAMPA. The FEC also contains additional protection for the input to all SAMPA channels (see next section).

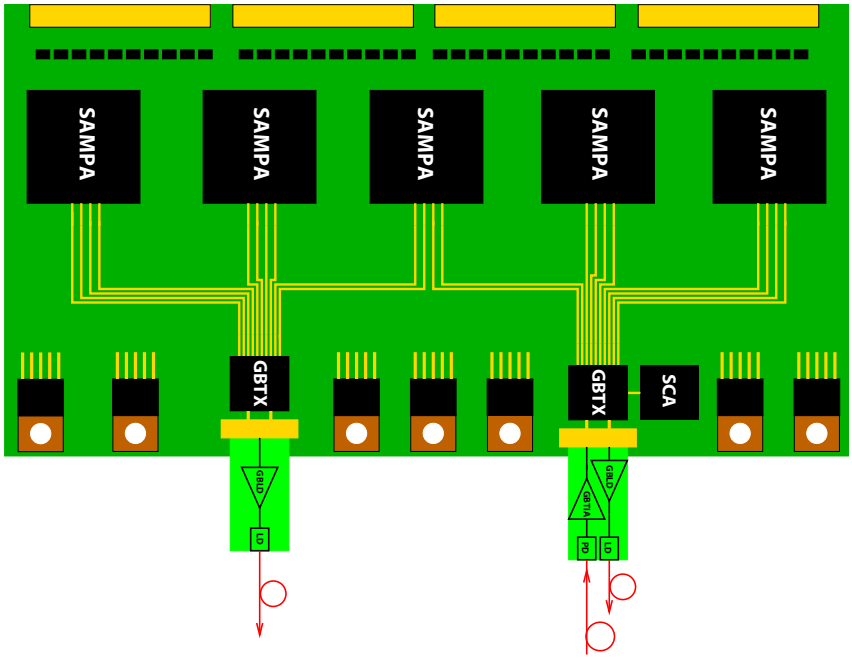

Figure 6.8: Schematic of the front-end card (FEC) with SAMPA. The connectivity is realized through the GBT system via optical links.

Control and monitoring of the SAMPA is implemented via the GBT-SCA ASIC. Physics and monitoring data are multiplexed on the FEC by up to two GBTx ASICs. The uni-directional versatile links [4] for the data to be sent to the CRU and online farm are driven by bi-directional optical transceivers (VTRx) or

uni-directional twin transmitters (VTTx). Since the bandwidth requirements in the up- and downstream directions are asymmetric, less VTRx are needed to receive trigger and timing information via the ALICE TTS[34] system. We aim at installing one TTS link on every second FEC. Also configuration data and control commands to the FECs are sent via the TTS links. A possible distribution of optical components and links on the 36 TPC sectors is shown in Tab. 6.1, where we consider that less bandwidth is needed for the outermost readout partitions due to lower occupancies in this region.

6.5.3 System level input protection

The protection strategy foresees the implementation of system-level protection on the front-end card in the form of diode pairs, on top of the device-level protection in the SAMPA. Within the SRS project and the RD 51 collaboration a hybrid readout board for MPGD detectors has been developed. The module (RD51 APV25 HYBRID) is based on the APV25 chip and successfully uses an IC[35] with diode protection for 4 channels.

Broken channels may lead to a short to ground which in fact makes the whole FEC inoperable. This could be avoided by separate voltage regulation for the analog power of each SAMPA (or possibly for each pair of SAMPAs).

6.5.4 Testing

The assembled FECs for the current TPC readout system were tested on the bench at Frankfurt University. This test step benefits from a final readout system being operational, which allows parallel testing of many FECs as well as long term testing (stress tests). The purpose of the test is to find assembly errors, chips which have broken during the mounting and handling, as well as any other malfunctioning of any component. The test procedures have been described in [2] and on the web page [15] and are a good starting point for the testing of the future FECs.

6.5.5 Irradiation campaign

The radiation levels expected for the high luminosity phase (50 kHz Pb–Pb collision rate) impose requirements on the radiation hardness/tolerance of the innermost FECs of the ALICE TPC. Fast hadrons can lead to a Single Event Upset (SEU) in digital structures, or to a Single Event Latch-up (SEL), a type of short circuit that triggers parasitic effects which can disrupt proper functioning of the element, or possibly even lead to its destruction.

The flux of fast hadrons (> 20 MeV) at the TPC inner (outer) layer is expected to reach 3.4 kHz/cm^2 (0.7 kHz/cm^2), including a safety factor of 2 [5]. The TPC electronics located at the inner radius of the service support wheel has to stand a dose of 2.1 krad.

The SAMPA has to be designed carefully in order to avoid SELs and to protect critical logic against SEUs. FEC prototypes and all components will be irradiated in test beams of fast protons or neutrons, either individually in dedicated campaigns for critical components (e.g. FE ASIC) and/or finally after being mounted on FEC prototypes.

6.6 Common Readout Unit

The Common Readout Unit (CRU) is described in [5]. It provides the interface between the on-detector electronics and the trigger system, the online farm, and the DCS[36]. The CRU units are located in the

[34] Trigger and Timing distribution System (TTS)
[35] NUP4114UPXV6T1G from ON semiconductor.
[36] Detector Control System (DCS)

control room outside the radiation area and will receive data from the detectors through optical fibers via the GBT link. A schematic is shown in Fig. 6.9.

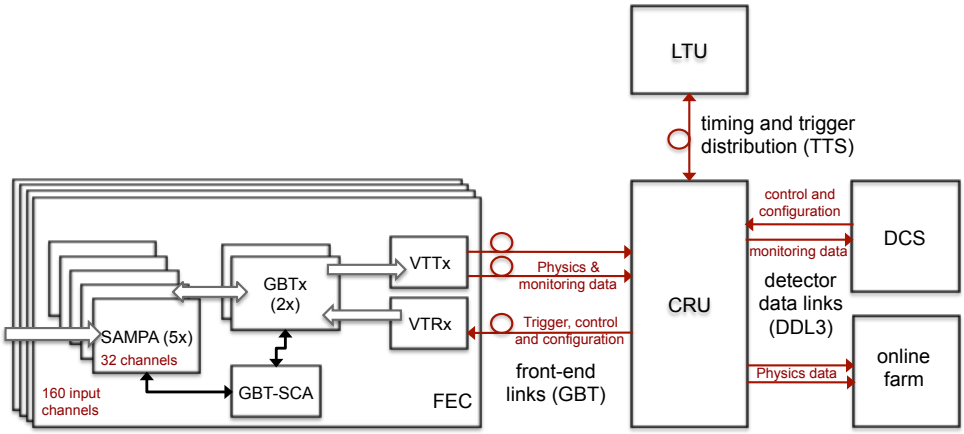

Figure 6.9: Schematic of the TPC readout system with the CRU as central part interfacing the front-end electronics to the trigger system, the DCS and the online farm.

The CRU steers and controls the configuration, readout and monitoring of the FEE and the trigger handling. When the TPC data are forwarded from the CRU to the online system, the individual data fragments are ordered by the geometrical position of the pad rows and pads on which the charge cluster signals were read such that the data are sent consecutively pad-by-pad, pad-row-by-pad-row. Also a cluster finder algorithm could be implemented on the CRU.

On each FEC the data from 5 SAMPAs are multiplexed by 2 GBTx ASICs [3] (only 1 for the outermost readout partitions due to lower occupancies in this region) and sent to the CRU and online farm through a double optical transmitter. The effective bandwidth for data readout is $2 \times 3.2\,\mathrm{Gbit/s}$ using a special, SEU robust transport protocol with forward error correction. The trigger, timing and clock distribution and control and configuration data are transfered to the FEE on each TPC sector using fewer (e.g. one per 2 FECs) uni-directional GBT links (TTS [5]).

The CRU is the physical and logical interface to the ALICE online farm, to the DCS and to the trigger system. Different firmware modules are required, that implement these interfaces:

- The trigger module receives trigger and timing information, forwards a clock and a synchronisation (or a trigger) signal to the FECs and prepares a timestamp header.
- The data acquisition module receives the data from the FECs and checks its integrity. This module will need to be a TPC specific implementation due to special requirements for the continuous readout of data.
- The TPC specific data formatter re-orders the channel data, adds header information into the data stream and sends the data to the firmware module servicing the optical uplink.
- A TPC specific DCS module may perform monitoring (voltages, currents and temperatures) and time critical operations like switching off FECs in case of overheating.

The configuration, control and monitoring of the TPC FEE (SAMPA chips, FECs and CRUs) is integrated into the existing hierarchical control structure of the ALICE DCS. A software FeeServer[37] at the CRU configures the front-end electronics and monitors its status (see Sec. 10.2).

[37] Front-End Server (FeeServer)

Chapter 7

Simulation and detector performance

The expected performance of the upgraded GEM TPC during RUN 3 is described in this chapter. It starts with an overview on the performance of the current TPC, followed by a discussion of the intrinsic resolution of the GEM TPC (Sec. 7.2) and of the performance with track pileup from different interactions (Sec. 7.3). In Sec. 7.4 distortions due to space charge are discussed. In particular, the importance of space-charge fluctuations is pointed out. Finally, in Sec. 7.5 the performance including also space-charge distortions of the expected magnitude, and corrected with the online calibration tools discussed in Chap. 8, is presented.

7.1 Current performance

The current ALICE TPC was installed in the ALICE experimental cavern in 2007 and successfully operated since the LHC start-up in 2009. The observed performance is in agreement with or better than the design specifications reported in [1, 2].

7.1.1 Tracking performance

In pp collisions the particle tracking efficiency within the TPC is better than 98 % for findable tracks[1]. In Pb–Pb collisions it decreases by about 1 – 3 % due to the higher occupancy [3] ($\mathrm{d}N_{\mathrm{ch}}/\mathrm{d}\eta \approx 1600$ in 0 – 5 % central collisions at $\sqrt{s_{\mathrm{NN}}} = 2.76\,\mathrm{TeV}$).

The achievable momentum resolution is driven by multiple scattering at low p_{T}, and by the space-point resolution and residual mis-calibration after all distortion corrections at high p_{T}. Both contributions are discussed in the following.

Space-point resolution The parameters dominating the space-point resolution of the TPC are diffusion (which depends on drift length z_{d}), track inclination angle and total cluster charge on a given pad row. For tracks with large transverse momentum p_{T}, and thus vanishing deflection angle, the space-point resolution in local-y ($r\varphi$) direction[2] is around 400 μm (800 μm) for short (long) drift length [4]. The current results are at the level of the intrinsic (statistical) limit. From the covariance matrix of the tracks, the track resolution at different reference points can be obtained. For high-p_{T} tracks the intrinsic track resolution is approximately $\sigma_{\mathrm{intr}} = 200\,\mu\mathrm{m}$ at the entrance of the TPC inner field cage and 2 mm extrapolated to the interaction point. This intrinsic track resolution determines the precision that is required for all calibrations and drift field distortion corrections, e.g. the drift velocity, alignment, $E \times B$ and space-charge distortion corrections.

[1] Findable tracks are defined by a minimum track length in the active zones of the TPC.

[2] The space-point resolution in $r\varphi$ determines the transverse momentum (p_{T}) resolution. For the coordinate system see App. A.

Drift field distortion corrections For RUN 1 the largest systematic correction applied to the space-point coordinates is due to the $E \times B$ effect, which reaches 1 cm (in very localized regions). The precision of this correction is limited by the residual misalignment of the electric and magnetic fields.

So far, space-charge effects due to ions in the TPC drift volume have been small. In the 2011 Pb–Pb data a space-charge induced track distortion of $\sim 200\,\mu$m (when extrapolated to the interaction point) was observed.

Momentum resolution Figure 7.1 shows the resolution σ_{1/p_T} for the current status of the calibration and for a data set from p–Pb collisions at $\sqrt{s_{NN}} = 5.02$ TeV. Expressing the momentum resolution using σ_{1/p_T} has the advantage that the distributions based on this variable are approximately Gaussian, even at large p_T. The performance shown in Fig. 7.1 translates into a p_T resolution of $\sigma_{p_T}/p_T \lesssim 3.5\,\%$ at $p_T = 50\,\text{GeV}/c$ and below 1 % at $p_T = 1\,\text{GeV}/c$.

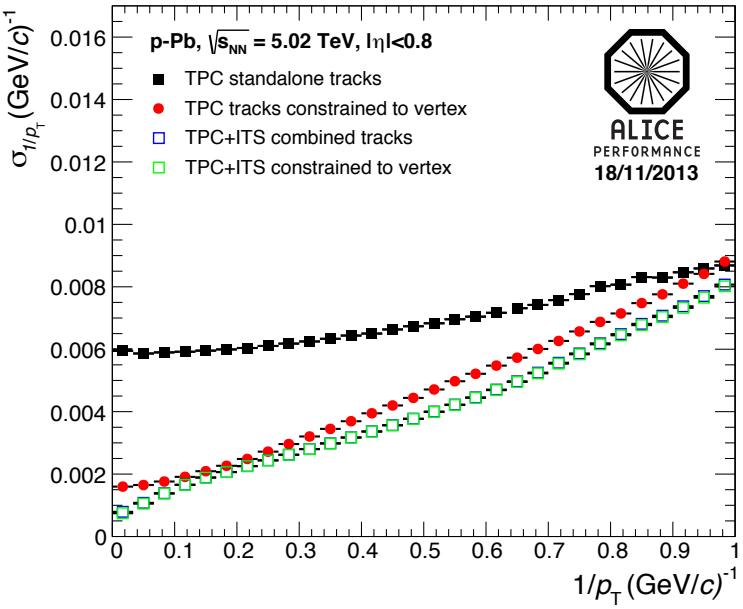

Figure 7.1: Resolution in $1/p_T$ as a function of $1/p_T$ for the ALICE central barrel (current system). The plot shows the $1/p_T$ resolution for TPC standalone tracks and for global tracks combining tracking in ITS and TPC with and without vertex constraint. The data is from p–Pb collisions collected in 2013.

7.1.2 Particle identification performance

The specific energy loss $\mathrm{d}E/\mathrm{d}x$ is obtained for each track by calculating the truncated mean of the cluster charges on currently up to 159 pad rows[3], which adds significant PID[4] capabilities to the ALICE central barrel. Identification of pions, kaons, and protons is possible also in the relativistic rise region of the Bethe-Bloch energy-loss curve [5] at high p_T. The p_T reach is currently limited to $20\,\text{GeV}/c$ by statistics. With the event sample anticipated in RUN 2 and further improved understanding of the characteristics of the energy-loss curve in the relativistic rise region, the identification of pions, kaons and protons up to $50\,\text{GeV}/c$ is within reach. The usage of high-momentum cosmic muons to improve the understanding of the energy loss in this p_T region is under study.

In pp and central Pb–Pb collisions the $\mathrm{d}E/\mathrm{d}x$ resolution is about 5.5 % and 7 %, respectively. The resolution in pp is consistent with the intrinsic $\mathrm{d}E/\mathrm{d}x$ resolution dominated by the ionization fluctuations (Landau tail), folded with gas gain fluctuations, the detector readout granularity and threshold effects. In

[3] In the GEM TPC the number of pad rows is reduced to 158, see Sec. 4.5.
[4] Particle IDentification (PID)

Pb–Pb collisions the performance deteriorates at large multiplicities mainly due to an increasing overlap of clusters.

7.2 Intrinsic performance of the upgraded TPC

The expected performance of the TPC after upgrade with GEM-based readout is quantified using microscopic simulations. For these studies, the current ITS design is used. Since the performance will improve with the upgraded ITS [6, 7], the results on the global tracking performance reported in this chapter can be considered as conservative.

7.2.1 Microscopic GEM simulations

The most important parameters for the microscopic simulation of the intrinsic performance are:

- **Gas choice**: The baseline gas mixture is Ne-CO_2-N_2 (90-10-5), see Chap. 3.
- **Pad geometry**: The baseline pad geometry of the upgraded TPC is very close to that of the current system, see Sec. 4.5.
- **Pad response function**: The shape of the induced charge distribution on the readout plane of a GEM detector is very narrow, due to the parallel plate geometry of the induction gap. A purely projective pad response function is used in the simulation, i.e. electrons create signals only on the pad directly below their arrival point on the first GEM plane.

Table 7.1 shows the parameters used for the simulations. The microscopic simulation algorithm is described in [1] and has been validated with test beam data [8]. Here, only a short summary of the simulation steps is given.

Item		Value
Mean number of primary electrons for MIP		14.0
First ionization potential I_0	(eV)	20.77
Effective energy for e-ion pair creation W_i	(eV)	37.3
Drift velocity at 400 V/cm	(cm/μs)	2.58
Longitudinal diffusion constant (D_{L})	(μm/$\sqrt{\mathrm{cm}}$)	221
Transverse diffusion constant (D_{T})	(μm/$\sqrt{\mathrm{cm}}$)	209
$\omega\tau$ (for magnetic field $B = 0.5$ T)		0.32
Oxygen content	(ppm)	5
Effective GEM gain		2000
System noise (RMS)	(e)	670
Dynamic range		2 V; 10 bits
Conversion gain	(mV/fC)	20
Peaking time	(ns)	160
Sampling frequency	(MHz)	10
Zero suppression settings		3 LSB[5] threshold; glitch filter

Table 7.1: Parameters used in the simulation: Gas properties, GEM effective gain (which includes the signal coupling to the readout plane) and electronics parameters.

The simulation is based on a modified version of GEANT3 [1]. The ionization by charged particles entering the active gas volume is simulated using a TPC-specific energy-loss method. Based on the average number of primary electrons per cm of track length, the interaction length is calculated and a step

[5]Least Significant Bit (LSB)

length is randomly generated. A random energy-loss value is assigned to this step according to $1/E^{2.2}$ ($I_0 \leq E \leq 10\,\mathrm{keV}$, where I_0 is the first ionization potential). The total number of ionization electrons including secondaries is calculated. Each of these electrons is drifted to the readout chambers, taking into account diffusion and residual distortions. Space-charge distortions are not taken into account at this point; they are discussed separately in Secs. 7.4 and 7.5. At the GEM readout stack an exponential gain variation is assumed for each electron. The charge is projected onto the pad plane using the described pad response function in space and a semi-Gaussian shaping function in time. The reconstruction of events simulated in this way does not differ from that of real data.

The described simulation algorithm is routinely used in the ALICE simulation and reconstruction framework and was thoroughly validated in the past years.

7.2.2 Tracking performance

Figure 7.2 shows that the momentum resolution in the acceptance of the central barrel detectors of ALICE will be maintained for the TPC with GEM-based readout. The plot indicates a slight deterioration of the resolution in $1/p_\mathrm{T}$ for tracks using only TPC information. This deterioration is however fully recovered for global tracks combining tracking in ITS and TPC. The good agreement of the simulated data shiown in Fig. 7.2 (left panel) with the measured p–Pb data shown in Fig. 7.1 indicates a thorough understanding of material budget and detector response.

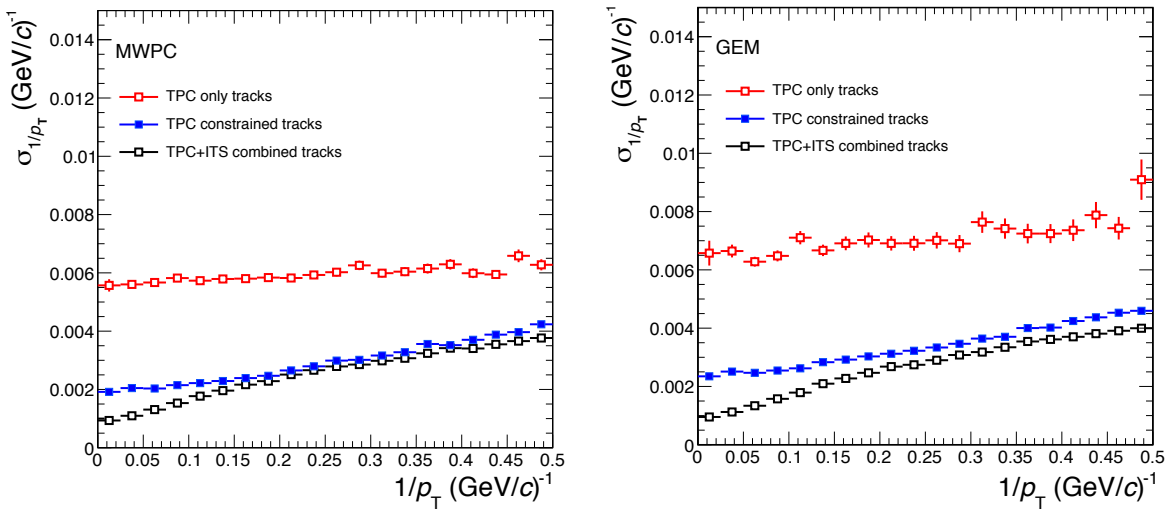

Figure 7.2: Resolution in $1/p_\mathrm{T}$ as a function of $1/p_\mathrm{T}$ for MWPC (left panel) and GEM readout (right panel). The open red squares are for tracks based on TPC information only, while the closed blue squares show TPC track fits including the vertex point. The open black squares show the result for combined fits to TPC and ITS track points.

The deterioration of the resolution for TPC-only tracks is consistent with the slightly worse position resolution due to the narrower pad response function for the GEM-based readout chambers as compared to the present MWPCs (see Sec. 4.5). However, in most of the acceptance region $|\eta| < 0.9$ clusters with signals on more than one pad dominate, as shown in Fig. 4.16.

7.2.3 Particle identification performance

The relative $\mathrm{d}E/\mathrm{d}x$ resolution $\sigma_{\mathrm{d}E/\mathrm{d}x}/\langle \mathrm{d}E/\mathrm{d}x\rangle$ for isolated electron and pion tracks ($1 < p < 6\,\mathrm{GeV}/c$) was measured with a triple-GEM IROC prototype at the CERN PS test beam. The results reported in Sec. 5.2.6 show that the $\mathrm{d}E/\mathrm{d}x$ resolution observed with the GEM IROC is compatible with that of the MWPC IROCs. This behavior is confirmed in the simulation: Figure 7.3 (left panel) shows the $\mathrm{d}E/\mathrm{d}x$ resolution as a function of the momentum for MWPC and GEM readout at low track multiplicity. Only a small difference between MWPC and GEM is observed.

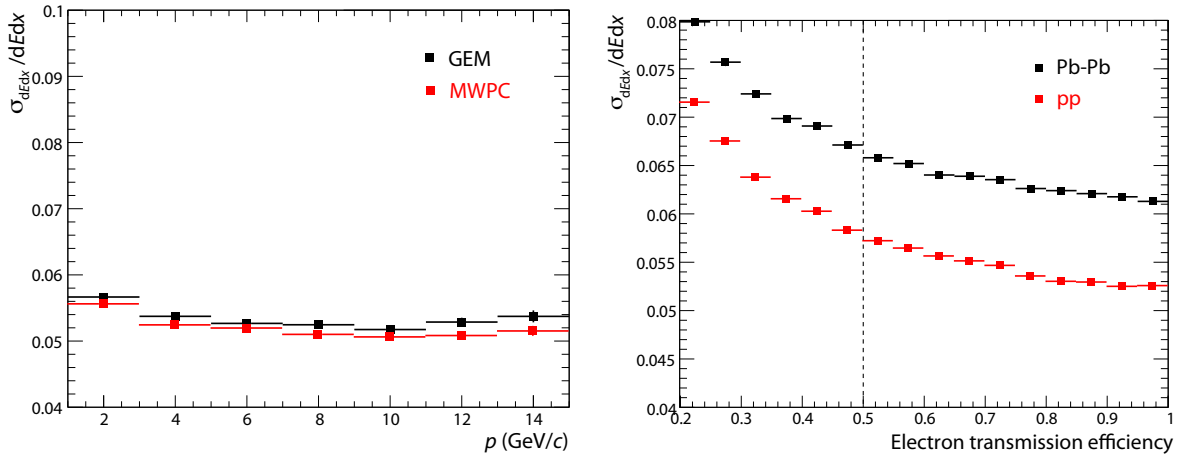

Figure 7.3: (Left) dE/dx resolution as a function of track momentum for MWPC and GEM readout. The simulation is carried out at low multiplicity (pp). The performance at high multiplicities and with event pileup is discussed in Sec. 7.3. (Right) Simulated dE/dx resolution for MIP tracks crossing 158 pad rows as a function of the electron transmission efficiency in the GEM stack for pp and Pb–Pb collisions.

An important effect to be considered for a GEM readout system is the transmission efficiency of the readout stack for primary electrons. While for an MWPC a transmission efficiency of 100 % can be safely assumed, for a GEM stack it may be reduced due to the finite electron collection efficiency at the first GEM stage. As shown in Sec. 5.1.3 (e.g. Fig. 5.9), this effect is enhanced for settings which minimize the ion backflow. In measurements with an ^{55}Fe source it manifests itself in a degradation of the energy resolution at 5.9 keV relative to the optimal value of about $\sigma(^{55}\mathrm{Fe}) = 8.5\,\%$.

As shown in Fig. 7.3 (right), the dE/dx resolution, which depends on the energy resolution, degrades significantly only for values of the electron transmission efficiency below 0.5, both for pp and Pb–Pb collisions. If we consider the first GEM foil the main contributor to the energy resolution, a transmission efficiency of 0.5 corresponds to a degradation of the energy resolution to $\sigma(^{55}\mathrm{Fe}) = 8.5\,\%/\sqrt{0.5} \approx 12\,\%$.

Due to the results shown in Fig. 7.3 (right), we consider a transmission efficiency of 0.5 the lower limit (and an energy resolution of 12 % the upper limit) for the operation of the GEM readout system. In the simulations shown in the rest if this chapter the additional effect of the finite transmission efficiency is not included.

7.3 Performance with event pileup

The GEM TPC will operate at a Pb–Pb interaction rate of 50 kHz, where particle tracks from $N_{\mathrm{pileup}} = 5$ events on average are superimposed in the drift volume of the TPC. The resulting pad occupancies lead to an increased probability for clusters to overlap and thus to be wrongly assigned during the tracking step. In this section we study the impact of event pileup on the tracking performance. For more details on the LHC running conditions see Sec. 8.1.1.

The current TPC was designed for a charged particle multiplicity of $\mathrm{d}N_{\mathrm{ch}}/\mathrm{d}\eta = 8000$ in central Pb–Pb collisions. Comprehensive studies showed that the required performance can be achieved at such extreme conditions [1]. For the anticipated data taking scenario at $R_{\mathrm{int}} = 50$ kHz, corresponding to an equivalent charged-particle multiplicity (see Sec. 6.2) of $\mathrm{d}N_{\mathrm{ch}}/\mathrm{d}\eta|_{\mathrm{equiv}} \approx 2500$, the effect of event pileup is thus expected to be minor. However, the track topology in overlapping events is different from a single high-multiplicity collision due to the displacement of the vertex positions. The performance of the TPC under such conditions was verified in simulated central (0 – 5 %) Pb–Pb events ($\langle \mathrm{d}N_{\mathrm{ch}}/\mathrm{d}\eta \rangle$ scaled to 2000) embedded in different pileup scenarios. A varying number of minimum bias events ($\langle \mathrm{d}N_{\mathrm{ch}}/\mathrm{d}\eta \rangle$ scaled to 500) are added at random distances within a time window of $\pm 80\,\mu$s. Several jets are added to the

central event (simulated with Pythia) in order to enhance the fraction of high-p_{T} particles. Naturally, in this simulation the actual tracks seen from the pileup events are constrained by the readout time window defined by the central event.

Figure 7.4 shows that the TPC standalone tracking efficiency at the different interaction rates is essentially the same for the current TPC and for the GEM TPC. In these data, the lower bound scenario (central event at $R_{\mathrm{int}} = 20\,\mathrm{kHz}$) corresponds to an equivalent multiplicity $\mathrm{d}N_{\mathrm{ch}}/\mathrm{d}\eta|_{\mathrm{equiv}} = 2500$, while the most extreme scenario (central event at $R_{\mathrm{int}} = 70\,\mathrm{kHz}$) corresponds to $\mathrm{d}N_{\mathrm{ch}}/\mathrm{d}\eta|_{\mathrm{equiv}} = 5000$. Figure 7.5 shows the resolution in $1/p_{\mathrm{T}}$ for the GEM TPC for these different scenarios. The tracking performance is essentially unaffected by the additional track load.

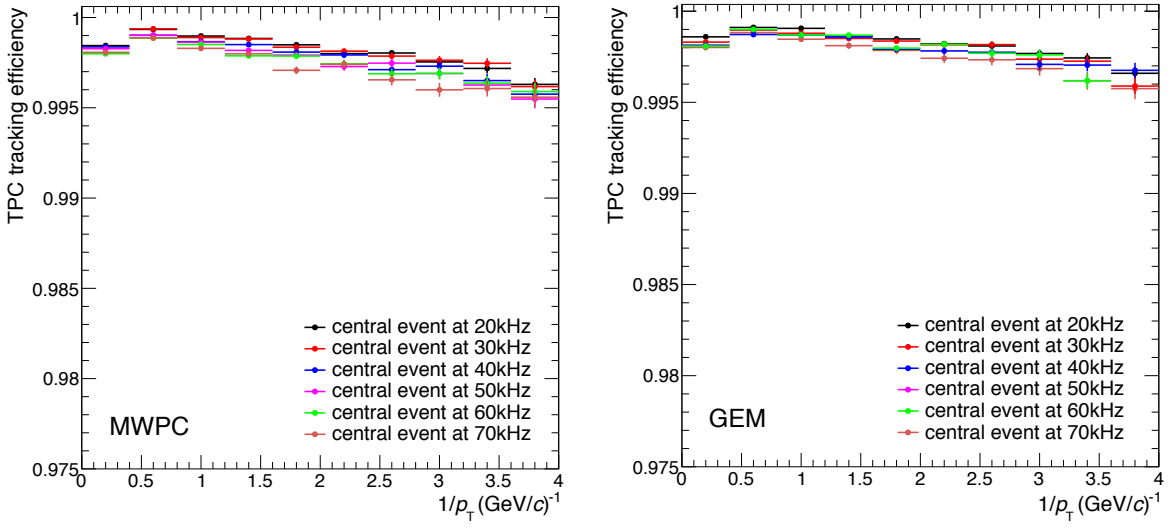

Figure 7.4: TPC standalone tracking efficiency for MWPC (left panel) and GEM (right panel) readout. In the simulated data central events ($\langle \mathrm{d}N_{\mathrm{ch}}/\mathrm{d}\eta \rangle$ scaled to 2000) are embedded in the avereage background given by minimum bias events ($\langle \mathrm{d}N_{\mathrm{ch}}/\mathrm{d}\eta \rangle$ scaled to 500) at different interaction rates.

Figure 7.6 compares the $\mathrm{d}E/\mathrm{d}x$ resolution for MWPC and GEM readout at different interaction rates. For the MWPC readout the simulated performance is slightly better than the measured resolution of around 7 %, since in the current framework the deterioration due to the ion tail is not part of the simulation. This does however not affect the results obtained for the GEM readout. We can conclude that the $\mathrm{d}E/\mathrm{d}x$ resolution is not compromised by the upgrade with GEM readout.

7.4 Space-charge distortions and corrections

At high collisions rates and large charged-particle multiplicities, the TPC drift volume contains a large number of positive ions that pile up due to the slow ion drift velocity. The ion pileup effect can lead to a significant accumulation of space charge. The resulting field distortions modify the electron drift lines, introducing drift field distortions that have to be corrected. The correction of space-charge distortions with sufficient precision is one of the major challenges within the TPC upgrade scheme. The goal is to keep the residual distortions (after calibration) at a level not significantly larger than the intrinsic resolution, i.e. a few hundred μm, as is achieved for the current TPC.

7.4.1 Space-charge sources

The ion pileup consists of the prompt contribution of the gas ionization by charged particles in the TPC drift volume and the delayed contribution due to ion backflow from the GEM readout system. In case of the upgraded TPC, the latter contribution is larger by a factor of 2ε on average, where ε is the number of

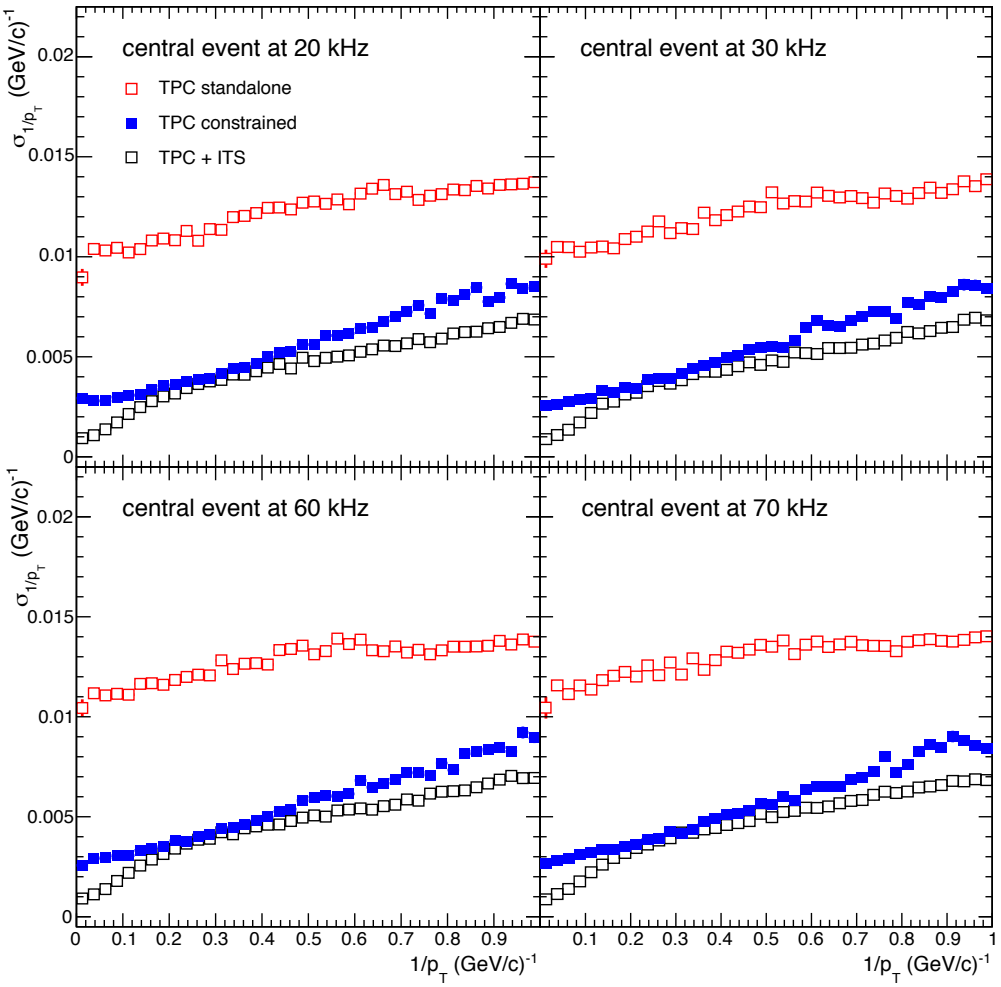

Figure 7.5: Resolution of $1/p_{\mathrm{T}}$ as a function of $1/p_{\mathrm{T}}$ for GEM readout. In the simulated data central events ($\langle \mathrm{d}N_{\mathrm{ch}}/\mathrm{d}\eta \rangle$ scaled to 2000) are embedded in a background of minimum bias events ($\langle \mathrm{d}N_{\mathrm{ch}}/\mathrm{d}\eta \rangle$ scaled to 500) at different interaction rates.

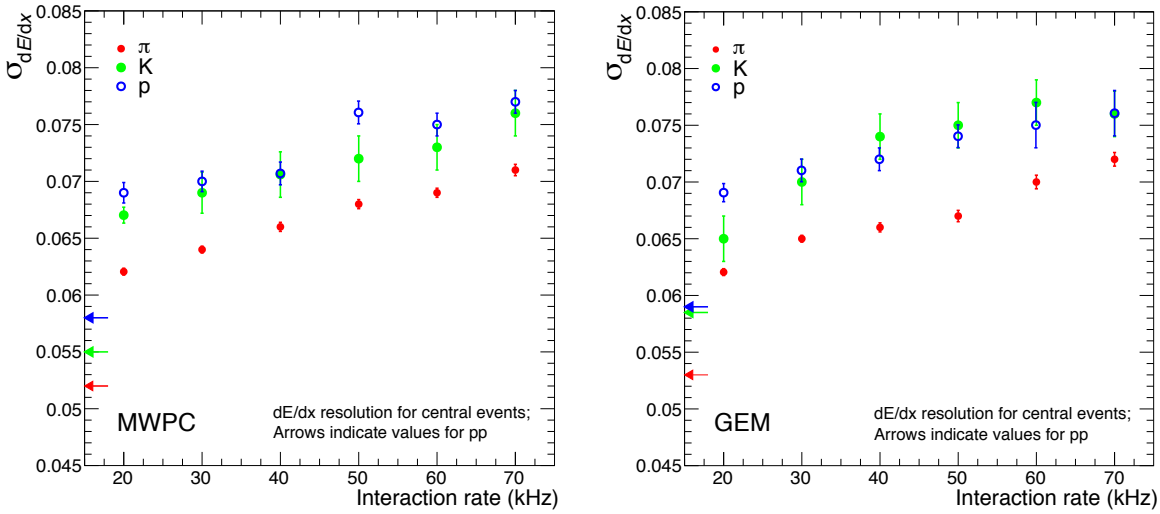

Figure 7.6: $\mathrm{d}E/\mathrm{d}x$ resolution for central events as a function of the interaction rate for MWPC (left panel) and GEM (right panel) readout. In the simulated data central events ($\langle \mathrm{d}N_{\mathrm{ch}}/\mathrm{d}\eta \rangle$ scaled to 2000) are embedded in a background of minimum bias events ($\langle \mathrm{d}N_{\mathrm{ch}}/\mathrm{d}\eta \rangle$ scaled to 500). Only tracks in the momentum range from 4 to 5 GeV/c are used.

ions drifting back into the TPC drift volume for each electron entering the multiplication region[6]. For a residual ion backflow of 1 % and an effective gain of 2000 the value of the ε parameter is 20.

The average space-charge density is proportional to ε, to the interaction rate $R_{\rm int}$ and to the ion drift time $t_{\rm d}^{\rm ion}$. For $R_{\rm int} = 50\,{\rm kHz}$ and $t_{\rm d}^{\rm ion} = 0.16\,{\rm s}$ the tracks of ~ 8000 interactions contribute to the ion pileup at any given moment.

The magnitude of the space-charge distortions can be calculated using parametrized charged particle density distributions under the assumption of certain symmetries:

$$\rho_{\rm sc}(r,z) = \frac{a - b\,z + c\,\varepsilon}{r^d}\,. \tag{7.1}$$

The resulting space-charge density map for $R_{\rm int} = 50\,{\rm kHz}$ and $\varepsilon = 20$ is shown in Fig. 7.7. The distribution is symmetric in φ and linear in z (due to the constant ion drift velocity[7]). From data we extract a radial dependence with a value of d between 1.5 and 2 (see Sec. 7.4.4). The small step at $z \approx 0$ is due to addditional background from the muon absorber on the C side.

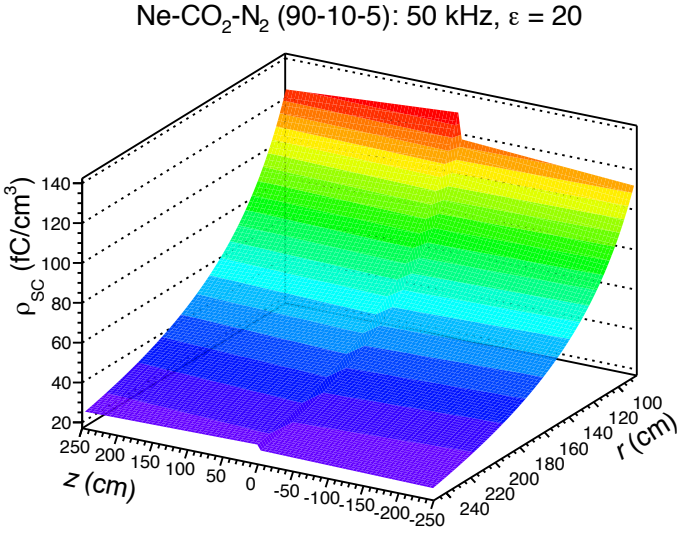

Figure 7.7: Average space charge density for Ne-CO_2-N_2 (90-10-5), $R_{\rm int} = 50\,{\rm kHz}$ and $\varepsilon = 20$.

7.4.2 Magnitude of the distortions

The magnitude of the space-charge distortions (without fluctuations) is calculated using parametrized space-charge density distributions as in Eq. (7.1). The resulting average distortions in r, $r\varphi$ and z directions are shown in Fig. 7.8.

The space charge has a focusing effect, forcing the drifting electrons to divert from the ideal drift path towards larger (smaller) radii at the inner (outer) field cage of the TPC. Moreover, the emerging radial electric field component in the presence of the magnetic field leads to distortions in $r\varphi$ due to the $E \times B$ effect. In general, the effect is strongest close to the central electrode ($|z| \approx 0$) and at the inner and outer field cage.

The magnitude of the distortions at the central electrode of the TPC (at $z \approx 0\,{\rm cm}$) is shown in Fig. 7.9. At the inner field cage the space-point distortions reach up to 19 cm in r direction and 7 cm in $r\varphi$ direction. However, in the largest part of the volume, the distortions are well below 10 cm. Distortions of similar

[6]The factor of 2 describes the average drift length difference for ions from primary ionization and ions from ion backflow.
[7]The average interaction rate is also constant on the short timescales considered here.

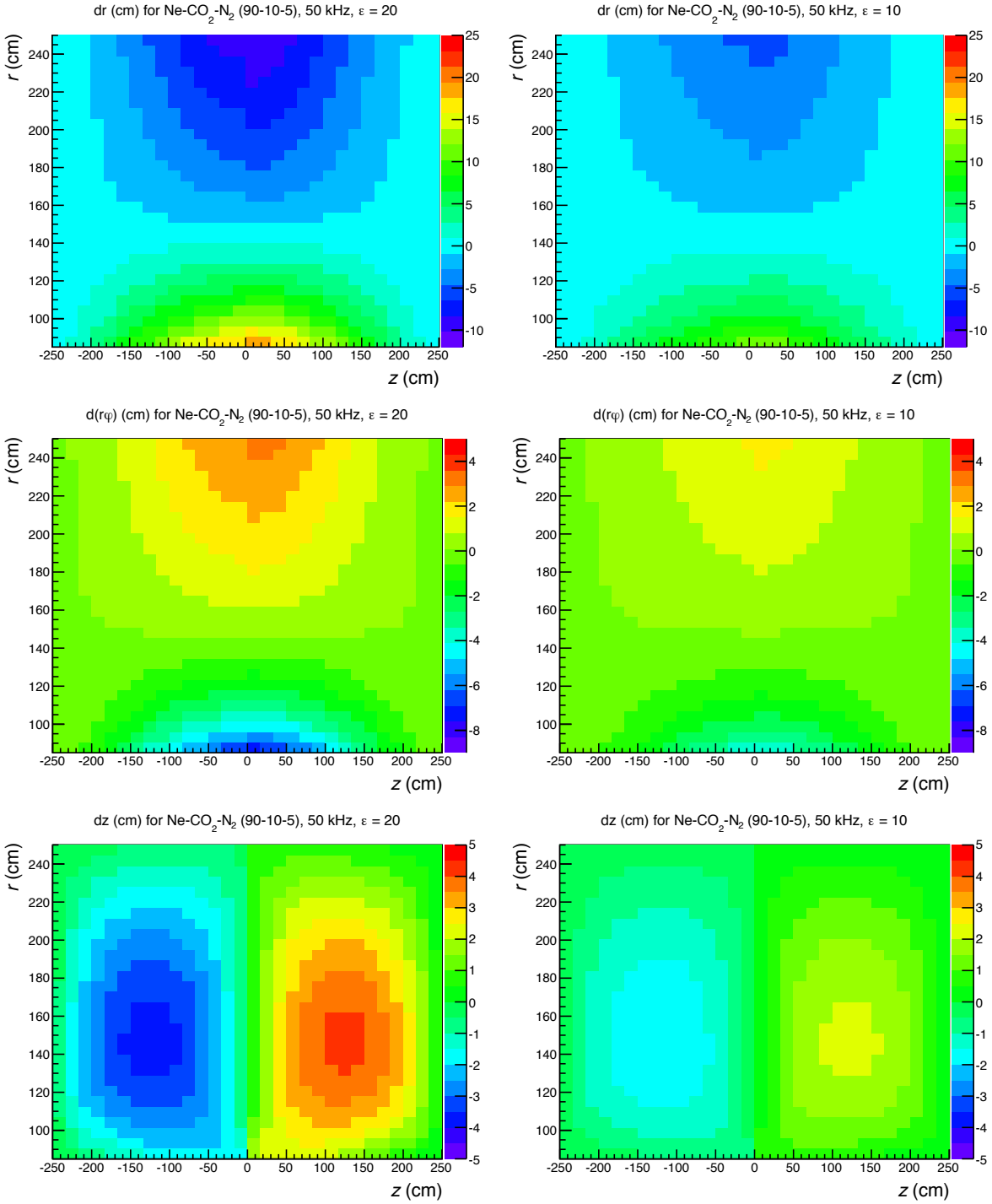

Figure 7.8: Space-point distortions in r (top panels), $r\varphi$ (center panels) and z (bottom panels) for Ne-CO_2-N_2 (90-10-5), $R_{\text{int}} =$ 50 kHz and $\varepsilon = 20$ (left panels) and 10 (right panels). The data shows the integrated distortions for an electron originating at z, r as it drifts to the GEM readout at $z = \pm 250$ cm.

magnitude are encountered or expected in the near future in the TPC of the STAR experiment at RHIC [9, 10]. The distortions expected for the TPC considered for the PANDA experiment at FAIR [11] are smaller by an order of magnitude.

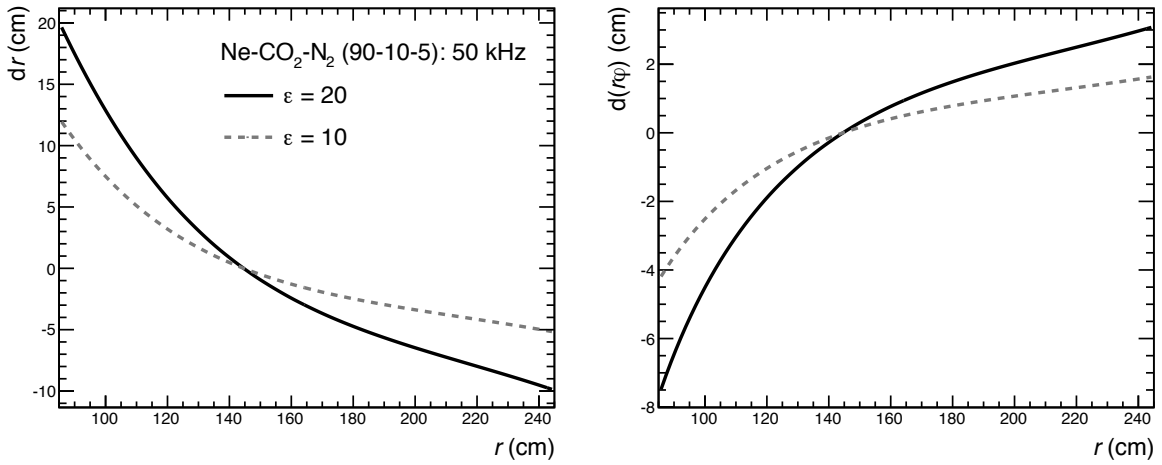

Figure 7.9: Space-point distortions in r (left panel) and $r\varphi$ (right panel) as a function of the radial position r close to the central electrode ($z \approx 0\,\text{cm}$) for Ne-CO_2-N_2 (90-10-5), $R_{\text{int}} = 50\,\text{kHz}$, $\varepsilon = 10$ and 20.

The space-charge distortions do not increase linearly with ε. A drifting electron will be deflected by the space-charge field towards regions with lower field gradients. The resulting saturation effect is shown in Fig. 7.10.

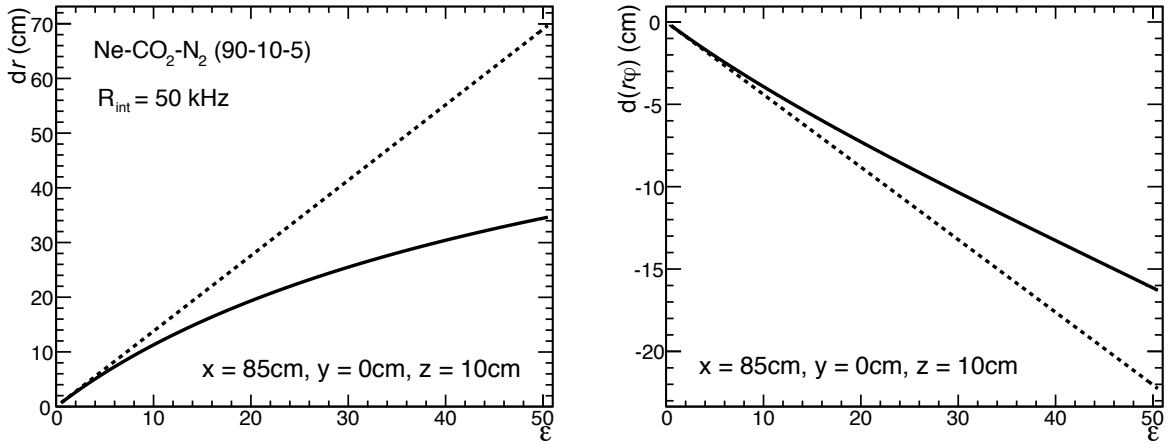

Figure 7.10: Space-point distortions in r (left panel) and $r\varphi$ (right panel) close to the central electrode ($z \approx 10\,\text{cm}$) and in the center of a readout chamber ($y = 0$) as a function of ε. The broken line is an eye guide representing linear increase with ε.

7.4.3 Simulation of the space-charge distortions

Equation (7.1) provides a straightforward solution to calculate the magnitude of the space-charge distortions. However, fluctuations in the space-charge density distribution are not taken into account. Consequently, it describes well a situation with the main contribution to the space-charge distribution coming from primary ionization ($\varepsilon \to 0$). In case of the upgraded ALICE TPC, however, the main contribution to the space-charge distribution arises from ion backflow. Here, the non-active regions along the sector boundaries together with local variations of gain and ε break the azimuthal symmetry. As we will see, also the fluctuations in the number of interactions per unit time, and in the charged track multiplicity

per event have to be considered, as they give rise to space-charge fluctuations along z. Each interaction actually creates a disc of slowly moving ions within the TPC volume, and the space charge density distribution at 50 kHz interaction rate consists of the superposition of ~ 8000 such disks with fluctuating density.

In the following, an detailed simulation procedure for space-charge distortions is described, that deals with these features. It consists of the following steps:

1. **Calculation of the space-charge density maps**: Detailed 3-dimensional average space-charge maps can be calculated without any symmetry assumptions utilizing real raw data from minimum bias Pb–Pb collisons from RUN 1. Appoximately 130,000 events were used for this purpose. The individual events are compressed along the z direction by a factor $t_{\mathrm{d}}/t_{\mathrm{d}}^{\mathrm{ion}}$ and superimposed with random positions along z. Moreover, space-charge maps for randomly selected groups of events are used to mimic the fluctuations of the space-charge distribution in space and time. A subset of 8000 events is needed to simulate an interaction rate of 50 kHz. The individual events are superimposed with random positions along the z direction with a spacing defined by the interaction rate and the ion drift velocity.

2. **Calculation of the space-charge field**: Based on the space-charge maps obtained in the previous step, the resulting electric field components are calculated. Taking into account the precision requirement and the granularity of the space charge, it is clear that the electric field has to be calculated in 3 dimensions and with high spatial granularity. In the following studies a granularity of 360 bins in $r\varphi$, 125 bins in z, and 158 bins in r is used. A 3D electric field calculation is done using a customized implementation of the Poisson relaxation method [12]. The originally proposed analytical approach does not provide a 3D solution with sufficient spatial granularity.

3. **Calculation of the distortion maps**: The electric field deviations $\Delta\vec{E}$ based on ρ_{sc} can be computed by solving the inhomogeneous Laplace equation. This task is usually performed by solving the Poisson equation with the help of discrete numerical methods like Finite Elements as applied in STAR [9] and PANDA [11] or by using an analytical approach based on the Green's function as proposed for ALICE [13]. However, these approaches turn out to be not able to cope with the granularity requirements and instead the Poisson relaxation method is used.

   To compute the distortion maps as a function of the starting position of the drifting primary electron, the Langevin equation of motion for electrons in electric and magnetic fields is integrated along the drift line with a fourth-order Runge Kutta algorithm [14].

Repulsive electrostatic forces between the ions are not yet considered in this calculation.They will cause distortions of the ion drift path as well, which will lead to smoother space-charge distributions than those discussed in this TDR.

7.4.4 Space-charge density fluctuations

In this section we investigate the fluctuations of the space-charge density distribution using data obtained with the simulation method described in Sec. 7.4.3 and with an analytical formula for the expected fluctuations.

Features of the space-charge map distributions

Figure 7.11 shows the xy and rz projections of 2 example space-charge density maps and of the full analysed event sample of 130,000 events.

An almost regular sector modulation of the space charge due to the dead zones between the readout chambers is observed. Moreover, there is a step in the density distribution between the IROC and OROC

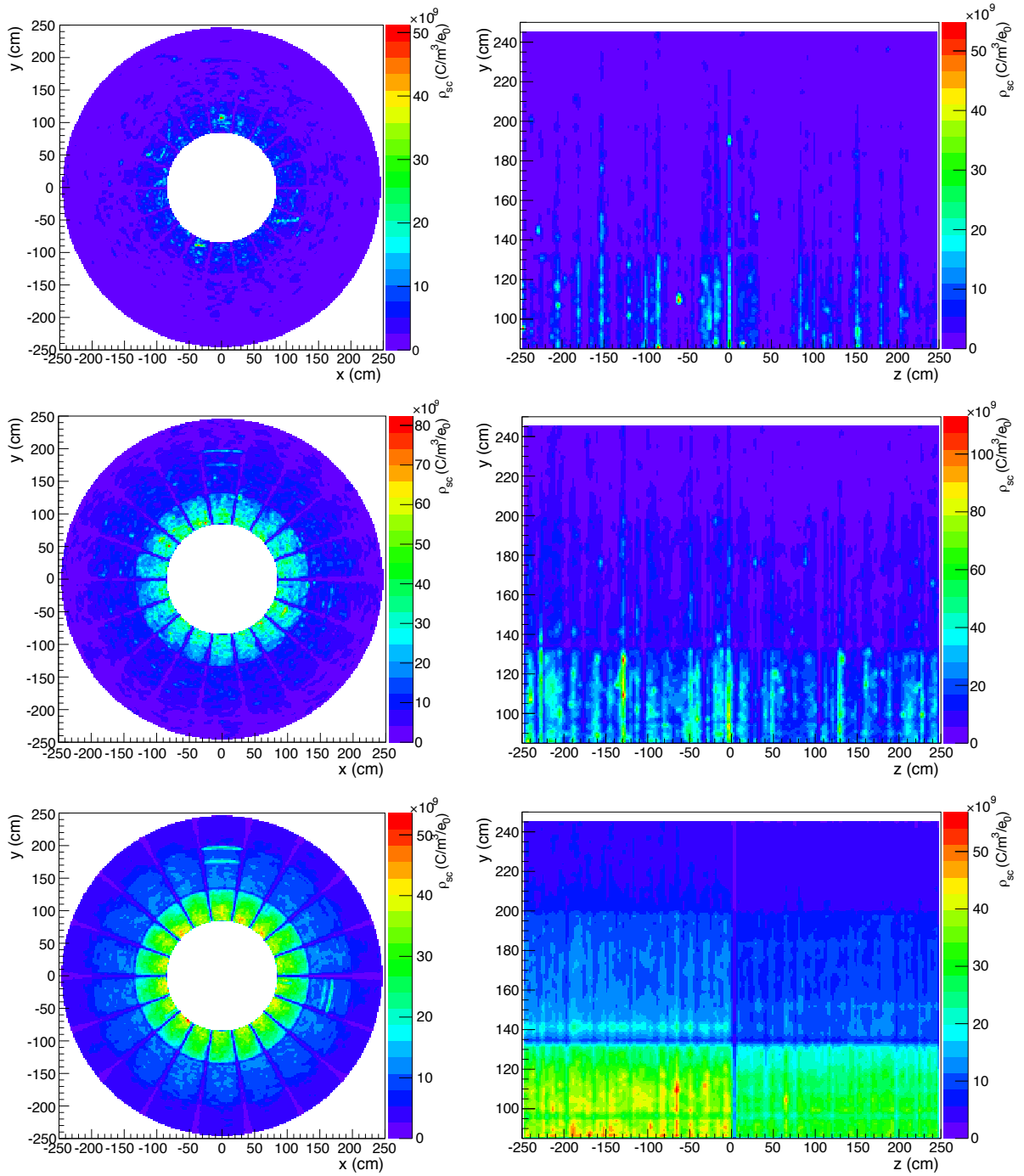

Figure 7.11: Calculated space-charge density maps for an ion pileup of 2000 (top row), 8000, and 130,000 (bottom row). The histograms are normalized to 10,000 ion pileup events. Left column: xy projection at $z = 10\,\text{cm}$. Right column: rz projection at $\varphi = 0.05$. In these plots on the horizonal axis the full drift length $|z| = z_{\text{roc}} = 250\,\text{cm}$ corresponds to the ion drift time $t_{\text{d}}^{\text{ion}} = 0.16\,\text{s}$. The data is based on the superposition of minimum bias Pb–Pb collisions recorded in RUN 1. The increased charge density in a few sectors at certain radial positions is explained by a few floating wires in the MWPC readout system used in RUN 1, which increase the local gas gain.

regions, caused by the systematically different gas gain applied in order to keep the same signal-to-noise ratio in these two regions with different pad and wire geometry. An $r^{-1.5}$-scaling is found for the radial dependence in the full analysed event sample (130,000 events), in contrast to the r^{-2} scaling used by STAR [15].

Strong local variations of the space-charge density are observed. The effect is most pronounced in the z direction, where regions of high ion density corresponding to central events are clearly visible.

In Fig. 7.12 the expected $r\varphi$ distortion maps are shown without (left) and with (right) magnetic field. The figure illustrates the effect of a sector modulation that can be explained by the lower space-charge density close to the dead zones in between readout chambers. The positive ion charge attracts the drifting electrons towards the center of the readout chamber. In the setup with magnetic field the symmetry is broken due to the $E \times B$ effect. Consequently, the mean value of the distortion is shifted.

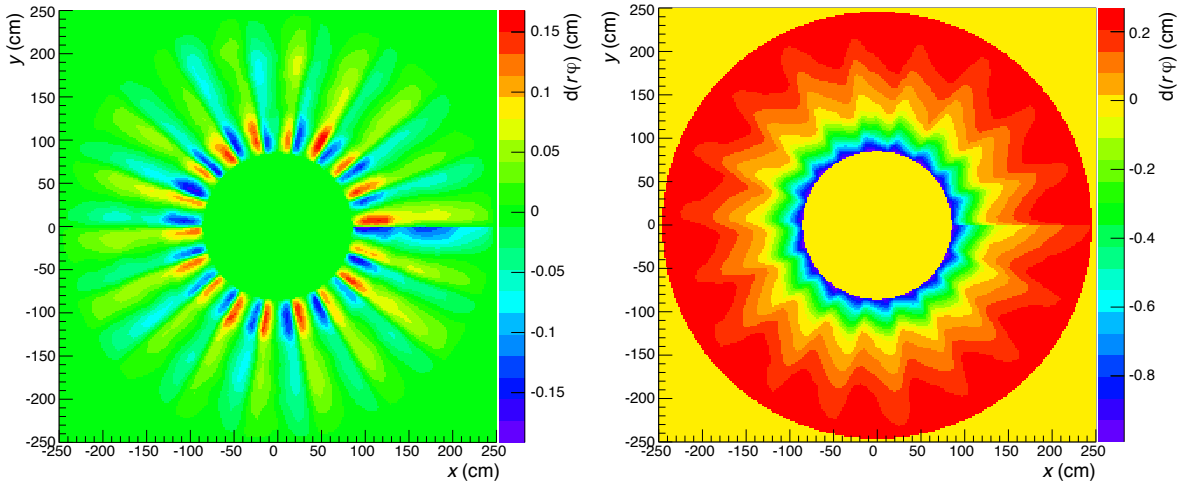

Figure 7.12: xy projection of the $r\varphi$ distortion map close to the TPC central electrode (at $z = 10\,\text{cm}$). The data are based on a detailed 3-dimensional space charge map normalized to $\varepsilon = 5$ (in order to avoid complications due to non-linearities). The figures illustrate the effect of a sector modulation that is modified by the magnetic field, which is set to $B = 0\,\text{T}$ (left) and $B = 0.5\,\text{T}$ (right).

Contributions to the space-charge fluctuations

The average number of interactions contributing to the ion pileup in the TPC drift volume is $N^{\text{ion}}_{\text{pileup}} \approx 8000$. The actual number of interactions is described by a Poissonian distribution around this mean value. The relative fluctuation of the space-charge density $\sigma_{\text{sc}}/\mu_{\text{sc}}$, where $\mu_{\text{sc}} = \langle \rho_{\text{sc}} \rangle$ is the average space-charge density, can then be written as:

$$\frac{\sigma_{\text{sc}}}{\mu_{\text{sc}}} = \frac{1}{\sqrt{N^{\text{ion}}_{\text{pileup}}}} \sqrt{1 + \left(\frac{\sigma_{N_{mult}}}{\mu_{N_{mult}}}\right)^2 + \frac{1}{F\,\mu_{N_{mult}}} \left(1 + \left(\frac{\sigma_{Qtrack}}{\mu_{Qtrack}}\right)^2\right)} \,. \tag{7.2}$$

The relative fluctuation of the space-charge density depends on three contributions:

1. $1/\sqrt{N^{\text{ion}}_{\text{pileup}}} \approx 1.1\,\%$ is the relative fluctuation of the number of ion pileup events. Already this contribution is larger than the required precision of a few ‰.
2. $\frac{\sigma_{N_{\text{mult}}}}{\mu_{N_{\text{mult}}}} \approx 1.4\,\%$ is the relative RMS of the multiplicity distribution.
3. $\frac{\sigma_{Qtrack}}{\mu_{Qtrack}} \approx 1.7\,\%$ is the relative variation of the ionization of a single track.

F is a geometrical factor describing the spatial range over which the space-charge fluctuations are relevant for the distortions. To describe the fluctuation in the space-point distortions, the relevant scale is determined by the range of the Coulomb interaction.

A fast Monte Carlo (MC) simulation has been developed in order to estimate the contributions to the space-charge fluctuations (events, tracks and charge). The result is shown in Fig. 7.13. Here, subvolumes of 10 % of the size of a TPC sector are considered.

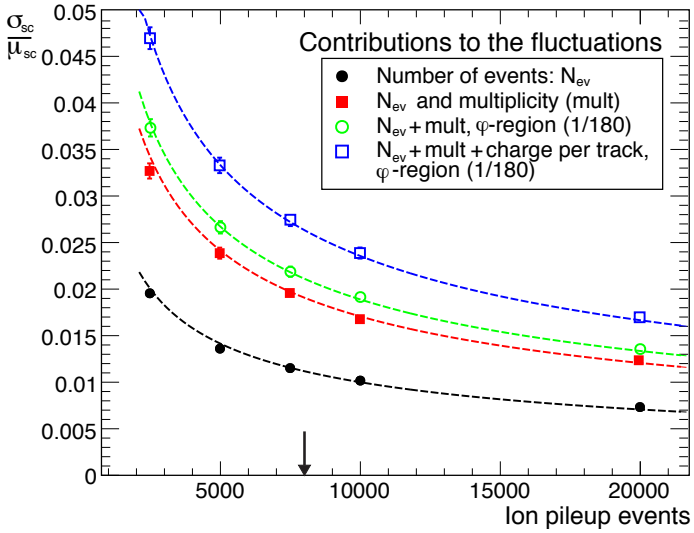

Figure 7.13: Relative fluctuation of the number of events, tracks and energy deposit (charge) from a MC simulation compared to expectations based on Eq. (7.2) as a function of $N^{\text{ion}}_{\text{pileup}}$.

The RMS of the space-charge fluctuations as obtained from the fast MC algorithm agrees well with the expectations from the analytical formula, Eq. (7.2), for fluctuations of the number of events, number of tracks (a Poissonian convoluted with the multiplicity distribution) and energy deposit. The relative fluctuation scales with $1/\sqrt{N^{\text{ion}}_{\text{pileup}}}$. Depending on the spatial granularity, the relative fluctuation is around $2-3$ % for $N^{\text{ion}}_{\text{pileup}} = 8000$. This result agrees well with the observations for the fluctuations of the charge density reported in Sec. 7.4.3 and the fluctuations on the track level (see Sec. 7.4.5).

7.4.5 Impact of the fluctuations on the distortion corrections

To estimate the effect of fluctuations on the space-charge distortion corrections, 50 different space-charge configurations are created. By random superposition of real Pb–Pb events, the number of ion pileup events $N^{\text{ion}}_{\text{pileup}}$ is varied between 2000 and 8000 in order to study different magnitudes of the ion pileup.

For each space-charge configuration, the distortion maps are calculated. The distorted tracks are corrected using an *average map* based on the full sample of 130,000 interactions, that is normalized to the corresponding $N^{\text{ion}}_{\text{pileup}}$. The $r\varphi$ position of the tracks after correction is compared to that of undistorted tracks. While the correction works well on average, there is a considerable spread. The RMS of this spread as shown in Fig. 7.14 is characteristic for the expected space-charge fluctuations. For tracks with $p_{\text{T}} > 1\,\text{GeV}/c$ the residual distortions yield up to ~ 2.8 mm, which is significantly larger than the intrinsic resolution limit σ_{intr}.

Finally, we demonstrate the importance of the knowledge of the z distribution of the space charge and estimate the frequency by which the space-charge distortion map needs to be updated. To this end, the following procedure is carried out:

1. The space-points of the TPC tracks are modified using a given distortion map.

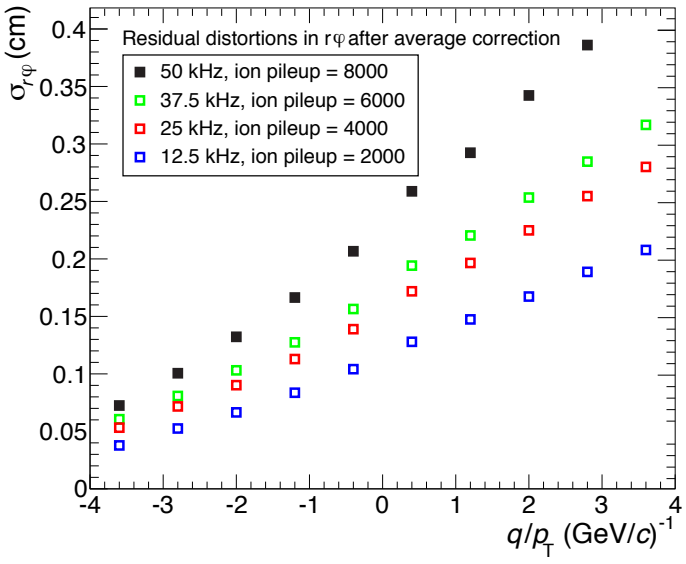

Figure 7.14: Residual $r\varphi$ distortions as function of rigidity q/p_{T} after correction using an average space-charge distortion map (full sample of 130,000 interactions to the corresponding multiplicity). The asymmetry between positive and negative rigidity is related to the sector modulation effect, caused by the lower space-charge density close to the dead zones between readout chambers, as shown in Fig. 7.12 (right).

2. A second distortion map using the same space-charge density distribution, but shifted in z direction, is used for correction: $\rho_2(x,y,z') = \rho_1(x,y,z+\Delta_z)$.

The result of the correction is compared to the undistorted track position. The RMS of the observed residual distributions is shown in Fig. 7.15 as a function of $1/p_{\mathrm{T}}$. The residuals are increasing with Δ_z and saturate at the random limit which is comparable with Fig. 7.14. The results shown in Fig. 7.15 reach the intrinsic resolution limit of a few hundred μm already at effective displacements of $\Delta_z = 16$ cm, corresponding to an ion drift time of 10 ms. This defines the requirement to update the space-charge correction maps during the online calibration procedure after about 5 ms, as described in Chap. 8.

7.5 Performance with residual space-charge distortions

The large space-charge densities expected during the high luminosity running in RUN 3 create distortions which can locally exceed 10 cm, while being below that value in the largest part of the drift volume. In order to preserve the performance of the detector, the space-charge distortions have to be corrected with a precision comparable to the intrinsic track resolution, which is of the order of a few hundred μm. The implementation of a correction framework in the general calibration scheme is discussed in detail in the following Chap. 8.

Figure 7.16 shows the ITS-TPC matching effiency (left) as well as the transverse momentum resolution (right) obtained from a full MC, implementing the remaining residual space charge distortions after applying the calibration procedure described in Sec. 8.4 (“second reconstruction stage”).

The matching efficiency is above 95% for all momenta. For standalone TPC tracks (red), the p_{T} resolution is slightly worse than the one obtained without distortions (see also Fig. 7.5), while for TPC tracks constrained to the interaction vertex (blue) and tracks matched to the ITS (black) the performance is practically the same as for the ideal case without space-charge distortions.

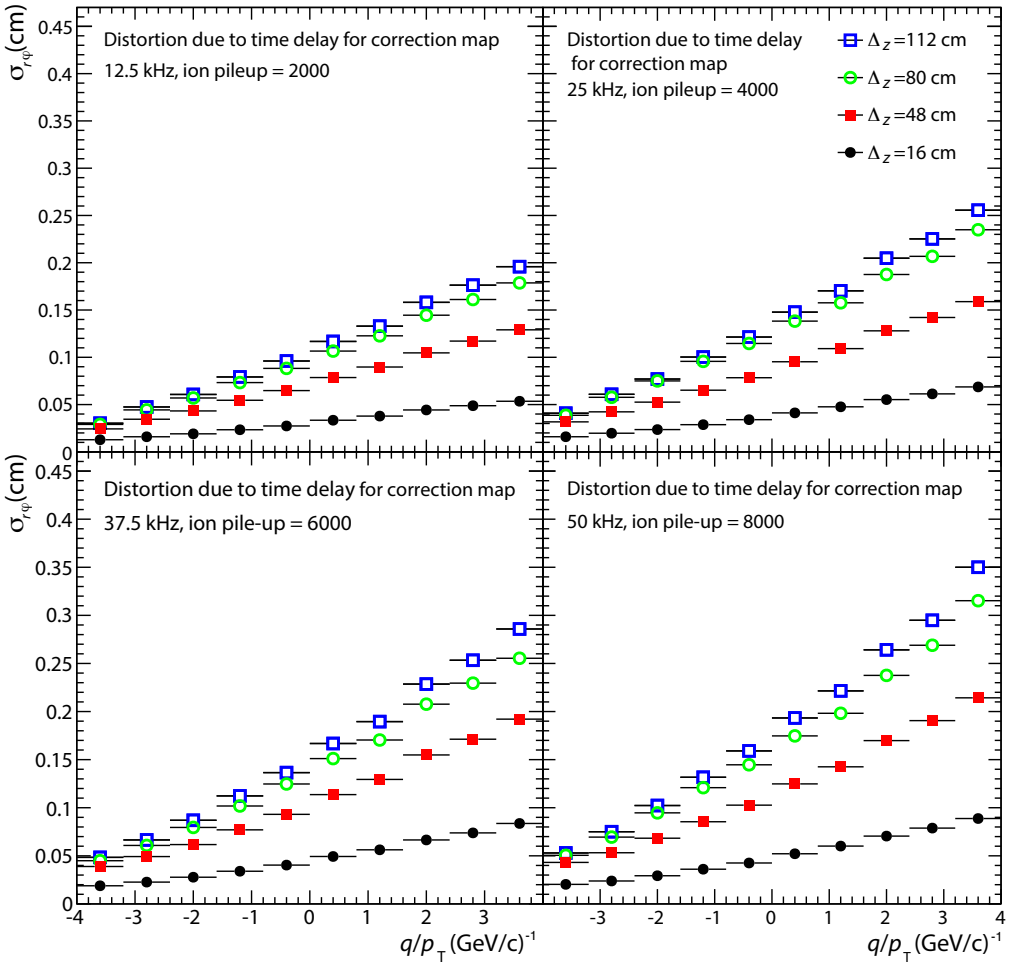

Figure 7.15: Residual $r\varphi$ distortions of the tracks. The space points are distorted using randomly selected raw data with ion pileup numbers of 2000, 4000, 6000 and 8000 and corrected using the same space-charge map but shifted by an offset Δ_z.

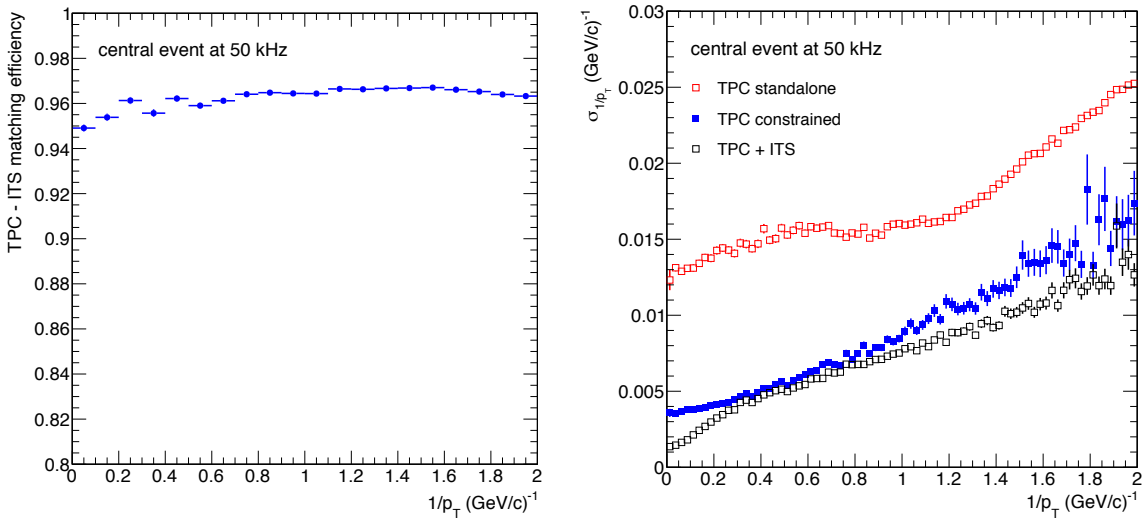

Figure 7.16: ITS-TPC track matching efficiency (left) and p_{T} resolution (right) with residual distortions after the second reconstruction stage.

Chapter 8

Online reconstruction, calibration, and monitoring

Operation of the TPC in a continuous readout mode in the high-luminosity environment at the LHC in RUN 3 will produce a vast amount of data. This necessitates a change of the ALICE computing model towards massive online reconstruction, because only in this way it is possible to achieve sufficient data reduction such that the data can be stored.

Efficient online cluster and track reconstruction implies that also a number of calibration steps need to be performed online. In particular, an online correction scheme for the space-point distortions induced by back-drifting ions must be applied to ensure efficient cluster-to-track association. Moreover, the online corrections have to be sufficiently precise to match TPC tracks efficiently to the external detectors ITS and TRD. If this can be achieved, a final calibration based on global tracks can be performed in a subsequent processing step.

8.1 Continuous TPC operation at high luminosities

The online reconstruction and calibration strategy is determined by the expected running conditions, defined by the LHC, as well as by the constraints given by the detector (continuous readout) and the online systems (need for data compression). In this section, the relevant operational conditions in RUN 3 are summarized and an overview of the general online reconstruction and calibration scheme is given.

8.1.1 LHC conditions in RUN 3

The expected running conditions in RUN 3 are defined by beam energy, luminosity and interaction rates, and interaction spacing.

Average interaction rates

During the first Pb–Pb run in November 2010 a peak luminosity of $\mathscr{L}_{\text{peak}} = 2.5 \cdot 10^{25}\,\text{cm}^{-2}\text{s}^{-1}$ and a hadronic interaction rate of $\sim$200 Hz was reached [1]. In the second Pb–Pb run in 2011 the peak luminosity reached $\mathscr{L}_{\text{peak}} = 4 \cdot 10^{26}\,\text{cm}^{-2}\text{s}^{-1}$ with a hadronic interaction rate of $\sim$3.5 kHz [2]. At the same time the readout rate was limited to a few hundred Hz by the readout speed of the current TPC electronics [3].

In RUN 3 the LHC will reach minimum bias hadronic interaction rates of $R_{\text{int}} = 50\,\text{kHz}$ in Pb–Pb collisions at the design center-of-mass energy of $\sqrt{s_{\text{NN}}} = 5.5\,\text{TeV}$, corresponding to a luminosity of $\mathscr{L} = 6 \cdot 10^{27}\,\text{cm}^{-2}\text{s}^{-1}$. For this TDR we assume a constant interaction rate of 50 kHz throughout a fill

of the LHC. An effective data-taking time of 10^6 s per year is assumed. This allows to collect a total integrated luminosity of at least $\mathscr{L}_{\text{int}} = 10\,\text{nb}^{-1}$ during RUN 3.

Beam structure and interaction spacing

A possible (simplified) LHC filling scheme for Pb-ions in RUN 3 consists of 12 equally-spaced bunch trains with 48 bunches each, leading to 576 bunches in each ring. The filling scheme and corresponding bunch train structure are depicted in Fig. 8.1.

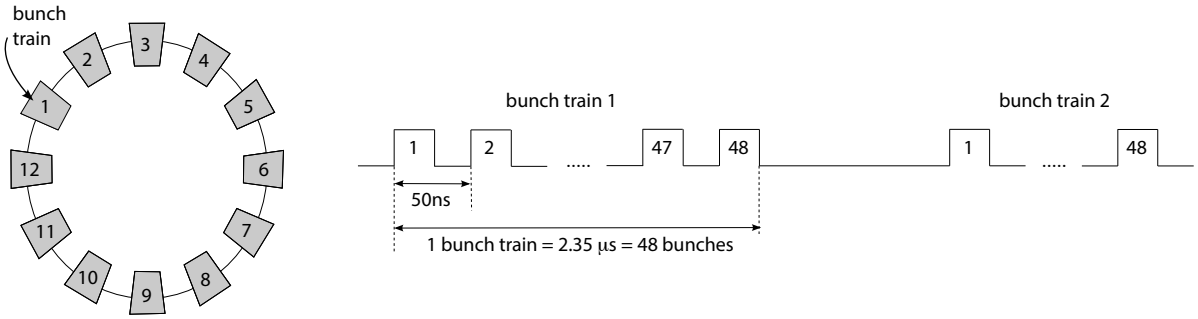

Figure 8.1: Schematic LHC filling scheme and bunch train structure.

When two bunch trains are passing, the instantaneous bunch-crossing rate is 20 MHz, while the average bunch-crossing rate is 6.3 MHz. The interaction rate of 50 kHz translates into a probability $\mu = 0.0079$ for a collision to occur in a single bunch crossing[1]. Therefore, the probability for at least one hadronic interaction (for more than one interaction) within one bunch train crossing (2.35 μs) is $\sim$32 % (resp. $\sim$5.5 %).

Event pileup

Event pileup in the TPC arises if more than one collision occurs within a time interval that corresponds to the maximum electron drift time, i.e. within $t_{\text{d}} \approx 100\,\mu$s. Even though the effect increases the detector occupancy, it does not complicate the pattern recognition significantly, as demonstrated in Sec. 7.3.

Not only the average number of pileup events is of importance, but also their spacing in time. At an interaction rate of 50 kHz on average $N_{\text{pileup}} = 5$ interactions are contained in a time interval t_{d}. The average spacing between two collisions is 20 μs or 52 cm of drift length. The distribution of time differences between two collisions is Poissonian with the bunch train structure of the LHC beam superimposed, as illustrated in Fig. 8.2. Following the argumentation of the previous section, in $\sim$17 % of the cases a second collision occurs within the same bunch train crossing, i.e. within 2.35 μs, corresponding to the first peak in Fig. 8.2. Separation of the tracks from two such collisions will be possible using external detector information, i.e. from the ITS.

Beam induced background

For colliding Pb beams in RUN 3 it is not expected that machine background contributes significantly to the charged track rates in the TPC. The beam currents ($\sim$85 mA) will not be large enough to trigger electron-cloud effects, which need at least 310 mA [4]. In the case of pp collisions, the beam currents will exceed the ones achieved in RUN 1, which were large enough to produce a background rate comparable to the interaction rate. However, several improvements are foreseen that should result in an improved background situation. These improvements include the replacement of the existing collimator at the end of the transfer line (TDI), which is now a major source of electron-cloud effects, the removal of bulky vacuum equipment near the ALICE interaction region, and the improvement of the vacuum at and near Interaction Point 2 (IP 2).

[1] $\mu = 50\,\text{kHz}/11\,\text{kHz}/576 = 0.0079$, with the LHC orbit frequency 11 kHz.

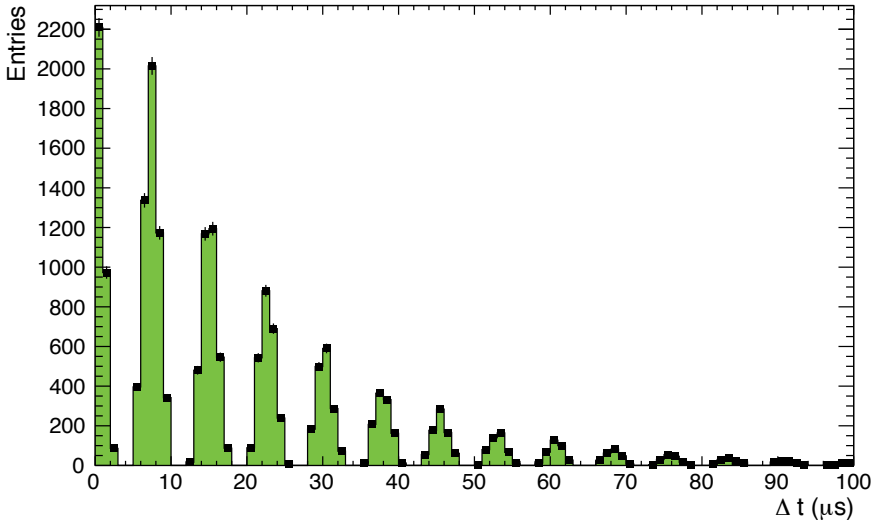

Figure 8.2: Distribution of time differences between two collisions at $R_{\mathrm{int}} = 50\,\mathrm{kHz}$. A Poissonian distribution is superimposed to the bunch train structure of the LHC beam.

8.1.2 TPC reconstruction, calibration, and data compression in RUN 3

The ALICE upgrade requires a major change of the computing concept in order to be able to process and store the large amount of data produced in Pb–Pb collisions. The main contributor to the data volume will be the TPC. Most of the data processing and reconstruction will be performed on the computing cluster of the new online systems [5]. New requirements to calibration and reconstruction algorithms emerge in terms of running stability, processing time, memory consumption, as well as parallelizability on different levels. These requirements build strict constraints on the data reconstruction and calibration, as well as on data compression. A massive use of hardware co-processors, such as FPGAs for the early processing steps, as well GPGPUs[2] for the later processing is foreseen.

Overview of the TPC reconstruction scheme

The choice of the reconstruction algorithms is strongly driven by the constraints of the online processing. However, in the discussion below we will focus on demonstrating the overall strategy and the general feasibility of online reconstruction under the operational conditions described above.

A two-stage process, as depicted in Fig. 8.3, is foreseen for the online data processing. The first stage (see below) will focus on cluster finding and the association of clusters to tracks, which are needed in order to perform the necessary data size reduction (see Sec. 8.3). The compressed data will be written to permanent storage. The reconstructed tracks have sufficient precision to allow matching to the external detectors, mainly ITS and TRD. This is needed to improve the quality of the subsequent calibration step during the next reconstruction stage.

The second reconstruction stage (see Sec. 8.4) will also be performed on the online computing cluster, but in an asynchronous mode, and can thus be repeated any time. It aims at a further improvement of the data quality, in particular in terms of the space-charge distortion calibrations, and employs information from external detectors as well as more refined calibration input.

[2] General-Purpose Graphics Processing Units (GPGPUs)

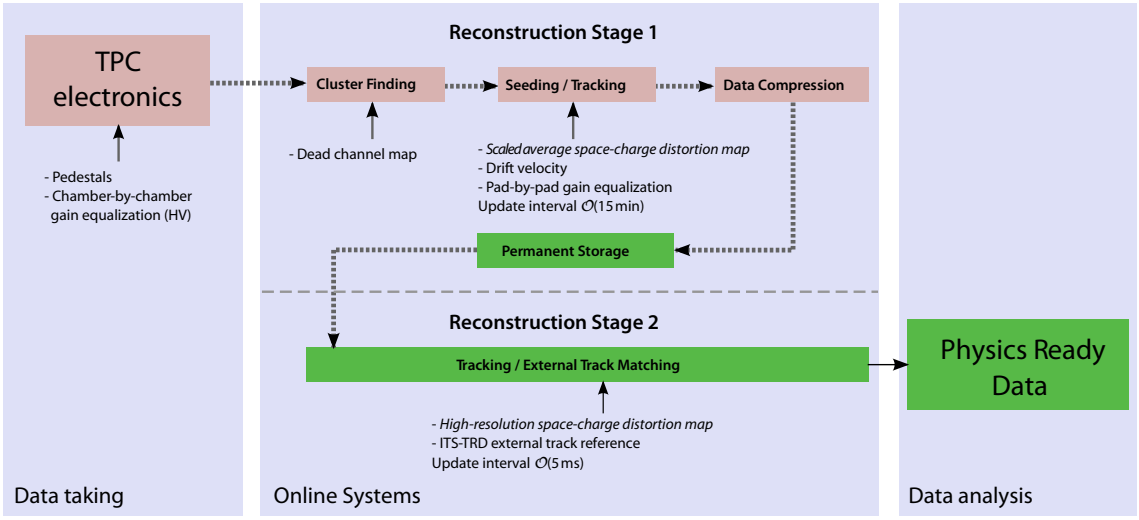

Figure 8.3: Schematic outline of the calibration flow during the data-taking and reconstruction process.

Data size and data compression

After zero suppression on the level of the front-end electronics, the average TPC raw data size in minimum bias Pb–Pb interactions is $\sim$20 MByte (see Sec. 6.3). Without any further compression applied, this would result in an input rate of about 1 TByte/s to the online systems at an interaction rate of 50 kHz, and a total amount of 3 EByte (10^{18} Byte) of TPC data recorded in RUN 3. Such numbers exceed the predicted available bandwidth and storage space by a large factor. Thus, in order to permit permanent data storage, additional compression on top of zero suppression to below 1 MByte per interaction is required. This can be achieved by different levels of pattern recognition that are performed in the online systems.

The zero-suppressed raw data are decoded at the input to the online farm, where the raw data digits (which consist of arrival time at the front-end electronics and signal amplitude) are associated with the corresponding geometrical position (pad row and pad coordinates). Cluster finding is performed on the digits, which produces three-dimensional charge clusters[3].

As the x_{ro} coordinate[4] is fixed by the well-separated pad rows, cluster finding is reduced to a two-dimensional problem in the pad–time plane. A two-dimensional algorithm, as used in the current TPC offline cluster finder, scans the pad–time plane for charge maxima using a sliding window. It allows a good separation of close-by clusters. A different method is based on a one-dimensional algorithm, as used in the current High Level Trigger (HLT) system. It processes the pads sequentially, which allows to find the maxima within neighboring pads on the same pad row. In this case the separation of close-by clusters is done separately in both dimensions. The algorithm allows massive parallelization and, therefore, an easy implementation into an FPGA[5]. It is the baseline solution for RUN 3, as it fits the necessity of an early data reduction already at the input to the online systems.

The cluster finding is accompanied by a further compression step based on intelligent Huffmann Coding [6] of selected parameters.

Such a compression scheme has already been applied to TPC data during the 2011 Pb–Pb data taking in RUN 1, resulting in a data compression factor of $\sim$4 as compared to zero-suppressed raw data (see Fig. 8.4). Further optimizations of the cluster data format and of the compression algorithm for RUN 3 will allow a total data reduction by a factor five to seven during the cluster finding step [5].

[3] Alternatively the cluster finding could also be performed on the Common Readout Unit (CRU) modules for the TPC.
[4] Details on the local and global coordinate system can be found in App. A.
[5] Field Programmable Gate Array (FPGA)

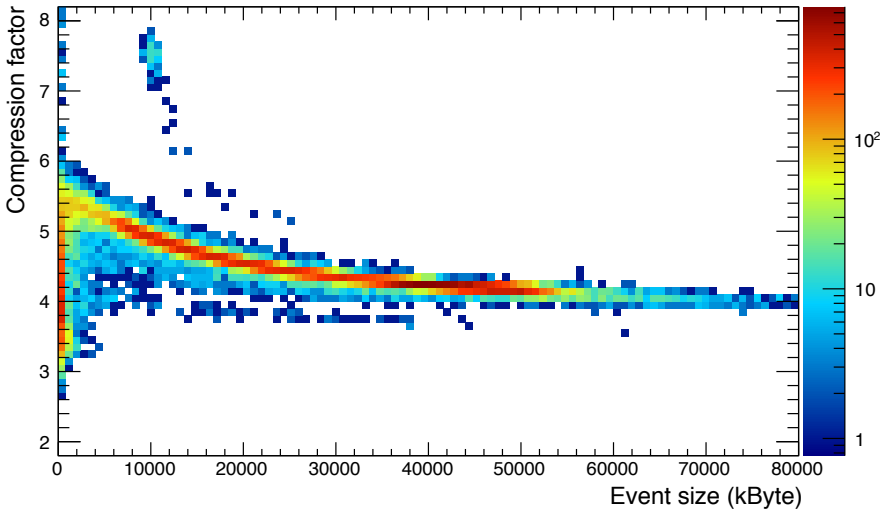

Figure 8.4: Data compression factor versus raw data size achieved using cluster finding and data-format optimizations in the High-Level Trigger during the Pb–Pb data taking in RUN 1. Adopted from [7].

A further reduction in data size can be performed by tracking, where clusters are assigned to particle tracks. This step, which is discussed in Sec. 8.3, allows to remove clusters that are not associated to physics tracks (e.g. from delta electrons or noise) from the data stream. The possible reduction factor, based on the experience from the past data taking in RUN 1, is of the order of two. The tracking step also enables more advanced transformation schemes to optimize the parameter distributions for entropy encoding as well as the possible replacement of some of the individual cluster parameters by track-based properties. We estimate the further reduction potential to be of the order of two to three.

In total, the envisaged compression factor in the online system is of the order 20, resulting in an average data size per interaction of less than 1 MByte. This will lead to a storage rate of $\sim$50 GByte/s and a total amount of $\sim$150 PByte of stored data during RUN 3. To store the cluster information associated to the reconstructed tracks is an advantage, allowing a possible re-calibration of individual clusters at a later stage and, therefore, an improvement of the TPC performance. A summary of the consecutive data compression factors is presented in Tab. 8.1.

Data Format	Data Compression Factor	Event Size (MByte)
Zero Suppression (FEE)		20
Clusterization	5-7	3
Remove clusters not associated to relevant tracks	2	1.5
Data format optimization	2-3	< 1

Table 8.1: The TPC event size and data compression factors for the different data compression steps performed in the front-end electronics and the online systems.

Online calibration

Online reconstruction implies that also calibration information must be available at run time. Since some of the calibration parameters change with time, the calibration information has to be retrieved and updated synchronously to the data collection process.

The calibration process is embedded in the two-stage reconstruction process, as schematically shown in Fig. 8.3. The calibration flow is described in the following. In the first reconstruction stage, the calibration needs to be precise enough to associate clusters to tracks in order to allow the data compression (see

Sec. 8.1.2). In the second reconstruction stage the calibration aims at providing the detector performance required for physics analysis[6].

1. Before the start of data taking, the front-end electronics need to be configured with the correct pedestal values and zero suppression thresholds for each readout channel (see also Sec. 6.4.8) and with the current map of active channels. These values are extracted from data recorded in special pedestal runs between LHC fills. The high voltage of the readout chambers is set such that the average gain of the chambers is equalized throughout the TPC. The settings are based on data obtained using the Krypton calibration method (see Sec. 8.6.1).

2. During data taking the cluster finder accesses the map of active channels in order to account for broken or malfunctioning readout equipment.

3. For the **first reconstruction stage** the relevant calibrations include drift velocity, effective gain, and space-charge distortions. The corresponding calibration parameters change with time and have to be updated in intervals of $\mathcal{O}(15\,\text{min})$, but also the static pad-by-pad equalization of the gain extracted using the Krypton calibration method is applied at this stage. An average space-charge map, updated in intervals $\mathcal{O}(15\,\text{min})$ as well, is used for a coarse space-charge distortion correction. It accounts for slow variations of the luminosity, pressure and temperature and for malfunctioning sectors. To improve the precision for use during the first reconstruction stage, the average space-charge map is scaled by the actual charged-particle multiplicity integrated over the preceding 160 ms, i.e. the maximum ion drift time in the TPC. This scaling procedure is based on a running integral of TPC current and amplitude information over the corresponding time window and reduces significantly the error due to temporal ion density fluctuations in the TPC.

4. During the **second reconstruction stage** a high-resolution distortion correction map is derived to achieve the required momentum resolution. The final distortion correction is based on external reference tracks using information from ITS and TRD and combines them with the space-charge information based on TPC clusters with high granularity in space and time. According to the typical time scales of space-charge fluctuations (see Sec. 7.4.5) the final distortion correction map must be determined in time intervals of a few ms.

8.2 Space-charge distortion corrections

The largest contribution to drift distortions in the GEM TPC are due to the accumulation of space charge in the drift volume. The magnitude and implications of such distortions are described in detail in Sec. 7.4. Below we describe how distortions due to space charge are treated when the TPC is operated in continuous readout, discuss how distortion corrections are obtained, and describe different levels of precision that can be reached depending on the available calibration input.

8.2.1 TPC coordinate transformation

Each TPC raw data digit consists of a geometrical position at the readout plane (pad row and pad coordinates), the arrival time at the front-end electronics (t_{digit}) and the corresponding signal amplitude. Charge clusters usually spread over a few pads and time bins, and the center-of-mass of a charge cluster corresponds to a three-dimensional space point $\vec{r}_{\text{cls}} = (x, y, z)$. The proper assignment of $\vec{r}_{\text{cls}}$ requires a precise knowledge of the drift time t_{d} of the cluster:

$$\vec{r}_{\text{cls}} = \vec{r}_{\text{ro}} + \int_0^{-t_{\text{d}}} \vec{v}_{\text{d}}(x, y, z)\, \mathrm{d}t \ , \tag{8.1}$$

[6]The achievable TPC performance is discussed in detail in Chap. 7.

where $\vec{v}_{\rm d}$ is the drift velocity vector of electrons in the TPC and $\vec{r}_{\rm ro} = (x_{\rm ro}, y_{\rm ro}, z_{\rm roc})$ is the position of the center-of-mass of the charge cluster at the readout plane ($z_{\rm roc}$ is the z-position of the read-out chamber). Neglecting distortions, i.e. for $\vec{v}_{\rm d} = (0,0,v_{\rm d})$, Eq. (8.1) translates into

$$\vec{r}_{\rm cls} = (x_{ro},\ y_{ro},\ z_{\rm roc} - v_{\rm d} t_{\rm d}) \ . \tag{8.2}$$

In a triggered readout mode there is a strict relation between $t_{\rm digit}$ and $t_{\rm d}$,

$$t_{\rm d} = t_{\rm digit} - t_0 \ , \tag{8.3}$$

where t_0 is the time of the interaction that triggers the readout. In data aquired with a TPC in continuous readout mode the important parameter t_0 is a priori unknown, but can be derived using the information from external detectors. However, even in a TPC standalone tracking scheme without external detector information, t_0 can be estimated by extrapolation of track segments to $x = y = 0$, as discussed in Sec. 8.5.1.

8.2.2 Space point corrections

In practice, the drift velocity vector is approximated by $\vec{v}_{\rm d} = (0,0,v_{\rm d})$ and drift-field distortions, i.e. the effect of non-vanishing $v_{\rm x}$ and $v_{\rm y}$ are treated by effective corrections:

$$\vec{r}_{\rm cls} = (x_{\rm ro}, y_{\rm ro}, z_{\rm ro}) + \vec{\Delta}(x_{\rm ro}, y_{\rm ro}, z_{\rm ro}) \ , \tag{8.4}$$

with $z_{\rm ro} = z_{\rm roc} - v_{\rm d} t_{\rm d}$ and the drift time $t_{\rm d} = t_{\rm digit} - t_0$ (see Eq. (8.3)).

Numerical as well as analytical calculations of $\vec{\Delta}$ are based on the knowledge of the density distribution of the space charge ($\rho_{\rm sc}$), as described in 7.4.3. Such maps are available with different levels of precision as described below.

8.2.3 Space-charge density maps

During the two reconstruction stages, estimates of the current space charge distribution with different precision and granularity are used for distortion correction.

- The **reference map** $\rho_{\rm ref}$ can be obtained from simulations. It is based on the geometric acceptance of the readout chambers (incorporating non-active regions at the sector boundaries), dead regions of the GEM system and the known variations of gain and ε, the number of back-drifting ions per primary electron. This map can serve as an input at the startup of the data taking.

- The **average map** $\rho_{\rm av}$, updated several times per fill, accounts for slow variations of luminosity, ambient conditions and readout chamber status. It can be derived for example from an external, high-$p_{\rm T}$ track sample ($\mathcal{O}$(1 min) statistics).

For the first reconstruction stage, space point corrections at the level of the single cluster resolution ($\mathcal{O}$(mm)) are sufficient in order to perform the cluster-to-track association. The second reconstruction stage aims at reaching the intrinsic performance of the detector, therefore requiring effective residual space-charge distortions at the level of the intrinsic track resolution of a few 100 μm in $r\varphi$. At both stages space-charge maps with better precision, including also the effect of fluctuations, are necessary.

- The **scaled average map** ρ_{scaled} is based on ρ_{av}, but scaled by the instantaneous ion current during the last $t_{\text{d}}^{\text{ion}} = 160\,\text{ms}$. This covers the largest part ($\sim 2\,\%$) of the space-charge fluctuations (see also Fig. 7.14), which are the contributions due to fluctuations in the number of ion pileup events[7] and the fluctuations in the track multiplicity (centrality). These parameters are accessible online through external detectors (collision counter, centrality measure) or from the TPC (r and $r\varphi$ averaged signal charges or GEM currents).

- The **high-resolution map** $\rho_{\text{high-res}}$ also contains topological fluctuations in r and $r\varphi$, which are responsible for the remaining fluctuations of the space charge of $\sim 1\,\%$. It can be obtained by the calibration of TPC cluster residuals with respect to a track interpolation from the ITS and TRD detectors, as described in Sec. 8.4.1

We aim at using ρ_{scaled} and $\rho_{\text{high-res}}$ for distortion corrections in the first and second reconstruction stage, respectively.

8.3 First reconstruction stage

Online reconstruction is necessary in order to achieve data compression by a factor of 20 as compared to the raw data size, and to allow for permanent storage of the data. Such compression factors can be achieved if the association of clusters to tracks can be performed online, which implies also the necessity for sufficient online correction of the space-charge distortions. In order to correct for these distortions using Eq. (8.4), an estimate for the time of the interaction t_0 is needed, such that the cluster arrival time t_{digit} can be related to the drift time t_{d} (see Sec. 8.2.1). The standard TPC offline tracking approach employs t_0 information from external trigger detectors and was used to study the expected performance of the first reconstruction stage, as described below.

8.3.1 Standard tracking approach

In this section we discuss the application of the standard TPC tracking algorithm in the first online reconstruction stage, where t_0 information from external trigger detectors is used. In this tracking scheme, distortion corrections are applied to all clusters found within a time interval $(t_{0,i},\, t_{0,i} + t_{\text{d}})$, where $t_{0,i}$ is the time of the interaction i, which is recorded in a trigger detector. Here, we assume that all clusters found within this time interval emerge from the interaction with collision time $t_{0,i}$. The distortion correction is performed by employing the scaled average map ρ_{scaled}. This implies that residual distortions due to fluctuations on the level of a few percent of the initial distortions will remain. For those clusters which belong to tracks from the interaction at time $t_{0,i}$, such residual distortions may reach up to a few mm. Clusters from interactions which occurred not at $t_{0,i}$ are not properly corrected due to the improper drift time assumption and form background to this interaction. After tracking of interaction i is finished, the procedure is repeated for interaction $i+1$ at time $t_{0,i+1}$.

8.3.2 Performance using corrections from the scaled average map

The performance of the tracking algorithm in this approach is studied using the full microscopic simulation chain described in Sec. 7.3. Residual distortions as expected after correction with ρ_{scaled} are imposed to the clusters in the simulation. The space charge is described using the data-driven description given in Sec. 7.4, assuming $\varepsilon = 20$.

Figure 8.5 shows a comparison of the TPC tracking efficiency (left) and the TPC-ITS matching efficiency (right) without and with space charge distortions. Even with residual distortions applying corrections

[7] The number of ion pileup events during $t_{\text{d}}^{\text{ion}}$ is described by a Poissonian with mean $N_{\text{pileup}}^{\text{ion}} = R_{\text{int}}\, t_{\text{d}}^{\text{ion}} \approx 8000$ at $R_{\text{int}} = 50\,\text{kHz}$.

from the scaled average map (red points), i.e. in the first reconstruction stage, the efficiency of the TPC tracking is not affected compared to the ideal case without distortions (blue points). The TPC-ITS matching efficiency is lower by about 5% at high p_{T} and 2% at low p_{T} (0.5 GeV). This slightly lower efficiency does not affect the requirements of the calibration, though, and is recovered in the second reconstruction stage (black points) described in Sec. 8.4.

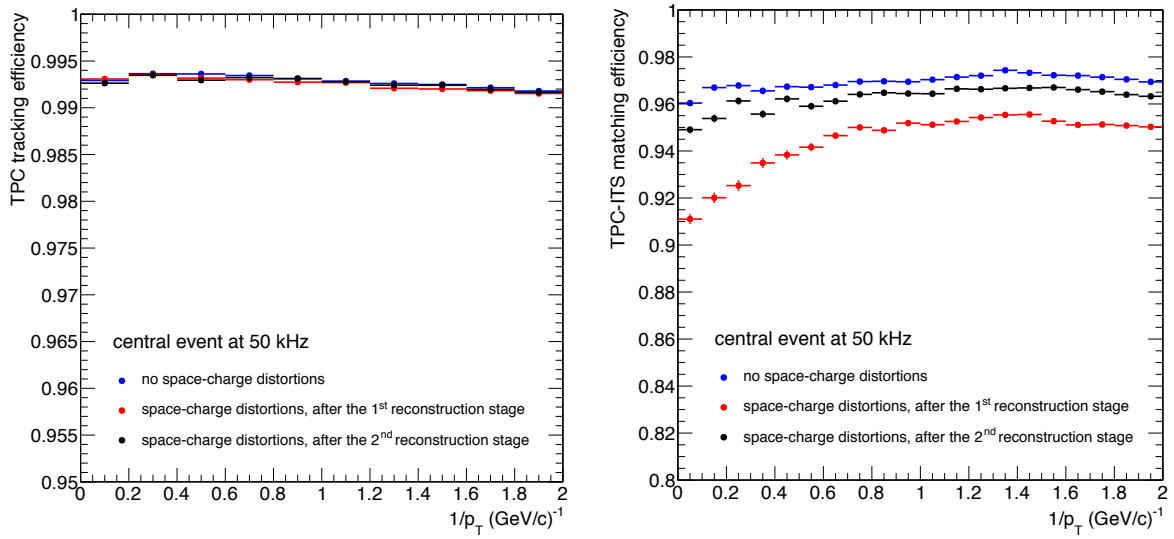

Figure 8.5: TPC track reconstruction efficiency (left) and TPC-ITS track matching efficiency (right) in Pb–Pb collisions at 50 kHz without distortions and with residual distortions after the first and second reconstruction stage.

The fraction of assigned clusters, defined as the number of associated clusters divided by the maximum number of assignable clusters in the active region, is shown in Fig. 8.6. It is compared for the ideal case without distortions (blue points) and with residual distortions using the scaled average space-charge map (red points) or a high-resolution map (black points). There is no significant modification in the cluster association when residual distortions are present.

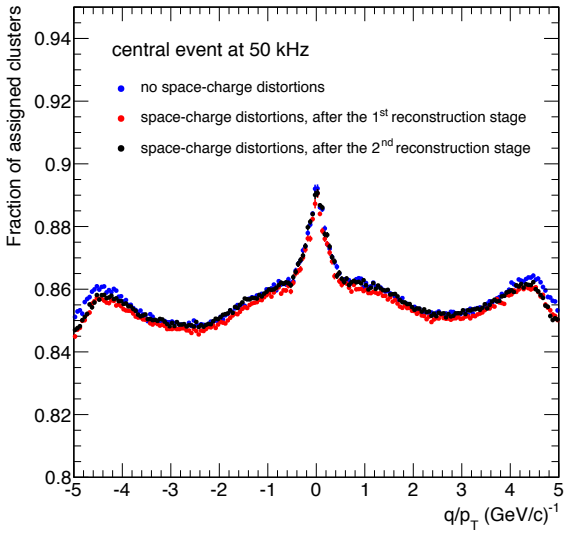

Figure 8.6: Cluster-to-track association efficiency in Pb–Pb collisions at 50 kHz without and with residual distortions using the scaled average map (first stage) and a high-granularity distortion correction (second stage).

This clearly demonstrates that space-charge corrections using time-averaged maps, scaled by the instantaneous ion density, provide sufficient precision for efficient online tracking and cluster-to-track asso-

ciation. This allows for powerful data compression and matching to the external detectors to perform high-granularity distortion corrections for the second reconstruction stage.

It should be noted that the procedure described above is not optimized in terms of computing speed. It implies multiple corrections of each cluster in the case of event pile-up, i.e. on average five times at 50 kHz. As a possible improvement, an alternative TPC standalone approach was developed, where an initial estimate of the collision time, t_0^{seed}, is derived from TPC track seeds. This procedure is described in Sec. 8.5.1.

8.4 Second reconstruction stage

The second reconstruction stage aims to restore the intrinsic detector resolution. Therefore, the main objective is to reduce the effective residual space-charge distortions to the level of the intrinsic track resolution of a few $100\,\mu$m in $r\varphi$. Essentially, this implies a correction of the remaining local space-charge fluctuations, which were not accounted for by the usage of the scaled average map ρ_{scaled} during the first reconstruction stage.

Such a residual miscalibration can be directly determined by measuring the TPC cluster residuals with respect to an external track reference obtained from interpolation between ITS and TRD track segments. This straightforward calibration procedure relies on the availability and proper calibration of those detectors. It is eventually limited by the available track statistics in a typical calibration interval. The procedure is described below.

8.4.1 ITS-TRD track interpolation approach

In this approach the TPC volume is subdivided into a number of volume elements ('voxels'). Each voxel is aligned by minimizing the mean residual of the TPC clusters within this voxel with respect to external reference tracks. The number of voxels must be sufficiently large to account for the local variations of the residual distortions with sufficient granularity. On the other hand, the voxel size determines the statistical precision that can be achieved within a typical calibration interval. For the present study a total number of 72,000 voxels in the TPC is assumed, corresponding to a voxel size of 10 cm, 16 cm and $1/72\,\pi$ in z, r, and $r\varphi$ direction, respectively. The optimization of the granularity is based on a detailed study of the residual distortion pattern after the first reconstruction stage. The required precision calls for a certain cluster statistics within a voxel. The resolution achieved from a single track within a voxel, σ_{vxl}, is given by

$$\sigma_{\text{vxl}} = \sqrt{\sigma_{\text{tr}}^2 + \left(\frac{\sigma_{\text{cl}}}{\sqrt{N_{\text{cl}}}}\right)^2}\,, \tag{8.5}$$

where σ_{tr} is the external track precision, σ_{cl} the local single cluster resolution, and N_{cl} the number of clusters of the track in the voxel.

Figure 8.7 shows the precision of external reference tracks in $r\varphi$ inside the TPC for momenta above $1\,\text{GeV}/c$ as a function of r, assuming perfectly aligned detectors. Extrapolation from the ITS and interpolation between ITS and TRD are shown on the upper and middle panel, respectively. The ITS extrapolation uncertainty ranges from <1 mm at the inner radius to ~ 1.5 cm at the outer radius of the TPC. For high-momentum tracks the extrapolation uncertainty is ≤ 1 mm for all radii. Using the ITS-TRD interpolation the precision is always better than ~ 0.8 mm for momenta above $1\,\text{GeV}/c$ and falls below $100\,\mu$m for high-momentum tracks.

The track interpolation approach was studied using a fast MC[8], assuming perfectly aligned detectors.

[8] Monte Carlo (MC)

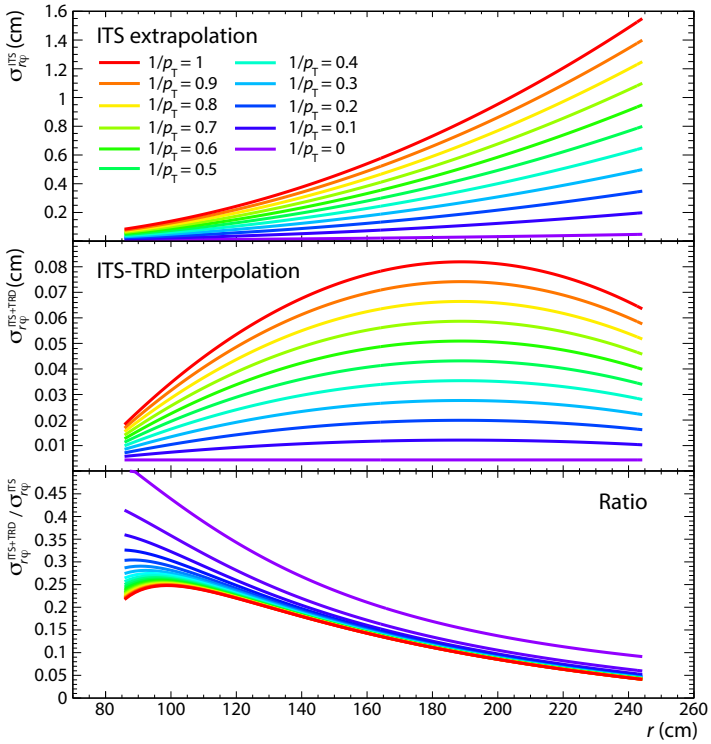

Figure 8.7: Precision of external tracks as a function of the radius inside the TPC. The color scale represents different values of $1/p_{\mathrm{T}}$. Top: Extrapolation error of ITS tracks; center: Interpolation error for ITS-TRD tracks; bottom: Ratio of the two.

In this MC, tracks from interactions at different t_0 are propagated through the detector, creating track points along their trajectory. Those track points are distorted according to the expected space-charge distortions for $\varepsilon = 20$ and smeared with the intrinsic cluster resolution (~ 1 mm in local-y and z). Typical space-charge density fluctuations are considered. In the reconstruction step, the distorted space points were corrected using the scaled average map ρ_{scaled}. A realistic parametrization of the charged-particle momentum distribution based on measurements was used to generate the tracks. The simulated track statistics corresponds to 5 ms of data taking at 50 kHz, i.e. tracks from 250 minimum bias Pb–Pb events. This corresponds to a typical calibration interval over which the space-charge density can be considered static (see Sec. 7.4.5). For the analysis only tracks reaching the TRD detector were used.

The measured local distortion $\mathrm{d}r\varphi'$ is correlated with the radial distortion $\mathrm{d}r$, if the track crosses the padrow under an inclination angle, see Fig. 8.8 (left). In this case, the true distortion $\mathrm{d}r\varphi$ and the radial distortion can be extracted employing a linear relation:

$$\mathrm{d}r\varphi' = \mathrm{d}r\varphi + \mathrm{d}r \cdot \tan\alpha \tag{8.6}$$

where α is the local track inclination angle. An example of such a fit is shown in Fig. 8.8 (right).

Figure 8.9 shows an example of the comparison between the measured residual distortions as determined by the ITS-TRD interpolation method (points) and the real residual distortions from MC (line). The comparison is shown in the region of smallest radius and largest drift length, i.e. $86 < r < 102$ cm and $0 < z < 10$ cm, where the residual distortions are largest. Each data point corresponds to the fit result in a single voxel and is used as a local correction to all space points within this voxel. The pattern of the residual distortions is well described by the interpolation method. The momentum resolution after application of this correction will be presented in Sec. 8.4.2.

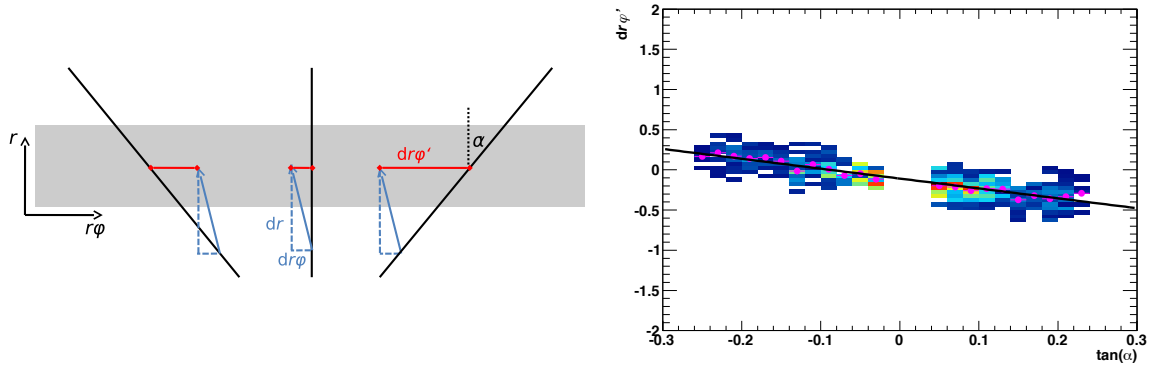

Figure 8.8: (Left) Illustration of the measured $r\varphi$ distortions being composed of the real $r\varphi$ distorions and the radial distortions, shown for three example tracks crossing a pad row (grey area) under different local track inclination angles α. (Right) Measured correlation between $\mathrm{d}r\varphi'$ and $\tan(\alpha)$ (see text).

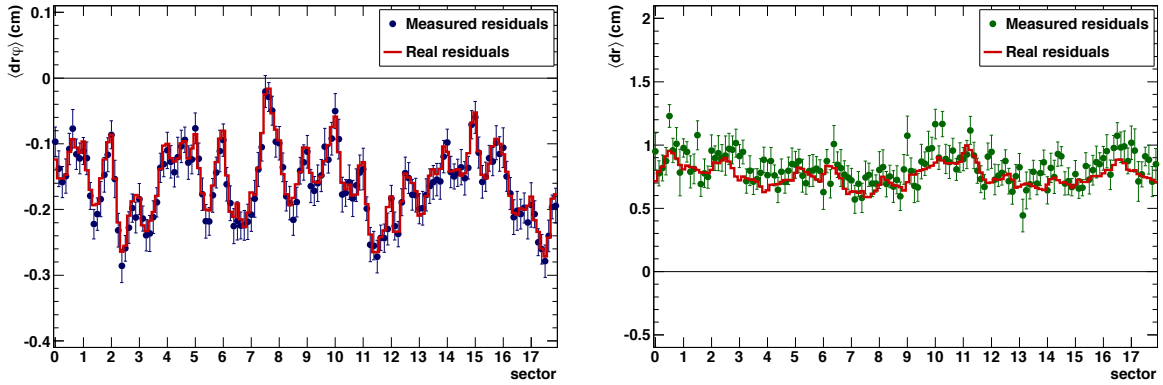

Figure 8.9: Comparison of measured and real residual distortions in $r\varphi$ (left) and r (right) for the region with the largest residual distortions ($86 < r < 102\,\mathrm{cm}$ and $0 < z < 10\,\mathrm{cm}$).

In Fig. 8.10 the resolution of the interpolation method is shown as the difference between the measured and the real residual distortions. The results are integrated over the full TPC acceptance.

In $r\varphi$ the remaining residual distortions are $\sim 300\,\mu\mathrm{m}$, i.e. compatible with the intrinsic track resolution. The remaining distortions in radial direction are $\sim 1.3\,\mathrm{mm}$.

It should be noted that the distortion vectors in nearby voxels are correlated. Exploiting the knowledge of the functional dependence of the residual distortions on variations of the space-charge density will allow to constrain the extracted distortion correction, and thus further improve the precision of the method and relax the required statistics per voxel.

In addition, the statistics at low radii, where the distortions are largest, can be enhanced by adding tracks that do not reach the TRD. By also using the ITS extrapolation method the precision of the measurement will be improved, in particular in this region.

8.4.2 Momentum resolution after residual correction

In order to verify the final tracking performance after application of the high-granularity corrections derived from the ITS-TRD interpolation method, the remaining residual distortions were mapped and used as input for the microscopic MC. The results presented in the following are for central Pb–Pb collisions at a minimum bias collision rate of 50 kHz.

Figure 8.5 (in Sec. 8.3.2) shows a comparison of the TPC tracking efficiency (left) and the TPC-ITS matching efficiency (right). The results are shown for the ideal scenario without space-charge distor-

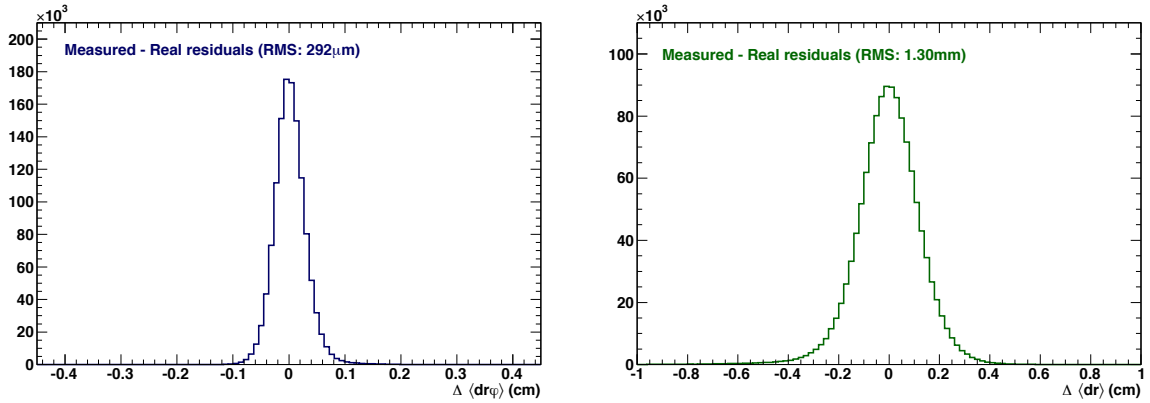

Figure 8.10: Distribution of measured minus real residual distortions for all fluctuation scenarios integrated over full acceptance of the TPC. (Left) $r\varphi$-distortions. (Right) r-distortions.

tions (blue points) and including the expected residual distortions after the first reconstruction stage (red points) and after the second reconstruction stage (black points), i.e. after application of the high-granularity corrections derived from the ITS-TRD interpolation method as described above.

The TPC tracking efficiency is not affected by the residual space-charge distortions, even when only the scaled average correction map is applied (first reconstruction stage). The TPC-ITS matching efficiency is about 1% lower compared to undistorted tracks, after application of the high-granularity space-charge corrections using the interpolation method. A better tuning, taking into account the measured residual distortions, will further improve the matching. For residual distortions as expected during the first reconstruction stage, the matching efficiency is further reduced, however this does not significantly affect the requirements for the subsequent calibration step in the second reconstruction stage.

Figure 8.11 shows a comparison of the transverse momentum resolution for undistorted tracks (left panel) as well as for tracks with residual distortions expected after the first (middle panel) and second reconstruction stage (right panel). After the first reconstruction stage, the residual distortions lead to a deterioration of the p_{T} resolution by about a factor $\sim 1.5-2$ as compared to the ideal case. A significant improvement is achieved after application of the corrections derived in the second reconstruction stage. While the TPC standalone resolution after the second stage is still somewhat lower than in the ideal case, the detector resolution of the undistorted case is practically fully restored if combined TPC-ITS tracks are considered.

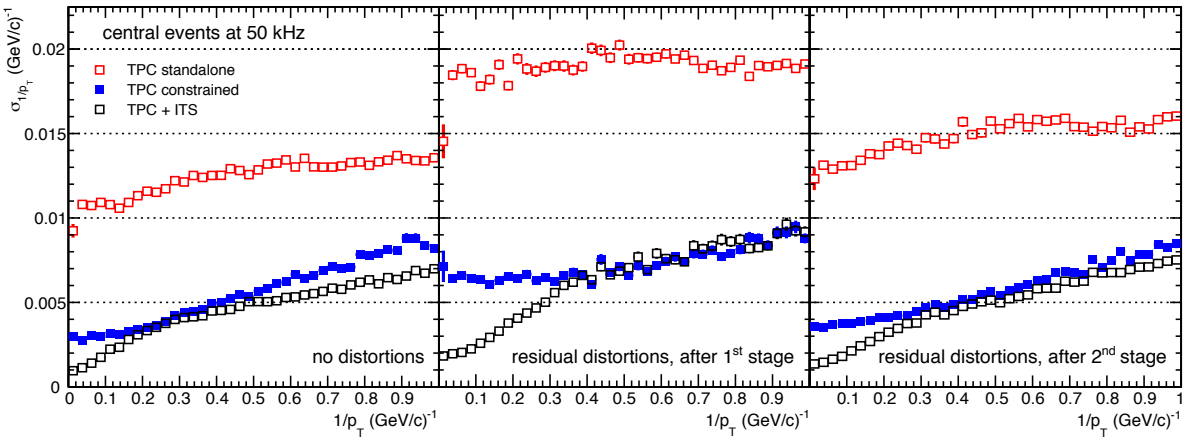

Figure 8.11: Comparison of the momentum resolution without distortions (left) and with residual distortions after the first (middle) and second (right) reconstruction stage in Pb–Pb collisions at 50 kHz.

In summary, the voxel alignment approach employing interpolation of track segments from the ITS and

TRD detectors provides a method to minimize the remaining residual distortions and to restore the detector performance without distortions. It is expected that further optimizations of the described method will improve the results. This includes further optimization of the voxel size to account for the radial dependence of the reference track resolution, of the hit density and of the residual distortion magnitude and variation. Further improvement is also expected by considering the correlations of the distortions in consecutive calibration time intervals. The current measurement approach described in Sec. 8.5.2 will lead to an improved description of the local space-charge density fluctuations. Application of such an improved space-charge map before the ITS-TRD interpolation method will considerably reduce the local variations of the distortions. This will allow for a larger voxel size and thus for an improved statistical precision of the correction.

8.5 Further optimizations

In addition to the studies presented above, further improvements of the online pattern recognition as well as the space-charge distortion correction can be achieved following the concepts described below.

8.5.1 TPC standalone tracking approach

In order to improve computational aspects of the online reconstruction, an alternative tracking approach which does not rely on t_0 information from external detectors was studied. To this end, a "fast" MC simulation was developed, that allows to vary the essential parameters and to develop and validate the reconstruction strategy. In this MC, tracks from interactions at different t_0 are propagated through the detector, creating track points along their trajectory. Those track points are distorted according to the expected space-charge distributions assuming 50 kHz Pb–Pb collisions and $\varepsilon = 20$ (see Sec. 7.4) and are smeared with the expected intrinsic cluster resolution (~ 1 mm in local-y and z).

Seeding

In this approach, seeding is the first online tracking step after the cluster finding. A track seed is defined as a set of several clusters being close in space. The seeding procedure developed for the current TPC, described in detail in [8], is used for these studies. It starts with a pair of points in pad rows (k) and ($k-n$). Clusters that are found within a search road between the starting points are associated to the seed. The seed is rejected if less than $n/2$ clusters are found.

In order to maximize the efficiency of the seeding step, a coarse space-charge distortion correction is applied to each cluster. It is based on the scaled average space-charge map, ρ_{scaled}, not taking into account topological fluctuations. Moreover, the t_0 of the corresponding interaction is not known at this stage. It is thus assumed, that all clusters belong to a track that has about half of the maximum drift length, i.e. $|\eta| = 0.45$. Under this assumption, a hypothetical z_{ro}-position can be assigned to each cluster and allows an ad-hoc distortion correction following Eq. (8.4). In this way, the maximal distortions are reduced to about one half which improves the seeding efficiency. It should be noted that seeding is performed in regions where the distortions are not largest, and that distortions vary only slowly over the length of the seed.

Initial t_0 estimate

An initial estimate of the time of the interaction can be derived from a track seed by extrapolating it in the x,y,t space to the interaction region ($x = y = 0$). This procedure is schematically depicted in Fig. 8.12. The calculated time from the extrapolation, t_{extrapol}, can be associated with the time of the interaction, t_0^{seed}, using the relation $z = z_{\text{roc}} - v_{\text{d}}\, t_{\text{d}}$ (from Eq. (8.2)):

$$t_0^{\text{seed}} = t_{\text{extrapol}} - \frac{z_{\text{roc}} - z_{\text{vtx}}}{v_{\text{d}}} \,. \tag{8.7}$$

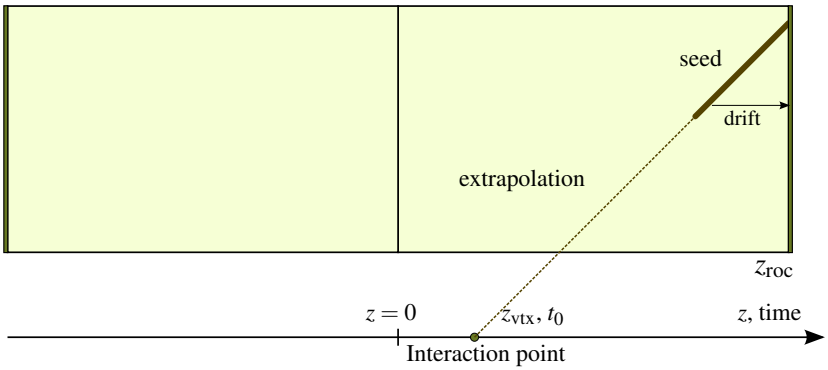

Figure 8.12: Schematic of the seeding procedure and t_0 estimation.

Here, z_{vtx} is the z-position of the interaction vertex which can be approximated by $z_{vtx} \approx 0$. In this case the extrapolated time at the interaction region $t_{extrapol}$ is one full drift time ($t_d = z_{roc}/v_d$) after the t_0 of the interaction:

$$t_0^{seed} \approx t_{extrapol} - \frac{z_{roc}}{v_d} \,. \tag{8.8}$$

This assumption leads to an irreducible uncertainty in t_0^{seed} due to the spread of the collision vertices around the nominal interaction point ($\sigma_z = 7\,\text{cm}$ corresponding to a drift time of $2.7\,\mu\text{s}$), to which the finite precision of the distortion correction adds.

Figure 8.13 shows the track-by-track distribution of the difference between the estimated t_0^{seed} and the true interaction time t_0, multiplied by the drift velocity. The distribution has a width of about 5.2 cm. In the simulation only events with vertices within 10 cm of the nominal interaction point were kept. The RMS of the simulated event vertices is 4.7 cm, which implies that the precision of t_0^{seed} is dominated by the irreducible contribution from the vertex spread.

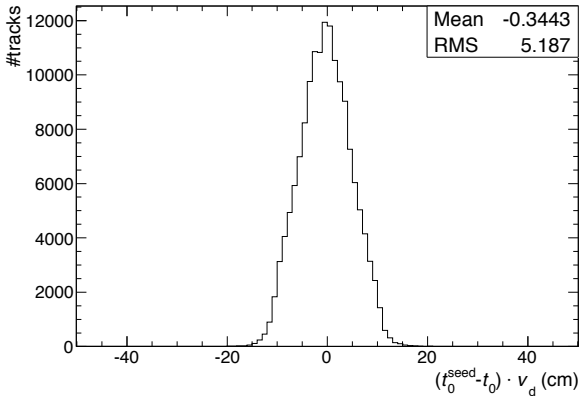

Figure 8.13: Deviation of t_0^{seed} from the real t_0, multiplied by v_d, for a space-charge scenario at $\varepsilon = 20$ in the fast MC.

Cluster-to-track association

The cluster-to-track association is an integral part of the first stage of the reconstruction. Starting from track seeds, the track parameters are extrapolated inwards (smaller radii) and outwards (larger radii). Then, within a road in the z and local-y directions, clusters are searched that are close to the track extrapolation.

The efficiency of this procedure suffers from the coarse distortion corrections in the first step, in particular in regions where the distortions are large, i.e. at small r and z. Therefore, the search road of the tracking is

modified according to the local distortions estimated from t_0^{seed}. The t_0^{seed} resolution presented in Fig. 8.13 implies that the uncertainty on the cluster drift time can be reduced from the maximum (about $\pm 50\,\mu$s to only a few microseconds (corresponding to the width of Fig. 8.13). Consequently, the distortions can be corrected to the level of a few percent using t_0^{seed}, assuming that the distortions scale approximately linear with the drift time. On this level, $\mathcal{O}(1\,\text{mm})$, the remaining distortions do not affect the cluster-to-track association.

It should be noted that at this point of the reconstruction the remaining distortions could be improved by matching the track t_0^{seed} to the closest t_0 from the list of collision times from an external trigger detector. Given the t_0^{seed} resolution of $\sim 2.7\,\mu$s quoted above, unambiguous matching to the proper interaction t_0 is possible if no other collision occurred in the same bunch train crossing. This is the case for $\sim 83\,\%$ of the collisions, see Fig. 8.2. In the remaining cases, the achievable precision will be limited to that of t_0^{seed}, as long as no external tracking information from ITS is included.

Matching with external detectors

A key issue for the calibration and reconstruction is the matching of TPC tracks to external detectors, mainly ITS and TRD. Here, we focus on the implications for ITS matching since the occupancies and distortions at smaller radii are much larger, and therefore, more demanding for the internal track calibration.

For the matching with the ITS we assume that a standalone ITS tracking will be performed based on the ITS hits. This will allow a matching on the track level, in terms of the following track parameters: the local-y and z position, the sine of the inclination angle in the bending plane, the tangent of the dip angle of the track, and the curvature expressed as $1/p_{\text{T}}$. In addition, by propagating the ITS track, a comparison of the track parameters at the inner wall of the TPC rather than at the ITS can be performed. This allows a better matching precision since the uncertainties on the track points of the ITS are much smaller than for the TPC. Therefore, an extrapolation of the ITS track towards the TPC is more precise than vice versa.

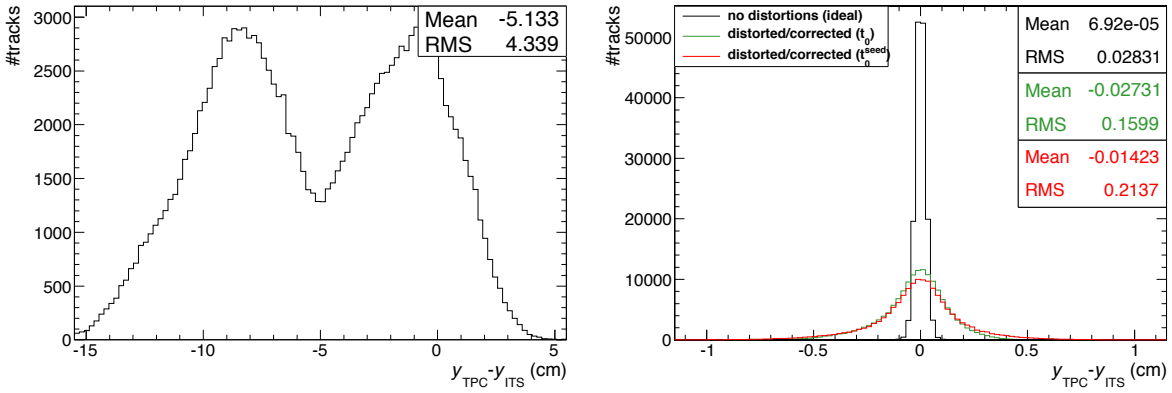

Figure 8.14: Matching of the local-y coordinate of ITS and TPC tracks. (Left) For tracks from undistorted clusters at the outermost ITS layer (red) and the inner wall of the TPC (black). (Right) For tracks from fully distorted clusters without correction (at the inner wall of the TPC).

The challenge of matching TPC tracks distorted due to space-charge with ITS information is manifest in Fig. 8.14 (left panel). It shows the local-y matching built from distorted clusters without performing any correction on the distortions. The shift and asymmetry of the distribution arises from an interplay between charge and curvature of the track and the $E \times B$ effect. The deviations are large, which makes unambiguous track matching at high occupancies impossible.

Figure 8.14 (right panel) shows the local-y matching of ITS tracks and TPC tracks built from distorted clusters and corrected with the z-position estimate obtained from t_0^{seed} (red histogram). The RMS of this

distribution is about 2.1 mm, being half the width of the readout pads of the inner readout chamber. In comparison to Fig. 8.14 (left panel), a strong improvement of the matching precision is observed. This leads to a large reduction of the combinatorial background in the TPC-ITS matching procedure. Note that this resolution is a result of the first online reconstruction stage based entirely on TPC information.

Matching with the proper ITS track will provide t_0 information and thus further improvement of the space-point distortion corrections, as shown in the same figure (green histogram). In addition, the matching is compared with the intrinsic resolution (black histogram). For performing the final matching, all possible TPC-ITS track combinations within a matching window are formed, each time refitting the TPC track parameters using the correct t_0 information delivered by the ITS for the z-position estimate. By using all five track parameters for the matching, the number of candidates can be reduced further.

After this step, the residual distortions of the TPC clusters are dominated by the space-charge fluctuations, which are not accounted for by using the scaled space-charge map ρ_{scaled} for distortion correction. As discussed in Sec. 8.5.2, the quality of the employed space-charge distortion maps can be further improved by making use of the measured currents with high temporal and spacial granularity. Consequently, also a large improvement on the matching precision is expected.

8.5.2 Space-charge calibration by current measurements

For the first reconstruction stage it is foreseen to base the space-charge distortion correction on the scaled average space-charge density map, where the total space charge integrated over the ion drift time, $t_{\text{d}}^{\text{ion}}$, of 160 ms is used for scaling (see Sec. 8.3). This method can, however, be refined by using the detailed ion density distributions in time and space. Using such a procedure would yield a much more precise description of the space-charge distortions. The idea is described in the following.

The space-charge density is proportional to the 'signal current' I_{roc} at the readout chambers multiplied by ε:

$$\rho_{\text{sc}} \sim I_{\text{roc}} \cdot \varepsilon \; . \tag{8.9}$$

Two methods are considered to measure I_{roc}:

- **Hardware-based method**: The currents on the GEM HV sectors are proportional to the charge locally produced by gas amplification. They can be measured with high temporal granularity (see Secs. 4.4, 10.3, and 11.4.1). A similar current measurement is currently being prepared for RUN 2 for a subset of the HV channels, albeit for a different purpose (current spike detection for the data taking with the TPC in gated mode).

- **Software-based method**: The cluster charges in the raw data are proportional to the current I_{roc}. They offer the ultimate granularity in space and time required to derive a high-resolution space-charge map. The data are available at the input to the online farm on the FPGAs which perform the cluster finding.

From either, or a combination of these methods, it will be possible to follow the amount of ions created in space and time with high granularity. An integration over the full drift of the ions allows the calculation of the present space-charge density maps ρ_{scaled} and $\rho_{\text{high-res}}$.

From any space-charge density map ρ_{sc}, obtained e.g. from the current measurement approach, the distortions can be derived analytically. However, with the methods currently available this will not be possible on the required time scale of a few ms. To overcome this limitation, the following method is foreseen:

The actual space-charge distortion map, $\vec{\Delta}$, is estimated by performing a Taylor expansion of a reference distortion map, $\vec{\Delta}_{\mathrm{ref}}$, obtained for a reference space-charge distribution[9], ρ_{ref}, over volume cells i:

$$\vec{\Delta} = \vec{\Delta}_{\mathrm{ref}} + \sum_i \frac{\partial \vec{\Delta}_{\mathrm{ref}}}{\partial_{\rho^i_{\mathrm{sc}}}} \delta\rho^i_{\mathrm{sc}} \ , \tag{8.10}$$

where $\partial/\partial_{\rho^i_{\mathrm{sc}}}$ is the partial derivative with respect to a change of the space-charge density in a volume cell i and $\delta\rho^i_{\mathrm{sc}} = \rho^i_{\mathrm{ref}} - \rho^i_{\mathrm{sc}}$ the variation of the space-charge density in cell i. The local derivatives can be pre-calculated analytically and stored in lookup tables for fast access. Together with the measured actual space charge density ρ_{sc}, this will allow a fast calculation of the present space-charge distortion map $\vec{\Delta}$.

For the expected space-charge densities, the distortions do not scale linearly with the average space-charge density. Therefore, if the deviation of $\langle\rho_{\mathrm{sc}}\rangle$ is large, $\mathcal{O}(10\,\%)$, compared to $\langle\rho_{\mathrm{ref}}\rangle$, $\vec{\Delta}_{\mathrm{ref}}$ needs to be updated. This can happen e.g. due to a change in luminosity. Such updates are expected at most on the level of $\mathcal{O}(1-10\,\mathrm{min})$, making feasible the analytic recalculation of $\vec{\Delta}_{\mathrm{ref}}$.

8.6 Additional calibration requirements, monitoring, and quality control

This section summarizes the additional calibration steps that have to be applied to the TPC data and discusses the requirements for online monitoring and quality control.

8.6.1 Additional calibration requirements

As most of the TPC calibration methods have been already developed for RUN 1, they are only briefly mentioned in this section. According to their characteristic dependence on ambient conditions over time, they are divided in time-independent and time-dependent calibrations.

Time-independent calibrations

Time-independent calibrations are characterized by a stable behavior over long periods. The pedestal values and zero suppression thresholds for the individual front-end electronics channels, as well as the map of dead channels, only change on time scales of the order of weeks or longer.

A proper calibration of the effective gain of the GEM readout system is mandatory for providing particle identification with best quality. The gain needs to be corrected for time-independent pad-by-pad and chamber-by-chamber variations. The retrieval of these calibration parameters is done typically once per year based on the Krypton calibration method, originally developed by the ALEPH [9, 10] and DELPHI [11] collaborations. The decay clusters of radioactive ^{83}Kr, which is released into the TPC gas, are analyzed and allow the extraction of the mean gain per readout chamber and the relative gain of each readout pad with respect to the mean. The method was already successfully used for the gain calibration of a GEM based TPC [12, 13].

An additional method for pad-by-pad gain calibration is based on charged-particle tracks. The relative pad gain factors can be retrieved from large statistics samples of clusters from a selected sample of tracks with well-defined mean energy loss, e.g. MIPs. This method allows a higher granularity in time, but needs additional attention when running in an environment of high space-charge distortions, due to the compression of tracks in radial direction and the merging of ionization clusters.

Time-dependent calibrations

The calibration of the drift velocity v_{d} and the gas gain have a time-dependent component that is connected to changes of the ambient conditions and of the gas composition. Moreover, the average space-

[9] This could be e.g. be the long term average map, ρ_{av}, see Sec. 8.2.3

charge map has to be updated periodically in order to account for slow variations of luminosity, ambient conditions, and for malfunctioning sectors.

Different methods for determining the drift velocity and gain are described below. An update of the corresponding calibration parameters every 15 min has proven sufficient in the calibration scheme for RUN 1. Between updates, a simple scaling based on pressure and temperature changes is performed. Such a scaling can be used also for RUN 3, but also other possibilities are investigated.

Drift velocity The variations of the drift velocity v_d in time are mainly induced by changes of the ambient conditions (pressure and temperature) and of the gas composition. Two methods for determining v_d have been routinely used in RUN 1.

Laser measurements yield a very robust estimate for the drift velocity, which is independent of reference detectors. Laser events are triggered and, therefore, the t_0 of the laser event is known. The arrival time of photo-electrons emitted from the central electrode (CE), which are created by scattered laser light inside the TPC, determines the drift time for the full drift length. The method allows to extract local drift velocity gradients and thus to monitor local temperature variations in the gas [14].

Track matching with external detectors (in particular the matching with ITS tracks) allows the determination of the drift velocity with high granularity in time[10]. The drift velocity can be determined using a Kalman-filter approach, fitting the differences in the z-positions of the TPC and ITS track. The method is also used for the other track parameters and allows to simultaneously fit the distortions (see also Sec. 7.4.5).

Readout chamber gain Like the drift velocity, the gas amplification is influenced by the ambient conditions. The variations of the effective gain in the readout chambers can be followed using tracks with a constant $\mathrm{d}E/\mathrm{d}x$. Minimum ionizing (MIP) pions or electrons are used for this purpose. Pions are abundant, the MIP region is easy to identify, and the signal is clean from contamination. Electrons can be extracted using topological reconstruction of conversion photons in the detector material. The advantage of electrons is that their energy-loss is about 50 % higher than that of MIPs, and therefore, usually less prone to threshold effects. However, it requires the reconstruction of secondary vertices and thus they need either longer integration times or yield lower precision. Methods using both particles will be applied for gain calibration of the upgraded TPC on the readout chamber level, allowing to follow the gain variations.

8.6.2 Monitoring and quality control

The concept of online Quality Control (QC) combines continuous monitoring and control of the data in order to ensure prompt reaction on data quality issues already during the data taking. The specific monitoring tasks are based on the solutions developed already in RUN 1. In addition, the monitoring of the space-charge distortions and their correction must be an integral part of this strategy.

In case of problems with the quality of the reconstrucion, the basic strategy has been to restart the reconstruction process (i.e. start a new reconstruction pass) for the data collected in RUN 1. This procedure is very successful in order to utilize a maximum of recorded data for physics analysis, but can not be transferred to RUN 3, due to the online reconstruction paradigm. Therefore, an optimized concept for data quality monitoring is needed for RUN 3, which is discussed below.

[10] In the RUN 1 calibration scheme laser measurements were used as an initial estimate for the reconstruction. However, track matching was the main source of the drift velocity calibration.

Monitoring

Different kinds of input data will be used for the QC in RUN 3. These data comprise not only different levels of reconstructed data and global, environmental observables, but also the calibration parameters produced online. The key feature of QC will be the time-wise trending of those observables. This has been demonstrated to be very successful during RUN 1 in the offline QA, as well as HLT online QA on a run-by-run basis.

The observables, which have been already defined, will be used also for RUN 3, as they have been proven to allow a good and comprehensive judgment of the performance of the TPC. A list of observables to be monitored is given here:

- **External Parameters** such as as instantaneous and integrated luminosity, beam-background, ambient pressure, and temperature, which slowly change in time.
- **Global Event Propertie**s such as data sizes per interaction or per time frame, track multiplicities, and compression factors.
- **Calibration Objects** such as alignment stability, drift velocity, gain stability, and space-charge distortions.
- **Cluster Parameters** such as cluster charge and width, as well as fraction of clusters associated to tracks from interactions.
- **Track Parameters** such as number of clusters associated to tracks, pseudo-rapidity, angular, and momentum distributions, as well as $\langle \mathrm{d}E/\mathrm{d}x \rangle$ signal and $\mathrm{d}E/\mathrm{d}x$ resolution for MIPs. Furthermore, also distances-of-closest-approach to the primary vertex, as well as the track matching efficiency to the external detectors, such as ITS, TRD, and TOF belong to this category.
- **Advanced Physics Observables** such as fits to the invariant mass distributions of V0 particles (K^0_s and Λ), fits to the transverse momentum distributions, as well as parameters of tracks from cosmic particles within normal collisions events. Finally, also the particle identification performance can immediately be verified.

Space-charge calibration monitoring

The TPC laser system is an ideal tool to monitor the quality of the space-charge calibration because it provides reproducible straight ionization tracks at known positions. In the TPC laser system the laser light is split in several beams through an optical system of semi-transparent beam splitters, micro mirrors and prisms, and guided into the TPC at different entry points through quartz windows (see Sec. 11.4.4 and [15]). The individual position and inclination angle of each micro mirror has been measured and is available in a database. Laser tracks can thus be easily associated to a micro mirror from the different angles and z-positions of the reconstructed track parameters. Figure 8.15 shows simulated laser tracks with the space-charge distortions expected for $\varepsilon = 20$ at 50kHz. Together with the different layers along the z-axis such data allow to verify the quality of the extracted correction maps with sufficient precision. Therefore, laser data are ideally suited for quality assurance purposes.

Quality control

The calibration parameters applied in the online reconstruction process have to be closely monitored and validated. This will allow to identify wrongly calculated values or even outliers in a trend, in cases where a fit to data might have failed. A similar validation step has been already applied during RUN 1 before the created calibration objects have been uploaded to the Offline Conditions DataBase (OCDB).

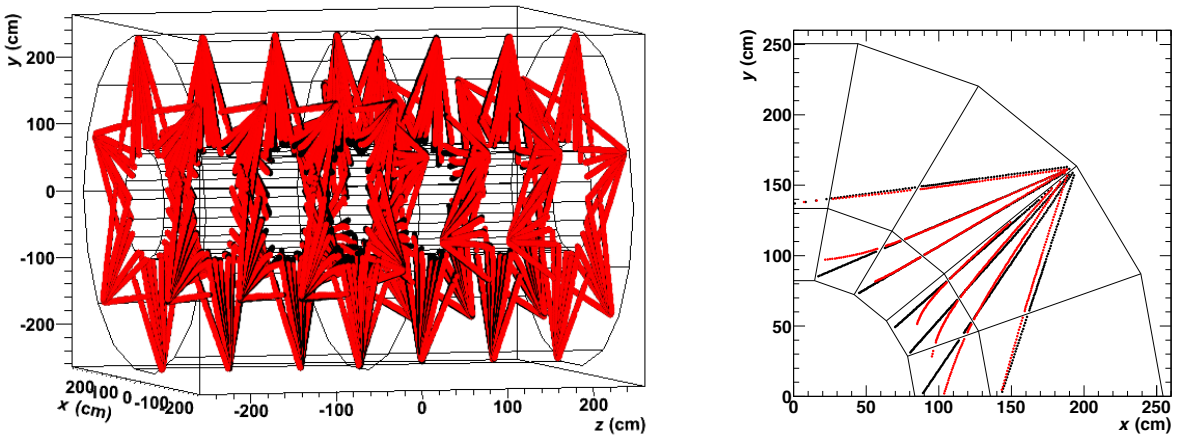

Figure 8.15: Simulated laser event. Black points indicate undistorted clusters, red points show distorted clusters for $\varepsilon = 20$ at 50 kHz Pb–Pb data taking. (Left) All laser tracks are shown. (Right) Laser tracks from one micro-mirror bundle are shown.

In order to establish these monitoring and control layers, a high level of automation is required not only to allow fast reaction, but also to minimize manual interventions by shift personnel. Automatic alarms on basis of smaller subsets of key trending histograms will be constantly available, in order to inform about potential problems. A more detailed set of observables has to be collected at the same time in order to allow the experts to react quickly in case of issues with the quality of the data or the performance of the online reconstruction. Predefined procedures for fast detection of error conditions are crucial to ensure a prompt reaction. Actually, error conditions could be anticipated using predictions based on trending information on changing detector behaviour and/or conditions.

Chapter 9

Alternative R&D options

This chapter describes the R&D status of alternative options for the upgrade of the TPC readout.

The baseline proposal for the design of the readout chambers of the upgraded TPC foresees a quadruple GEM stack with asymmetric field configurations, as described in Chap. 4. This approach fulfills the requirements listed in Chap. 1. In parallel, alternative R&D efforts have been made to study and develop options to further improve the detector performance. The following key issues have been addressed:

- minimization of the ion backflow,
- minimization of the pileup of tracks from different events and
- preservation or improvement of the space-point, momentum, and d$E/$dx resolutions.

In particular, COBRA GEMs, perspectives of using a different gas mixture containing CF_4 in combination with chevron-shaped readout pads, and a gas amplification option based on 2 GEMs and one MMG[1] were studied in detail.

9.1 R&D with COBRA GEMs

A COBRA GEM is a GEM with a patterned electrode on the surface, which helps to block back-flowing ions very efficiently [1, 2]. To characterize the properties of COBRA GEMs in a TPC application, a comprehensive R&D study was performed.

Three kinds of COBRA GEMs have been developed in collaboration with SciEnergy Co. Ltd [3]. Table 9.1 summarizes their specifications. In addition, two types of standard GEMs were used for the present measurements, which are also listed in Tab. 9.1. Figure 9.1 shows a photograph of COBRA 1.

	thickness (μm)	hole size (ø) (μm)	pitch (μm)	rim size (μm)	insulator
COBRA 1	400	300	1000	100	FR5
COBRA 2	200	150	500	50	FR5
COBRA 3	100	100	400	0	LCP
GEM 50	50	70	140	0	LCP
GEM 100	100	70	140	0	LCP

Table 9.1: Geometries of COBRA GEMs and standard GEMs used for the measurements.

[1] MicroMegas: Micro-Mesh Gaseous Structure (MMG)

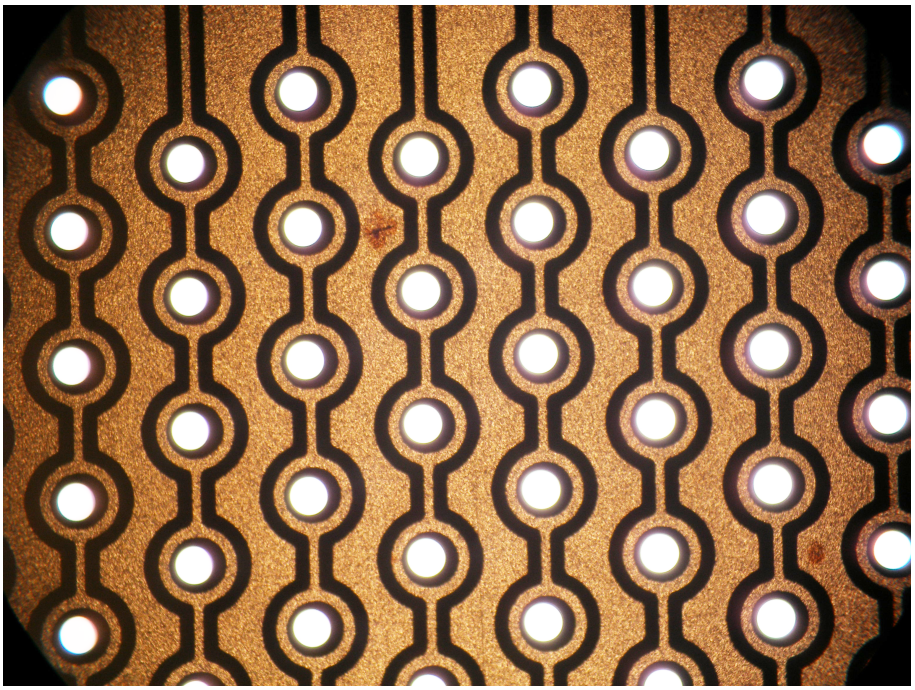

Figure 9.1: Photograph of COBRA 1 showing the GEM (around the holes) and COBRA electrodes.

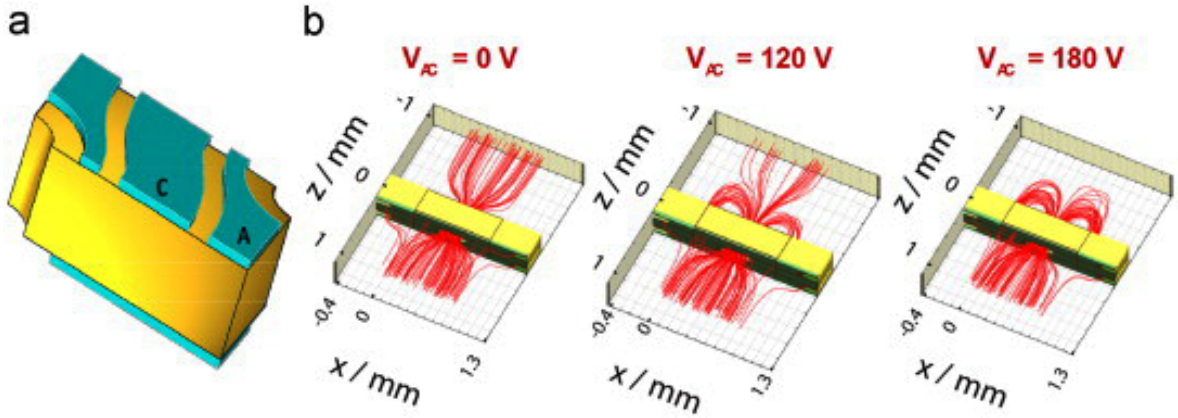

Figure 9.2: (a) COBRA GEM unit cell built in the simulation program ANSYS (b) ion drift lines in a COBRA GEM with three different potential differences ΔU_{AC} between GEM electrode (A) and COBRA electrode (C). Image from [1].

COBRA 1 and COBRA 2 are based on glass epoxy laminate (FR5) as insulator and 6 μm Cu layers, covering an active area of $3 \times 3\,\mathrm{cm}^2$. The holes are pierced by a mechanical drilling technique. The additional pattern on the top and bottom surfaces of the GEMs are produced by wet etching. Clearances from the edge of the hole (rim) of 100 μm and 50 μm, respectively, are introduced to protect from discharges. However, charge-up of the FR5 insulator at the rim occurs, which negatively affects the gas gain and long term stability. To avoid this effect, a new production method for a COBRA GEM with standard thickness (100 μm) and standard insulator (LCP[2]) without rim was started[3] (COBRA3).

Figure 9.2 shows a COBRA unit cell built in the simulation software ANSYS and drift lines of ions at different potential differences ($\Delta U_{\mathrm{AC}} = U_{\mathrm{GEM}} - U_{\mathrm{COBRA}}$ of 0, 120, and 180 V) between GEM electrode (A) and COBRA electrode (C). The reduction of the ion backflow as the potential ΔU_{AC} increases is evident.

[2]Liquid Crystal Polymer (LCP)

[3]The production of COBRA3 is still underway at the time of writing this TDR, such that no test results are available yet.

9.1.1 Characterization of single COBRA GEMs

Measurements of gas gain and ion backflow with a single COBRA 1 and COBRA 2 have been performed at different voltages U_{GEM} and ΔU_{AC}. All measurements have been performed in Ne-CO_2 (90-10). Figure 9.3 shows the schematics of the measurement setup. The length of the drift volume is 3 mm. X-rays are emitted into the detector from the top of the chamber. Primary electrons created between shield and mesh (cathode) do not contribute to the multiplication of electrons, whereas the electrons created between the mesh and the GEM (drift region) enter the multiplication region. The currents on the mesh and on the pad anode are read by picoammeters (ADC R8240 x2 or KEITHLEY 6487), while the currents on the GEM electrodes are read out by high voltage power supply modules (CAEN N1471) with 0.5 nA resolution. The tube current of the X-ray generator is varied between 0.03 and 3 mA, which results in a current on the readout pad anode of between around 1 and 100 nA at a gas gain of $\sim$2000 in Ne-CO_2 (90-10). Since the expected current density in 50 kHz Pb–Pb collisions is of the order of 1 nA/cm^2, a tube current $\leq$0.3 mA was found to be best suited for the measurements.

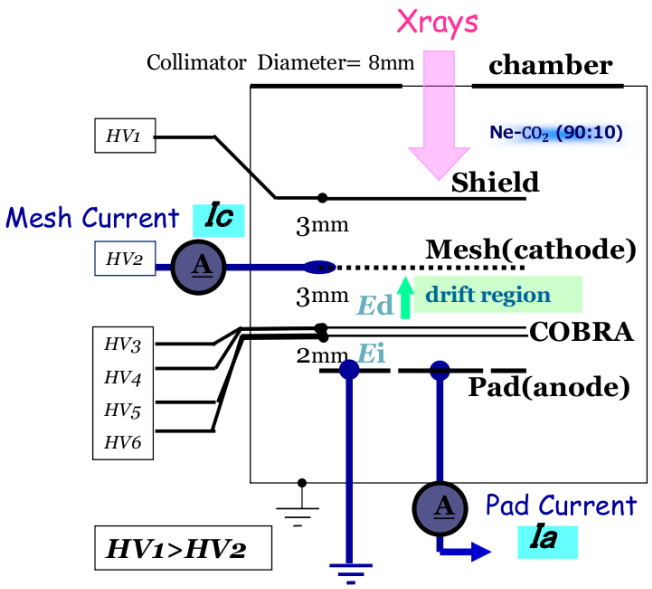

Figure 9.3: Schematic setup for the measurement of gas gain and ion backflow with an X-ray source.

The ion backflow is measured as $IB = (I_{\mathrm{cathode}} - I^0_{\mathrm{cathode}})/I_{\mathrm{anode}}$, where I_{cathode} is the current at the mesh, I^0_{cathode} is the current from primary ions and I_{anode} is the current at the readout pad plane. The current from primary ions is measured at a drift field $E_{\mathrm{drift}} = 0.4$ kV/cm applied both between shield and mesh, and between mesh and the top of the GEM electrode. No voltage difference is applied across the GEM for the measurement of I^0_{cathode}. Note that the sign of the electric field flips at the mesh. This means that ions from both sides of the mesh contribute to the primary current, but not electrons.

The effective gain is estimated by the ratio $I_{\mathrm{anode}}/(I^0_{\mathrm{cathode}}/2)$: the primary electron current contributing to the gas amplification is half the primary current I^0_{cathode} measured at the mesh. The electric fields in the drift and induction regions have been kept at 0.4 kV/cm and 3 kV/cm, respectively.

Dependence on ΔU_{GEM}

Figure 9.4 shows the effective gas gain and ion backflow of GEM 50, GEM 100 and COBRA 2 with ΔU_{AC}=0 V. The electric fields in the drift and induction regions are kept at 0.4 kV/cm and 3 kV/cm, respectively. The observed ion backflow for GEM 50 and GEM 100 is about 20 – 30 %. The ion backflow with COBRA 2 is $\sim$ 40 – 50 % and gradually decreases for gas gains larger than 200.

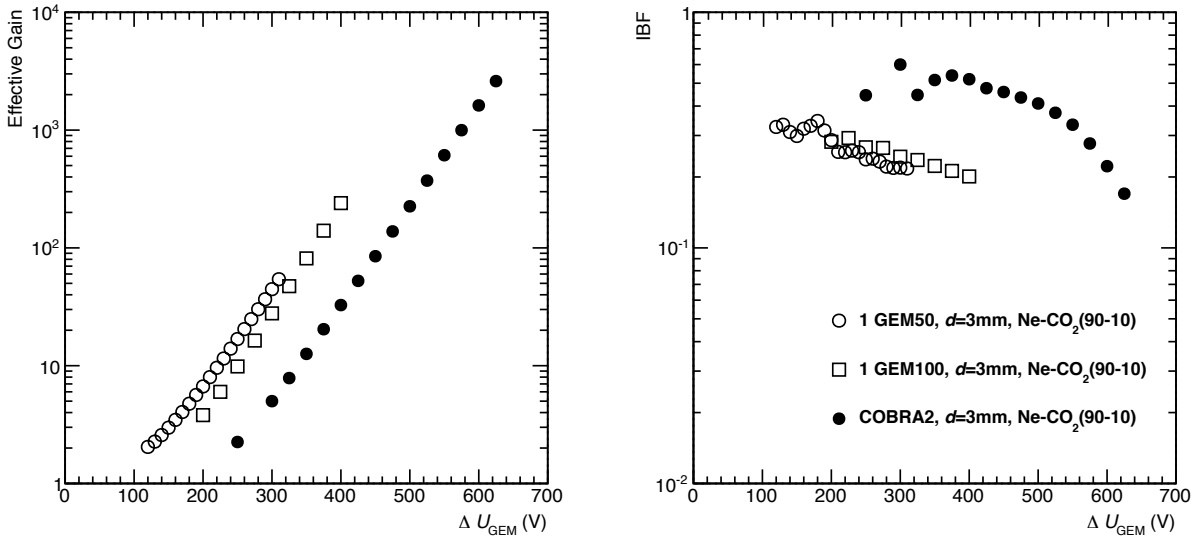

Figure 9.4: Effective gain (left panel) and ion backflow (right panel) in Ne-CO_2 (90-10) as a function of the voltage across the GEM for GEM 50 (open circles), GEM 100 (open squares) and COBRA 2 (closed circles). The voltage across the GEM and COBRA electrodes ΔU_{AC} is kept at 0 V.

Dependence on ΔU_{AC}

The effective gain and ion backflow of COBRA 2 as a function of ΔU_{AC} were measured in Ne-CO_2 (90-10) for $\Delta U_{\mathrm{GEM}} = 575$ V and 390 V. Figure 9.5 shows that positive $\Delta U_{\mathrm{AC}}^{\mathrm{up}}$ and negative $\Delta U_{\mathrm{AC}}^{\mathrm{bot}}$ tend to increase the effective gain, which may be related to an improved efficiency for the collection of the primary electrons into the GEM holes and for the extraction of avalanche electrons into the induction region. The ion backflow depends both on ΔU_{GEM} and ΔU_{AC} and is thus correlated with the effective gain. While the dependence of the ion backflow on ΔU_{GEM} is rather weak, a factor of 2 – 3 within the range of this study, the ion backflow drops by more than an order of magnitude if $\Delta U_{\mathrm{AC}}^{\mathrm{up}}$ is increased to 200 V. It should be noted that an ion backflow of 1 % or less can be achieved with a single COBRA GEM, albeit at rather large gas gains.

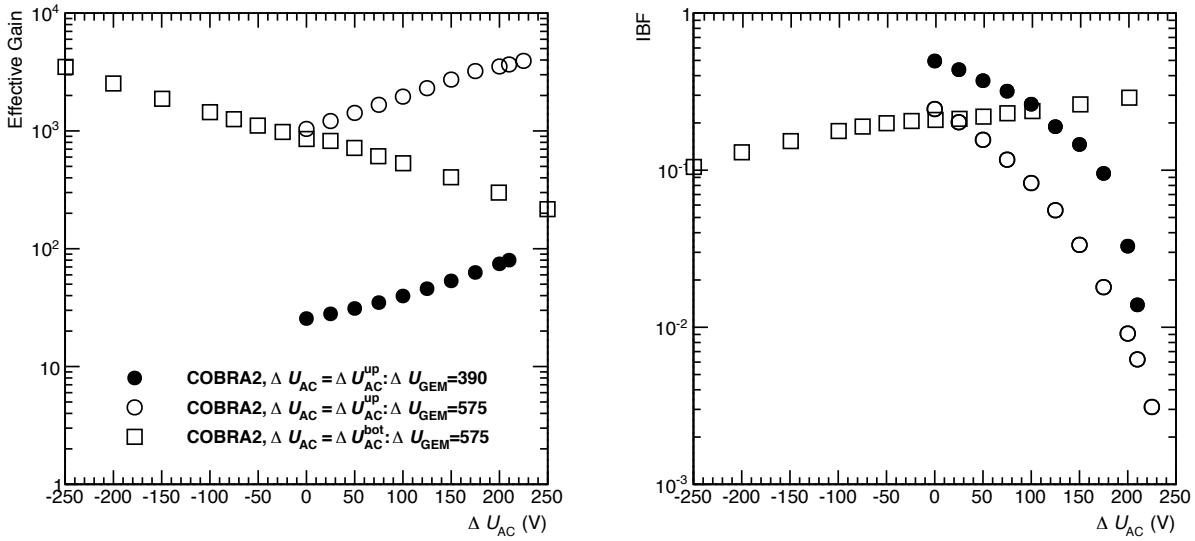

Figure 9.5: Effective gas gain (left panel) and ion backflow (right panel) of COBRA 2 in Ne-CO_2 (90-10) as a function of $\Delta U_{\mathrm{AC}}^{\mathrm{up}}$ (circles) with $\Delta U_{\mathrm{GEM}} = 575$ V (open circles), $\Delta U_{\mathrm{GEM}} = 390$ V (closed circles) and $\Delta U_{\mathrm{AC}}^{\mathrm{bot}}$ with $\Delta U_{\mathrm{GEM}} = 575$ V (open squares). The drift length is 3 mm, E_{drift} is 0.4 kV/cm in all measurements.

9.1.2 Triple structures with COBRA and standard GEMs

Studies of triple GEM systems including one or two COBRA GEMs were performed. It was found that a COBRA GEM placed as the first GEM layer is not effective for ion backflow suppression. This result was confirmed in electrostatic simulations and is the consequence of the large distance between the GEM surface and the drift electrode. Therefore, only configurations with COBRA GEMs in the second or third layer are considered in the following.

The effective gain and ion backflow are studied for the triple GEM configurations (GEM 1 – GEM 2 – GEM 3): GEM 50 – COBRA 2 – GEM 50 and GEM 50 – COBRA 2 – COBRA 2. In these measurements, the dependence on $\Delta U_{\mathrm{AC}}^{\mathrm{up}}$, on the second transfer field E_{T2}, and on the X-ray tube current were studied. The drift length and the transfer gaps all measure 3 mm. The electric fields E_{drift} and E_{T1} are set to 0.4 kV/cm, while E_{ind} is 3 kV/cm. The voltage across GEM 1 is set to 200 V. The X-ray tube current is varied from 0.03 mA to 3 mA.

Standard GEM – COBRA GEM – Standard GEM

Figure 9.6 shows the gas gain and the ion backflow measured with the GEM 50 – COBRA 2 – GEM 50 setup as a function of $\Delta U_{\mathrm{AC}}^{\mathrm{up}}$ on COBRA 2. The measurement is performed with $\Delta U_{\mathrm{COBRA2}} = 400$ V, $\Delta U_{\mathrm{GEM3}} = 300$ V and $E_{\mathrm{T2}} = 0.75$ kV/cm. The results were obtained with X-ray tube currents of 3 mA, 0.3 mA and 0.03 mA. The dependence of the gas gain on ΔU_{AC} and on the X-ray tube current is weak. The ion backflow depends strongly on ΔU_{AC}, as already observed in the single GEM setup. A significant dependence on the X-ray tube current is also observed, indicating the importance of space-charge effects for tube currents above 0.3 mA. At small tube currents, values of the ion backflow below 1 % can be achieved. Note that the COBRA GEM in the triple GEM setup is operated at rather low gain ($\Delta U_{\mathrm{COBRA2}} = 400$ V, see also Fig. 9.5).

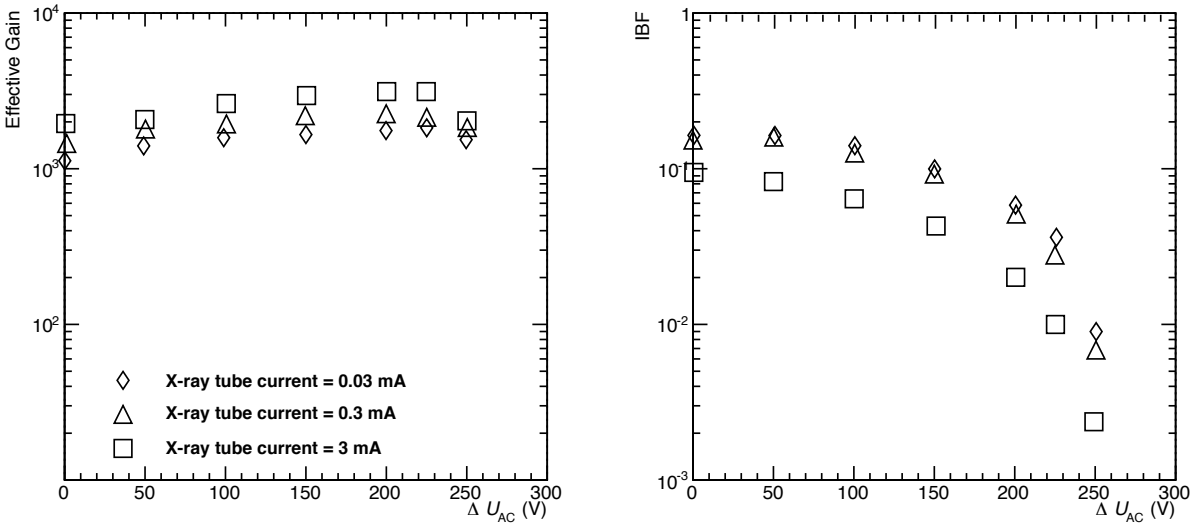

Figure 9.6: Gas gain (left panel) and ion backflow (right panel) measured with the GEM 50 – COBRA 2 – GEM 50 configuration as a function of $\Delta U_{\mathrm{AC}}^{\mathrm{up}}$ on COBRA 2 for different X-ray tube currents. The second transfer field is $E_{\mathrm{T2}} = 0.75$ kV/cm.

For the same setup, the gas gain and ion backflow as a function of $\Delta U_{\mathrm{AC}}^{\mathrm{up}}$ on COBRA 2 is shown in Fig. 9.7 for different transfer fields E_{T2} in the range 0.25 – 1 kV/cm. The voltage on GEM 3 (ΔU_{GEM3}) is adjusted for each E_{T2} setup to provide an effective gas gain in the range 1000 – 2000. The tube current of the X-ray generator used in these measurements is 0.03 mA. A significant reduction of the ion backflow can be achieved by lowering E_{T2}, which matches the observations in a standard triple GEM system (see Sec. 5.1). For the triple GEM system with one COBRA GEM, an ion backflow of 0.5 % can be achieved.

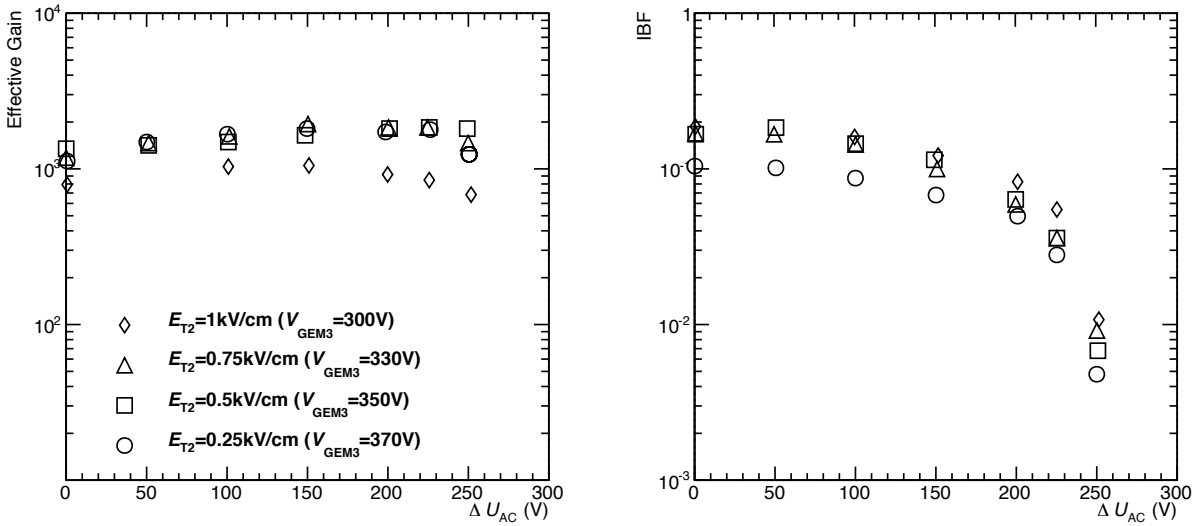

Figure 9.7: Effective gas gain (left panel) and ion backflow (right panel) measured as a function of $\Delta U_{\mathrm{AC}}^{\mathrm{up}}$ on COBRA 2 with the GEM 50 – COBRA 2 – GEM 50 configuration. The X-ray tube current is 0.03 mA.

Standard GEM – COBRA GEM – COBRA GEM

In the following, we present measurements with a standard GEM in the first layer, and COBRA GEMs in the second and third layer (GEM 50 – COBRA 2 – COBRA 2). Figure 9.8 shows the gas gain and the ion backflow as a function of $\Delta U_{\mathrm{AC}}^{\mathrm{up}}$ on the COBRA GEMs at different X-ray tube currents. Open symbols correspond to measurements where $\Delta U_{\mathrm{AC}}^{\mathrm{up}}(\mathrm{GEM\,2}) = \Delta \mathrm{U}_{\mathrm{AC}}^{\mathrm{up}}(\mathrm{GEM3})$, i.e. both voltages are varied simultaneously, while the closed symbols correspond to results where one of the $\Delta U_{\mathrm{AC}}^{\mathrm{up}}$ voltages are fixed. The GEM voltage and the field configurations are $\Delta U_{\mathrm{GEM1}} = 200\,\mathrm{V}$, $\Delta U_{\mathrm{GEM2}} = 430\,\mathrm{V}$, $\Delta U_{\mathrm{GEM3}} = 430\,\mathrm{V}$, $E_{\mathrm{drift}} = 0.4\,\mathrm{kV/cm}$, $E_{\mathrm{T1}} = 0.4\,\mathrm{kV/cm}$, $E_{\mathrm{T2}} = 0.4\,\mathrm{kV/cm}$ and $E_{\mathrm{ind}} = 3\,\mathrm{kV/cm}$. For $\Delta U_{\mathrm{AC}} \sim 250\,\mathrm{V}$, an ion backflow of $\sim 0.5\%$ is achieved at the lowest X-ray tube currents.

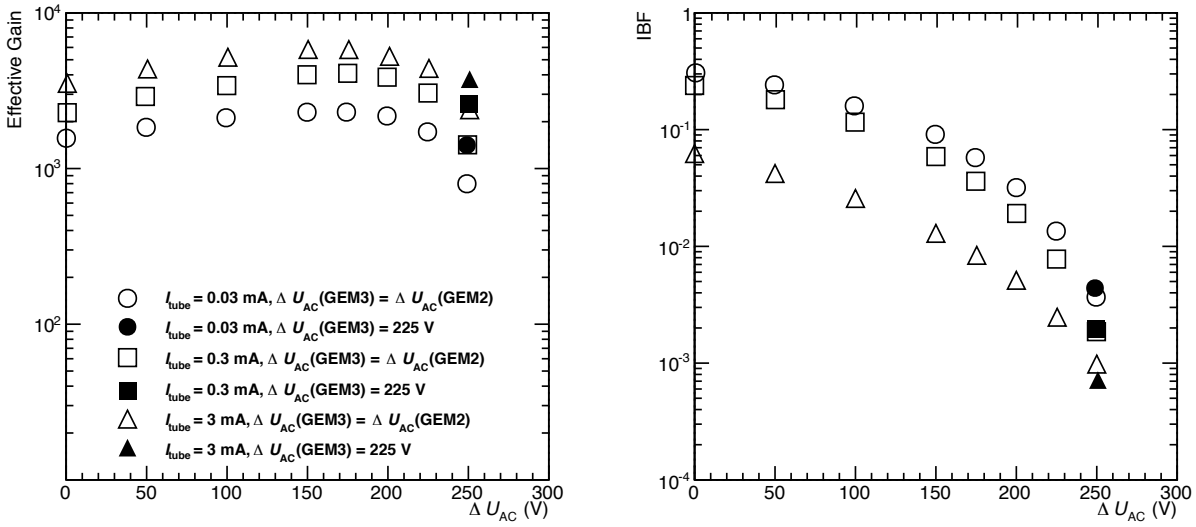

Figure 9.8: Effective gas gain (left panel) and ion backflow (right panel) measured with the GEM 50 – COBRA 2 – COBRA 2 configuration as a function of $\Delta U_{\mathrm{AC}}^{\mathrm{up}}$ on the COBRA GEMs for different X-ray tube currents. Open symbols correspond to the settings with $\Delta U_{\mathrm{AC}}^{\mathrm{up}}(\mathrm{GEM2}) = \Delta \mathrm{U}_{\mathrm{AC}}^{\mathrm{up}}(\mathrm{GEM3})$, while the closed symbols are for $\Delta U_{\mathrm{AC}}^{\mathrm{up}}(\mathrm{GEM2}) = 250\,\mathrm{V}$ and $\Delta U_{\mathrm{AC}}^{\mathrm{up}}(\mathrm{GEM3}) = 225\,\mathrm{V}$.

Further reduction of the ion backflow is possible by tuning the values of ΔU_{GEM2} and ΔU_{GEM3}. Figure 9.9 shows the gas gain and the ion backflow as a function of $\Delta U_{\mathrm{AC}}^{\mathrm{up}}$ changed simultaneously on GEM 2 and GEM 3 (so that $\Delta U_{\mathrm{AC}}^{\mathrm{up}}(\mathrm{GEM2}) = \Delta \mathrm{U}_{\mathrm{AC}}^{\mathrm{up}}(\mathrm{GEM3})$) at different values of ΔU_{GEM2} and ΔU_{GEM3}. An ion

backflow of less than 0.25% is achieved with $\Delta U_{\mathrm{GEM2}} \leq 390\,\mathrm{V}$ and $\Delta U_{\mathrm{GEM3}} \geq 470\,\mathrm{V}$.

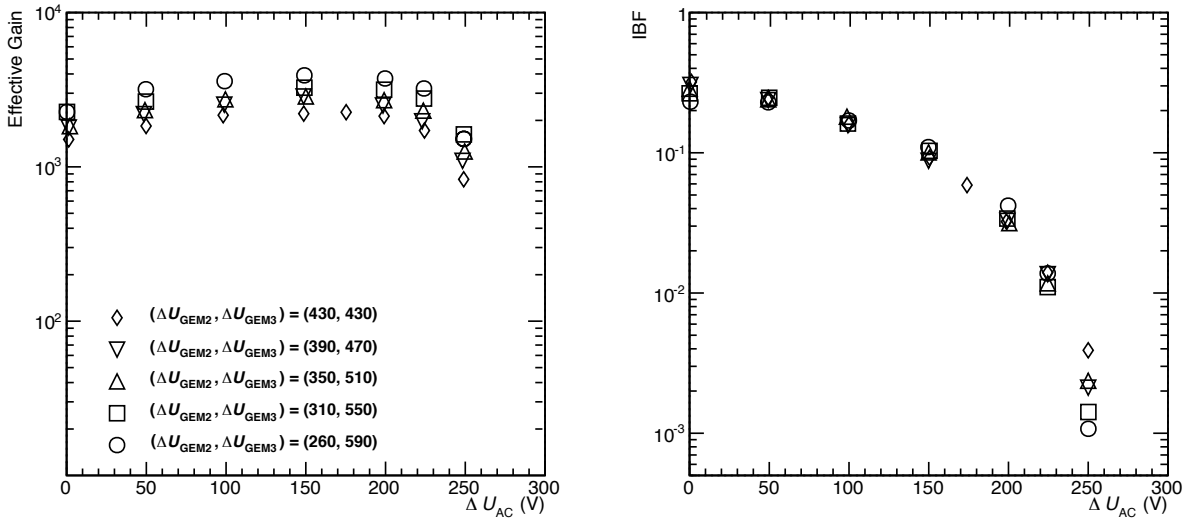

Figure 9.9: Effective gas gain (left panel) and ion backflow (right panel) as a function of $\Delta U_{\mathrm{AC}}^{\mathrm{up}}$ of the COBRA GEMs (with the condition $\Delta U_{\mathrm{AC}}^{\mathrm{up}}(\mathrm{GEM2}) = \Delta \mathrm{U}_{\mathrm{AC}}^{\mathrm{up}}(\mathrm{GEM3})$) measured with the GEM 50 – COBRA 2 – COBRA 2 configuration at different ΔU_{GEM2} and ΔU_{GEM3}.

9.1.3 Energy resolution

The energy resolution as a function of $\Delta U_{\mathrm{AC}}^{\mathrm{up}}$ has been measured in a GEM 50 – COBRA 2 – COBRA 2 configuration. Like in all other measurements reported here, we used the gas mixture Ne-CO_2 (90-10). The drift length is 30 mm and a ^{55}Fe source radiates from the top of the drift field. Induced signals on the anode pad ($3\times3\,\mathrm{cm}^2$) are amplified by a pre-amplifier and shaper and read out by an MCA (KromeK K102). In these measurements, ΔU_{GEM1}, ΔU_{GEM2}, and ΔU_{GEM3} are fixed to 200 V, 430 V, and 430 V, respectively, while $\Delta U_{\mathrm{AC}}^{\mathrm{up}}$ is varied between 0 and 200 V. ΔU_{GEM2} and ΔU_{GEM3} are increased to 445 V at $\Delta U_{\mathrm{AC}}^{\mathrm{up}} = 200\,\mathrm{V}$ in order to keep the gain constant. Further settings are: $E_{\mathrm{drift}} = 0.4\,\mathrm{kV/cm}$, $E_{\mathrm{T1}} = 0.4\,\mathrm{kV/cm}$, $E_{\mathrm{T2}} = 0.4\,\mathrm{kV/cm}$, and $E_{\mathrm{ind}} = 3\,\mathrm{kV/cm}$. Figure 9.10 shows the energy spectra obtained at the different settings of $\Delta U_{\mathrm{AC}}^{\mathrm{up}}$ V.

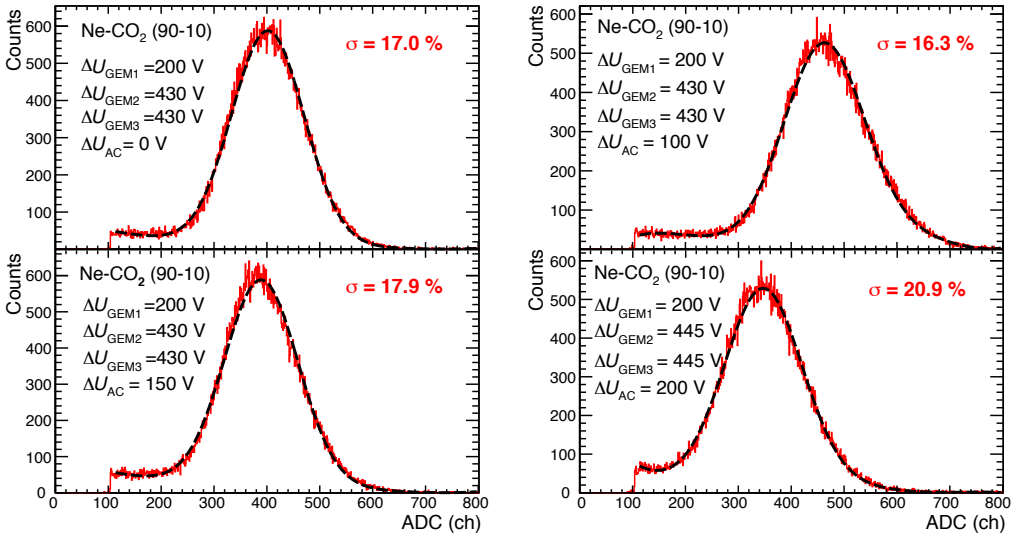

Figure 9.10: ^{55}Fe energy spectra measured in Ne-CO_2 (90-10) with a GEM 50 – COBRA 2 – COBRA 2 configuration for different values of $\Delta U_{\mathrm{AC}}^{\mathrm{up}}$.

An energy resolution (σ) of 17%, 16%, 18%, and 21% is achieved with $\Delta U_{\mathrm{AC}}^{\mathrm{up}} = 0\,\mathrm{V}$, 100 V, 150 V, and 200 V, respectively. The values are worse by a factor of almost 2 as compared to the resolution achieved with a prototype IROC (see Fig. 5.20). Most likely the deterioration can be explained by a decreased electron collection efficiency at GEM 1 due to the large pitch between the holes of the COBRA GEM or the non-uniform multiplication inside the hole due to the relatively small ratio of hole size to thickness.

9.1.4 Conclusion and outlook

Measurements with triple GEM systems including one or two COBRA GEMs show that an ion backflow of 0.25 – 0.5% can be achieved by tuning the potentials on the COBRA electrodes and the fields between the GEMs. However, the energy resolution obtained is not on the level required for the GEM TPC. The characterization of COBRA GEM systems will be continued in the future. In particular, the performance of COBRA3 (see Tab. 9.1) will be studied. Further plans include the characterisation of large-size COBRA GEMs ($50\times50\,\mathrm{cm}^2$) in terms of uniformity of gas gain, ion backflow, energy resolution, and long-term stability.

9.2 Studies with fast gas mixtures

In Ne-CO_2 (90-10) and Ne-CO_2-N_2 (90-10-5) the maximum electron drift time is $\sim 100\,\mu$s, resulting in an average overlap of $N_{\mathrm{pileup}} = 5$ minimum bias events at 50 kHz Pb–Pb operation. This motivates the search for alternative gas mixtures with significantly larger drift velocities at similar electric fields. One of these options implies the use of CF_4 as a quencher gas. As shown in Tab. 3.1, a drift velocity of more than 8 cm/μs can be achieved in Ne-CF_4 (80-20), which exceeds the drift velocity in Ne-CO_2 (90-10) by a factor of ~ 3 at the same drift field. As a result, the event pileup can be reduced by a similar factor.

The high electron mobility in Ne-CF_4 (90-10) implies also a large $\omega\tau$ factor and small diffusion at the nominal magnetic field of $B = 0.5\,\mathrm{T}$ (see also Tab. 3.1). This may potentially lead to a significant improvement of the position resolution, if the readout pads are accordingly reduced to achieve smaller cluster sizes.

In the following, results from detailed simulations of the TPC response in Ne-CO_2 (90-10) and Ne-CF_4 (90-10) including a microscopic description of a triple-GEM readout system are presented.

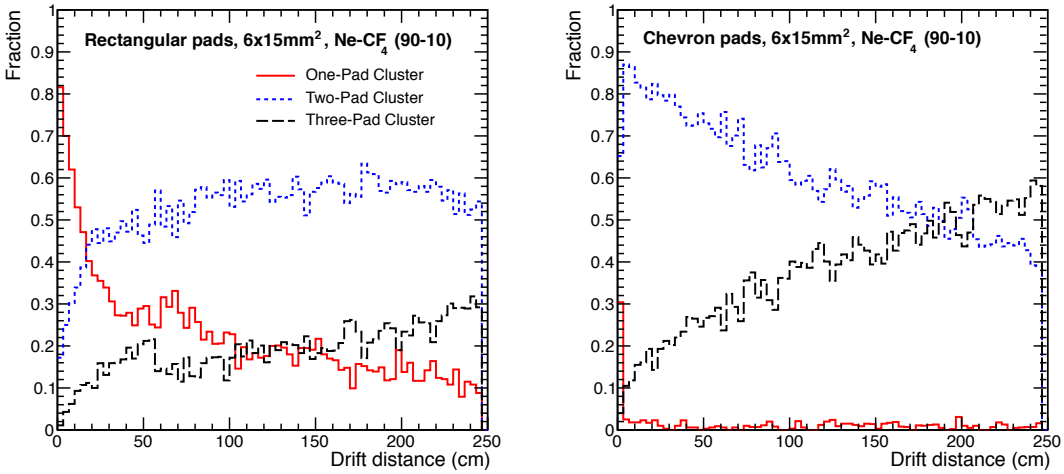

Figure 9.11: Fraction of one-, two-, and three-pad clusters for rectangular (left) and chevron-shaped (right) pads ($6 \times 15\,\mathrm{mm}^2$) in a triple GEM readout system with Ne-CF_4 (90-10).

As discussed in Sec. 4.5, the present pad geometry of the TPC readout chambers leads to a limitation of the space-point resolution. The narrower pad response function in GEMs, which is approximately equal

to the width of the charge cloud emerging from the last GEM, implies that charge sharing among adjacent pads is insufficient for small drift lengths. This is illustrated in Fig. 9.11 (left panel) where the fraction of clusters with $n = 1$, 2 and 3 pads is shown as a function of the drift distance. The calculation is performed for Ne-CF_4 (90-10), assuming rectangular readout pads of size $6 \times 15\,\mathrm{mm}^2$. The frequent occurrence of one-pad clusters at small drift distance results in a deterioration of the space-point resolution in this region. This can be overcome by choosing chevron-shaped pads [4] instead of rectangular ones. The frequency of n-pad clusters for $6 \times 15\,\mathrm{mm}^2$ pads with an n-fold chevron structure is shown in Fig. 9.11 (right panel). The majority of clusters have a signal on two or three adjacent pads, while the probability for one-pad clusters is negligible.

The space-point resolution in $r\varphi$ direction as a function of the drift length is shown in Fig. 9.12. For the gas mixture Ne-CO_2 (90-10) and with rectangular pads ($6 \times 15\,\mathrm{mm}^2$) a deterioration of the space-point resolution is seen at small drift length, which is due to the increasing fraction of one-pad clusters. In Ne-CF_4 (90-10) with rectangular pads this effect is even more pronounced, due to the smaller transverse diffusion. The space-point resolution can be improved by a factor ~ 3 in Ne-CF_4 (90-10) if chevron pads are used.

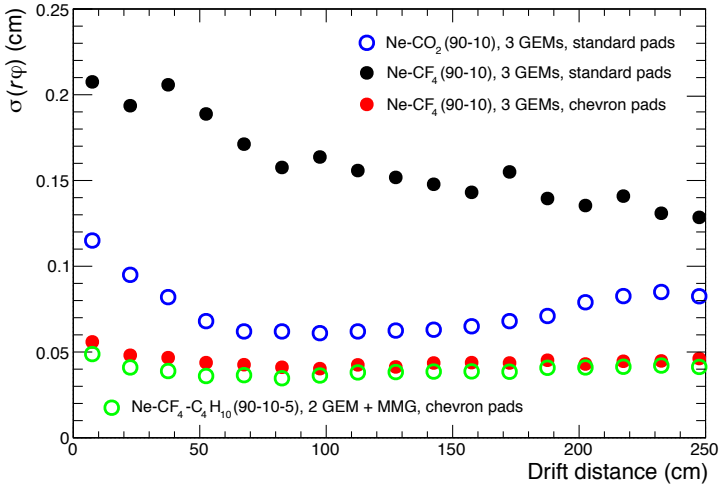

Figure 9.12: Space-point resolution in $r\varphi$ obtained with rectangular and chevron pads in different gas mixtures.

The combined ITS-TPC momentum resolution as a function of p_T is shown in Fig. 9.13. In a triple GEM system using Ne-CO_2 (90-10) and the present rectangular pad shape the resolution is worse by 5 – 10 % as compared with the present MWPC readout. When using Ne-CF_4 (90-10) as gas mixture and with chevron pad readout the resolution of the present MWPC readout is restored or even slightly improved.

9.2.1 Conclusion and outlook

As shown for a triple GEM system, the usage of Ne-CF_4 (90-10) and chevron-shaped readout pads could remove the deterioration of the p_T resolution with the baseline gas mixture and rectangular readout pads due to the reduced position resolution in certain parts of the drift volume (see Sec. 7.2.2). However, it should be noted that the full charged particle tracking scheme in the ALICE central barrel includes also the Transition Radiation Detector (TRD), which improves the overall resolution by about a factor two, making the differences between the different design choices in the TPC smaller. Still, a slight improvement using Ne-CF_4 (90-10) can be achieved if chevron pads are employed.

The strongest argument in favor of Ne-CF_4 (90-10) is the larger drift velocity that will lead to a significant decrease of the event pileup. However, comprehensive studies are necessary to investigate the chemical properties of CF_4 in combination with the materials used in the TPC. A detailed R&D study is presently being prepared.

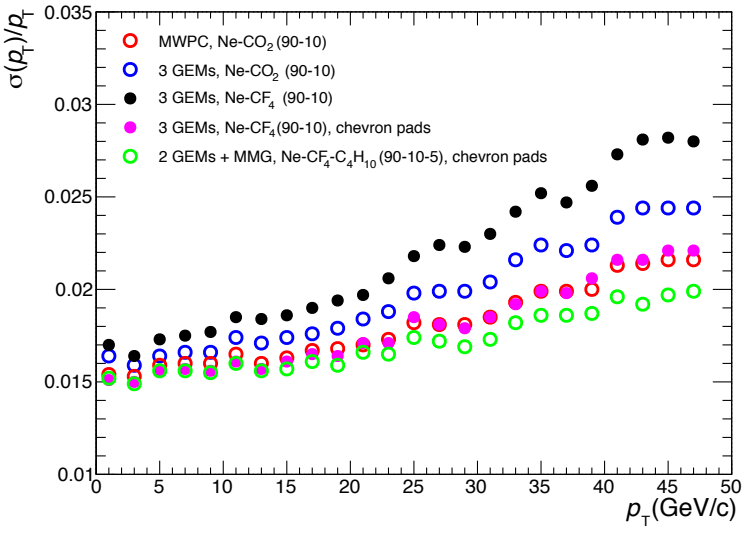

Figure 9.13: Combined ITS-TPC momentum resolution for MWPC (red open circles) and triple GEM system obtained with rectangular and chevron pads in different gas mixtures.

9.3 R&D with hybrid gain structures: 2 GEMs + MicroMegas

MicroMegas (MMG) intrinsically have very low ion backflow due to the very high ratio of the values of the electric fields in the small amplification gap to the drift field above the MMG. Ion backflow values of less than 1 % have been measured [5, 6].

Stable operation of an MMG detector at gains of $1-10\times10^3$, necessary to measure single-charged MIPs, is challenging. To overcome this limitation, studies have been carried out with hybrid GEM + MMG detectors, with the primary goal to achieve stable operation [7–9]. The addition of a GEM to the gain structure has the advantage of "preamplifying" the signal such that the MMG can be operated at a lower gain. Furthermore, the GEM spreads the electron cloud in space transverse to the drift direction, distributing the signal over a larger spot on the MMG. Both effects lead to an increased stability of the MMG. Discharge rates of $< 10^{-5}$ at gains of 10^4 were measured in [10] for such hybrid structures. It was also established that the MMG has very good energy resolution. Finally, the technology for large-scale production of MMG detectors is in hand [11].

Based on existing measurements and experience, a hybrid gain structure using two GEM foils above an MMG appears to be a promising candidate to be able to achieve very low IBF and stable operation, while maintaining good spatial and energy resolution. A detailed response simulation was carried out using 2 GEM + MMG with a chevron pad readout plane. The resulting $r\varphi$ and momentum resolutions are shown in Figs. 9.12 and 9.13 (see Sec. 9.2). The addition of a second GEM should reduce further the ion backflow and allow operation of all elements at modest gains.

A newly constructed hybrid 2 GEM + MMG chamber using standard $10\times10\,\mathrm{cm}^2$ GEM foils and an MMG with 400 LPI[4]of the same size was operated to perform ion backflow and energy resolution measurements. Figure 9.14 shows the setup. The measurements were performed using the two mixtures Ar-CO_2 (70-30) and Ar-CO_2 (90-10) with GEM foil voltages set to achieve a constant total GEM + MMG gain and the required drift, transfer and induction fields. Results are shown in Fig. 9.15. The voltage on the MMG mesh was varied to change the ratio of the fields above and below the MMG mesh (see Fig. 9.14). The ratios of the currents at the cathode and the at the anode have been measured using a radioactive source. The dependence of the ion backflow on the MMG voltage is shown in the left panel of Fig. 9.15 (red) along with the FWHM for the peak from ^{55}Fe X-rays (blue).

[4]Lines-Per-Inch (LPI)

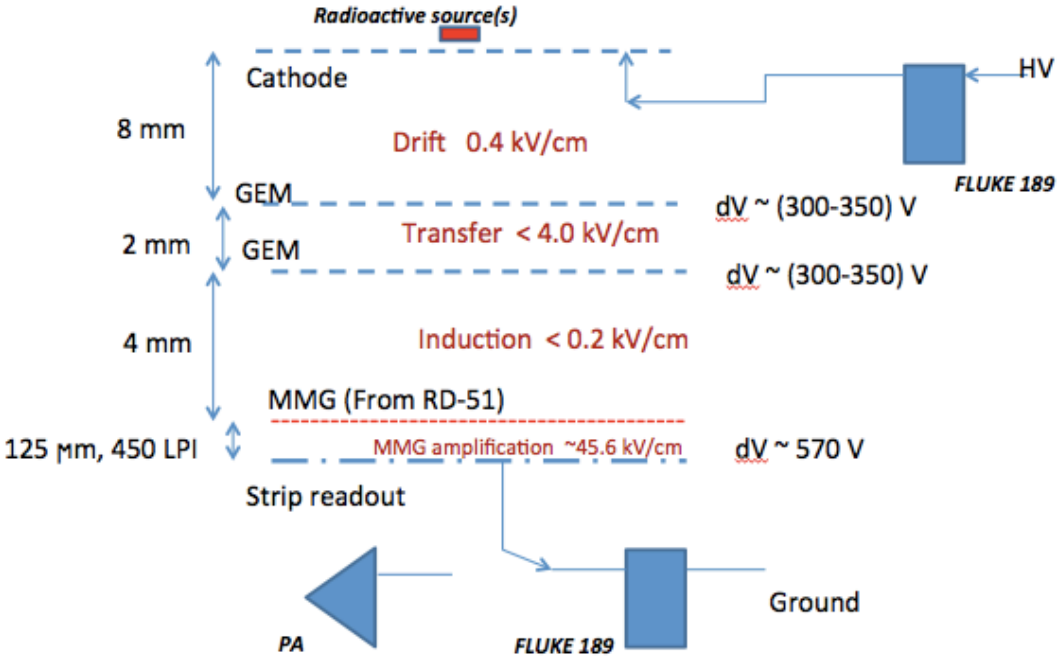

Figure 9.14: Setup used for preliminary ion backflow measurement for the hybrid 2 GEM + MMG system.

The following settings were used for these measurements: $E_{\text{drift}} = 0.4\,\text{kV/cm}$, $E_{\text{T1}} = 3.5\,\text{kV/cm}$, $E_{\text{ind}} = 0.125\,\text{kV/cm}$, total gain = $3.5\ (\pm\ 0.5) \times 10^3$. For the 620 V mesh setting four measurements were made over a range of source intensities varying by a factor of 10. All 4 ion backflow measurements are in the range $0.15 - 0.16\,\%$, consistent with the measurement error. At each MMG voltage setting the total gain was adjusted and the resolution checked by measuring the PH spectrum at the anode (read-out plane) with a standard CSP and shaper and an ADC with the chamber illuminated by a ^{55}Fe source (right panel in Fig. 9.15).

Encouraged by these measurements, a new MMG is being procured for further studies. Since also the mesh pitch influences the ion backflow performance of an MMG system [6], it is expected that the ion

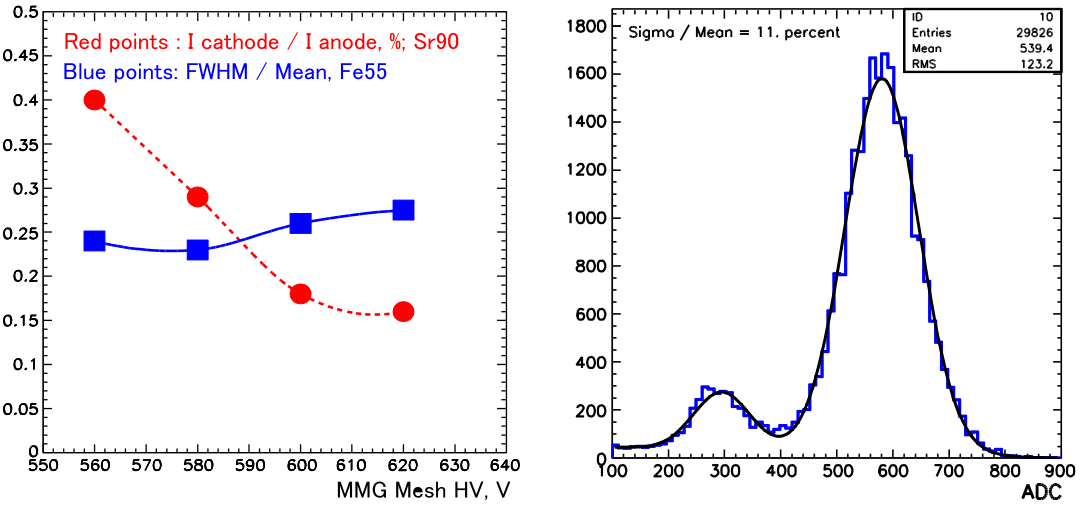

Figure 9.15: (Left) Preliminary ion backflow measurement for hybrid 2 GEM + MMG system. The horizontal scale is the voltage on the MMG mesh. The vertical scale is the ratio of cathode to anode currents in % (red points) and the FWHM of the ^{55}Fe peak (blue boxes). (Right) Typical PH spectrum from the hybrid 2 GEM + MMG system irradiated with an ^{55}Fe source.

backflow can be suppressed further by a factor of about $1.5-2$ by using a finer mesh with ≥ 600 lines-per-inch. Such an MMG is currently being sought for the continuation of the tests, which will include also the use of Ne-CO_2 and Ne-CF_4 gas mixtures.

9.3.1 Conclusion and outlook

The above R&D program is undertaken to explore the 2 GEM + MMG gain structure as a possible alternative to the present baseline quadruple GEM structures. In addition to ion backflow, energy resolution and discharge properties, we will also study the potential impact that the adoption of this alternative gain structure would have on the overall project execution plan including cost and schedule. A final report on this R&D is expected in spring 2015.

Chapter 10

Detector control system

The TPC detector control system (DCS) is part of the global ALICE DCS and will follow its evolution accordingly. Since a large part of the TPC hardware will not be replaced after RUN 2, also the corresponding DCS subsystems will not be redesigned. The implementation of the control of new TPC components will be adapted to the current one. This concerns the high voltage control for the new readout chambers (GEM HV control) as well as the front-end electronics configuration and monitoring.

10.1 Overview

The upgrade of the DCS system and its interface with the online farm will be described in detail in the Online Systems Technical Design Report, which will be available in the year 2014.

10.1.1 Hardware architecture

The hardware architecture of the TPC DCS can be divided into three functional layers. The *field layer* contains the actual hardware to be controlled (power supplies, front-end electronics...). The *control layer* consists of devices for collecting and processing information from the field layer and making it available to the *supervisory layer*. At the same time the devices of the control layer receive commands from the supervisory layer to be processed and distributed to the field layer. The equipment in the supervisory layer consists of computers and servers, providing the user interfaces and connecting to central DCS infrastructure consisting of fileservers, database servers managing the configuration and archival data, etc. The three layers interface mainly through a local area network (LAN).

10.1.2 Software architecture

The software architecture is a tree structure that represents the structure of the TPC, its subsystems and devices. The structure, as shown in Fig. 10.1, is composed of control and device units with a single top node (TPC DCS). The control unit steers the sub-tree below it and the device unit drives a device. The behavior and functionality of each control unit is implemented as a finite state machine.

The control system is built using a control framework that includes drivers for the different types of hardware, communication protocols, and configurable components for commonly used applications such as high or low voltage power supplies [1, 2].

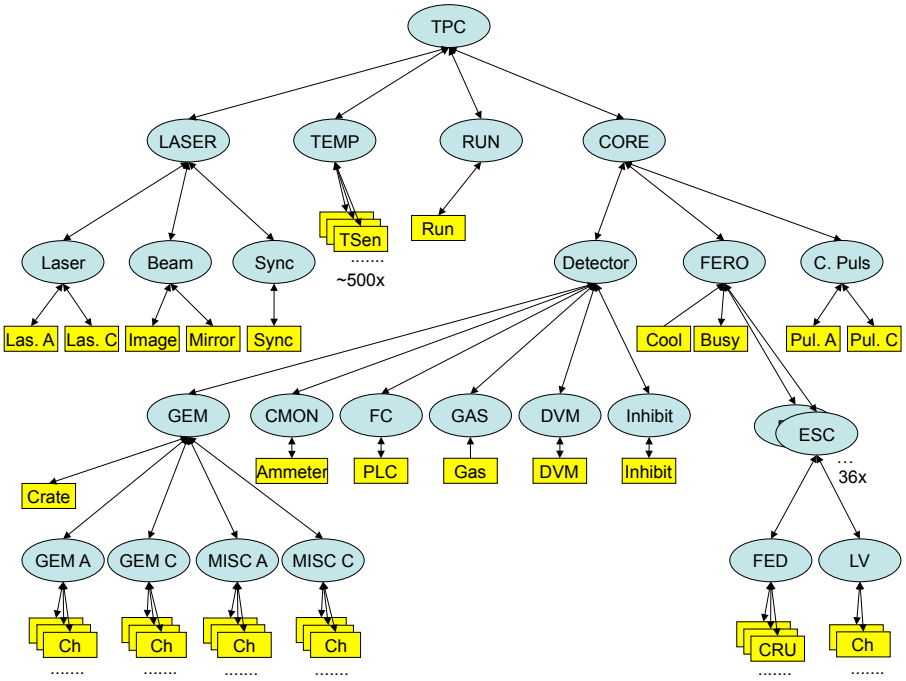

Figure 10.1: Overview of the software architecture of the DCS. The tree structure is build out of Device Units (boxes) and Control Units (ellipses).

10.1.3 System implementation

The core software of the control system is the commercial SCADA[1] system SIMATIC WinCC Open Architecture (OA), formerly known as PVSS II, from the company ETM [3]. WinCC OA is an object-oriented process visualization and control system that is used in industry as well as by the four LHC experiments. It is event-driven and has a highly distributed architecture. The SCADA System for the TPC is currently distributed over 12 computers.

10.1.4 Interfaces to devices

Where possible, commercial servers using the OPC[2] standard of process control are used to interface the SCADA system to devices. OPC servers interface the field cage high voltage, the front-end electronics low voltage and the temperature monitoring system. For the readout chamber HV control the usage of the OPC standard is envisaged as well. For non-commercial hardware the communication can be based on the communication framework Distributed Information Management (DIM [4]). In a similar approach DIM is currently used in the laser system, in the drift velocity monitor and the calibration pulser control and will be used for the front-end electronics control and monitoring.

10.1.5 Interlocks

The safety of the detector is based on three layers of interlocks:

- **Internal interlock**: The internal mechanism of devices (e.g. power supply trip) are used wherever applicable. The threshold and status of these interlocks are controlled by the SCADA system, but their function is independent of the communication between hardware and software.
- **External interlock**: The interlocks between different subsystems are realized using Programmable Logical Controller (PLC) systems with the possibility to enable or disable them.

[1] Supervisory Controls And Data Acquisition (SCADA)
[2] Open Platform Communications (OPC)

– **Software interlock**. Software interlocks are realized in the supervisory layer. They rely on the communication between the hardware and the SCADA system and are thus only used to prevent the system from unwanted but not harmful events like switching off the power supplies under full load. The safety of the equipment does not rely on the software interlocks.

Internal interlocks are used for the readout chamber high voltage, the field cage high voltage, the front-end electronics low voltage, the cooling and the gas system. External interlocks are implemented for the field cage high voltage, the front-end electronics low voltage and the cooling system. Software interlocks are used for the readout chamber high voltage, the front-end electronics low voltage and the front-end electronics. In addition to the interlocks, the alert system of the SCADA system is set up to inform the shift crew of unusual or potentially dangerous situations.

10.2 Front-end electronics control

The new front-end electronics (see Chap. 6) requires an updated DCS subsystem. It should provide monitoring of temperatures, voltages, currents and status information and the ability to configure the front-end electronics for data taking with different run types.

10.2.1 Overview

A schematic of the front-end electronics control is shown in Fig. 10.2. Between the common readout unit (CRU) system in the control room and the on-detector electronics (front-end cards), the readout architecture foresees 6336 GBT unidirectional links for the readout of the physics data. Interleaved with the physics data about 1 % or less of DCS monitoring data will be transmitted on the same links to the CRU where it is extracted and sent through a dedicated DCS output link to a DCS front-end processor. The DCS front-end processor is a computer that hosts a dedicated front-end server application, which pre-processes and filters the monitoring data and forwards it to the SCADA system for further processing (alarm handling) and display. It also handles configuration requests from the supervisory layer. The configuration data from the configuration data base and other control data (commands) are sent from the CRU to the FECs via 1584 unidirectional links for the timing, trigger and clock distribution system (TTS).

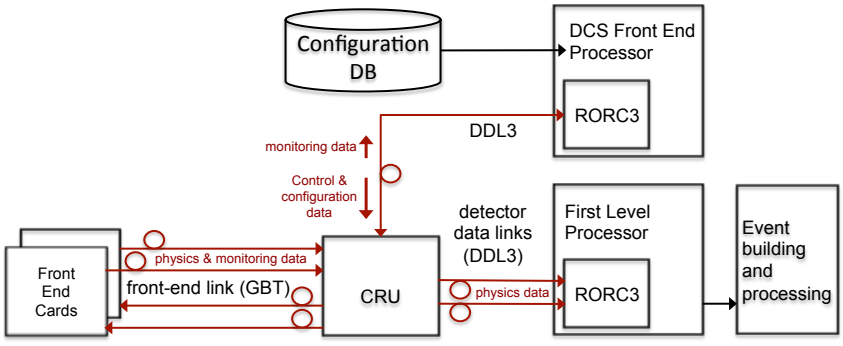

Figure 10.2: Schematic of the front-end electronics control and monitoring.

10.2.2 Monitoring

The SCADA system implements archiving and automatic checking of the monitoring data that it receives from the front-end server, mainly consisting of temperatures, voltages, currents and status information. Graphical user interfaces allow to display the data. Experience has shown that such functionality is very useful as it allows to identify problems such as voltage drops or locally reduced cooling performance.

10.2.3 Configuration and control

Each configuration of the TPC front-end electronics includes about 5 million configurable parameters. The parameters for the FE chips, FECs and CRUs are stored in a configuration database hosted on central DCS ORACLE servers. Configurations may change over time due to disfunctional or replaced hardware or due to changing hardware behavior.

Only simple configuration commands are passed from the supervisory layer to the FE server, which handles the actual configuration process. The command contains only a parameter which describes the configuration type. Based on this the FE server assembles queries to the configuration database which retrieve the configuration data for each CRU and its associated equipment.

10.3 Parameter export for online calibration and reconstruction

Many parameters that are gathered by the DCS system are of relevance for the online calibration and reconstruction in the online systems.

- **Environmental conditions data**: The temperature and pressure trends are of special importance for the drift velocity and gain calibration of the TPC data. They have to be made available to the online calibration and reconstruction algorithms with a time granularity of a few Hz.
- **GEM currents and detector status**: The currents measured in the different GEM HV segments are directly related to the amount of space charge produced in the corresponding section of the drift volume. In order to correct online for space-charge effects (see Sec. 7.4.3), the currents must be measured with a precision of nA and must be included in the TPC data stream in order to be immediately available (see Sec. 11.4.1). Moreover, the status of the HV channels has to be available in order to identify tripped GEM sectors where the voltage is below nominal or ramping. This can be achieved by reading the currents from digital current meters through ethernet into a computer that is included in the online processing farm. In this way the GEM currents and HV states can be continuously injected into the data stream. The same computer runs a server software making the currents available also to the DCS system (see Fig. 10.3).

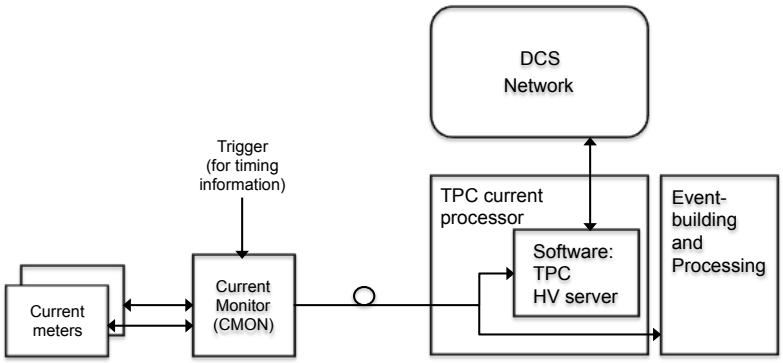

Figure 10.3: Schematic showing how the GEM current values can be read out for online calibration and DCS.

- **Front-end configuration**: The latest FE configuration parameters (e.g. inactive regions and analog and DSP parameters) are also of importance to the online calibration and reconstruction algorithms and are thus exported for each data taking session in a suitable format.
- **Further parameters** of relevance for the online calibration and reconstruction algorithms include the status of the laser system to identify periods with laser activity during a data taking session. The list of needed parameters will probably be extended.

Chapter 11

Installation, commissioning and services

11.1 General

In this chapter the installation of the GEM readout chambers into the TPC, the subsequent commissioning of the new front-end electronics and readout system, and the re-installation of the upgraded TPC in the ALICE cavern are described. In addition, all the required services to operate the TPC are discussed and necessary upgrades and modifications are introduced. The total time estimated for the exchange of the readout chambers and electronics, various upgrade activities and pre-commissioning on the surface is estimated to be approximately 40 weeks.

11.2 Installation

For the installation of the GEM readout chambers, the TPC is removed from its position in the ALICE cavern and moved into the so-called Delphi frame to give it the proper mechanical support. Then it can be moved by crane and truck to the clean room in building SXL2. Due to the sensitivity of the GEM foils to dust a clean room class ISO 7 (corresponding roughly to class 10,000) is envisaged.

Installation tool For the dismounting of the MWPCs and the installation of the GEM readout chambers (see Sec. 2.3) a special tool has been developed and successfully used in the past (photos see [1]). For the proper positioning of this tool, it is attached to a hydraulically controlled platform (the so-called Yellow Platform) and allows access to one side of the TPC at a time (Fig. 11.1). Save operation of the installation tool requires two trained persons.

11.3 Commissioning

After the installation of the GEM readout chambers they have to be aligned to ensure the planarity of the readout plane. This procedure is described in [1]. After the two SSWs are mounted in front of the end plates the front-end electronics can be mounted together with the connections to LV, HV, and the cooling distribution system. To ensure the proper working of the new chambers a pre-commissioning phase in the clean room follows. This includes pedestal and noise measurements as well as calibration pulser tests to validate the full functionality of the readout. For this purpose, a cooling system for at least two sectors at a time and the corresponding readout chain has to be available in the clean room. In the next step, the TPC is connected to a gas system and measurements of cosmic rays, using a dedicated trigger system, will be performed. In addition, a laser system generates tracks at well-defined positions for alignment purposes.

In Tab. 11.1 an overview of the main installation steps is given together with the corresponding time

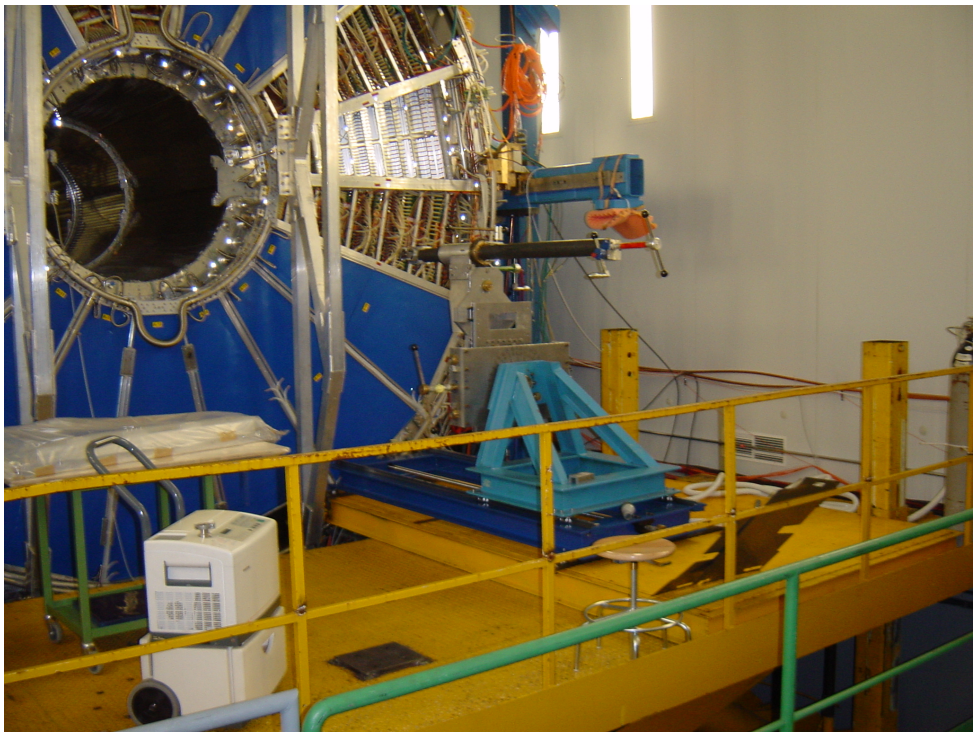

Figure 11.1: TPC with the Yellow Platform and the mounting tool.

estimates. These are partly based on past experience.

Activity		duration (weeks)
Dismantling of FEE, SSWs. Removal of temperature sensors etc.		3
Replacement of ROCs		12
Modification of SSWs	(4 weeks in parallel)	-
Resistor Rod modifications	(1 week in parallel)	-
Survey and ROC alignment		4
Mounting of temperature sensors etc.	(1 week in parallel)	-
Sealing		1
Leak test with He		1
FEE installation		5
Leak test with operating gas mixture	(1 week in parallel)	
Installation and upgrade of cooling pipes, cables		2
Pulser, cosmics and laser tests (2 sectors at a time)		10
Contingency		2
Total		40

Table 11.1: Time required for the most relevant activities of the GEM readout installation and commissioning in the clean room (SXL2), partly based on past pre-commissioning experience, partly estimated.

Installation in the ALICE cavern After all pre-commissioning measurements in the clean room are performed, the TPC can be moved from the clean room into the ALICE cavern. To protect against influences from ambient conditions i.e., rain and or large temperature gradients, the TPC will be properly packed before being placed on a truck and transported to the ALICE building where it is lowered into the pit by crane. Once installed, the final commissioning of the GEM TPC will be performed. Essentially all measurements from the clean room will be repeated in the cavern, now involving the full detector.

11.4 Services

In this section the various services necessary to operate the TPC are described and necessary modifications and upgrades are discussed.

11.4.1 High voltage

Readout chamber high voltage

For the operation of the GEM stacks new high voltage power supplies with negative output voltage are required. Due to the use of voltage dividers (see Sec. 4.4) the required current is much larger than before. We estimate 2 mA to achieve the necessary voltage stability. The use of actively regulated voltage dividers are an attractive option. They are presently under development [2] and would possibly allow to operate the divider chains at lower currents while still keeping voltage variations (relevant for the $\mathrm{d}E/\mathrm{d}x$ resolution) sufficiently small under changing loads.

A new fast high-precision current monitoring system for the GEM currents is foreseen to allow the estimation of space charge due to the positive ion backflow with high time granularity. It will monitor the currents to the individual GEM foils, i.e. after the voltage divider. The precision should allow to measure the GEM currents down to 100 pA and up to 10 μA at a sampling rate of 1 kHz. In total 8 x 72 channels are needed. A schematic drawing of the input stage of such a device is shown in Fig. 11.2. In Sec. 10.3 the overall setup with emphasis on the connection to DCS and DAQ is described.

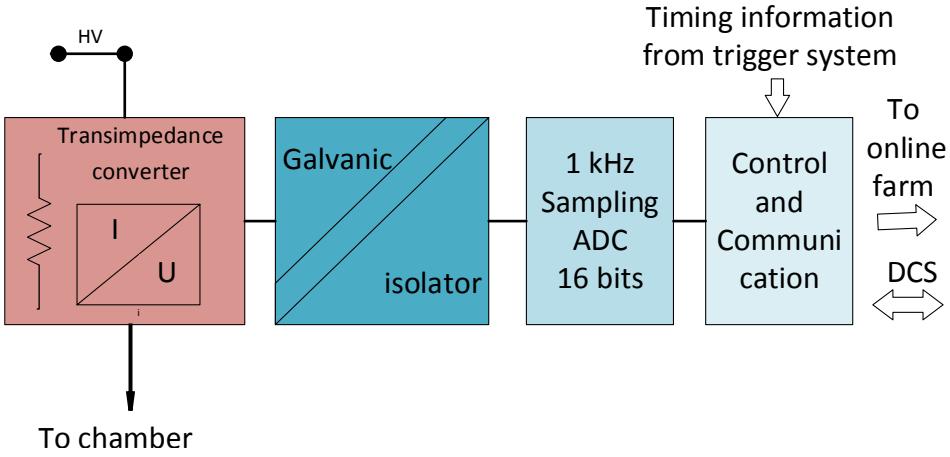

Figure 11.2: Schematic diagram illustrating the working principle of the current monitoring system.

The chamber high-voltage setup mapping the 32 channels of a set of HV modules to the 18 sectors per side of the TPC is schematically shown in Fig. 11.3. A similar scheme is used for the OROCs.

Field cage high voltage

The present system providing the drift high voltage of 100 kV for the field cage (Heinzinger power supply) has proven to work well and will remain unmodified. Since the upper side of the first GEM layer is on a potential of about -3 kV (see Sec. 2.4), depending on the gain settings, additional high voltage supplies are needed to allow the adjustment of the voltage at the ground end of the four voltage dividers (voltage of the last strip of the field cage) to different GEM gain settings. They are connected to the bottom of the voltage divider replacing the static last resistor in the present setup. This is illustrated in Fig. 11.4.

The total current across the four voltage dividers of the TPC is about 374 μA. Therefore, each of the four power supplies has to be able to work as a current sink and accommodate up to 100 μA current.

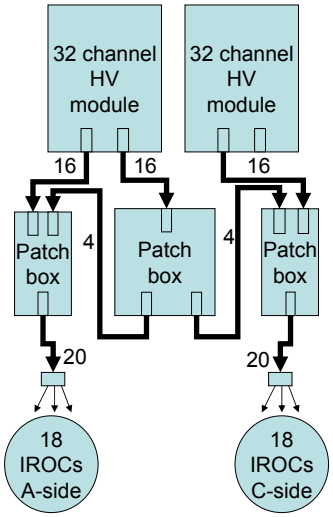

Figure 11.3: Mapping scheme of the high voltage power supplies to the IROCs.

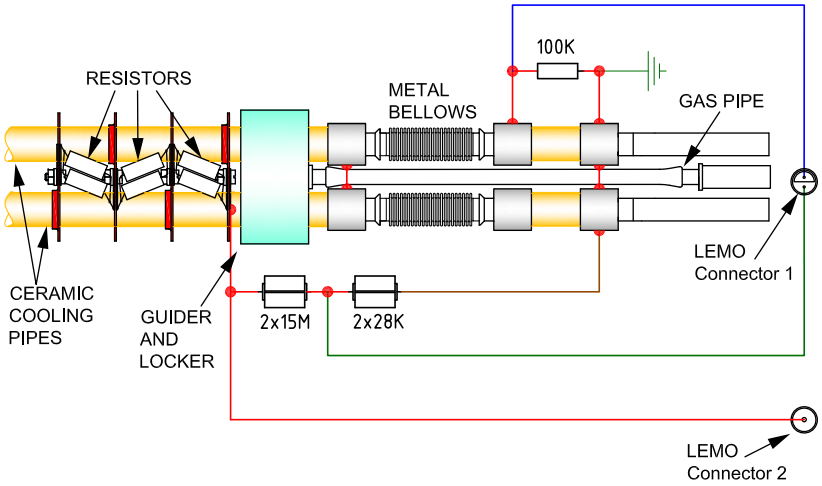

Figure 11.4: Schematic diagram of the ground sides of the four resistor rods indicating the connections to the current measuring system (connector 1) and to the new HV power supply (connector 2).

11.4.2 Low voltage

The present setup of the low voltage system supplying the voltages to the front-end electronics has worked well in the past and can be reused without modifications [1]. It provides separate voltages for the analog and digital parts of the front-end electronics. The presently foreseen new readout electronics for the GEM based chambers will most likely need less voltage and less overall power (see Tab. 6.2).

Also the LV cables connecting the power supply to the local distribution boards via bus bars running along the spokes of the SSW within the sectors can be reused. The low voltage setup is schematically shown in Fig. 11.5 indicating the supply of two sectors by one power supply module.

In Tab. 11.2 the parameters of the LV power supplies are listed.

11.4.3 Cooling

FEE cooling

The cooling system for the front-end electronics is an under-pressure leak-less water cooled system. It has gone through several upgrades in the past and is considered to be well suited for the cooling of the

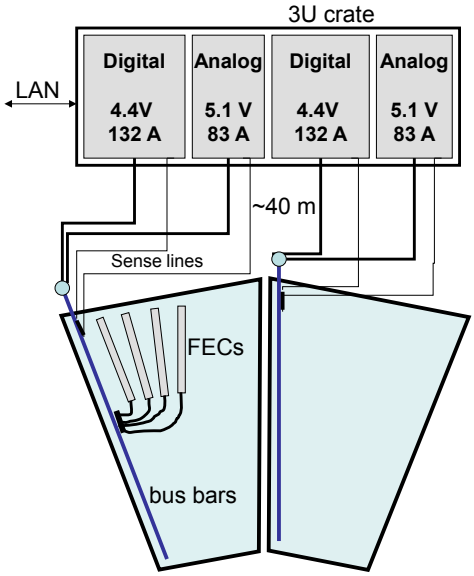

Figure 11.5: Schematic of the low voltage setup for two sectors indicating typical voltages and currents for the present system.

Supply	channels/crate	nom. power (W)	voltage (V)	max. current (V)	continuous current (A)
Analog	2	600	2 - 7	115	100
Digital	2	1200	2 - 7	230	200

Table 11.2: Specifications of the existing LV power supply system.

new front-end electronics. Due to the lower power consumption foreseen, also the presently available cooling power (25 kW) will be sufficient. Nevertheless, some minor modifications mainly regarding the leak tightness are envisaged.

Resistor rod cooling

For the cooling of the resistor rods a separate cooling plant is used. It is also an under-pressure leak-less water cooled system, however, with well controlled conductivity, since the water is exposed to the very high voltage (100 kV) of the field cage. For the future activities, only minor modifications are foreseen. These include better control of the flow through the resistor rods and better heat exchangers close to the TPC for better temperature control and stability.

Heat screens

To thermally separate the TPC from neighboring detectors two different heat screens are used. The outer heat screen isolates the TPC from the TRD and is supplied by the cooling plant of the TRD due to the use of aluminum cooling panels (unlike the FEE cooling system which uses copper based pipes and components). No changes are foreseen here. For the shielding against thermal effects from the ITS the inner heat screen is used. Due to the use of stainless steel cooling panels it can be supplied by the TPC cooling plant. No major changes are foreseen at this time.

11.4.4 Calibration

Calibration pulser

For the monitoring and gain calibration of the readout electronics a calibration pulser system will be installed. It is connected to the output side of the last GEM and injects charge into the pre-amplifiers by sending a voltage step to the bottom side of GEM 4. Its working principle is schematically shown in

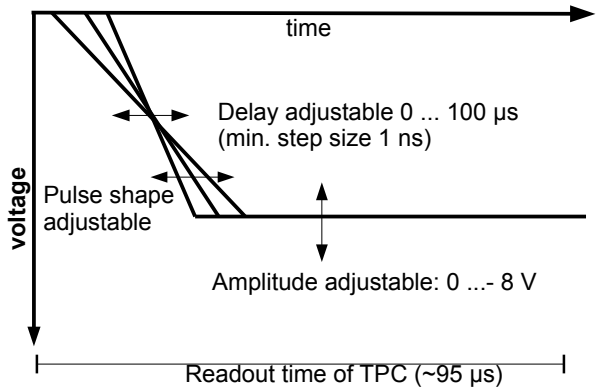

Figure 11.6: Working principle of the calibration pulser system.

Fig. 11.6. The potential of the bottom side of GEM 4 is determined by the induction field and is typically around 1 kV. Therefore, a decoupling HV capacitor is needed. Its capacity should be as small as possible in order not to store charge that could lead to damages of the front-end electronics in case of a discharge. Depending on the necessary signal amplitudes it may be possible to reuse the existing calibration pulser setup shown schematically in Fig. 11.7. The present design provides amplitudes of up to -3.5 V. Since it is foreseen to modify the ALICE trigger hardware, a new connection to the trigger and clock distribution needs to be developed. The remote control of the system by DCS will be modified to allow direct access via network.

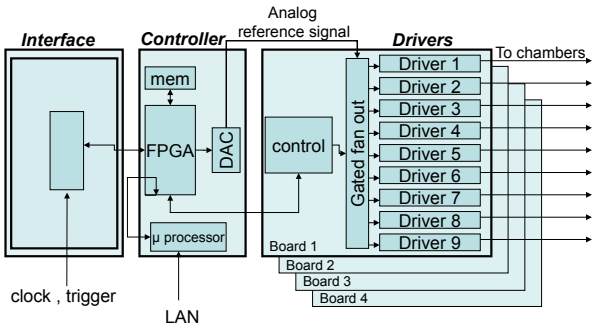

Figure 11.7: Schematic setup of the calibration pulser system.

Laser

The laser system provides tracks at well defined locations in the TPC and represents an important calibration tool [1]. The hardware may need some upgrades over time like the exchange of the frame grabbers of the cameras due to obsolete components of the system. To accommodate new requirements we may change to diode pumped lasers since it improves our capability to generate laser events at a higher rate compared to the present flashlight pumped laser system. This would facilitate the monitoring of space-charge distortion corrections (see Sec. 8.5.2). Like for the calibration pulser system, the connection to the trigger system and the control via network has to be upgraded when changing to continuous readout.

Krypton calibration

Another important calibration tool is the Krypton calibration, described in Sec. 8.6.1. The container with the Rubidium source decaying into the radioactive Krypton is connected to a bypass line in the gas system and there is no change foreseen in the way it is used [1].

Chapter 12

Project organization, cost estimate and time line

12.1 Participating institutions

The list of institutions participating in the TPC upgrade is shown in Tab. 12.1. About half of the groups were involved in the construction and operation of the present TPC. New institutes have recently joined the TPC collaboration, among them a large number of US groups, that bring in significant expertise in GEM technology, detector construction, engineering, electronics, and computing. The full TPC upgrade collaboration list is shown in App. B.

The TPC upgrade project is represented and coordinated by a project leader, two deputy project leaders and a technical coordinator, as shown in Fig. 12.1. The TPC upgrade project is split into a number of sub-projects, covering all relevant aspects of detector development, installation, software development, simulation, online computing and calibration. The TPC upgrade project emerges from the existing TPC project structure and partially overlaps with it. Items or components where only minor modifications to the present system are involved (e.g. laser system, gas system, detector control system) are not shown in Fig. 12.1.

The sharing of responsibilities for the TPC upgrade among the participating institutions is shown in Tab. 12.2.

12.2 Cost estimate

The CORE cost estimate for the TPC upgrade is summarized in Tab. 12.3. CORE costs include detector components and production cost as well as external manpower for production and installation. They do not include cost for internal manpower, basic infrastructure, and R&D.

A provisional funding scheme includes the following major contributions: The possibility of funds of the order of 50 % of the total cost is indicated by the German BMBF and HGF. A substantial contribution to the TPC upgrade is foreseen by the groups from the US, where the construction, assembly and test of the IROCs will be conducted. This will be part of a wider involvement of US-DOE into the upgrade of the ALICE central barrel detectors. A provisional funding scheme is consistent with a US-DOE CORE contribution to the TPC that corresponds to the IROC fraction of the total cost ($\sim 36\,\%$). The development of the SAMPA ASIC within a common ALICE project is conducted by the Electrical Engineering-Polytechnical School, University of São Paulo. Funds from Brazil for the development, production, and test of the TPC SAMPA chips are envisaged. The Common Readout Unit CRU is being developed by groups from the Wigner Research Center for Physics, Budapest, and from VECC, Kolkata,

Country Funding Agency	City	Institute
Croatia	Zagreb	Department of Physics, University of Zagreb
Denmark	Copenhagen	Niels Bohr Institute, University of Copenhagen
Finland	Helsinki	Helsinki Institute of Physics
Germany BMBF	Bonn	Helmholtz-Institut für Kern- und Strahlenphysik, Rheinische Friedrich-Wilhelms-Universität Bonn
Germany BMBF	Frankfurt	Institut für Kernphysik, Johann Wolfgang Goethe-Universität Frankfurt
Germany BMBF	Heidelberg	Physikalisches Institut, Ruprecht-Karls Universität Heidelberg
Germany BMBF	Munich	Physik Department, Technische Universität München
Germany BMBF	Tübingen	Physikalisches Institut, Eberhard Karls Universität Tübingen
Germany BMBF	Worms	FH Worms, Worms
Germany GSI	Darmstadt	Research Division and ExtreMe Matter Institute EMMI, GSI Helmholtzzentrum für Schwerionenforschung
Hungary	Budapest	Wigner Research Center for Physics, Budapest
India	Kolkata	Bose Institute
India	Bhubaneswar	Institute of Physics
India	Bhubaneswar	National Institute of Science Education and Research
India	Indore	Indian Institute of Technology
India	Mumbai	Indian Institute of Technology
India	Kolkata	Variable Energy Cyclotron Centre
Japan	Tokyo	University of Tokyo
Mexico	Mexico City	Instituto de Ciencias Nucleares, Universidad Nacional Autónoma de México
Norway	Bergen / Tonsberg	Department of Physics, University of Bergen, Vestfold University College, Tonsberg
Norway	Bergen	Faculty of Engineering, Bergen University College
Pakistan	Islamabad	Department of Physics, COMSATS Institute of Information Technology Islamabad
Poland	Cracow	The Henryk Niewodniczanski Institute of Nuclear Physics, Polish Academy of Science
Romania	Bucharest	National Institute for Physics and Nuclear Engineering
Slovakia	Bratislava	Faculty of Mathematics, Physics and Informatics, Comenius University
Sweden	Lund	Division of Experimental High Energy Physics, University of Lund
USA DOE	Omaha	Creighton University, Omaha, Nebraska
USA DOE	Houston	University of Houston, Houston, Texas
USA DOE	Berkeley	Lawrence Berkeley National Laboratory, Berkeley, California
USA DOE	Livermore	Lawrence Livermore National Laboratory, Livermore, California
USA DOE	Oak Ridge	Oak Ridge National Laboratory, Oak Ridge, Tennessee
USA DOE	West Lafayette	Purdue University, West Lafayette, Indiana
USA DOE	Knoxville	University of Tennessee, Knoxville, Tennessee
USA DOE	Austin	The University of Texas at Austin, Austin, Texas
USA DOE	Detroit	Wayne State University, Detroit, Michigan
USA DOE	New Haven	Yale University, New Haven, Connecticut
USA NSF	San Luis Obispo	California Polytechnic State University, San Luis Obispo, California
USA NSF	Chicago	Chicago State University, Chicago, Illinois

Table 12.1: List of institutions participating in the TPC upgrade.

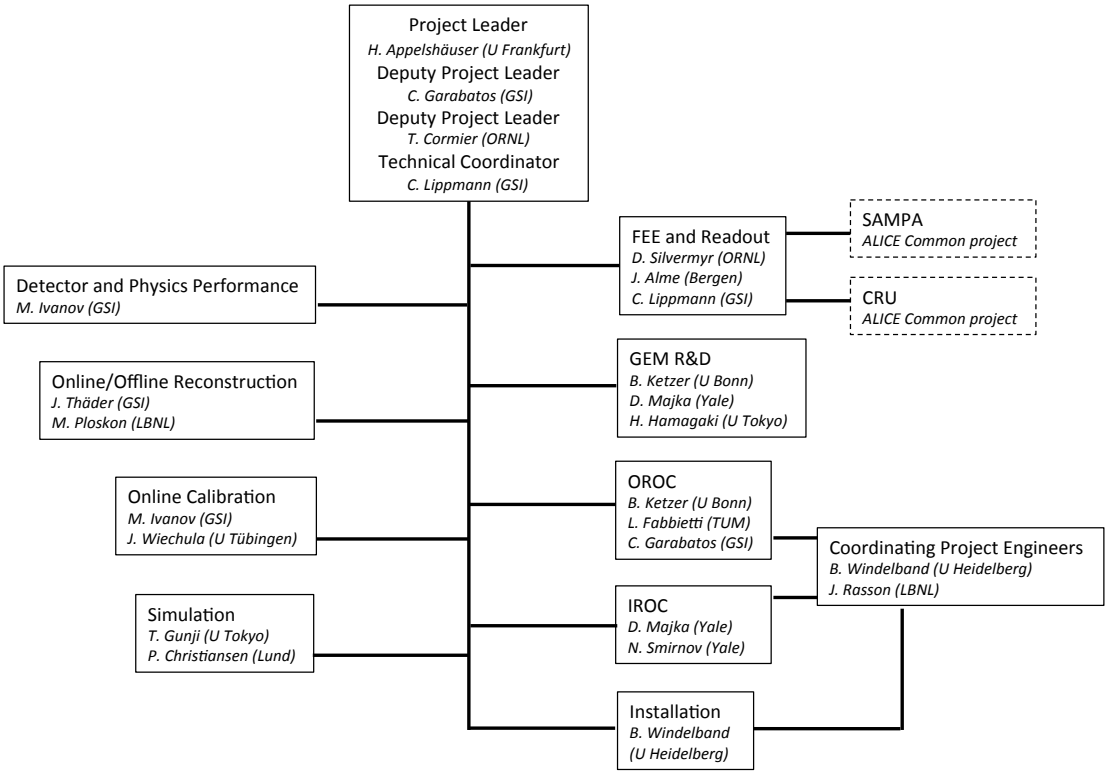

Figure 12.1: Structure of the TPC upgrade project.

Item	**Institution**
IROC	Yale, Detroit, Oak Ridge, Knoxville, Austin
OROC	Munich, Frankfurt, GSI, Heidelberg, Budapest, Bucharest
GEM R&D and QA	Helsinki, Munich, Tokyo, Yale, Zagreb, GSI
Frontend Card	Lund, Oak Ridge
FEE integration and test	Oak Ridge, Lund, Houston, Tokyo, Bergen, Oslo, GSI
HV, LV, cooling	Mexico-City, GSI, Munich
Detector Control	GSI, Worms
Installation and engineering	Heidelberg, Berkeley
Gas system and field cage	GSI
SAMPA ASIC	São Paulo, Bergen, Oslo
CRU	Budapest, Kolkata, Bergen

Table 12.2: Sharing of responsibilities for construction and installation of the TPC upgrade. Note that SAMPA ASIC and CRU are parts of common ALICE projects.

in close collaboration with CERN. India and Hungary have indicated the possibility of funding for the production cost of the TPC CRU. Further requests for funding are presently being prepared by the groups from Finland, Japan, Mexico, Norway, and Sweden.

Readout chambers	Quantity (incl. spares)	Cost (MCHF)
GEM foils[1]	480	0.5
Frames and components	960	0.1
Pad planes	160	0.4
Chamber bodies	80	0.3
HV divider	80	0.1
Assembly and installation tooling		0.4
Total Readout Chambers		**1.8**
Services		Cost (MCHF)
GEM HV system		0.2
Fast current monitoring		0.2
HV supply for last FC resistor		0.1
Other services		0.2
Total Services		**0.7**
FEE and Readout	Quantity (incl. spares)	Cost (MCHF)
SAMPA ASIC	19,500	0.78
Front-end card	3900	0.35
GBTx ASIC	7000	0.38
Optical transmitters/receivers	5500	0.79
CRU (control room, AMC40)		2.00
Optical fibers	9000	1.32
TPC Event Processing Nodes (TPC-EPN)		1.00
Other		0.02
Total Electronics		**6.64**
Total IROC	40	3.3
Total OROC	40	5.84
Total		**9.14**

Table 12.3: CORE cost estimate for the TPC upgrade.

12.3 Schedule

The current LHC schedule foresees LS2 to start in summer 2018. This defines the time schedule for the TPC upgrade, see Fig. 12.2. Major technological choices will have to be made by the middle of 2015 to allow finalization of the design, a timely procurement of detector materials and preparation of the series production. Such decisions involve a definition of the GEM geometry and configuration, as well as their operational point. This implies a sustained R&D effort in 2014 and early 2015. Particular emphasis will be put on a set of detailed measurements to characterize the discharge properties of the baseline system under exposure to different radiation sources. Besides proceeding the studies with small prototypes, a further test campaign of full-size IROC prototypes equipped with a quadruple GEM stack will be performed in autumn 2014. This includes a test beam time at the PS with mixed electron and pion beams to validate the $\mathrm{d}E/\mathrm{d}x$ performance of this configuration, and a stability test with hadron beams at the SPS. Similar studies are foreseen to allow a final conclusion on possible technological alternatives.

[1] This number assumes 4 GEM segments per IROC and 12 GEM segments per OROC, see Chap. 4. Two segments can be processed on a single foil. In addition, 50% spares are included. This yields a total of $0.5 \cdot 1.5 \cdot (40 \cdot 4 + 40 \cdot 12) = 480$ foils.

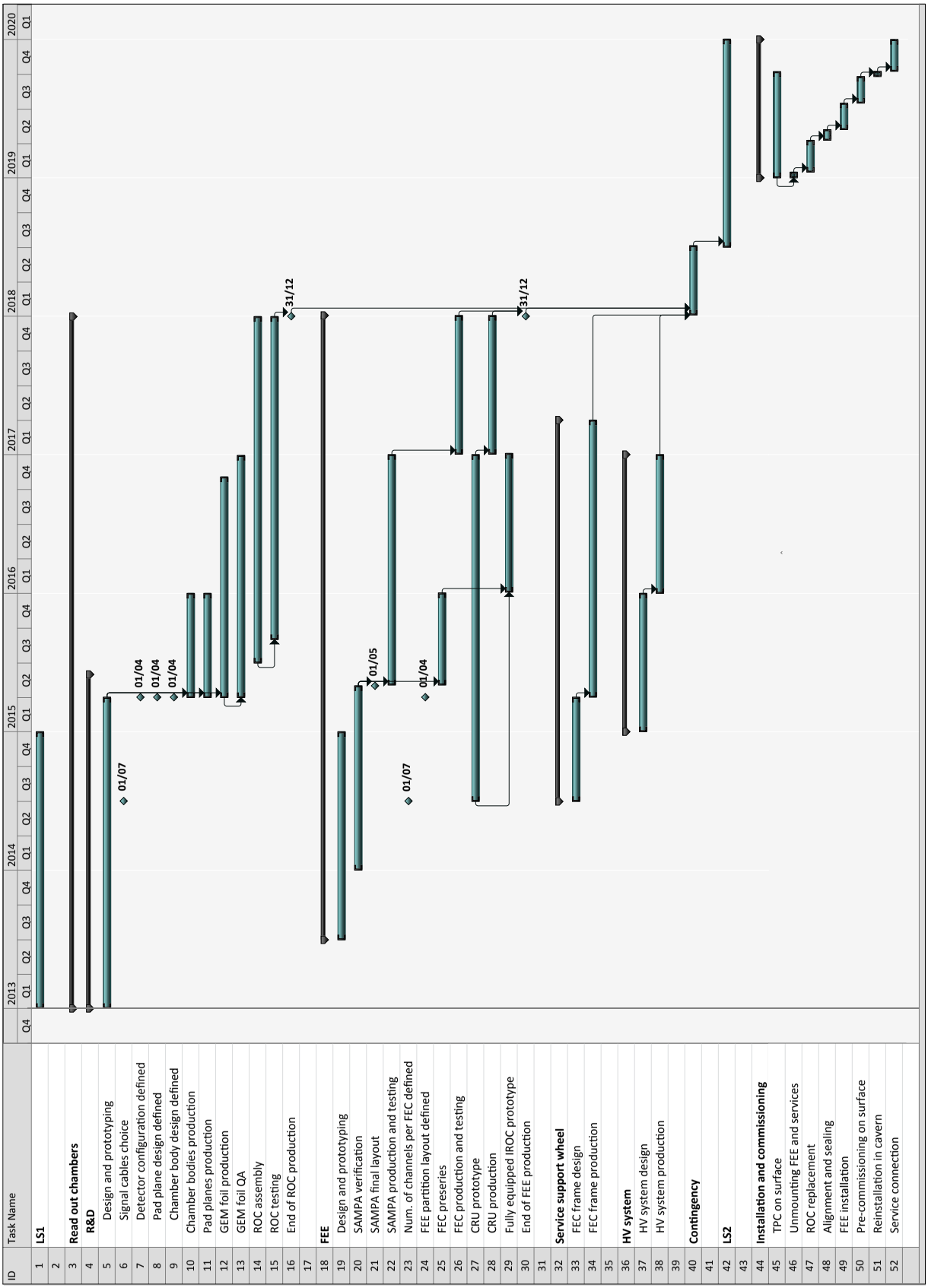

Figure 12.2: Time line for the TPC upgrade.

Moreover, the availability of GEM foils from different suppliers needs to be investigated. At present, three possible suppliers exist: TechEtch (USA), SciEnergy (Japan) and CERN TS-DEM. Foils from all three suppliers are being studied.

The assembly and test of the readout chambers will be distributed among various collaborating institutions in Europe (OROCs) and the US (IROCs), making optimum use of their experience, resources and facilities (see Tab. 12.2). Delivery of the tested readout chambers to CERN will happen at the beginning of 2018. A similar timeline for R&D, production and test is imposed to the frontend electronics.

Since the GEM readout chamber installation will have to be carried out in a clean environment, the TPC must be removed from the cavern and moved into the SXL2 cleanroom on the P2 surface. In order to maximize the available time for the readout chamber and electronics installation, the TPC removal will take place at the beginning of LS2. The total duration of LS2 is 18 months. This will leave approximately 40 weeks for replacing readout chambers, installation of the new electronics and pre-commissioning on the surface before re-installation towards the end of the shutdown period (see also Sec. 11.3).

12.4 TPC upgrade TDR editorial committee

The editorial committee of this TDR was formed by the following persons:

H. Appelshäuser, M. Ball, P. Christiansen, C. Garabatos, P. Gasik, T. Gunji, J. Harris, M. Ivanov, B. Ketzer, C. Lippmann, A. Oskarsson, N. Smirnov, R. Renfordt, D. Röhrich, J. Thäder, J. Wiechula.

12.5 TPC upgrade TDR task force

The following persons have contributed to the work presented in this TDR:

H. Appelshäuser, M. Ball, G. Barnaföldi, E. Bartsch, J. Bloemer, P. Christiansen, T. Cormier, K. Eckstein, L. Fabbietti, C. Garabatos, F. Garcia, P. Gasik, T. Gunji, H. Hamagaki, J. Harris, E. Hellbär, D. Heuchel, A. Hönle, M. Ivanov, B. Ketzer, M. Kowalski, C. Lippmann, M. Ljunggren, J. Margutti, S. Masciocchi, A. Mathis, A. Oskarsson, V. Peskov, R. Renfordt, D. Röhrich, R. Shahoyan, D. Silvermyr, N. Smirnov, K. Terasaki, J. Thäder, D. Vranic, M. Weber, J. Wiechula, Y. Yamaguchi.

Appendix A

Coordinate systems

A.1 Global coordinate system

The global ALICE coordinate system [1] is a right-handed orthogonal cartesian system, which has its origin at the beam interaction point. A sketch of the global coordinate system is given in Fig. A.1.

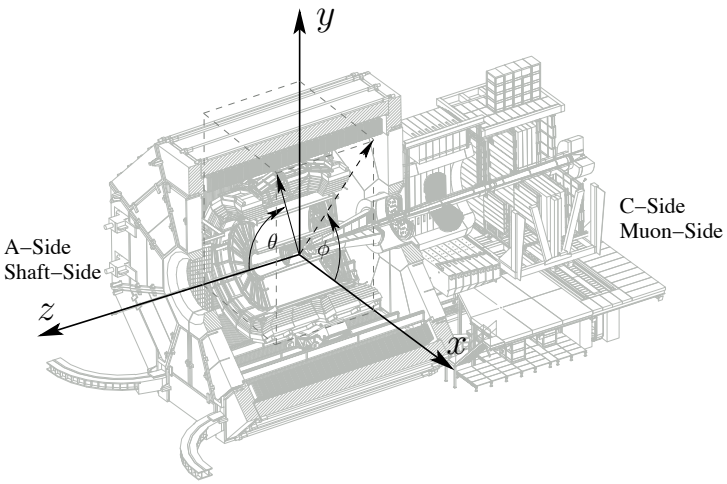

Figure A.1: ALICE global coordinate system.

Its z-axis is parallel to the mean beam direction, pointing towards the 'A-side', away from the muon arm. This side is also called shaft- or RB24-side. The opposite side (negative z values) is called C-side, or also Muon- or RB26-side. The x-axis is lying in the local horizontal accelerator plane, pointing towards the centre of the LHC ring. The side with positive x values is also called I-side (inner), the opposite side correspondingly O-side (outer). The y-axis is chosen to define a right-handed system, thus pointing upwards. The azimuthal angle φ is increasing counterclockwise, starting from the x-axis ($\varphi = 0$) and looking from the A-side towards the C-side. The polar angle θ is increasing from the z-axis towards the xy-plane.

A.2 Local coordinate system

To account for the azimuthal segmentation of the central barrel detectors, the reconstruction software uses a local coordinate system [2] related to a given sub-detector (TPC sector, ITS module etc.). The local coordinate system is a right-handed cartesian system as well. In case of the TPC, it has the same origin and z-axis as the global coordinate system, which is perpendicular to the sensitive planes of the TPC sectors. The local x-axis lies in the sensitive plane and is parallel to the pad rows. Therefore, the

pads in each row are in the direction of the y-axis. Small variations in the direction of the pads can be expressed as variations in $r \cdot \varphi$ and are often quoted as $r\varphi$. A sketch of the local coordinate system is given in Fig. A.2.

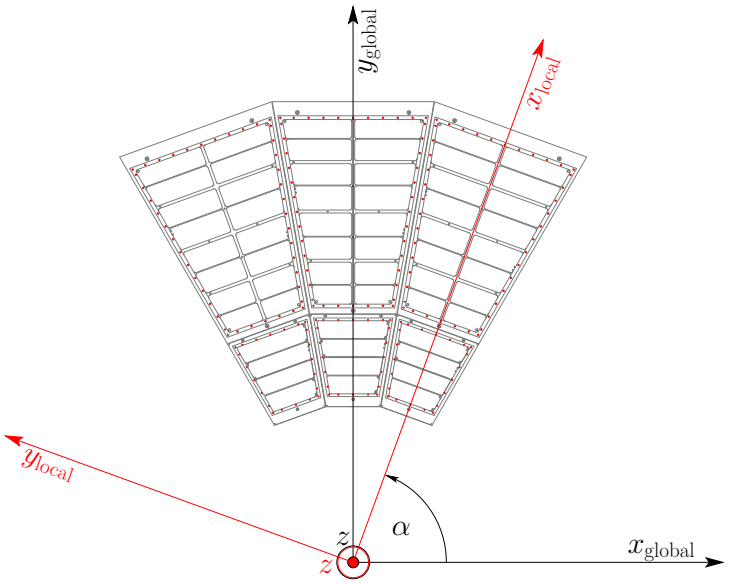

Figure A.2: ALICE local coordinate systems.

Appendix B

TPC upgrade collaboration

Department of Physics, University of Zagreb, Zagreb, Croatia
M. Planicic, N. Poljak, G. Simatovic, A. Utrobicic

Niels Bohr Institute, University of Copenhagen, Copenhagen, Denmark
J.J. Gaardhøje, B. Nielsen

Helsinki Institute of Physics, Helsinki, Finland
E. Brucken, F. Garcia, T. Hilden, J. Rak

Helmholtz-Institut für Kern- und Strahlenphysik, Rheinische Friedrich-Wilhelms-Universität, Bonn, Germany
F. Boehmer, B. Ketzer

Institut für Kernphysik, Johann Wolfgang Goethe-Universität, Frankfurt, Germany
W. Amend, H. Appelshäuser, M. Arslandok, E. Bartsch, T. Bröker, S. Heckel, E. Hellbär, D. Just, P. Lüttig, V. Peskov, F. Pliquett, P. Reichelt, R. Renfordt, A. Tarantola Peloni

Physikalisches Institut, Ruprecht-Karls Universität, Heidelberg, Germany
P. Glässel, J. Stachel, D. Vranic, B. Windelband

Physik Department, Technische Universität München, Germany
M. Ball, J. Bloemer, K. Eckstein, P. Gasik, D. Heuchel, A. Hönle, L. Fabbietti, J. Margutti, A. Mathis, S. Weber

Physikalisches Institut, Eberhard Karls Universität, Tübingen, Germany
H. Schmidt, J. Wiechula

FH Worms, Worms, Germany
R. Keidel

Research Division and ExtreMe Matter Institute EMMI, GSI Helmholtzzentrum für Schwerionenforschung, Darmstadt, Germany
A. Andronic, R. Averbeck, P. Braun-Munzinger, U. Frankenfeld, C. Garabatos, M. Ivanov, M. Köhler, M. Krzewicki, C. Lippmann, A. Marin, N. Martin, S. Masciocchi, D. Miskowiec, M. Nicassio, J. Otwinowski, C. Schmidt, K. Schweda, I. Selyuzhenkov, J. Thäder, J. Wagner

Wigner Research Center for Physics, Budapest, Hungary
G. Barnaföldi, G. Bencedi, G. Hamar, D. Varga

Bose Institute, Kolkata, India
S. Das, S.K. Ghosh, S.K. Prasad, S. Raha

Institute of Physics, Bhubaneswar, India
P. Sahu, N. Sharma

National Institute of Science Education and Research, Bhubaneswar, India
S. Biswas, L. Kumar, B. Mohanty

Indian Institute of Technology, Indore, India
A. Roy, R. Sahoo

Indian Institute of Technology, Mumbai, India
S. Dash, B.K. Nandi, R. Varma

Variable Energy Cyclotron Centre, Kolkata, India
Z. Ahammed, S. Chattopadhyay, A.K. Dubey, P. Ghosh, S.A. Khan, T.K. Nayak, S.K. Pal, J. Saini, R.N. Singaraju, Y.P. Viyogi

University of Tokyo, Tokyo, Japan
H. Hamagaki, T. Gunji, K. Terasaki, Y. Yamaguchi, K. Yukawa

Instituto de Ciencias Nucleares, Universidad Nacional Autónoma de México, Mexico-City, Mexico
G. Paic

Department of Physics and Technology, University of Bergen, Bergen, Norway
D. Röhrich, K. Ullaland, A. Velure

Faculty of Engineering, Bergen University College, Bergen, Norway
J. Alme, H. Helstrup

Department of Physics, University of Oslo, Oslo, Norway
K. Røed, S. Mahmood, C. Zhao

Department of Technology, Vestfold University College, Tonsberg, Norway
J. Lien, R. Langoey

Department of Physics, COMSATS Institute of Information Technology Islamabad, Islamabad, Pakistan
A. Bhatti, A. Rehman

The Henryk Niewodniczanski Institute of Nuclear Physics, Polish Academy of Science, Cracow, Poland
M. Kowalski, A. Matyja

National Institute for Physics and Nuclear Engineering, Bucharest, Romania
M. Petris, M. Petrovici

Faculty of Mathematics, Physics and Informatics, Comenius University, Bratislava, Slovakia
M. Pikna, B. Sitár, P. Strmeň, I. Szarka

Division of Particle Physics, University of Lund, Lund, Sweden
P. Christiansen, M. Ljunggren, L. Österman, E. Stenlund, A. Oskarsson, T. Richert

Creighton University, Omaha, Nebraska, USA
M. Cherney, M. Poghosyan, J. Seger

University of Houston, Houston, Texas, USA
R. Bellwied, S. Jena, D. McDonald, L. Pinsky, A. Timmins, M. Weber

Lawrence Berkeley National Laboratory, Berkeley, California, USA
D. Gangadharan, P.M. Jacobs, C. Loizides, M. Ploskon, J. Porter, J. Rasson, X. Zhang

Lawrence Livermore National Laboratory, Livermore, California, USA
R. Soltz

Oak Ridge National Laboratory, Oak Ridge, Tennessee, USA
T.M. Cormier, D.J. Dean, M. Middlebrook, K.F. Read, D. Silvermyr

Purdue University, West Lafayette, Indiana, USA
R.P. Scharenberg, B.K. Srivastava

University of Tennessee, Knoxville, Tennessee, USA
C. Nattrass, N. Sharma, S.P. Sorensen

The University of Texas at Austin, Austin, Texas, USA
A.G. Knospe, C. Markert, J. Schambach

Wayne State University, Detroit, Michigan, USA
R. Belmont, C.A. Pruneau, P. Pujahari, J. Putschke, M. Verweij, S. Voloshin

Yale University, New Haven, Connecticut, USA
H. Caines, M.E. Connors, J.W. Harris, R. Majka, R.J. Reed, T. Schuster, N. Smirnov

California Polytechnic State University, San Luis Obispo, California, USA
J. L. Klay

Chicago State University, Chicago, Illinois, USA
E. Garcia-Solis, A. Harton

Appendix C

The ALICE Collaboration

B. Abelev[72], J. Adam[37], D. Adamová[80], M.M. Aggarwal[84], M. Agnello[91,108], A. Agostinelli[26], N. Agrawal[44], Z. Ahammed[126], N. Ahmad[18], I. Ahmed[15], S.U. Ahn[65], S.A. Ahn[65], I. Aimo[91,108], S. Aiola[131], M. Ajaz[15], A. Akindinov[55], S.N. Alam[126], D. Aleksandrov[97], B. Alessandro[108], D. Alexandre[99], A. Alici[12,102], A. Alkin[3], J. Alme[35], T. Alt[39], S. Altinpinar[17], I. Altsybeev[125], C. Alves Garcia Prado[115], C. Andrei[75], A. Andronic[94], V. Anguelov[90], J. Anielski[50], T. Antičić[95], F. Antinori[105], P. Antonioli[102], L. Aphecetche[109], H. Appelshäuser[49], N. Arbor[68], S. Arcelli[26], N. Armesto[16], R. Arnaldi[108], T. Aronsson[131], I.C. Arsene[94,21], M. Arslandok[49], A. Augustinus[34], R. Averbeck[94], T.C. Awes[81], M.D. Azmi[18,86], M. Bach[39], A. Badalà[104], Y.W. Baek[40,67], S. Bagnasco[108], R. Bailhache[49], R. Bala[87], A. Baldisseri[14], M. Ball[89], F. Baltasar Dos Santos Pedrosa[34], R.C. Baral[58], R. Barbera[27], F. Barile[31], G.G. Barnaföldi[130], L.S. Barnby[99], V. Barret[67], J. Bartke[112], M. Basile[26], N. Bastid[67], S. Basu[126], B. Bathen[50], G. Batigne[109], B. Batyunya[63], P.C. Batzing[21], C. Baumann[49], I.G. Bearden[77], H. Beck[49], C. Bedda[91], N.K. Behera[44], I. Belikov[51], R. Bellwied[117], E. Belmont-Moreno[61], G. Bencedi[130], S. Beole[25], I. Berceanu[75], A. Bercuci[75], Y. Berdnikov[II,82], D. Berenyi[130], M.E. Berger[89], R.A. Bertens[54], D. Berzano[25], L. Betev[34], A. Bhasin[87], A.K. Bhati[84], B. Bhattacharjee[41], J. Bhom[122], L. Bianchi[25], N. Bianchi[69], C. Bianchin[54], J. Bielčík[37], J. Bielčíková[80], A. Bilandzic[77], S. Bjelogrlic[54], F. Blanco[10], D. Blau[97], C. Blume[49], F. Bock[90,71], A. Bogdanov[73], H. Bøggild[77], M. Bogolyubsky[52], F.V. Böhmer[89], L. Boldizsár[130], M. Bombara[38], J. Book[49], H. Borel[14], A. Borissov[93,129], F. Bossú[62], M. Botje[78], E. Botta[25], S. Böttger[48], P. Braun-Munzinger[94], T. Breitner[48], T.A. Broker[49], T.A. Browning[92], E. Bruna[108], G.E. Bruno[31], D. Budnikov[96], H. Buesching[49], S. Bufalino[108], P. Buncic[34], O. Busch[90], Z. Buthelezi[62], D. Caffarri[28], X. Cai[7], H. Caines[131], L. Calero Diaz[69], A. Caliva[54], E. Calvo Villar[100], P. Camerini[24], F. Carena[34], W. Carena[34], J. Castillo Castellanos[14], E.A.R. Casula[23], V. Catanescu[75], C. Cavicchioli[34], C. Ceballos Sanchez[9], J. Cepila[37], P. Cerello[108], B. Chang[118], S. Chapeland[34], J.L. Charvet[14], S. Chattopadhyay[126], S. Chattopadhyay[98], M. Cherney[83], C. Cheshkov[124], B. Cheynis[124], V. Chibante Barroso[34], D.D. Chinellato[117,116], P. Chochula[34], M. Chojnacki[77], S. Choudhury[126], P. Christakoglou[78], C.H. Christensen[77], P. Christiansen[32], T. Chujo[122], S.U. Chung[93], C. Cicalo[103], L. Cifarelli[12,26], F. Cindolo[102], J. Cleymans[86], F. Colamaria[31], D. Colella[31], A. Collu[23], M. Colocci[26], G. Conesa Balbastre[68], Z. Conesa del Valle[47], M.E. Connors[131], J.G. Contreras[11], T.M. Cormier[81,129], Y. Corrales Morales[25], P. Cortese[30], I. Cortés Maldonado[2], M.R. Cosentino[115], F. Costa[34], P. Crochet[67], R. Cruz Albino[11], E. Cuautle[60], L. Cunqueiro[69,34], A. Dainese[105], R. Dang[7], D. Das[98], I. Das[47], K. Das[98], S. Das[4], A. Dash[116], S. Dash[44], S. De[126], H. Delagrange[I,109], A. Deloff[74], E. Dénes[130], G. D'Erasmo[31], A. De Caro[29,12], G. de Cataldo[101], J. de Cuveland[39], A. De Falco[23], D. De Gruttola[12,29], N. De Marco[108], S. De Pasquale[29], R. de Rooij[54], M.A. Diaz Corchero[10], T. Dietel[50,86], R. Divià[34], D. Di Bari[31], S. Di Liberto[106], A. Di Mauro[34], P. Di Nezza[69], Ø. Djuvsland[17], A. Dobrin[54], T. Dobrowolski[74], D. Domenicis Gimenez[115], O. Dordic[21], S. Dørheim[89], A.K. Dubey[126],

A. Dubla[54], L. Ducroux[124], P. Dupieux[67], A.K. Dutta Majumdar[98], R.J. Ehlers[131], D. Elia[101], H. Engel[48], B. Erazmus[34,109], H.A. Erdal[35], D. Eschweiler[39], B. Espagnon[47], M. Esposito[34], M. Estienne[109], S. Esumi[122], D. Evans[99], S. Evdokimov[52], D. Fabris[105], J. Faivre[68], D. Falchieri[26], A. Fantoni[69], M. Fasel[90], D. Fehlker[17], L. Feldkamp[50], D. Felea[59], A. Feliciello[108], G. Feofilov[125], J. Ferencei[80], A. Fernández Téllez[2], E.G. Ferreiro[16], A. Ferretti[25], A. Festanti[28], J. Figiel[112], S. Filchagin[96], D. Finogeev[53], F.M. Fionda[31,101], E.M. Fiore[31], E. Floratos[85], M. Floris[34], S. Foertsch[62], P. Foka[94], S. Fokin[97], E. Fragiacomo[107], A. Francescon[28,34], U. Frankenfeld[94], U. Fuchs[34], C. Furget[68], M. Fusco Girard[29], J.J. Gaardhøje[77], M. Gagliardi[25], A.M. Gago[100], M. Gallio[25], D.R. Gangadharan[19,71], P. Ganoti[85,81], C. Garabatos[94], E. Garcia-Solis[13], C. Gargiulo[34], I. Garishvili[72], J. Gerhard[39], M. Germain[109], A. Gheata[34], M. Gheata[59,34], B. Ghidini[31], P. Ghosh[126], S.K. Ghosh[4], P. Gianotti[69], P. Giubellino[34], E. Gladysz-Dziadus[112], P. Glässel[90], A. Gomez Ramirez[48], P. González-Zamora[10], S. Gorbunov[39], L. Görlich[112], S. Gotovac[111], L.K. Graczykowski[128], A. Grelli[54], A. Grigoras[34], C. Grigoras[34], V. Grigoriev[73], A. Grigoryan[1], S. Grigoryan[63], B. Grinyov[3], N. Grion[107], J.F. Grosse-Oetringhaus[34], J.-Y. Grossiord[124], R. Grosso[34], F. Guber[53], R. Guernane[68], B. Guerzoni[26], M. Guilbaud[124], K. Gulbrandsen[77], H. Gulkanyan[1], M. Gumbo[86], T. Gunji[121], A. Gupta[87], R. Gupta[87], K. H. Khan[15], R. Haake[50], Ø. Haaland[17], C. Hadjidakis[47], M. Haiduc[59], H. Hamagaki[121], G. Hamar[130], L.D. Hanratty[99], A. Hansen[77], J.W. Harris[131], H. Hartmann[39], A. Harton[13], D. Hatzifotiadou[102], S. Hayashi[121], S.T. Heckel[49], M. Heide[50], H. Helstrup[35], A. Herghelegiu[75], G. Herrera Corral[11], B.A. Hess[33], K.F. Hetland[35], B. Hippolyte[51], J. Hladky[57], P. Hristov[34], M. Huang[17], T.J. Humanic[19], D. Hutter[39], D.S. Hwang[20], R. Ilkaev[96], I. Ilkiv[74], M. Inaba[122], G.M. Innocenti[25], C. Ionita[34], M. Ippolitov[97], M. Irfan[18], M. Ivanov[94], V. Ivanov[82], A. Jachołkowski[27], P.M. Jacobs[71], C. Jahnke[115], H.J. Jang[65], M.A. Janik[128], P.H.S.Y. Jayarathna[117], R.T. Jimenez Bustamante[60], P.G. Jones[99], H. Jung[40], A. Jusko[99], S. Kalcher[39], P. Kalinak[56], A. Kalweit[34], J. Kamin[49], J.H. Kang[132], V. Kaplin[73], S. Kar[126], A. Karasu Uysal[66], O. Karavichev[53], T. Karavicheva[53], E. Karpechev[53], U. Kebschull[48], R. Keidel[133], B. Ketzer[89], M.M. Khan[III,18], P. Khan[98], S.A. Khan[126], A. Khanzadeev[82], Y. Kharlov[52], B. Kileng[35], B. Kim[132], D.W. Kim[40,65], D.J. Kim[118], J.S. Kim[40], M. Kim[40], M. Kim[132], S. Kim[20], T. Kim[132], S. Kirsch[39], I. Kisel[39], S. Kiselev[55], A. Kisiel[128], G. Kiss[130], J.L. Klay[6], J. Klein[90], C. Klein-Bösing[50], A. Kluge[34], M.L. Knichel[94,90], A.G. Knospe[113], C. Kobdaj[110,34], M. Kofarago[34], M.K. Köhler[94], T. Kollegger[39], A. Kolojvari[125], V. Kondratiev[125], N. Kondratyeva[73], A. Konevskikh[53], V. Kovalenko[125], M. Kowalski[112,34], S. Kox[68], G. Koyithatta Meethaleveedu[44], J. Kral[118], I. Králik[56], F. Kramer[49], A. Kravčáková[38], M. Krelina[37], M. Kretz[39], M. Krivda[56,99], F. Krizek[80], M. Krzewicki[94], V. Kučera[80], Y. Kucheriaev[I,97], T. Kugathasan[34], C. Kuhn[51], P.G. Kuijer[78], I. Kulakov[39,49], J. Kumar[44], P. Kurashvili[74], A. Kurepin[53], A.B. Kurepin[53], A. Kuryakin[96], S. Kushpil[80], M.J. Kweon[46,90], Y. Kwon[132], P. Ladron de Guevara[60], C. Lagana Fernandes[115], I. Lakomov[47], R. Langoy[127], C. Lara[48], A. Lardeux[109], A. Lattuca[25], S.L. La Pointe[54,108], P. La Rocca[27], R. Lea[24], G.R. Lee[99], I. Legrand[34], J. Lehnert[49], R.C. Lemmon[79], V. Lenti[101], E. Leogrande[54], M. Leoncino[25], I. León Monzón[114], P. Lévai[130], S. Li[7,67], J. Lien[127], R. Lietava[99], S. Lindal[21], V. Lindenstruth[39], C. Lippmann[94], M.A. Lisa[19], H.M. Ljunggren[32], D.F. Lodato[54], P.I. Loenne[17], V.R. Loggins[129], V. Loginov[73], D. Lohner[90], C. Loizides[71], X. Lopez[67], E. López Torres[9], X.-G. Lu[90], P. Luettig[49], M. Lunardon[28], G. Luparello[54], C. Luzzi[34], R. Ma[131], A. Maevskaya[53], M. Mager[34], D.P. Mahapatra[58], S.M. Mahmood[21], A. Maire[51,90], R.D. Majka[131], M. Malaev[82], I. Maldonado Cervantes[60], L. Malinina[IV,63], D. Mal'Kevich[55], P. Malzacher[94], A. Mamonov[96], L. Manceau[108], V. Manko[97], F. Manso[67], V. Manzari[101,34], M. Marchisone[25,67], J. Mareš[57], G.V. Margagliotti[24], A. Margotti[102], A. Marín[94], C. Markert[113,34], M. Marquard[49], I. Martashvili[120], N.A. Martin[94], P. Martinengo[34], M.I. Martínez[2], G. Martínez García[109], J. Martin Blanco[109], Y. Martynov[3], A. Mas[109], S. Masciocchi[94], M. Masera[25], A. Masoni[103], L. Massacrier[109], A. Mastroserio[31], A. Matyja[112], C. Mayer[112], J. Mazer[120], M.A. Mazzoni[106], F. Meddi[22], A. Menchaca-Rocha[61], E. Meninno[29], J. Mercado Pérez[90], M. Meres[36], Y. Miake[122], K. Mikhaylov[63,55], L. Milano[34], J. Milosevic[V,21], A. Mischke[54], A.N. Mishra[45], D. Miśkowiec[94], J. Mitra[126], C.M. Mitu[59], J. Mlynarz[129], B. Mohanty[76,126], L. Molnar[51], L. Montaño Zetina[11], E. Montes[10], M. Morando[28], D.A. Moreira De Godoy[115],

S. Moretto[28], A. Morreale[109,118], A. Morsch[34], V. Muccifora[69], E. Mudnic[111], D. Mühlheim[50], S. Muhuri[126], M. Mukherjee[126], H. Müller[34], M.G. Munhoz[115], S. Murray[86], L. Musa[34], J. Musinsky[56], B.K. Nandi[44], R. Nania[102], E. Nappi[101], C. Nattrass[120], T.K. Nayak[126], S. Nazarenko[96], A. Nedosekin[55], M. Nicassio[94], M. Niculescu[59,34], B.S. Nielsen[77], S. Nikolaev[97], S. Nikulin[97], V. Nikulin[82], B.S. Nilsen[83], F. Noferini[12,102], P. Nomokonov[63], G. Nooren[54], A. Nyanin[97], J. Nystrand[17], H. Oeschler[90], S. Oh[131], S.K. Oh[VI,64,40], A. Okatan[66], L. Olah[130], J. Oleniacz[128], A.C. Oliveira Da Silva[115], J. Onderwaater[94], C. Oppedisano[108], A. Ortiz Velasquez[60,32], A. Oskarsson[32], J. Otwinowski[94], K. Oyama[90], P. Sahoo[45], Y. Pachmayer[90], M. Pachr[37], P. Pagano[29], G. Paić[60], F. Painke[39], C. Pajares[16], S.K. Pal[126], A. Palmeri[104], D. Pant[44], V. Papikyan[1], G.S. Pappalardo[104], P. Pareek[45], W.J. Park[94], S. Parmar[84], A. Passfeld[50], D.I. Patalakha[52], V. Paticchio[101], B. Paul[98], T. Pawlak[128], T. Peitzmann[54], H. Pereira Da Costa[14], E. Pereira De Oliveira Filho[115], D. Peresunko[97], C.E. Pérez Lara[78], A. Pesci[102], Y. Pestov[5], V. Petráček[37], M. Petran[37], M. Petris[75], M. Petrovici[75], C. Petta[27], S. Piano[107], M. Pikna[36], P. Pillot[109], L. Pinsky[117], D.B. Piyarathna[117], M. Płoskoń[71], M. Planinic[95,123], J. Pluta[128], S. Pochybova[130], P.L.M. Podesta-Lerma[114], M.G. Poghosyan[83,34], E.H.O. Pohjoisaho[42], B. Polichtchouk[52], N. Poljak[95,123], A. Pop[75], S. Porteboeuf-Houssais[67], J. Porter[71], B. Potukuchi[87], S.K. Prasad[129,4], R. Preghenella[12,102], F. Prino[108], C.A. Pruneau[129], I. Pshenichnov[53], M. Puccio[108], G. Puddu[23], P. Pujahari[129], V. Punin[96], J. Putschke[129], H. Qvigstad[21], A. Rachevski[107], S. Raha[4], J. Rak[118], A. Rakotozafindrabe[14], L. Ramello[30], R. Raniwala[88], S. Raniwala[88], S.S. Räsänen[42], B.T. Rascanu[49], D. Rathee[84], A.W. Rauf[15], V. Razazi[23], K.F. Read[120], J.S. Real[68], K. Redlich[VII,74], R.J. Reed[131,129], A. Rehman[17], P. Reichelt[49], M. Reicher[54], F. Reidt[34,90], R. Renfordt[49], A.R. Reolon[69], A. Reshetin[53], F. Rettig[39], J.-P. Revol[34], K. Reygers[90], V. Riabov[82], R.A. Ricci[70], T. Richert[32], M. Richter[21], P. Riedler[34], W. Riegler[34], F. Riggi[27], A. Rivetti[108], E. Rocco[54], M. Rodríguez Cahuantzi[2], A. Rodriguez Manso[78], K. Røed[21], E. Rogochaya[63], S. Rohni[87], D. Rohr[39], D. Röhrich[17], R. Romita[79,119], F. Ronchetti[69], L. Ronflette[109], P. Rosnet[67], A. Rossi[34], F. Roukoutakis[85], A. Roy[45], C. Roy[51], P. Roy[98], A.J. Rubio Montero[10], R. Rui[24], R. Russo[25], E. Ryabinkin[97], Y. Ryabov[82], A. Rybicki[112], S. Sadovsky[52], K. Šafařík[34], B. Sahlmuller[49], R. Sahoo[45], P.K. Sahu[58], J. Saini[126], C.A. Salgado[16], J. Salzwedel[19], S. Sambyal[87], V. Samsonov[82], X. Sanchez Castro[51], F.J. Sánchez Rodríguez[114], L. Šándor[56], A. Sandoval[61], M. Sano[122], G. Santagati[27], D. Sarkar[126], E. Scapparone[102], F. Scarlassara[28], R.P. Scharenberg[92], C. Schiaua[75], R. Schicker[90], C. Schmidt[94], H.R. Schmidt[33], S. Schuchmann[49], J. Schukraft[34], M. Schulc[37], T. Schuster[131], Y. Schutz[109,34], K. Schwarz[94], K. Schweda[94], G. Scioli[26], E. Scomparin[108], R. Scott[120], G. Segato[28], J.E. Seger[83], I. Selyuzhenkov[94], J. Seo[93], E. Serradilla[10,61], A. Sevcenco[59], A. Shabetai[109], G. Shabratova[63], R. Shahoyan[34], A. Shangaraev[52], N. Sharma[120,58], S. Sharma[87], K. Shigaki[43], K. Shtejer[25], Y. Sibiriak[97], S. Siddhanta[103], T. Siemiarczuk[74], D. Silvermyr[81], C. Silvestre[68], G. Simatovic[123], R. Singaraju[126], R. Singh[87], S. Singha[76,126], V. Singhal[126], B.C. Sinha[126], T. Sinha[98], B. Sitar[36], M. Sitta[30], T.B. Skaali[21], K. Skjerdal[17], N. Smirnov[131], R.J.M. Snellings[54], C. Søgaard[32], R. Soltz[72], J. Song[93], M. Song[132], F. Soramel[28], S. Sorensen[120], M. Spacek[37], I. Sputowska[112], M. Spyropoulou-Stassinaki[85], B.K. Srivastava[92], J. Stachel[90], I. Stan[59], G. Stefanek[74], M. Steinpreis[19], E. Stenlund[32], G. Steyn[62], J.H. Stiller[90], D. Stocco[109], M. Stolpovskiy[52], P. Strmen[36], A.A.P. Suaide[115], T. Sugitate[43], C. Suire[47], M. Suleymanov[15], R. Sultanov[55], M. Šumbera[80], T. Susa[95], T.J.M. Symons[71], A. Szabo[36], A. Szanto de Toledo[115], I. Szarka[36], A. Szczepankiewicz[34], M. Szymanski[128], J. Takahashi[116], M.A. Tangaro[31], J.D. Tapia Takaki[VIII,47], A. Tarantola Peloni[49], A. Tarazona Martinez[34], M.G. Tarzila[75], A. Tauro[34], G. Tejeda Muñoz[2], A. Telesca[34], C. Terrevoli[31], J. Thäder[94], D. Thomas[54], R. Tieulent[124], A.R. Timmins[117], A. Toia[105,49], H. Torii[121], V. Trubnikov[3], W.H. Trzaska[118], T. Tsuji[121], A. Tumkin[96], R. Turrisi[105], T.S. Tveter[21], J. Ulery[49], K. Ullaland[17], A. Uras[124], G.L. Usai[23], M. Vajzer[80], M. Vala[56,63], L. Valencia Palomo[47], S. Vallero[25,90], P. Vande Vyvre[34], L. Vannucci[70], J. Van Der Maarel[54], J.W. Van Hoorne[34], M. van Leeuwen[54], A. Vargas[2], M. Vargyas[118], R. Varma[44], M. Vasileiou[85], A. Vasiliev[97], V. Vechernin[125], M. Veldhoen[54], A. Velure[17], M. Venaruzzo[24], E. Vercellin[25], S. Vergara Limón[2], R. Vernet[8], L. Vickovic[111], G. Viesti[28],

J. Viinikainen[118], Z. Vilakazi[62], O. Villalobos Baillie[99], A. Vinogradov[97], L. Vinogradov[125], Y. Vinogradov[96], T. Virgili[29], V. Vislavicius[32], Y.P. Viyogi[126], A. Vodopyanov[63], M.A. Völkl[90], K. Voloshin[55], S.A. Voloshin[129], G. Volpe[34], B. von Haller[34], I. Vorobyev[125], D. Vranic[94,34], J. Vrláková[38], B. Vulpescu[67], A. Vyushin[96], B. Wagner[17], J. Wagner[94], V. Wagner[37], M. Wang[7,109], Y. Wang[90], D. Watanabe[122], M. Weber[34,117], S.G. Weber[94], J.P. Wessels[50], U. Westerhoff[50], J. Wiechula[33], J. Wikne[21], M. Wilde[50], G. Wilk[74], J. Wilkinson[90], M.C.S. Williams[102], B. Windelband[90], M. Winn[90], C. Xiang[7], C.G. Yaldo[129], Y. Yamaguchi[121], H. Yang[54], P. Yang[7], S. Yang[17], S. Yano[43], S. Yasnopolskiy[97], J. Yi[93], Z. Yin[7], I.-K. Yoo[93], I. Yushmanov[97], V. Zaccolo[77], C. Zach[37], A. Zaman[15], C. Zampolli[102], S. Zaporozhets[63], A. Zarochentsev[125], P. Závada[57], N. Zaviyalov[96], H. Zbroszczyk[128], I.S. Zgura[59], M. Zhalov[82], H. Zhang[7], X. Zhang[71,7], Y. Zhang[7], C. Zhao[21], N. Zhigareva[55], D. Zhou[7], F. Zhou[7], Y. Zhou[54], Zhou, Zhuo[17], H. Zhu[7], J. Zhu[109,7], X. Zhu[7], A. Zichichi[26,12], A. Zimmermann[90], M.B. Zimmermann[34,50], G. Zinovjev[3], Y. Zoccarato[124], M. Zyzak[49,39]

Affiliation Notes

[I] Deceased
[II] Also at: St. Petersburg State Polytechnical University
[III] Also at: Department of Applied Physics, Aligarh Muslim University, Aligarh, India
[IV] Also at: M.V. Lomonosov Moscow State University, D.V. Skobeltsyn Institute of Nuclear Physics, Moscow, Russia
[V] Also at: University of Belgrade, Faculty of Physics and "Vinča" Institute of Nuclear Sciences, Belgrade, Serbia
[VI] Permanent Address: Konkuk University, Seoul, Korea
[VII] Also at: Institute of Theoretical Physics, University of Wroclaw, Wroclaw, Poland
[VIII] Also at: University of Kansas, Lawrence, KS, United States

Collaboration Institutes

[1] A.I. Alikhanyan National Science Laboratory (Yerevan Physics Institute) Foundation, Yerevan, Armenia
[2] Benemérita Universidad Autónoma de Puebla, Puebla, Mexico
[3] Bogolyubov Institute for Theoretical Physics, Kiev, Ukraine
[4] Bose Institute, Department of Physics and Centre for Astroparticle Physics and Space Science (CAPSS), Kolkata, India
[5] Budker Institute for Nuclear Physics, Novosibirsk, Russia
[6] California Polytechnic State University, San Luis Obispo, CA, United States
[7] Central China Normal University, Wuhan, China
[8] Centre de Calcul de l'IN2P3, Villeurbanne, France
[9] Centro de Aplicaciones Tecnológicas y Desarrollo Nuclear (CEADEN), Havana, Cuba
[10] Centro de Investigaciones Energéticas Medioambientales y Tecnológicas (CIEMAT), Madrid, Spain
[11] Centro de Investigación y de Estudios Avanzados (CINVESTAV), Mexico City and Mérida, Mexico
[12] Centro Fermi - Museo Storico della Fisica e Centro Studi e Ricerche "Enrico Fermi", Rome, Italy
[13] Chicago State University, Chicago, USA
[14] Commissariat à l'Energie Atomique, IRFU, Saclay, France
[15] COMSATS Institute of Information Technology (CIIT), Islamabad, Pakistan
[16] Departamento de Física de Partículas and IGFAE, Universidad de Santiago de Compostela, Santiago de Compostela, Spain

[17] Department of Physics and Technology, University of Bergen, Bergen, Norway
[18] Department of Physics, Aligarh Muslim University, Aligarh, India
[19] Department of Physics, Ohio State University, Columbus, OH, United States
[20] Department of Physics, Sejong University, Seoul, South Korea
[21] Department of Physics, University of Oslo, Oslo, Norway
[22] Dipartimento di Fisica dell'Università 'La Sapienza' and Sezione INFN Rome, Italy
[23] Dipartimento di Fisica dell'Università and Sezione INFN, Cagliari, Italy
[24] Dipartimento di Fisica dell'Università and Sezione INFN, Trieste, Italy
[25] Dipartimento di Fisica dell'Università and Sezione INFN, Turin, Italy
[26] Dipartimento di Fisica e Astronomia dell'Università and Sezione INFN, Bologna, Italy
[27] Dipartimento di Fisica e Astronomia dell'Università and Sezione INFN, Catania, Italy
[28] Dipartimento di Fisica e Astronomia dell'Università and Sezione INFN, Padova, Italy
[29] Dipartimento di Fisica 'E.R. Caianiello' dell'Università and Gruppo Collegato INFN, Salerno, Italy
[30] Dipartimento di Scienze e Innovazione Tecnologica dell'Università del Piemonte Orientale and Gruppo Collegato INFN, Alessandria, Italy
[31] Dipartimento Interateneo di Fisica 'M. Merlin' and Sezione INFN, Bari, Italy
[32] Division of Experimental High Energy Physics, University of Lund, Lund, Sweden
[33] Eberhard Karls Universität Tübingen, Tübingen, Germany
[34] European Organization for Nuclear Research (CERN), Geneva, Switzerland
[35] Faculty of Engineering, Bergen University College, Bergen, Norway
[36] Faculty of Mathematics, Physics and Informatics, Comenius University, Bratislava, Slovakia
[37] Faculty of Nuclear Sciences and Physical Engineering, Czech Technical University in Prague, Prague, Czech Republic
[38] Faculty of Science, P.J. Šafárik University, Košice, Slovakia
[39] Frankfurt Institute for Advanced Studies, Johann Wolfgang Goethe-Universität Frankfurt, Frankfurt, Germany
[40] Gangneung-Wonju National University, Gangneung, South Korea
[41] Gauhati University, Department of Physics, Guwahati, India
[42] Helsinki Institute of Physics (HIP), Helsinki, Finland
[43] Hiroshima University, Hiroshima, Japan
[44] Indian Institute of Technology Bombay (IIT), Mumbai, India
[45] Indian Institute of Technology Indore, Indore (IITI), India
[46] Inha University, Incheon, South Korea
[47] Institut de Physique Nucléaire d'Orsay (IPNO), Université Paris-Sud, CNRS-IN2P3, Orsay, France
[48] Institut für Informatik, Johann Wolfgang Goethe-Universität Frankfurt, Frankfurt, Germany
[49] Institut für Kernphysik, Johann Wolfgang Goethe-Universität Frankfurt, Frankfurt, Germany
[50] Institut für Kernphysik, Westfälische Wilhelms-Universität Münster, Münster, Germany
[51] Institut Pluridisciplinaire Hubert Curien (IPHC), Université de Strasbourg, CNRS-IN2P3, Strasbourg, France
[52] Institute for High Energy Physics, Protvino, Russia
[53] Institute for Nuclear Research, Academy of Sciences, Moscow, Russia
[54] Institute for Subatomic Physics of Utrecht University, Utrecht, Netherlands
[55] Institute for Theoretical and Experimental Physics, Moscow, Russia
[56] Institute of Experimental Physics, Slovak Academy of Sciences, Košice, Slovakia
[57] Institute of Physics, Academy of Sciences of the Czech Republic, Prague, Czech Republic
[58] Institute of Physics, Bhubaneswar, India
[59] Institute of Space Science (ISS), Bucharest, Romania
[60] Instituto de Ciencias Nucleares, Universidad Nacional Autónoma de México, Mexico City, Mexico
[61] Instituto de Física, Universidad Nacional Autónoma de México, Mexico City, Mexico
[62] iThemba LABS, National Research Foundation, Somerset West, South Africa

[63] Joint Institute for Nuclear Research (JINR), Dubna, Russia
[64] Konkuk University, Seoul, South Korea
[65] Korea Institute of Science and Technology Information, Daejeon, South Korea
[66] KTO Karatay University, Konya, Turkey
[67] Laboratoire de Physique Corpusculaire (LPC), Clermont Université, Université Blaise Pascal, CNRS–IN2P3, Clermont-Ferrand, France
[68] Laboratoire de Physique Subatomique et de Cosmologie (LPSC), Université Joseph Fourier, CNRS-IN2P3, Institut Polytechnique de Grenoble, Grenoble, France
[69] Laboratori Nazionali di Frascati, INFN, Frascati, Italy
[70] Laboratori Nazionali di Legnaro, INFN, Legnaro, Italy
[71] Lawrence Berkeley National Laboratory, Berkeley, CA, United States
[72] Lawrence Livermore National Laboratory, Livermore, CA, United States
[73] Moscow Engineering Physics Institute, Moscow, Russia
[74] National Centre for Nuclear Studies, Warsaw, Poland
[75] National Institute for Physics and Nuclear Engineering, Bucharest, Romania
[76] National Institute of Science Education and Research, Bhubaneswar, India
[77] Niels Bohr Institute, University of Copenhagen, Copenhagen, Denmark
[78] Nikhef, National Institute for Subatomic Physics, Amsterdam, Netherlands
[79] Nuclear Physics Group, STFC Daresbury Laboratory, Daresbury, United Kingdom
[80] Nuclear Physics Institute, Academy of Sciences of the Czech Republic, Řež u Prahy, Czech Republic
[81] Oak Ridge National Laboratory, Oak Ridge, TN, United States
[82] Petersburg Nuclear Physics Institute, Gatchina, Russia
[83] Physics Department, Creighton University, Omaha, NE, United States
[84] Physics Department, Panjab University, Chandigarh, India
[85] Physics Department, University of Athens, Athens, Greece
[86] Physics Department, University of Cape Town, Cape Town, South Africa
[87] Physics Department, University of Jammu, Jammu, India
[88] Physics Department, University of Rajasthan, Jaipur, India
[89] Physik Department, Technische Universität München, Munich, Germany
[90] Physikalisches Institut, Ruprecht-Karls-Universität Heidelberg, Heidelberg, Germany
[91] Politecnico di Torino, Turin, Italy
[92] Purdue University, West Lafayette, IN, United States
[93] Pusan National University, Pusan, South Korea
[94] Research Division and ExtreMe Matter Institute EMMI, GSI Helmholtzzentrum für Schwerionenforschung, Darmstadt, Germany
[95] Rudjer Bošković Institute, Zagreb, Croatia
[96] Russian Federal Nuclear Center (VNIIEF), Sarov, Russia
[97] Russian Research Centre Kurchatov Institute, Moscow, Russia
[98] Saha Institute of Nuclear Physics, Kolkata, India
[99] School of Physics and Astronomy, University of Birmingham, Birmingham, United Kingdom
[100] Sección Física, Departamento de Ciencias, Pontificia Universidad Católica del Perú, Lima, Peru
[101] Sezione INFN, Bari, Italy
[102] Sezione INFN, Bologna, Italy
[103] Sezione INFN, Cagliari, Italy
[104] Sezione INFN, Catania, Italy
[105] Sezione INFN, Padova, Italy
[106] Sezione INFN, Rome, Italy
[107] Sezione INFN, Trieste, Italy
[108] Sezione INFN, Turin, Italy
[109] SUBATECH, Ecole des Mines de Nantes, Université de Nantes, CNRS-IN2P3, Nantes, France

[110] Suranaree University of Technology, Nakhon Ratchasima, Thailand
[111] Technical University of Split FESB, Split, Croatia
[112] The Henryk Niewodniczanski Institute of Nuclear Physics, Polish Academy of Sciences, Cracow, Poland
[113] The University of Texas at Austin, Physics Department, Austin, TX, USA
[114] Universidad Autónoma de Sinaloa, Culiacán, Mexico
[115] Universidade de São Paulo (USP), São Paulo, Brazil
[116] Universidade Estadual de Campinas (UNICAMP), Campinas, Brazil
[117] University of Houston, Houston, TX, United States
[118] University of Jyväskylä, Jyväskylä, Finland
[119] University of Liverpool, Liverpool, United Kingdom
[120] University of Tennessee, Knoxville, TN, United States
[121] University of Tokyo, Tokyo, Japan
[122] University of Tsukuba, Tsukuba, Japan
[123] University of Zagreb, Zagreb, Croatia
[124] Université de Lyon, Université Lyon 1, CNRS/IN2P3, IPN-Lyon, Villeurbanne, France
[125] V. Fock Institute for Physics, St. Petersburg State University, St. Petersburg, Russia
[126] Variable Energy Cyclotron Centre, Kolkata, India
[127] Vestfold University College, Tonsberg, Norway
[128] Warsaw University of Technology, Warsaw, Poland
[129] Wayne State University, Detroit, MI, United States
[130] Wigner Research Centre for Physics, Hungarian Academy of Sciences, Budapest, Hungary
[131] Yale University, New Haven, CT, United States
[132] Yonsei University, Seoul, South Korea
[133] Zentrum für Technologietransfer und Telekommunikation (ZTT), Fachhochschule Worms, Worms, Germany

Acknowledgements

The Collaboration wishes to thank the following persons for their contribution to the preparation of this TDR:
A. Augustinus, M. Berger, F. Böhmer, F. Carena, F. Costa, S. Dørheim, J. Hehner, H. D. Hernández, A. Jusko, M. Krivda, P. Martinengo, A. Di Mauro, T. Morhardt, R. de Oliveira, E. Oliveri, F. Raviel, L. Ropelewski, G. Scioli, M. Van Stenis, A. Tauro and A. Wasem.

References

Summary

[1] ALICE Collaboration. *Upgrade of the ALICE Experiment: Letter Of Intent*. CERN-LHCC-2012-012 / LHCC-I-022. 2012. URL: http://cds.cern.ch/record/1475243/.

[2] ALICE Collaboration. *Upgrade of the ALICE Read-Out and Trigger System*. Technical Design Report, CERN-LHCC-2013-019, ALICE-TDR-015. 2013. URL: http://cds.cern.ch/record/1603472.

References for Chapter 1

[1] ALICE Collaboration. "The ALICE experiment at the CERN LHC". In: *JINST* 3.08 (2008), S08002. DOI: 10.1088/1748-0221/3/08/S08002.

[2] ALICE Collaboration. *Upgrade of the ALICE Experiment: Letter Of Intent*. CERN-LHCC-2012-012 / LHCC-I-022. 2012. URL: http://cds.cern.ch/record/1475243/.

[3] ALICE Collaboration. *Upgrade of the ALICE Inner Tracking System*. Technical Design Report, CERN-LHCC-2013-024, ALICE-TDR-017. 2013. URL: http://cds.cern.ch/record/1625842.

[4] ALICE Collaboration. *Technical Design Report of the Time Projection Chamber*. CERN/LHCC 2000-001. 2000. URL: https://edms.cern.ch/document/398930/1.

[5] ALICE TPC Collaboration. "The ALICE TPC, a Large 3-Dimensional Tracking Device with Fast Read-out for Ultra-high Multiplicity Events". In: *Nucl. Instr. Meth. A* 622.1 (2010), pp. 316–367. DOI: 10.1016/j.nima.2010.04.042.

References for Chapter 2

[1] ALICE Collaboration. *Technical Design Report of the Time Projection Chamber*. CERN/LHCC 2000-001. 2000. URL: https://edms.cern.ch/document/398930/1.

References for Chapter 3

[1] ALICE TPC Collaboration. "The ALICE TPC, a Large 3-Dimensional Tracking Device with Fast Read-out for Ultra-high Multiplicity Events". In: *Nucl. Instr. Meth. A* 622.1 (2010), pp. 316–367. DOI: 10.1016/j.nima.2010.04.042.

References for Chapter 4

[1] ALICE Collaboration. *Upgrade of the ALICE Experiment: Letter Of Intent*. CERN-LHCC-2012-012 / LHCC-I-022. 2012. URL: http://cds.cern.ch/record/1475243/.

[2] F. Sauli. "GEM: A new concept for electron amplification in gas detectors". In: *Nucl. Instr. Meth. A* 386.2-3 (1997), pp. 531–534. DOI: 10.1016/S0168-9002(96)01172-2.

[3] R. Veenhof. *Garfield - simulation of gaseous detectors*. 1984 - 2010. URL: http://garfield.web.cern.ch.

[4] F. V. Böhmer et al. "Simulation of Space-Charge Effects in an Ungated GEM-based TPC". In: *Nucl. Instr. Meth. A* 719.0 (2013), pp. 101–108. DOI: 10.1016/j.nima.2013.04.020.

[5] S. Bachmann et al. "Discharge studies and prevention in the gas electron multiplier (GEM)". In: *Nucl. Instr. Meth. A* 479.2-3 (2002), pp. 294–308. DOI: 10.1016/S0168-9002(01)00931-7.

[6] S. Blatt et al. "Charge transfer of GEM structures in high magnetic fields". In: *Nucl. Phys. B (Proc. Suppl.)* 150.0 (2006), pp. 155–158. DOI: 10.1016/j.nuclphysbps.2004.07.005.

[7] C. Altunbas et al. "Construction, test and commissioning of the triple-GEM tracking detectors for COMPASS". In: *Nucl. Instr. Meth. A* 490.1-2 (2002), pp. 177–203. DOI: 10.1016/S0168-9002(02)00910-5.

[8] B. Ketzer et al. "Performance of triple GEM tracking detectors in the COMPASS experiment". In: *Nucl. Instr. Meth. A* 535.1 (2004), pp. 314–318. DOI: 10.1016/j.nima.2011.06.028.

[9] B. Ketzer et al. "A triple-GEM detector with pixel readout for high-rate beam tracking in COMPASS". In: *Nuclear Science Symposium Conference Record, 2007. NSS '07. IEEE*. Vol. 1. Piscataway, NJ: IEEE, 2007, pp. 242–244. DOI: 10.1109/NSSMIC.2007.4436323.

[10] P. Abbon et al. "The COMPASS Experiment at CERN". In: *Nucl. Instr. Meth. A* 577.3 (2007), pp. 455–518. DOI: 10.1016/j.nima.2007.03.026.

[11] G. Bencivenni et al. "A triple GEM detector with pad readout for high rate charged particle triggering". In: *Nucl. Instr. Meth. A* 488.3 (2002), pp. 493–502. DOI: 10.1016/S0168-9002(02)00515-6.

[12] Z. Fraenkel et al. "A hadron blind detector for the PHENIX experiment at RHIC". In: *Nucl. Instr. Meth. A* 546.3 (2005), pp. 466–480. DOI: 10.1016/j.nima.2005.02.039.

[13] M. G. Bagliesi et al. "The TOTEM T2 telescope based on triple-GEM chambers". In: *Nucl. Instr. Meth. A* 617.1-3 (2010), pp. 134–137. DOI: 10.1016/j.nima.2009.07.006.

[14] G. Bencivenni and D. Domenici. "An ultra-light cylindrical GEM detector as inner tracker at KLOE-2". In: *Nucl. Instr. Meth. A* 581.1-2 (2007), pp. 221–224. DOI: 10.1016/j.nima.2007.07.082.

[15] D. Abbaneo et al. "Characterization of GEM detectors for application in the CMS muon detection system". In: *Nuclear Science Symposium Conference Record (NSS/MIC), 2010 IEEE*. 2010, pp. 1416–1422. DOI: 10.1109/NSSMIC.2010.5874006.

[16] M. Alfonsi et al. "High-rate particle triggering with triple-GEM detector". In: *Nucl. Instr. Meth. A* 518.1-2 (2004), pp. 106–112. DOI: 10.1016/j.nima.2003.10.035.

[17] S. Duarte Pinto et al. "Progress on large area GEMs". In: *JINST* 4.12 (2009), P12009. DOI: 10.1088/1748-0221/4/12/P12009.

[18] M. Alfonsi et al. "Activity of CERN and LNF groups on large area GEM detectors". In: *Nucl. Instr. Meth. A* 617.1-3 (2010), pp. 151–154. DOI: DOI:10.1016/j.nima.2009.06.063.

[19] A. Balla et al. "Construction and test of the cylindrical-GEM detectors for the KLOE-2 Inner Tracker". In: *Nucl. Instr. Meth. A* (2013). DOI: 10.1016/j.nima.2013.08.021.

[20] D. Abbaneo et al. "The status of the GEM project for CMS high-η muon system". In: *Nucl. Instr. Meth. A* (2013). DOI: 10.1016/j.nima.2013.08.015.

[21] B. Ketzer. “A Time Projection Chamber for High-Rate Experiments: Towards an Upgrade of the ALICE TPC”. In: (2013). arXiv:1303.6694 [physics.ins-det].

[22] M. Alfonsi et al. “The triple-GEM detector for the M1R1 muon station at LHCB”. In: *Nuclear Science Symposium Conference Record (NSS/MIC), 2005, IEEE*. 2005, pp. 811–815. DOI: 10.1109/NSSMIC.2005.1596379.

[23] F. Garcia et al. “GEM-TPC Prototype for Beam Diagnostics of Super-FRS in NUSTAR Experiment - FAIR”. In: *Nuclear Science Symposium Conference Record (NSS/MIC), 2009, IEEE*. 2009, pp. 269–272. DOI: 10.1109/NSSMIC.2009.5401762.

[24] F. Garcia et al. “Prototype development of a GEM-TPC for the Super-FRS of the FAIR facility”. In: *Nuclear Science Symposium Conference Record (NSS/MIC), 2011, IEEE*. 2011, pp. 1788–1792. DOI: 10.1109/NSSMIC.2011.6154683.

[25] M. Kalliokoski et al. “Optical scanning system for quality control of GEM-foils”. In: *Nucl. Instr. Meth. A* 664.1 (2012), pp. 223–230. DOI: 10.1016/j.nima.2011.10.058.

References for Chapter 5

[1] M. Killenberg et al. “Charge transfer and charge broadening of GEM structures in high magnetic fields”. In: *Nucl. Instr. Meth. A* 530.3 (2004), pp. 251–257. DOI: 10.1016/j.nima.2004.04.241.

[2] Leszek Ropelewski. *Private communication*.

[3] S Bachmann et al. “Discharge studies and prevention in the gas electron multiplier (GEM)”. In: *Nucl. Instrum. Methods Phys. Res., A* 479.CERN-EP-2000-151. 2-3 (2000), 294–308. 25 p.

[4] Alessandro Cardini, Giovanni Bencivenni, and Patrizia De Simone. “The Operational Experience of the Triple-GEM Detectors of the LHCb Muon System: Summary of 2 Years of Data Taking”. In: (2012).

[5] M Alfonsi et al. “High-rate particle triggering with triple-GEM detector”. In: *Nucl. Instrum. Methods Phys. Res., A* 518 (2004), pp. 106–112.

[6] H. Schindler and R. Veenhof. *Garfield - simulation of tracking detectors*. 2014. URL: http://garfieldpp.web.cern.ch.

[7] *ANSYS®*. Academic Research, Release 13.0. 2012.

[8] I. Smirnov. *Interactions of particles with gases*. URL: http://consult.cern.ch/writeup/heed/.

[9] S.F. Biagi. “Monte Carlo simulation of electron drift and diffusion in counting gases under the influence of electric and magnetic fields”. In: *Nucl. Instr. Meth. A* 421 (1999), pp. 234–240.

[10] H. W. Ellis et al. “Transport properties of gaseous ions over a wide energy range”. In: *Atomic Data and Nuclear Data Tables* 17 (1976), pp. 177–210. DOI: 10.1016/0092-640X(76)90001-2.

[11] H. W. Ellis et al. “Transport properties of gaseous ions over a wide energy range II”. In: *Atomic Data and Nuclear Data Tables* 22 (1978), pp. 179–217. DOI: 10.1016/0092-640X(78)90014-1.

[12] H. W. Ellis et al. “Transport properties of gaseous ions over a wide energy range III”. In: *Atomic Data and Nuclear Data Tables* 31 (1984), pp. 113–151. DOI: 10.1016/0092-640X(84)90018-4.

[13] ALICE TPC Collaboration. “The ALICE TPC, a Large 3-Dimensional Tracking Device with Fast Read-out for Ultra-high Multiplicity Events”. In: *Nucl. Instr. Meth. A* 622.1 (2010), pp. 316–367. DOI: 10.1016/j.nima.2010.04.042.

[14] *Huntsman Advanced Materials (Schweiz) GmbH, Klybeckstrasse 200, 4057 Basel, Switzerland*. URL: http://www.huntsman.com/advanced_materials.

[15] C. Altunbas et al. "Construction, test and commissioning of the triple-GEM tracking detectors for COMPASS". In: *Nucl. Instr. Meth. A* 490.1-2 (2002), pp. 177–203. DOI: 10.1016/S0168-9002(02)00910-5.

[16] S. Bachmann et al. "Discharge studies and prevention in the gas electron multiplier (GEM)". In: *Nucl. Instr. Meth. A* 479.2-3 (2002), pp. 294–308. DOI: 10.1016/S0168-9002(01)00931-7.

References for Chapter 6

[1] ALICE Collaboration. *Technical Design Report of the Time Projection Chamber*. CERN/LHCC 2000-001. 2000. URL: https://edms.cern.ch/document/398930/1.

[2] ALICE TPC Collaboration. "The ALICE TPC, a Large 3-Dimensional Tracking Device with Fast Read-out for Ultra-high Multiplicity Events". In: *Nucl. Instr. Meth. A* 622.1 (2010), pp. 316–367. DOI: 10.1016/j.nima.2010.04.042.

[3] P. Moreira et al. "The GBT Project". In: *Proceedings of the Topical workshop on electronics for particle physics in Paris, France, September 2125* (2009), pp. 342–346. DOI: 10.5170/CERN-2009-006.

[4] J. Troska et al. "The Versatile Transceiver Proof of Concept". In: *Proceedings of the Topical workshop on electronics for particle physics in Paris, France, September 2125* (2009), pp. 347–349. DOI: 10.5170/CERN-2009-006.

[5] ALICE Collaboration. *Upgrade of the ALICE Read-Out and Trigger System*. Technical Design Report, CERN-LHCC-2013-019, ALICE-TDR-015. 2013. URL: http://cds.cern.ch/record/1603472.

[6] ALICE Collaboration. "Centrality dependence of the charged-particle multiplicity density at mid-rapidity in Pb-Pb collisions at $\sqrt{s_{\mathrm{NN}}} = 2.76\,\mathrm{TeV}$". In: *Phys. Rev. Lett.* 106 (2011), p. 032301. DOI: 10.1103/PhysRevLett.106.032301.

[7] ALICE Collaboration. "Charged-particle multiplicity density at mid-rapidity in central PbPb collisions at $\sqrt{s_{NN}} = 2.76\,\mathrm{TeV}$". In: *Phys. Rev. Lett.* 105 (2010), p. 252301. DOI: 10.1103/PhysRevLett.105.252301.

[8] J. Wiechula. "Commissioning and Calibration of the ALICE TPC". PhD thesis. Goethe-Universität Frankfurt am Main, 2009.

[9] H. K. Soltveit et al. "The preamplifier-shaper for the ALICE TPC-Detector". In: *Nucl. Instr. Meth. A* 676.0 (2012), pp. 106–119. DOI: 10.1016/j.nima.2012.02.012.

[10] H. Stelzer et al. *The ALICE TPC Readout Chamber: From Prototypes to Series Production*. ALICE-INT-2003-017. 2003. URL: https://edms.cern.ch/document/384259.

[11] M. De Gaspari. "Systems-on-Chip (SoC) for applications in High-Energy Physics". PhD thesis. Ruprecht-Karls-Universität Heidelberg, 2012.

[12] G. Trampitsch. "Design and Characterization of an Analogue Amplifier for the Readout of Micro-Pattern Gaseous Detectors". PhD thesis. Graz University of Technology, 2007.

[13] L. Jönsson. *Front end electronics for a TPC at future linear colliders*. EUDET-Memo-2010-30. 2010. URL: http://www.eudet.org/e26/e28/e86887/e105928/EUDET-Memo-2010-30.pdf.

[14] D. A. Huffman. "A Method for the Construction of Minimum-Redundancy Codes". In: *Proc. IRE* 40.9 (1952), pp. 1098–1101. DOI: 10.1109/JRPROC.1952.273898.

[15] *Mass production Tests of the ALICE TPC Front End Electronics*. 2007. URL: http://ep-ed-alice-tpc.web.cern.ch/ep-ed-alice-tpc/testing.htm.

References for Chapter 7

[1] ALICE Collaboration. *Technical Design Report of the Time Projection Chamber*. CERN/LHCC 2000-001. 2000. URL: https://edms.cern.ch/document/398930/1.

[2] ALICE Collaboration. *Performance of the ALICE Experiment at the CERN LHC*. 2014. arXiv:1402.4476 [nucl-ex].

[3] ALICE Collaboration. "Centrality Dependence of Charged Particle Production at Large Transverse Momentum in Pb–Pb Collisions at $\sqrt{s_{\mathrm{NN}}} = 2.76$ TeV". In: *Phys. Lett. B* 720.1-3 (2013), pp. 52–62. DOI: 10.1016/j.physletb.2013.01.051.

[4] ALICE TPC Collaboration. "The ALICE TPC, a Large 3-Dimensional Tracking Device with Fast Read-out for Ultra-high Multiplicity Events". In: *Nucl. Instr. Meth. A* 622.1 (2010), pp. 316–367. DOI: 10.1016/j.nima.2010.04.042.

[5] A. Ortiz Velasquez. "Production of pions, kaons and protons at high p_T in $\sqrt{s_{\mathrm{NN}}} = 2.76$ TeV Pb-Pb collisions". In: *Nucl. Phys. A* 904-905.0 (2013), pp. 763c–766c. DOI: 10.1016/j.nuclphysa.2013.02.129.

[6] ALICE Collaboration. *Upgrade of the ALICE Experiment: Letter Of Intent*. CERN-LHCC-2012-012 / LHCC-I-022. 2012. URL: http://cds.cern.ch/record/1475243/.

[7] ALICE Collaboration. *Upgrade of the ALICE Inner Tracking System*. Technical Design Report, CERN-LHCC-2013-024, ALICE-TDR-017. 2013. URL: http://cds.cern.ch/record/1625842.

[8] P. Christiansen et al. "The influence of detector effects on TPC performance". In: *Nucl. Instr. Meth. A* 609.1 (2009), pp. 149–155. DOI: 10.1016/j.nima.2009.08.052.

[9] G. Van Buren et al. "Correcting for distortions due to ionization in the STAR TPC". In: *Nucl. Instr. Meth. A* 566.1 (2006), pp. 22–25. DOI: 10.1016/j.nima.2006.05.131.

[10] G. Van Buren. *private communication*.

[11] F. V. Böhmer et al. "Simulation of Space-Charge Effects in an Ungated GEM-based TPC". In: *Nucl. Instr. Meth. A* 719.0 (2013), pp. 101–108. DOI: 10.1016/j.nima.2013.04.020.

[12] M. Mager, S. Rossegger, and J. Thomas. *Composed correction framework for modeling the TPC field distortions in AliRoot*. ALICE-INT-2010-018, 2010. URL: https://edms.cern.ch/document/1113105/1/.

[13] S. Rossegger, B. Schnizer, and W. Riegler. "Analytical solutions for space charge fields in TPC drift volumes". In: *Nucl. Instr. Meth. A* 632.1 (2011), pp. 52–58. DOI: 10.1016/j.nima.2010.12.213.

[14] M. Mager, S. Rossegger, and J. Thomas. *The Langevin equation expanded to 2nd order and comments on using the equation to correct for space point distortions in a TPC*. ALICE-INT-2010-016, 2010. URL: https://edms.cern.ch/document/1108138/1.

[15] M. Mager, S. Rossegger, and J. Thomas. *Space-charge effects in the ALICE TPC: a comparison between expected ALICE performance and current results from the STAR TPC*. ALICE-INT-2010-017, 2010. URL: https://edms.cern.ch/document/1113087/1.

References for Chapter 8

[1] LHC Programme Coordination. *LHC Luminosity Plots for the 2010 Heavy-Ion Run. Website*. 2010. URL: http://lpc.web.cern.ch/lpc/lumiplots_ions_2010.htm.

[2] LHC Programme Coordination. *LHC Luminosity Plots for the 2011 Heavy-Ion Run. Website*. 2011. URL: http://lpc.web.cern.ch/lpc/lumiplots_ion.htm.

[3] The ALICE DAQ group. *ALICE Electronic Logbook. Website*. 2012. URL: https://alice-logbook.cern.ch/logbook.

[4] G. Bregliozzi. Private Communication. 2013.

[5] ALICE Collaboration. *Upgrade of the ALICE Experiment: Letter Of Intent*. CERN-LHCC-2012-012 / LHCC-I-022. 2012. URL: http://cds.cern.ch/record/1475243/.

[6] D. A. Huffman. "A Method for the Construction of Minimum-Redundancy Codes". In: *Proc. IRE* 40.9 (1952), pp. 1098–1101. DOI: 10.1109/JRPROC.1952.273898.

[7] T. Kollegger. "The ALICE high level trigger: The 2011 run experience". In: *Real Time Conference (RT), 2012 18th IEEE-NPSS*. 2012, pp. 1–4. DOI: 10.1109/RTC.2012.6418366.

[8] ALICE Collaboration. *Technical Design Report of the Time Projection Chamber*. CERN/LHCC 2000-001. 2000. URL: https://edms.cern.ch/document/398930/1.

[9] D. Decamp et al. "ALEPH: A detector for electron-positron annihilations at LEP". In: *Nucl. Instr. Meth. A* 294.1-2 (1990), pp. 121–178. DOI: 10.1016/0168-9002(90)91831-U.

[10] Walter Blum. *The ALEPH handbook*. CERN-ALEPH-89-077. Geneva: CERN, 1989. URL: http://cdsweb.cern.ch/record/227125.

[11] A. De Min et al. "Performance of the HPC calorimeter in DELPHI". In: *IEEE Trans. Nucl. Sci.* 42 (1995), pp. 491–498. DOI: 10.1109/23.467923.

[12] M. Ball et al. "Technical Design Study for the PANDA Time Projection Chamber". In: (2012). arXiv:1207.0013 [physics.ins-det].

[13] B. Ketzer. "A Time Projection Chamber for High-Rate Experiments: Towards an Upgrade of the ALICE TPC". In: (2013). arXiv:1303.6694 [physics.ins-det].

[14] J. Wiechula. "Commissioning and Calibration of the ALICE TPC". PhD thesis. Goethe-Universität Frankfurt am Main, 2009.

[15] ALICE TPC Collaboration. "The ALICE TPC, a Large 3-Dimensional Tracking Device with Fast Read-out for Ultra-high Multiplicity Events". In: *Nucl. Instr. Meth. A* 622.1 (2010), pp. 316–367. DOI: 10.1016/j.nima.2010.04.042.

References for Chapter 9

[1] J. F. C. A. Veloso et al. "THCOBRA: Ion back flow reduction in patterned THGEM cascades". In: *Nucl. Instr. Meth. A* 639.1 (2011), pp. 134–136. DOI: 10.1016/j.nima.2010.10.083.

[2] F. D. Amaro et al. "The Thick-COBRA: a new gaseous electron multiplier for radiation detectors". In: *JINST* 5.10 (2010), P10002. DOI: 10.1088/1748-0221/5/10/P10002.

[3] *SciEnergy Co. Ltd.* URL: http://www.scienergy.jp/.

[4] B. Yu et al. "Investigation of Chevron Cathode Pads for Position Encoding in Very High Rate, Gas Proportional Chambers". In: *IEEE Trans. Nucl. Sci.* 38.2 (1991), pp. 454–460. DOI: 10.1109/23.289339.

[5] Takayuki Sumiyoshi et al. "Development of a gaseous PMT with micro-pattern gas detectors". In: *Nucl.Instrum.Meth.* A639 (2011), pp. 121–125. DOI: 10.1016/j.nima.2010.10.032.

[6] P. Colas, I. Giomataris, and V. Lepeltier. "Ion backflow in the Micromegas TPC for the future linear collider". In: *Nucl. Instr. Meth. A* 535.1-2 (2004), pp. 226–230. DOI: 10.1016/j.nima.2004.07.274.

[7] S. Kane et al. *A STUDY OF MICROMEGAS WITH PREAMPLIFICATION WITH A SINGLE GEM*. World Scientfic. 2004.

[8] M. Vandenbroucke et al. *Discharge reduction technologies for Micromegas detectors in high hadron flux environments*. 2nd International Conference on Micro Pattern Gaseous Detectors. 2011.

[9] G. Charles et al. "Discharge studies in Micromegas detectors in low energy hadron beams". In: *Nucl.Instrum.Meth.* A648 (2011), pp. 174–179. DOI: 10.1016/j.nima.2011.05.056.

[10] M. Vandenbroucke. *Development and Characterization of Micro-Pattern Gas Detectors for Intense Beams of Hadrons*. Ph.D. Thesis, Universite Pierre et Marie Curie and Technische Universitat Munchen. 2012.

[11] G. Sekhniadze. *Construction and experience with a 2.4 x 1. m2 MMG chamber*. RD51 meeting, Zaragoza, 2013. 2013.

References for Chapter 10

[1] S. Schmeling. "Common tools for large experiment controls: A common approach for deployment, maintenance, and support". In: *IEEE Trans. Nucl. Sci.* 53.3 (2006), pp. 970–973. DOI: 10.1109/TNS.2006.873706.

[2] B. Franek and C. Gaspar. "SMI++: An Object Oriented Framework for Designing Distributed Control Systems". In: *IEEE Trans. Nucl. Sci.* 45.4 (1998), pp. 1946–1950. DOI: 10.1109/23.710969.

[3] *ETM professional control GmbH, A Siemens Company, Marktstrae 3, A-7000 Eisenstadt, Austria*. URL: http://www.etm.at.

[4] C. Gaspar, M. Dönszelmann, and Ph. Charpentier. "DIM, a portable, light-weight package for information publishing, data transfer and inter-process communication". In: *Computer Phys. Communi.* 140 (2001), pp. 102–109. URL: http://dim.web.cern.ch/dim/papers/CHEP/DIM.PDF.

References for Chapter 11

[1] ALICE TPC Collaboration. "The ALICE TPC, a Large 3-Dimensional Tracking Device with Fast Read-out for Ultra-high Multiplicity Events". In: *Nucl. Instr. Meth. A* 622.1 (2010), pp. 316–367. DOI: 10.1016/j.nima.2010.04.042.

[2] H. Müller. *SRS commercial status 2013*. Talk at the RD51 Collaboration Meeting, Zaragosa, Spain, July 1 – 6. 2013. URL: http://indico.cern.ch/contributionDisplay.py?contribId=129&sessionId=6&confId=258852.

References for Chapter A

[1] L. Betev and P. Chochula. *Definition of the ALICE Coordinate System and basic rules for Sub-Detector Components numbering*. ALICE-INT-2003-038. 2003. URL: https://edms.cern.ch/document/406391/2.

[2] ALICE Collaboration. "ALICE: Physics Performance Report, Volume II". In: *J. Phys.* G32 (2006), pp. 1295–2040. DOI: 10.1088/0954-3899/32/10/001.

List of Figures

List of Tables